Novel reductive alkali roasting for Cr^{6+}-free extraction of Cr_2O_3 from chromite ores

Lidia Escudero Castejón

Submitted in accordance with the requirements for the degree of
Doctor of Philosophy

The University of Leeds
School of Chemical and Process Engineering

November, 2018

ACKNOWLEDGEMENTS

Firstly, I express my gratitude to my supervisor, Professor Animesh Jha, for his guidance and supervision during this research project. I thank Prof. Jha for the opportunity of coursing my PhD studies forming part of the Minerals Research group under his supervision. I am also very grateful to my co-supervisor and Postdoc researcher of the Minerals Research group, Dr. Sergio Sanchez-Segado, for his valuable suggestions and continuous encouragement during the PhD process, including the writing stage. He has been not only a colleague, but also a real friend.

I would like to thank my research group colleagues: Kwabena Gyimah, Terry Makanyire and, specially, Stephen Parirenyatwa, with who I have shared the good and difficult moments of my studies and who has offered his help in innumerable occasions, and to Yotamu Hara, for his guidance on the early stages of the research project. I am also thankful to Mr. M. Javed, Mr. S. Lloyd, Mr S. Micklethwaite and Dr. T. Comyn and Jenny Forrester, for general laboratory assistance, XRF analysis support, SEM training and XRD training. I acknowledge, in general, the School of Chemical and Process Engineering for affording me the opportunity to complete my studies here.

I am grateful to my parents and my sister, Laura, and to all my friends, for supporting and encouraging me through my 4-years stay at the University of Leeds. A special thank you to Antonis, and of course, to Dimitris, Lina, Alejandro and Ana; because you all made me feel at home, and without you, Leeds wouldn't have been the same. Σαν το Λιντς, δεν έχει.

Finally, thanks to Giorgos, for his relentless support, patience and love; for making all this possible, and because I am sure the best is still to come.

ABSTRACT

Chromite ore is the raw material used in the manufacturing of ferrochromium, which is an important metallurgical product employed in the stainless-steel industry. Chromium-based chemicals have also a wide range of applications, including pigments industry, leather tanning processes and surface treatments. The production of chromium chemicals is based on the alkali roasting of chromite ore in oxidising atmosphere in order to extract chromium as water soluble alkali chromate (Na_2CrO_4, K_2CrO_4). The main drawback of this process is the inevitable generation of a hazardous processing waste containing highly toxic hexavalent chromium. This residue needs to be landfilled and presents a serious environmental concern due to the lethal effects of Cr^{6+} in flora and fauna.

With the purpose of avoiding the formation of highly toxic Cr^{6+}, a novel process for extraction of Cr_2O_3 based on the carbothermal reduction of chromite ore in the presence of alkali, is proposed. During the reductive alkali roasting (or alkali reduction) of chromite, iron is reduced to metallic form and chromium reacts with Na_2O to form sodium chromite ($NaCrO_2$). Reduced samples are subjected to wet magnetic separation obtaining a magnetic fraction rich in metallic iron and a non-magnetic fraction which contains the $NaCrO_2$ formed. The non-magnetic fraction is further treated to extract a Cr_2O_3-rich product, which may be used as raw material for manufacturing of high grade Cr_2O_3. 85.6% Cr_2O_3 recovery was achieved after chromite reduction with Na_2CO_3 and activated charcoal (1050°C, 2.5 hours), followed by magnetic separation and leaching of the non-magnetic fraction with water and 0.5 M sulfuric acid. A final 83.6% Cr_2O_3-rich product was obtained. This process does not generate toxic waste in gas, liquid or solid form, as the formation of Cr^{6+} is completely avoided by maintaining chromium in (3+)-state at all stages of the process.

The fundamentals of the different stages of the process were investigated, including the thermodynamics, kinetics and physico-chemistry of the reduction reaction as a function of the process parameters. Mass balance and energy balance, and the environmental aspects of the process were also studied based on the proposed flowsheet of the reductive alkali roasting process.

TABLE OF CONTENTS

LIST OF FIGURES

LIST OF TABLES

LIST OF PUBLICATIONS

A. PATENT AND PAPERS PUBLISHED

A patent for the novel alkali roasting reduction process presented and discussed in this manuscript has been filed. The details of the patent can be found herein:

https://patents.google.com/patent/WO2016139461A1/en?oq=PCT%2fGB2016%2f050533

The list of journal and conference papers published are also presented below.

- **Parirenyatwa, Stephen, Escudero-Castejon, Lidia, Sanchez-Segado, Sergio, Hara, Yotamu and Jha, Animesh (2015) 'Comparative study of alkali roasting and leaching of chromite ores and titaniferous minerals'. *Hydrometallurgy*.** https://doi.org/10.1016/j.hydromet.2015.08.002. This publication was written in collaboration with Mr. Stephen Parirenyatwa. The results of alkali roasting experiments with NaOH and KOH are presented in this paper, which discusses and compares the physical chemistry of the alkali roasting of chromite and ilmenite ores.
- **Escudero-Castejon, L., Sanchez-Segado, S., Parirenyatwa, S., et al. (2016) 'Formation of Chromium-Containing Molten Salt Phase during Roasting of Chromite Ore with Sodium and Potassium Hydroxides' Journal for Manufacturing Science and Production, 16(4), pp. 215-225.** https://doi.org/10.1515/jmsp-2016-0023. This in an extended publication based on a conference paper presented in the 10th International Conference on Molten Slags, Fluxes and Salts (May 2016, Seattle, Washington, USA). The manuscript includes a discussion on the role of the molten salt phase formed during roasting of chromite ores by studying the thermodynamic aspects involved, the reaction mechanism and phase analysis and the effect of alkali ration on the efficiency of the extraction.
- **Escudero-Castejon, L, Sanchez-Segado, S, Parirenyatwa, S, Hara, Y and Jha, A (2017) 'A Cr^{6+}-Free Extraction of Chromium Oxide from Chromite Ores Using Carbothermic Reduction in the Presence of Alkali', in *Applications of Process Engineering Principles in Materials Processing, Energy and Environmental Technologies*, Springer, pp. 179–188.** https://doi.org/10.1007/978-3-319-51091-0_16. Conference paper presented in the international conference TMS 2017: 146th Annual Meeting & Exhibition, February 26-March 2, 2017, San Diego, California, USA. The articles presents the main principles of the alkali reductive roasting of chromite ores, including the process flowsheet and the characterisation of the main streams involved [1].

- **Sanchez-Segado, S, Makanyire, T, Escudero-Castejon, L, Hara, Y and Jha, A (2015) 'Reclamation of reactive metal oxides from complex minerals using alkali roasting and leaching–an improved approach to process engineering'. Green Chemistry, 17(4), pp. 2059–2080.** https:/doi.org/10.1039/C4GC02360A. I collaborated in this review article which includes part of the results obtained from the study of alkali roasting of chromite ores in oxidative atmosphere.

B. PUBLICATIONS FOR FUTURE SUBMISSION

The papers listed below have been written and are going to be submitted for publication between September and December 2018.

- **L. Escudero-Castejon, S. Sanchez-Segado, S. Parirenyatwa and A. Jha 'Novel reductive roasting of chromite ores in the presence of alkali for Cr^{6+}-free extraction of Cr_2O_3.'** Based on the process flowsheet of the alkali reduction of chromite, presented in this paper, the mass and energy balances and the main environmental considerations of the process are discussed in this paper. Chapter 9 of the present manuscript contains most of the experimental results and discussion included in this paper.

- **L. Escudero-Castejon, S. Sanchez-Segado, S. Parirenyatwa and A. Jha 'The physical chemistry of the reductive alkali roasting chromite ore in the presence of an alkali salt.'** This paper discusses the alkali reduction of S.A. chromite ore, including thermodynamics, kinetics and mechanism analysis. It includes part of the results presented and discussed in Chapter 7 of the present manuscript.

Chapter 1

INTRODUCTION

Chapter content

The research project is contextualised, summarised and justified in this chapter. The subject of the research is presented, and the research problem is introduced alongside the general objective of the study. The structure of the thesis document is also defined in this introductory chapter and a summary of the contents of each chapter is included.

Chapter conclusions

The production of sodium chromate from chromite ores by the alkali roasting process in oxidative atmosphere represents a serious environmental hazard due to the generation of Cr^{6+}*-containing solid waste. The lethal effects of hexavalent chromium on flora, fauna and human beings have been extensively studied and confirmed, and therefore the management and landfilling of process waste with varying quantities of* Cr^{6+} *is a current environmental burden for the chrome industry. Based on this, the main objective of this investigation is to explore a new technology, based on the alkali roasting of chromite ores in reductive atmosphere, able to produce a* Cr_2O_3*-enriched material avoiding the generation of* Cr^{6+} *throughout the entire process.*

1.1. INTRODUCTION AND MAIN OBJECTIVE

Reactive metal, namely Cr, because of their multiple valences determined by the 3d-electronic structure, form a range of complex oxides in nature. Chromium is present in many different minerals, nevertheless, just chromite, which can be expressed with the general formula $(Fe^{2+}, Mg)(Cr, Al, Fe^{3+})_2O_4$, is used for commercial extraction of chromium [2,3]. Global economic growth in the last decades has caused an increasing demand for stainless steel and other chromium-containing high-technology alloys, which has triplicated the world total production of chromite ores and concentrates in the last 30 years [4], as shown in FIGURE 1-1. The global resources of shipping-grade chromite are more than 12 billion tonnes, and the world mine production of marketable chromite ore is 30.4 Mtpy; with South Africa and Kazakhstan being the main producers with 46% and 18% of the share, respectively [5]. The global stainless-steel production has increased from just under 20 million of metric tonnes in 2000 to 45 million in 2016.

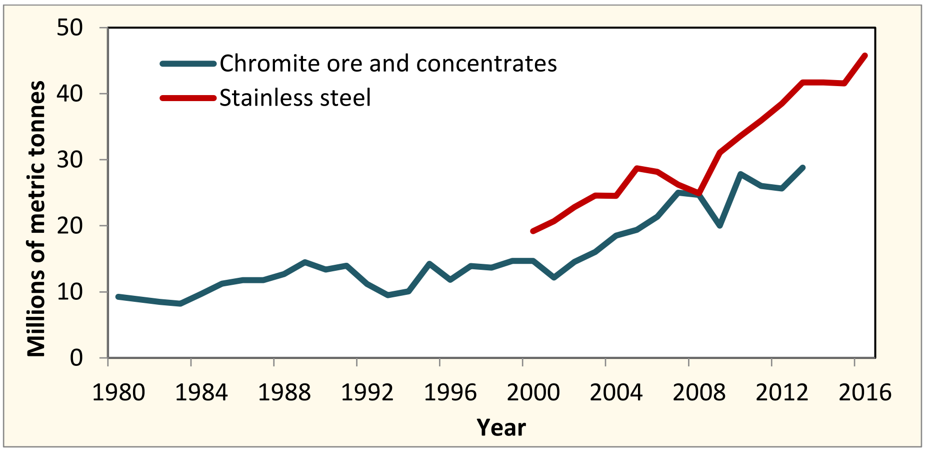

FIGURE 1-1. World total output of chromite ore and stainless steel from 1980 to 2015 [4,6].

With increasing environmental burden on industry, the future manufacturing of nonferrous metals is dependent on the improvement of the traditional beneficiation processes and/or the development of alternative processing routes which minimise the generation of hazardous wastes and the energy required to process the mineral feedstock [7]. Although the chromium chemicals industry has been reducing the environmental impact by designing safer disposal procedures for process waste and handling, the landfill sites require ongoing maintenance [8]. Only a fraction of the chromium industry wastes is recycled, which implies that there is no long-term solution for the management of these hexavalent chromium containing materials.

Chromium compounds are widely used in manufacturing of metals and production of chromium-based chemicals and refractory materials. Chromium is an important alloying element for increasing the oxidation resistance of iron and nickel in stainless steels, high-alloy steels and superalloys. China stands as the leading country in the chrome market, as it is the main chromium consumer and the main ferrochromium and stainless steel producer [5]. Different chromium chemicals are also used as pigments, mordants in the leather industry, in electroplating and surface treatments and for manufacturing of refractory materials [9].

The most important application of chromite is in the production of high-grade ferro-chromium, which is used in the metallurgical industry for manufacturing of stainless steels and chromium-containing metal alloys [10]. Ferro-chromium is produced by smelting of chromite ore in reducing atmosphere in an arc submerged furnace with coke at high temperatures (above 1600°C). With the aim of decreasing the high energy consumption of the smelting process, the partial solid state reduction of chromite is carried out in a rotary kiln at high temperature (1200°C to 1400°C), before smelting [11]. However, this process has its own limitations such as the high temperature required and the slow kinetics of chromium reduction process [12]. The reduction of chromium oxide takes place as shown in reaction (r.1):

$$Cr_2O_3\,(s) + 3\,[C]_{Fe} \leftrightarrow 2\,[Cr]_{Fe} + 3\,CO\,(g) \qquad \text{(r.1)}$$

where $[C]_{Fe}$ and $[Cr]_{Fe}$ represent the concentration of carbon and chromium in the alloy respectively. The equilibrium constant for reaction (eq.1) may be expressed as:

$$\mathrm{k} = \frac{(\mathrm{P_{CO}})^3 \cdot (\mathrm{a_{[Cr]_{Fe}}})^2}{(\mathrm{a_{[C]_{Fe}}})^3 \cdot \mathrm{a_{Cr_2O_3}}} \qquad \text{(eq.1)}$$

where a_i is the activity of each specie elevated to its respective stoichiometric coefficient; and Pco is the equilibrium partial pressure of CO gas. As it is evident from (eq.1), the activity of carbon must be kept high in order to retain the major amount of Cr in the alloy phase, as $a_{[C]_{Fe}} \propto P_{CO}$ and $a_{[Cr]_{Fe}} \propto (a_{[C]_{Fe}})^{\frac{3}{2}}$ if $a_{Cr_2O_3}$ and Pco are considered fixed at a given temperature. However, the presence of high amounts of carbon may lead to the formation of chromium carbides which are undesirable for the formability of stainless steel products. Moreover, the production of Fe-Cr needs expensive metallurgical coke, cannot use chromite fines and requires a great supply of energy for operating the electric arc furnace [13].

Besides the production of ferrochromium, various oxidative processes such as soda-ash roasting [14], acid leaching [15,16], alkali leaching [17] and alkali fusion [18], have been developed for the processing of chromite in order to produce sodium chromate (Na_2CrO_4).

Sodium chromate is the primary product used for the manufacturing of a wide range of chromium chemicals. Because of economic and technical reasons, just soda-ash roasting has been used worldwide on a commercial scale, either in a rotary kiln or in a rotary hearth furnace [2].

Le Chatelier, in the 19th century, first applied alkali roasting in oxidising conditions for the extraction of sodium chromate from chromite ores [2,19]. This discovery set the basis for the industrial process which is still practiced today. The application of the alkali roasting process to the extraction of different metal oxides, such as Ti, Al or V, from complex minerals has also been investigated with satisfactory results [20,21,22,23,24,25,26].

Worldwide manufacturing of sodium chromate, sodium dichromate, chromic acid and many other chromium chemicals relies on the alkali roasting of chromite in oxidising conditions, which yields water-soluble sodium chromate. The process of oxidative roasting of chromite ore in the presence of alkali salts is based on the oxidation of Cr^{3+} to Cr^{6+} and subsequent combination with the alkali metal to form water soluble chromates (Na_2CrO_4, K_2CrO_4). During the traditional roasting process, chromite is reacted with sodium carbonate in oxidising conditions, at a typical roasting temperature of 1100-1200°C (Maliotis 1996), to form sodium chromate following equation (r.2).

$$FeCr_2O_4\,(s) + 2\,Na_2CO_3\,(s) + 7/4\,O_2\,(g) \rightarrow 2\,Na_2CrO_4\,(s) + 1/2\,Fe_2O_3\,(s) + 2\,CO_2\,(g) \qquad (r.2)$$

The roasted material is subsequently leached with water in order to selectively solubilise sodium chromate. The remaining insoluble solid, known as chromite ore processing residue (COPR), mainly contains iron oxide, magnesium oxide, insoluble silicates and unreacted chromite. The unreacted chromite core retains Cr^{6+} ions which are very difficult to leach completely [8,27]. Silica is often present in chromite and it can vary between 2 wt.% in S. African ores and more than 8 wt.% in lower grades of chromites, used for chemicals manufacture. As a result of increasing silica, a viscous silicate liquid is formed during the roasting, which limits the oxygen transport during the oxidation reaction; and it also increases the consumption of alkali as it is required to neutralize silica [24,28]. Although the South African (S.A.) ores are most widely used, there is a general tendency in the sector to use indigenous resources for chromium chemicals, which has then implications on using more energy for handling and managing chromium-(VI) wastes. As a result, the extraction efficiency of chromium decreases with increasing silica content [29]. The landfilling of the COPR generated is an important source of hexavalent chromium, as the waste typically contains approximately 0.1-0.2 wt.% Cr^{6+} which remains entrapped within the solid residue after water leaching.

Hexavalent chromium is highly hazardous not only to human beings but also to aquatic environment, soil, flora and fauna [30], and therefore, the pollution-related problem associated with waste disposal has not been eliminated and it represents the main limitation of the alkali roasting process.

Previous investigations on alkali roasting of chromite ores have focused on the study of the thermodynamics and optimization of the process parameters in order to maximize chromium extraction and minimize toxic waste generation [28,31,32,33,34,35]. Sodium and potassium hydroxide leaching of chromite ore at moderate temperatures (320-400°C) have also been recently developed by [36]. The parameters affecting the degree of extraction include chromite ore composition, roasting temperature and time, oxygen potential and the origin and quantity of gangue materials present in the ore.

Considering the environmental problems caused by solid Cr^{6+}-containing waste from soda-ash roasting and the disadvantages of the current ferrochrome process, a new process for extraction of Cr_2O_3 from chromite ore was the subject of this investigation. The process has been designed focusing on avoiding the generation of Cr^{6+} by maintaining chromium as Cr^{3+} through the entire process. This is achieved by subjecting the chromite ore feedstock to roasting at moderate temperatures between 950 °C to 1050°C under reducing atmosphere and in the presence of alkali.

The first step of the process consists on the chromite carbothermic reduction in the presence of alkali. The reaction of chromium oxide with Na_2CO_3 to form sodium chromite ($NaCrO_2$) occurs under reducing conditions with simultaneous reduction of iron oxides to metallic iron, following reaction (r.3).

$$FeCr_2O_4\ (s) + Na_2CO_3\ (s) + 2\ C\ (s) \rightarrow Fe\ (s) + 2\ NaCrO_2\ (s) + 3\ CO\ (g) \qquad (r.3)$$

The reduction of chromite under these conditions does not suffer from the complex balance between high carbon activity and partial pressure of CO gas, since the chromium oxide activity is lowered by forming the alkali chromite. Furthermore, the generation of Cr^{6+}-species is eliminated in this process due to the presence of a reducing atmosphere throughout the alkali complexation process at elevated temperature.

Reduced samples are subjected to magnetic separation where a magnetic fraction containing the metallic iron formed is separated from a non-magnetic fraction rich in $NaCrO_2$. The non-magnetic fraction is subsequently treated via a series of leaching steps, and the result is a Cr_2O_3-rich product which can be further purified so as to obtain high grade chromium(III)-oxide (Cr_2O_3).

The Cr_2O_3-rich product derived from this process may be used as raw material for the manufacturing of chromium chemicals, chrome metal or chromium-containing alloys.

The **main objective of this investigation** is therefore to develop the principles of a new process methodology for the production of an enriched Cr_2O_3 material from chromite ore that does not yield Cr^{6+} containing waste in solid, liquid or gaseous forms, and can be used as starting material for the production of high-purity chrome metal or chrome compounds. The process eliminates in this way the risks associated with Cr^{6+} and excludes the dependency on waste handling.

1.2. DOCUMENT STRUCTURE

This document is divided in *11 Chapters*, whose content is summarised below. Abstract, acknowledgements, table of contents, list of figures and tables and bibliographic references are also included.

TABLE 1-1. Summary of the chapters content.

Chapter 1
INTRODUCTION

The research project is contextualised, summarised and justified in this chapter. The subject of the research is presented, and the research problem is introduced alongside the general objective of the study. The structure of the thesis document is also defined in this introductory chapter and a summary of the contents of each chapter is included.

Chapter 2
LITERATURE REVIEW

Chapter 2 provides an outline of the previous research on chromite mineral, applications of chromium-containing materials, and industrial processing of chromite ore by carbothermic reduction and alkali roasting. The framework for the research presented in this thesis is given in this chapter, and the specific objectives and the contribution of the current study to existing research are defined on the basis of the literature survey carried out.

Chapter 3
MATERIALS AND METHODS

Chapter 3 describes the chromite ores and rest of chemical reagents used in the experimental part of the study, as well as the experimental procedures employed in the different sets of tests. It also includes a description of the characterisation techniques used and the sample preparation protocols.

Chapter 4
CHARACTERISATION OF CHROMITE ORES

Three different chromite ores were used in the experimental part of this investigation. The characterisation of the chromite ores was carried out by using XRPD, EPMA, SEM-EDX and XRF analytical techniques. Phase mapping analysis of the Brazilian chromite ore was performed using SEM with Mineralogic Mining software attached. The results obtained for each chromite are presented and compared in this chapter.

Chapter 5
THERMODYAMIC ANALYSIS AND THERMAL DECOMPOSITION STUDY

Chapter 5 aims to present the main thermodynamic aspects related with the alkali reduction of chromite ore and the phase transformations taking place at different temperatures and chemical potentials. Gibbs free energy calculations and a phase equilibria study have been performed and compared for the alkali roasting of chromite in reducing and oxidising atmosphere. Isochronal and isothermal thermogravimetric experiments of chromite ore under different chemical potentials were performed, and the samples were characterised by XRPD and Rietveld refinement.

Chapter 6
ALKALI ROASTING OF CHROMITE ORE IN OXIDISING ATMOSPHERE

The physical chemistry of the alkali roasting of S.A. chromite ore in oxidative atmosphere was studied. Roasting experiments with NaOH/KOH at different reaction temperatures and times were performed, followed by water leaching for Na_2CrO_4 extraction. The processing residues were characterised by XRPD and SEM. The influence of the alkali ratio on the chromium extraction yield is also analysed in this chapter, and the results obtained with both hydroxides are compared. Sample characterisation and thermodynamic analysis, including phase diagrams, equilibrium calculations and computation of liquidus curves, are combined to study the formation of the molten salt phase and its effect on the Na_2CrO_4 extraction yield.

Chapter 7
REDUCTIVE ALKALI ROASTING OF CHROMITE ORES

The reductive alkali roasting of chromite ore is the key stage of the novel Cr^{6+}-free process. The physico-chemistry reduction reaction was studied by means of a number of batch reduction experiments in controlled oxygen-free atmosphere. The effect of process parameters, namely time, temperature, alkali ratio, carbon ratio, iron content and silica content, on the products of reaction and the microstructure of the reduced chromite was studied. XRPD and SEM-EDX were employed for characterisation of reduced samples. The kinetics of the reductive alkali roasting were studied by using experimental thermogravimetric data, and the mechanism of reduction was discussed.

Chapter 8
PRODUCTION OF Cr_2O_3-RICH MATERIAL FROM REDUCED SAMPES

Reduced samples are subjected to magnetic separation in order to obtain a non-magnetic fraction enriched in $NaCrO_2$ and depleted in iron. The magnetic and non-magnetic fractions were obtained and characterised, and the results are presented in this Chapter. The final Cr_2O_3-rich solid is produced by different leaching steps of the non-magnetic fraction in water and acid media. Different acids were tested during the acid leaching stage, and the effect of the leaching parameters on the purity of the final Cr_2O_3-rich product was studied and discussed.

Chapter 9

PROCESS FLOWSHEET, MASS AND ENERGY BALANCE AND ENVIRONMENTAL CONSIDERATIONS

Chapter 9 shows a detailed description of the alkali reduction process illustrated in the process flowsheet. The composition and masses of the main process streams obtained experimentally were used to calculate the mass balance of the process; and the energy balance of individual steps and the overall process is included in this chapter. The environmental considerations of the process, including the water consumption, characterisation of liquid waste and greenhouse gas emissions are discussed in this chapter. Additionally, the novel process is compared with traditional technology in terms of energy consumption and waste generation.

Chapter 10

REMEDIATION OF COPR WASTE AND Cr_2O_3 RECOVERY BY ALKALI REDUCTION

This chapter shows the characterisation of the COPR material produced and its treatment by the reductive alkali roasting process. The analysis of the reduced COPR samples is presented herein, as well as the results of their treatment by magnetic separation and leaching. The overall mass balance of the reduction of COPR was calculated and is presented with the process flowsheet. The chapter includes preliminary results obtained for the co-processing of COPR with chromite ores by alkali reduction.

Chapter 11

CONCLUSIONS AND FUTURE WORK

The last chapter of this document shows a summary of the conclusions of the research project. A section with the proposed future work is also included.

Chapter 2
LITERATURE REVIEW

Chapter content

Chapter 2 provides an outline of the previous research on chromite mineral, applications of chromium-containing materials, and industrial processing of chromite ore by carbothermic reduction and alkali roasting. The framework for the research presented in this thesis is given in this chapter, and the specific objectives and the contribution of the current study to existing research are defined on the basis of the literature survey carried out.

Chapter conclusions

The alkali roasting of chromite ores in oxidising atmosphere with different alkali salts is a well-stablished process for the production of chromium chemicals, including Cr_2O_3*, and it has been extensively investigated. The process has been improved along the last decades by increasing the extraction yield of* Na_2CrO_4 *and eliminating the addition of lime. However, the generation of processing waste containing* Cr^{6+} *in a range of concentrations and the need of low silica feedstock (<1wt.%* SiO_2*) required, are still important limitations of the process. The thermodynamics and kinetics of alkali roasting have been discussed by different authors, who have reported the reaction mechanism for the oxidation of chromite ore in the presence of alkali salts. On the other side, the production of ferro-chrome for stainless steel by smelting of chromite ore with coke is a high energy-demanding process which requires high temperatures (above 1600°C). In this context, the reductive alkali roasting process aims to extract a* Cr_2O_3*-rich product from chromite ores at lower temperature (900-1050°C) and avoiding any generation of* Cr^{6+}*-containing waste.*

A little piece of chromium history….

Chromium was discovered in 1761, when Johann Gottlob Lehmann described an orange-red mineral while visiting the Siberian Bersof gold mines in the Ural Mountains. This mineral turned out to be crocoite ($PbCrO_4$) [3]. Some years later, in 1797, Louis-Nicholas Vauquelin identified an oxide of an unknown metal combined in crocoite [37]. Due to its colourful compounds, the new metallic element was named “chrome” (chromium), adapted from the Greek word *χρώμα* meaning colour.

In 1798, a new chromium-bearing mineral, named chromite ($FeCr_2O_4$) later on, was found forming part of a heavy black mineral in the Ural Mountains, Russia [37]. Since then, chromite has been found in commercial quantities all around the world, and it continues to be the only raw material for all chromium products and compounds. The supply of chromite from the Ural Mountains, from 1797 to 1827, supported and helped the development of the paint industry, being chromite ore the primary raw material of the manufacturing of Cr-containing chemicals. Chromite deposits were later found in many different locations such as USA, Turkey and South Africa [2].

Paint pigments were the first main industrial use of chromium compounds, but many other applications soon emerged. The utilisation of potassium dichromate ($K_2Cr_2O_7$) as mordant in the dyeing industry and the commercial use of chromium salts in the leather industry for tanning processes are examples of this. Chromium has also played an important role in metallurgy as alloying element [3]. In 1865, the first patent for the use of chromium in steel manufacturing was issued, but it was not until the 1910’s and 1920’s that the alloying role of chromium with iron to produce stainless steel was developed in France, Germany, United Kingdom and the United States.

2.1. CHROMIUM APPLICATIONS

Chromium is considered a strategic metal with several direct applications, and there is a wide range of manufacturing processes in which chromium is used. In the early nineteenth century, chromium was primarily used as a component of paints and in tanning salts. Nowadays, 90% percent of the chrome ore is used in metallurgical industry [38], with chromium being a key element in stainless steels, superalloys for tools manufacture, armour-plating and jet engines making, among others. Chromium is added in iron alloys, nonferrous alloys and steel in order to enhance the hardenability or resistance to corrosion and oxidation [39]. The remainder is used in the chemical, refractory and foundry industries in applications like pigments, catalysts, leather processing and surface treatments.

The International Chromium Development Association (ICDA) categorises chromite ore applications by end use sector as *metallurgical*, *chemical* and *refractory and foundry salt*. The percentage of chromite used in each sector is indicated in Figure 2-1. The applications of chromium in the different industrial areas are explained in this chapter in further detail.

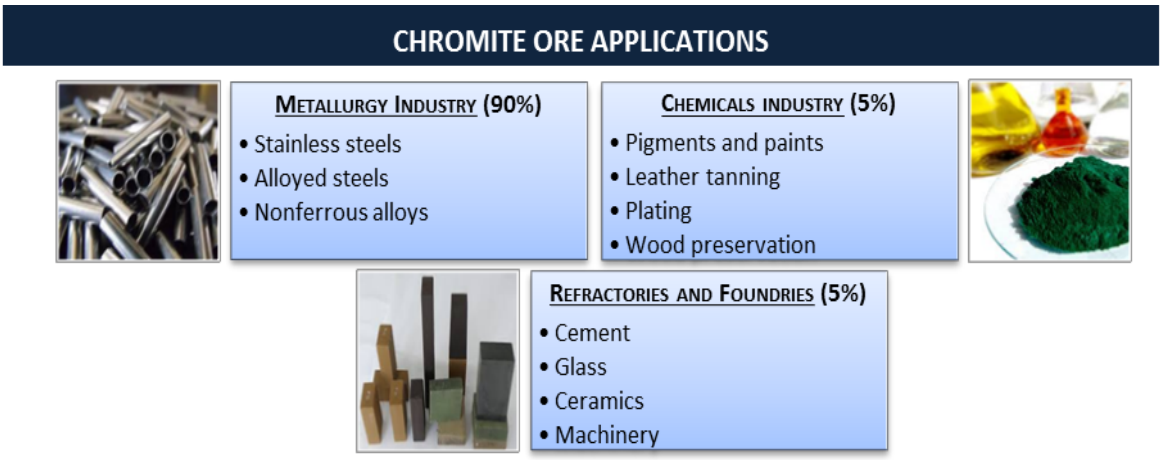

Figure 2-1. Classification of main chromite ore applications by end use. Adapted from ICDA [38].

2.1.1. METALLURGICAL INDUSTRY

Chromium is a key element in many ferrous and nonferrous alloys as it contributes to enhance mechanical properties such as hardenability, creep strength, impact values and resistance to corrosion and oxidation [40]. The addition of other alloying elements, such as nickel, manganese, silicon, vanadium, etc., and the carbon content have also an important effect on the properties and uses of chromium alloys [41]. Chromium metal and non-ferrous chromium alloys are broadly used in high-technology applications; while ferrochromium is the metallurgical product mainly used for manufacturing of stainless steel, which is a ferrous alloy with high resistance to corrosion and oxidation. The main metallurgical products of chromium are discussed below.

2.1.1.1. Stainless steel

The term stainless steel covers a range of ferrous alloys that are resistant to corrosion. Chromium is present in these alloys and is the element responsible of stainless steel strength and external chemical attack resistance. Cr-containing steel cannot be replaced in applications where rigidity of the material under high temperatures and resistance to abrasion and corrosion are required [40]. Chromium is highly reactive and able to form strong carbides providing high hardness strength and wear resistance. In stainless steels, chromium atoms replace iron atoms in substitutional lattice positions.

The formation of a continuous, non-porous and insoluble protective passive layer on the surface of the metal determines the resistance of these type of steels to external corrosion [42], which is reduced to minimum levels. For passivity to occur and remain stable, chromium content in steel should be at least 10.5% with a maximum of 1.2% carbon [42]. Corrosion resistance increases as the chromium content in Fe-Cr alloy increases [3]. This range of products may also contain other alloying elements such as nickel, titanium and molybdenum, which are added with the aim of providing technical characteristic to steels for special applications.

2.1.1.2. Ferrochromium

As mentioned before, ferrochromium is an industrial product used in the metallurgical industry for the manufacturing of stainless steels and chromium-containing metal alloys [10]. It contains a percentage of chromium that ranges significantly from 35% to 75%, and variable quantities of iron, carbon and other alloying elements. Maliotis (1996) [2] presented a classification of ferrochromium based on its chemical composition: *high-carbon ferrochromium*, *charge chrome*, *low-carbon ferrochromium* *and* *ferro-chromium-silicon*. Typical values for Cr, C and Si content for each type of ferrochrome can be seen in TABLE 2-1.

TABLE 2-1. Typical compositional ranges of Cr, C and Si in the different ferrochromium groups.

Weight (%)	**Cr (%)**	**C (%)**	**Si (%)**
High-carbon	62-72	4-9.5	Max 3.0
Charge chrome			
Low Fe	52-64	4-6	8-14
High Fe	52-58	6-8	Max 6.0
Low-carbon	67-75	0.75-0.025	Max 1.0
Ferro-chromium-silicon	34-38	0.06	38-42

The different types of ferrochromium are manufactured by high temperature reduction using metallurgical chromite ore as feedstock. The Cr:Fe ratio of the ore is an important factor which determines the reducibility of the ore and the chromium grade of the ferrochromium obtained. The main reducing agents used are carbon and silicon. The production of ferrochromium by pre-reduction of chromite ore followed by smelting in a submerged-arc furnace will be discussed in detail in section 2.3.

2.1.1.3. Chrome metal and nonferrous alloys

Chromium metal is employed in the manufacturing process of a wide range of products, being the production of high performance alloys its main application [43]. These alloys require high resistance to corrosion as they are used in high technology applications in the aeronautic industry, petrochemical processing, turbines manufacturing, etc. [38]. Chromite ore of metallurgical grade is used as feedstock in the production of chrome metal. There are two main processes for the production of chromium metal, the electrolytic process and the aluminothermic process [43]. The final chromium metal has a purity ranging from 99% to 99.4%, which can be further refined achieving a chromium grade of 99.8% [38].

Nonferrous alloys such as nickel and cobalt alloys may include chromium in their formulation in other to achieve higher resistance to corrosion and hardness. As example, Co-Cr-W alloys are widely used in the manufacturing of cutting tools.

2.1.2. CHEMICAL INDUSTRY

The range of applications of chromium compounds is rather broad, being used in pigments, tanning compounds, surface treatments, biocides and catalysts. The use of chromium in metal finishing processes and leather tanning are two of the main applications of chromium compounds [38].

Chromite ore is the main feedstock for the manufacturing of chromium chemicals. Alkali roasting at high temperature is the process traditionally used for extraction of chromium from the ore as water soluble sodium chromate (Na_2CrO_4). The process of roasting using alkali salts (usually sodium carbonate) is discussed in further detail in section 2.4. Sodium dichromate, which is the intermediate product from which the rest of chromium compounds are produced [38], is obtained from sodium chromate solution by lowering the pH below 7 (FIGURE 2-2). Darrie (2001) [44] listed the different conversion processes by which the different chromium-containing compounds are obtained, and represented these conversions using the E_h-pH diagram described by Pourbaix (1974) [45](see FIGURE 2-2). Conversions A to G in the diagram correspond to:

A) Chromate to dichromate
B) Trivalent chromium in ore to chromate
C) Chromic oxide to chromium metal
D) Dichromate to basic chromium sulphate
E) Dichromate to chromic oxide
F) Soluble trivalent chromium to metal by electrolysis
G) Chromic acid to metal by electrolysis

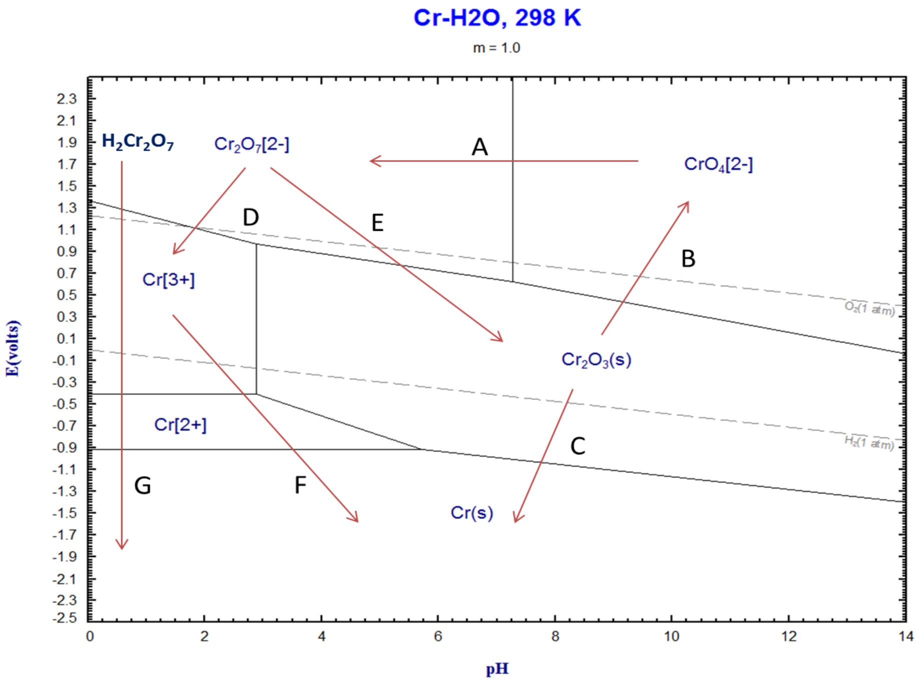

FIGURE 2-2. Modified Pourbaix Eh-pH diagram representing the manufacture of chromium chemicals. A-G: conversions for production of chromium compounds. Adapted from Darrie (2001) [44] using FactSage 6.4 software [46].

2.1.2.1. Main applications of chromium chemicals

Chromium compounds present a broad range of bright colours, and hence, they are extensively used in the pigments industry [9]. Chromic green, chrome yellow, chrome orange or zinc green are examples of the many pigments that are obtained from chromium chemicals. An excellent discussion of these groups of pigments was done by Patton (1973) [47]. Pigments are used in plastics, ceramics and paints, being also surface treatments an important application.

An important share of the sodium dichromate produced goes into the textile industry, where chromium compounds in (6+)-state, such as basic chromium sulphate, are employed for chrome tanning of leather [48]. In this process, chromium gets fixed into the hide providing water resistance and flexibility to the leather.

Chromium chemicals are also used in surface treatments and corrosion control, including applications such as plating, chromizing, anodizing of aluminium and treatment of zinc and magnesium [38]. Application of either chrome electroplating or chromium surface techniques gives excellent protection for corrosion to active metals, and therefore, chromium compounds are considered of high value by the metal finishing industry.

2.1.3. REFRACTORY INDUSTRY AND FOUNDRY SALTS

Characteristics of chromium like high melting point (2180°C), moderate thermal expansion, stable crystalline form at high temperatures and neutral chemical behaviour, make chromium a suitable refractory material [2]. Refractory materials are highly resistant at high temperatures and are also unaffected by thermal shock, abrasion or impact. The specifications for the different applications can vary significantly and therefore there is a wide choice of materials which satisfy special requirements [2]. Basic refractories can be made of chromite, dolomite, magnesite and combinations of magnesite and chromite. Chromite refractories are mostly used in the cement and glass industry, in the copper industry and in the steel sector [38].

Chromite sand, which is a chromite refractory material in granular form, is broadly employed for casting in the foundry industry (e.g. iron and copper casting). The automotive and heavy engineering sectors are two of the main areas of application of these materials. They present high resistance to metal penetration and slag attack [9] and therefore, may be used as part of the mould in which the liquid metal solidifies.

2.2. CHROMITE ORE

Chromite is a rock-forming mineral that occurs characteristically in ultrabasic rocks such as pyroxenite or peridotites and consists of a mixture of chromium and iron oxides with varying amounts of magnesium and aluminium. Chromite ore belongs to the spinel group, AB_2O_4, where X and Y represent divalent and trivalent metal ions, respectively. It has an ideal composition of $FeCr_2O_4$, however, the natural mineral is usually represented by the general formula $(Fe^{2+},Mg)(Cr,Al,Fe^{3+})_2O_4$, with sometimes small quantities of Mn, Ti and V included in the crystal structure. Chromic oxide content in chromite varies from approximately 15% to 65% due to isomorphous substitution of Cr^{3+} by Fe^{3+} and Al^{3+} [44,49,50]. The common gangue minerals associated with chromite are enstatite ($MgSiO_3$), olivine ($(Mg,Fe)_2SiO_4$), talc ($Mg_3Si_4O_{10}(OH)_2$) and serpentine ($(Mg,Fe)_3Si_2O_5(OH)_4$).

2.2.1. CHROMIUM-CONTAINING MINERALS

Chromium is a rock-forming element which occurs in spinels, simple silicates, aluminosilicates and complex salts [51]. It is present in complex oxide minerals, occasionally combined with iron oxides and other transition metals oxides such as manganese, titanium, vanadium, niobium and tantalum [26].

In most chromium-containing minerals, trivalent chromium can be found octahedrally coordinated with oxygen due to the high crystal field and octahedral site preference energies of Cr^{+3} ions [52]. Many Cr^{3+} compounds and minerals are isostructural with equivalent Al^{3+} and Fe^{3+} phases, with Cr^{+3} ions often replacing or being replaced by aluminium, iron or titanium ions in many rock-forming minerals. This can be explained by looking at the octahedral radius of Cr^{+3}, equal to 0.615 Å [53], which is in the range of values of Al^{+3} (0.68 Å), Fe^{+3} (0.78 Å) and Ti^{+4} (0.65 Å), all in tetrahedral coordination [54]. As a consequence, there is a wide variety of minerals which contain chromium in a percentage that may vary significantly. A list of some chromium-bearing minerals including their formula and crystal system are presented in TABLE 2-2.

FIGURE 2-3. Chromite ore [3].

As mentioned before, chromite ore [3] is the only source for commercial extraction of chromium, as rest of chromium-containing minerals are found in deposits that cannot be economically mined for chromium production (Maliotis 1996).

TABLE 2-2. List of chromium-bearing minerals including their mineral class, formula and crystal system. Adapted from Burns (1975) [55].

Mineral	Mineral Class	Formula	Crystal System
Barbertonite	Carbonate mineral	$Mg_6(Cr,Al)_2[(OH)_{16}\|CO_3]\cdot$	Hexagonal
Brezinaite	Sulphide mineral	Cr_3S_4	Orthorhombic
Calsbergite	Native elements	CrN	Isometric-hexoctahedral
Chromite	**Oxide mineral**	$\mathbf{(Mg,Fe)(Cr,Al,Fe)_2O_4}$	**Isometric-**
Crocoite	Anhydrous chromate	$PbCrO_4$	Monoclinic
Daubreelite	Sulfide mineral	$Fe^{+2}Cr_2S_4$	Isometric-hexoctahedral
Eskolaite	Oxide mineral	Cr_2O_3	Trigonal-hexagonal
Guyanaite	Oxide and hydroxide	CrOOH	Orthorhombic

Isovite	Native elements	$(Cr,Fe)_{23}C6$	Isometric-hexoctahedral
Knorringite	Nesosilicate	$Mg_3(Cr,Al)_2(SiO_4)_3$	Isometric-hexoctahedral
Lopezite	Anhydrous chromates	$K_2Cr_2O_7$	Triclinic
Magnesiochromite	Multiple oxides- spinel	$MgCr_2O_4$	Isometric-hexoctahedral
Mcconnellite	Multiple oxides	$CuCrO_2$	Trigonal-hexagonal
Stichtite	Carbonate mineral	$Mg_6Cr_2(CO_3)(OH)_{16} \cdot 4H_2O$	Trigonal-hexagonal
Uvarovite	Nesosilicate	$Ca_3Cr_2(SiO_4)_3$	Isometric-hexoctahedral
Vauquelinite	Compound	$Pb_2Cu(CrO_4)(PO_4)(OH)$	Monoclinic
Zincochromite	Multiple oxides-spinel	$ZnCr_2O_4$	Isometric-hexoctahedral

2.2.2. CHROMITE AS SOLID SOLUTION

According to the rule of parsimony stated by Linus Pauling in 1929 [56], some mineral structures may need to locate a certain number of ions while they tend to have limited different atomic positions within the crystal lattice [56]. As a consequence, when a mineral has a complex composition with limited structural positions, chemical elements substitute each other in specific atomic sites, giving as a result what is called solid solution [54]. This is applicable to chromite mineral, which is a solid solution resulting from the combination of six potential end members: $FeAl_2O_4$, $MgAl_2O_4$, $FeCr_2O_4$, $MgCr_2O_4$, Fe_3O_4 and $MgFe_2O_4$. A range of combinations of solid solution therefore emerges, which coexist in a given ore body. The non-fixed composition of chromite and its mineralogical properties are considerably different from one geographic location to another [2,57], having important effects on the treatment of the ore. The grade of a particular chromite, which determines its industrial application, can be classified based on the characteristics of the ore [40].

2.2.3. CRYSTAL STRUCTURE OF CHROMITE

Chromite spinel is considered a complex mixed-crystal system with oxygen atoms arranged in a face centred cubic closed-packed spinel lattice. All oxygen atoms are surrounded by three octahedral and one tetrahedral cation. Within one spinel unit cell, containing eight formula units, there are 64 tetrahedral and 32 octahedral sites with just 1/8 and 1/2 of them occupied by cations, respectively [52]. Hence, there are eight divalent cations (A^{+2} = Fe^{2+}, Mg^{+2}) occupying tetrahedral positions and 16 trivalent cations (B^{3+} = Cr^{3+}, Al^{3+}, Fe^{3+}) octahedrally coordinated with oxygen. The crystal structure of chromite can be seen in Figure 2-4.

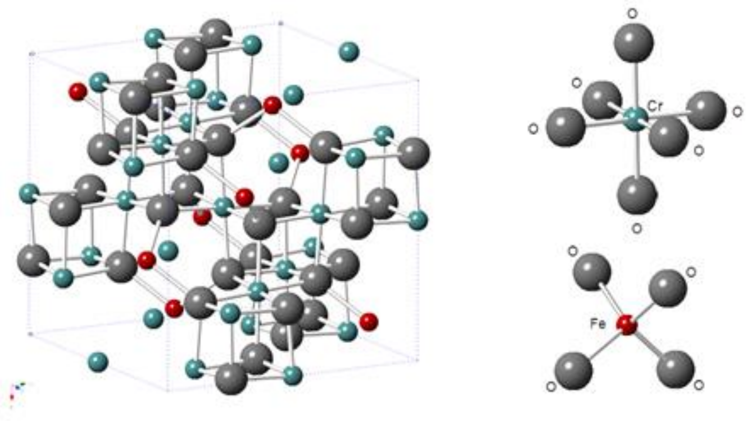

FIGURE 2-4. Crystal structure of chromite ore (O = grey, Fe = red, Cr = green) represented using CrystalMaker® software [58].

Spinels structures can present two different structural forms, normal and inverse spinels, which differ in the distribution of divalent and trivalent cations between tetrahedral and octahedral positions in the lattice. Every normal spinel unit cell (AB_2O_4) has 8 A^{2+} divalent ions occupying tetrahedral sites, while 16 B^{3+} trivalent cations are located in octahedral voids of the closed-packed array of oxygen atoms. In inverse spinels ($B(AB)O_4$) trivalent cations are located in tetrahedral voids and in half of the octahedral positions, with the other half of octahedral sites occupied by the totality of divalent cations [34].

$MgAl_2O_4$ and $FeCr_2O_4$ are examples of normal spinels while we can find inverse spinel in magnetite (Fe_3O_4) structure. In natural minerals, most spinels have an intermediate state between normal and inverse structural forms [54].

2.2.3.1. Octahedral site preference energies (OSPE)

The arrangement of cations between octahedral and tetrahedral sites in pure chromite structure cannot be explained by just looking at radius difference of elements [52]. Coordination number is supposed to increase with increasing ionic radius; hence trivalent chromium cations should be in tetrahedral sites and larger divalent iron in octahedral sites. Although, this is true for chromite spinel and other spinel members. It is clear that traditional principles of ionic radius do not dominate site occupancies by themselves, being stabilization energies a very important parameter to take into account in ions arrangement study and prediction [54].

By comparing Octahedral Site Preference Energies (OSPE) of the different cations, defined as the difference of Crystal Field Stabilization Energy (CFSE) of a cation for octahedral or tetrahedral sites, it is possible to explain arrangement of cations within the chromite crystal structure.

CFSE represents the stability gain as a result of the splitting of d-orbitals of transition metals into two different levels by rearrangement of d-electrons and filling of lower energy d-levels [52]. The larger the OSPE value for a certain metal cation is, the higher is its tendency to occupy octahedral voids in chromite crystal structure. However, it is not the only factor contributing to ions distribution within the lattice.

OSPE values of some transition metal ions in oxide structures are presented in TABLE 2-3. It can be observed that Cr^{3+} has a high OSPE value compared with Fe^{2+}, and therefore, $FeCr_2O_4$ is expected to have the cation distribution of normal spinel with chromium ions housed in octahedral voids and divalent iron tetrahedrally coordinated with oxygen.

TABLE 2-3. Octahedral site preference energies (OSPE) of transition metals in oxide structures. Adapted from Dunitz (1975) [59].

Cation	Cr^{3+}	Fe^{2+}	Fe^{3+}	V^{3+}	Mn^{3+}	Ti^{3+}	Ti^{4+}	Ni^{2+}
OSPE (kcal/mole)	-37.7	-4	0	-12.8	-22.8	-6.9	0	-20.6

Conversely, when a trivalent cation has low OSPE, such as Fe^{3+} with OSPE equal to zero, it may be expected to form inverse spinels, as its tendency to occupy octahedral sites is not very strong. This could explain why ferrite spinels tend to form inverse spinels or structures with intermediate structural configuration between normal and inverse. Thus, the inversion parameter may be predicted by looking at OSPEs values of transition metal cations in a certain spinel structure.

2.2.4. CLASSIFICATION OF CHROMITE ORES

By tradition, chromite ores were classified depending on their industrial use, being the requirements different for its several applications. Chromite ores were traditionally categorized in three grades [2]: *metallurgical*, *refractory* and *chemical grade*. These types could be used interchangeably to a limited extent [40]. Maliotis (1996) [2] introduced a new classification, based on the composition of the ore, which was divided in three categories: *high chromium chromite*, *high iron chromite* and *high aluminium chromite*. Each type is prevalently destined to a specific industrial area (high-chromium ore for metallurgical industry, high-iron ore for chemicals, and high-alumina ore for refractories), although, the applications of the different groups may overlap to some level as mentioned for the previous classification. Both classifications are presented in TABLE 2-4, where the main characteristics of the different groups are summarised.

Table 2-4. Characteristics of the different types of chromite ores classified by industrial use and chemical composition. Adapted from Maliotis (1996) [2].

		Type of deposit	**Chemical Composition**				**Observations**
			% Cr_2O_3	**Cr:Fe**	**% Al_2O_3**	**% SiO_2**	
A) DEPENDING ON INDUSTRIAL USE	Metallurgical Grade	Podiform and stratiform	> 40	> 1.5:1	---	< 3	---
	Refractory Grade	Podiform	33-38*	2-2.5:1	22-34	< 3	The combined value of %Cr_2O_3 and %Al_2O_3 must be higher than 57%.
	Chemical Grade	Stratiform	40-46	---	---	< 1	No restrictions regarding Cr:Fe ratio, being chromite content the main consideration.
B) DEPENDING ON CHEMICAL COMPOSITION	High Chromium	Podiform and stratiform	46-55	> 2:1	---	< 3	For metallurgical applications
	High Iron	Stratiform	40-46	1.5-2:1	---	< 1	For metallurgical and chemical applications
	High Aluminium	Podiform	33-38	2-2.5:1	22-34	< 1	For refractory applications

2.3. CARBOTHERMIC REDUCTION OF CHROMITE ORE FOR THE PRODUCTION OF HIGH-CARBON FERROCHROMIUM

As explained in section 2.2.1, ferrochromium is an important ferroalloy, and about 90% of the ferrochromium produced is employed in the manufacturing of stainless steels [38]. High-carbon ferrochromium is produced by carbothermic reduction of chromite in a submerged-arc furnace, and this process is one of the highest energy-consuming stages within the stainless steel production process [12].

The smelting process for ferrochromium production is a continuous process where reduction of both iron and chromium oxides present in chromite ore takes place.

The raw materials consist of chromite ore, a reducing agent and fluxes. A mixture of metallurgical coke and coal is used as reductant and some of the most common fluxes are quartz, slag from ferro-silicon-chromium smelting and bauxite [60]. The final chromium recovery in the alloy depends on the extent of metallization achieved and the chemical composition of the ore, especially in the Cr:Fe ratio [61]. Chromium oxide is reduced following reactions (r.4) and (r.5).

$$\frac{2}{3}\ Cr_2O_3\ (s) + \ 2\ C\ (s) \rightarrow \ \frac{4}{3}\ Cr\ (s) + \ 2\ CO\ (g) \qquad (r.4)$$

$$\frac{2}{3}\ Cr_2O_3\ (s) + \ \frac{18}{7}\ C\ (s) \ \rightarrow \ \frac{4}{21}\ Cr_7C_3\ (s) \ + \ 2\ CO\ (g) \qquad (r.5)$$

The smelting process has been intensively developed. Most investigations focused on the need of reducing the energy consumption and improving the quality of the alloy obtained. This ferrochromium production method places several limitations on the operational efficiency and product quality. Its main drawbacks are the high electrical energy requirement, the need of expensive metallurgical coke and the impossibility of using chromite fines [13]. Bearing this in mind, the pre-reduction stage prior to the smelting was adopted with the aim of overcoming these limitations. In the pre-reduction process, chromite ore and the reducing agent are mixed and converted to pellets, which are roasted in a rotary kiln at 1350ºC [12].

The pre-reduction process has been subject of many studies aiming to understand the kinetics and mechanism of chromite reduction by carbon, in order to maximise Cr recovery into the alloy with low levels of energy consumption. The main findings and conclusions achieved by previous authors in this area are discussed in this section.

2.3.1. ADVANTAGES AND DISADVANTAGES OF THE PRE-REDUCTION STAGE

Traditionally, about 60% of Fe and Cr metallization was obtained during the pre-reduction stage, with almost complete metallization of Fe and about 30% metallization of Cr [12].

This contributes to the decrease of the energy required during the smelting process. Besides that, other reasons that justify the need of pre-reducing the chromite ore. For example, the palletisation of raw materials prior to the pre-reduction process allows the treatment of abundant chromite fines not suitable for the submerged-arc furnace [62].

During the pre-reduction step, the use of cheaper sources of carbon as reductants is also possible. The cost associated to the carbon-rich raw material is reduced with part of the metallisation being achieved using cheaper reductants instead of the high quality metallurgical coke needed for the smelting process [63].

Finally, the Cr recovery in the submerged-arc furnace during smelting is higher, improving the quality of the ferrochrome produced [12]. Nevertheless, this process has also its own limitations. Dawson and Edwards (1986) [12] highlighted the low degree of reduction achieved as a consequence of the slow kinetics of the process, especially for Cr_2O_3 reduction. The reaction kinetics could be improved by increasing the operation temperature, but also this parameter is limited to 1350°C. Above 1350°C, there is partial melting due to the properties of the reactants at that temperature, causing ring formation in the rotary kiln and poor operation conditions. Consequently, many investigations have focused on the improvement of the reduction kinetics and the explanation of the reaction mechanism.

2.3.2. KINETICS AND REACTION MECHANISM OF THE CARBOTHERMIC REDUCTION OF CHROMITE ORES

Previous authors pointed out the importance of understanding the mechanism of reduction in the presence of carbon particles and the role of CO in this reaction.

Kekkonen (1995) [11] supported that diffusion of CO_2 through the product layer was the limiting step when chromite is roasted in the presence of carbon in Ar atmosphere at temperatures ranging between 1420°C and 1595°C. The following steps for the solid-gas reaction inside the pellets were proposed:

a. Boudouard reaction.
b. Transfer of CO from carbon surface to chromite particles surface.
c. Diffusion of gaseous reductant through the porous product layer of the particle to the reaction surface.
d. Absorption of CO, chemical reaction and desorption of the gaseous product (CO_2).
e. Diffusion of CO_2 through porous product layer to carbon surface. Diffusion of metallic and cationic species of Fe and Cr in the chromite lattice.
f. Diffusion of the gaseous reaction product to the outer gas phase of the pellet.

Several authors [12,63,64,65,66,67,68,69,70] have explained different mechanisms for the reduction of chromite with carbon at high temperatures.

Most publications agree in the fact that iron reduction occurs first, and chromium reduction starts once iron is in metallic form [63,68,70]. The reduction of iron is a fast process, whereas chromium reduction is more difficult to achieve and therefore significantly slower. An example of that is the work carried out by Dawson and Edwards (1986) [12] who observed that total metallisation of iron to metallic phase was rapidly achieved, while reduction of Cr_2O_3 was slow and incomplete. Chakraborty (2005) [63] studied the reduction of two chromite ores with different reductants (petroleum coke, devolatilized coke and graphite) at temperatures ranging between 900°C to 1300°C and concluded that reduction of chromium starts once Fe is completely reduced, being the two reduction processes controlled by different rate-limiting factors.

The reduction of chromite at 1300°C was studied by Algie and Finn (1984) [65], who concluded that the reaction proceeds in three different stages: reduction of Fe^{3+} to Fe^{2+}, reduction of Fe^{2+} to metallic iron and reduction of Cr^{3+} to metallic chromium. Xiao (2004) [69] proposed a more detailed chromite reduction mechanism which included the following steps:

1. Diffusion of CO gas to the chromite surface and inside the pellet.
2. Cation diffusion to the reaction sites in the chromite particle.
3. Reduction of Fe^{3+} to Fe^{2+} and Fe^{2+} to iron metal.
4. Nucleation of metallic Fe at the surface of the chromite particles.
5. Reduction of Cr^{3+} to metallic Cr.
6. Dissolution of metallic chromium into metallic iron and outward diffusion of CO_2.

Dawson and Edwards (1986) [12] obtained chromium and iron reduction curves with time when chromite was roasted at temperatures up to 1350°C. They proposed a mechanism based on ion diffusion in which Fe^{2+} and Cr^{3+} diffuse through a defective spinel lattice towards the surface of the grain, where metallization takes place. Fe^{2+} cations migration causes vacant sites on the spinel lattice enabling Cr^{3+} diffusion. However, once the usual M^{2+} to M^{3+} ratio is achieved in the new $Mg^{2+}/Al^{3+}/Cr^{3+}$ spinel, Cr^{3+} diffusion stops, which explains why complete metallization of chromium could not be accomplished. They concluded that neither diffusion through the product layer nor chemical reaction were the limiting steps. According to the ion diffusion model, the chemical composition of the mineral was found to be the limiting factor, with iron and aluminium-rich chromites yielding higher levels of metallization.

The analysis of the phases formed during reduction has also been discussed in different investigations. Perry (1988) [66] presented a point-defective model to explain the formation of different phases during the solid-state reduction of chromite with carbon, considering that CO is present at the surface of the particle.

This model explained the formation of distinct species by the exchange of cations between unit cells in a chromite particle. At the first stages of reaction, there is a core enriched in iron with some spinel cells deformed due to reduction of trivalent iron to divalent iron, which occurs at the surface of the grain. The formation of chromium and aluminium oxides and magnesium-chromium-aluminium spinel occurs after metallization of iron and reduction of Cr^{3+} to Cr^{2+}. The next step is the metallization of Fe^{2+} followed by reduction of Cr^{2+}.

Soykan (1991) [61] studied the reduction of chromite at 1416°C. They found concentration gradients in the outer regions of the chromite particle that suggested that Fe^{2+} and Cr^{3+} ions diffuse outwards and Cr^{2+}, Al^{3+} and Mg^{2+} diffuse inwards during the reaction (FIGURE 2-5). As previously explained by Dawson and Edwards (1986) [12], the stoichiometry of the unreacted spinel phase remains constant which explains the diffusion process.

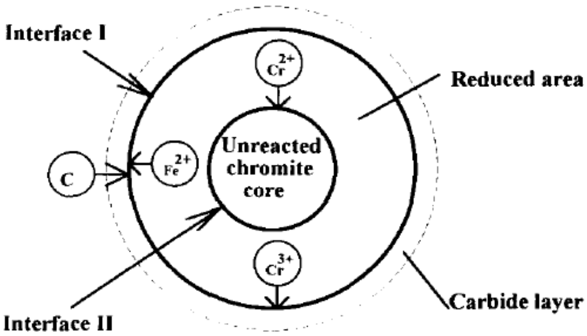

FIGURE 2-5. Schematic diagram of the reduction mechanism of chromite with carbon, as explained by Soykan (1991) [13,67].

The predominance phase diagram of the Fe-Cr-C system at 1350°C is presented in FIGURE 2-6. As seen in the diagram, the formation of carbide phases during chromite reduction is possible in the operating conditions and it has been reported by different authors. Rankin (1979) [71] studied the reduction of chromite ore with no gangue material using graphite and CO gas as reductants. The main product of the reduction was chromium-iron carbide $(Cr,Fe)_7C_3$ and it was found that iron was reduced preferentially when using both reducing agents.

The formation of carbides compounds, Cr_3C_2 or Cr_7C_3 could be seen in the reduction of synthetic chromite including Al and Mg [63]. In a recent publication by Wang (2014) [70], the formation of metallic species is described with the sequence Fe-C alloy, $(Fe,Cr)_7C_3$ and finally Fe-Cr-C alloys. On the other hand, Sundarmurti and Seshadri (1985) [72] studied the reduction of chromite in a range of temperatures ranging between 1513 K to 1583 K, and did not report the formation of carbide phases.

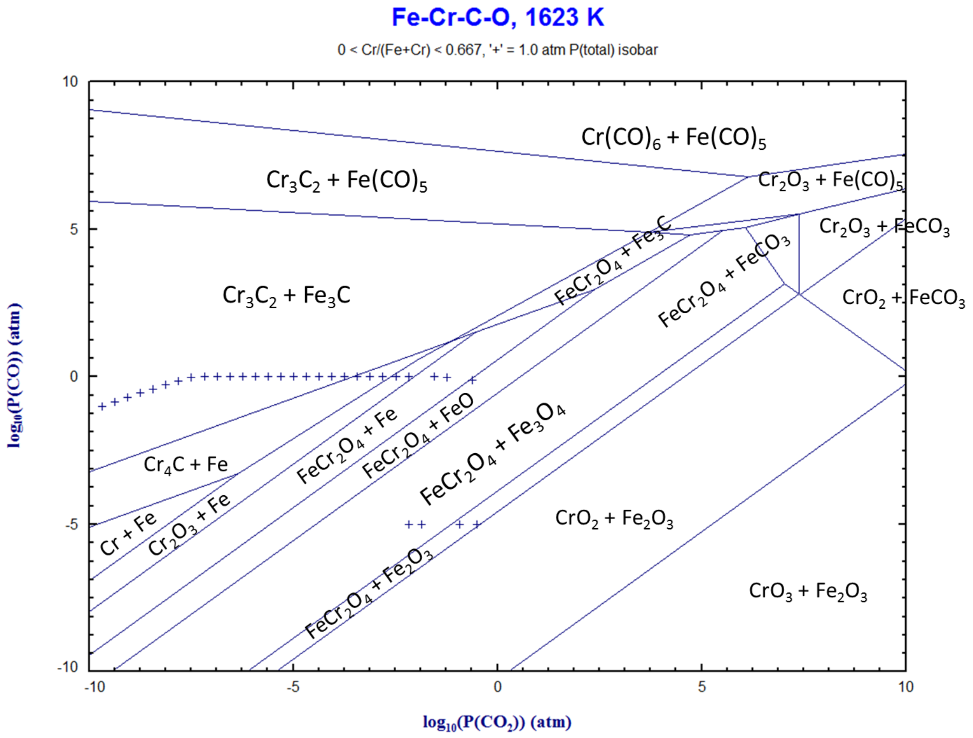

FIGURE 2-6. Predominance area diagram of the Fe-Cr-C-O system at 1623 K (1350°C). Represented using FactSage 6.4 software [46].

Kinetic studies on carbothermic reduction of chromite determined different rate-controlling steps. The kinetic model described by Soykan (1991) [61] determined that the interfacial area controlled the rate of the reaction when reduction is below 40%. Above 40%, diffusion was the rate-limiting step. The diffusion of oxygen after reduction of iron and chromium was pointed out by Murti and Seshadri (1982) [73] as the rate-controlling step, while Chakraborty (2005) [63] concluded that diffusion and either chemical reaction or nucleation were the limiting steps for iron and chromium reduction, respectively. Wang (2014) [70] concluded that nucleation was also limiting the rate of the first stage of the reaction, whereas the second step depended on the rate of crystallo-chemical transformations taking place.

2.3.3. ROLE OF SOLID CARBON AND CO AS REDUCING AGENTS

The reduction of chromite ore by direct reaction with solid carbon can be expressed by reaction (r.6):

$$FeCr_2O_4\,(s) + 4\,C\,(s) \rightarrow 2\,Cr\,(s) + Fe\,(s) + 4\,CO\,(g) \qquad (r.6)$$

Reduction can also occur by a gas/solid reaction between CO and the ore, according to reactions (r.7) and (r.8).

$M_2O_3 + 3\,CO \rightarrow 2\,M + 3\,CO_2\,(g)$ (r.7)

$C\,(s) + CO_2\,(g) \rightarrow 2\,CO\,(g)$ (r.8)

Previous authors pointed out the importance of understanding the mechanism of reduction in the presence of carbon particles and the role of CO in this reaction. Some publications [62,69,74] reported that reduction with CO is possible but the presence of solid carbon is also needed. Barcza (1971) [74] attributed this to the effect of solid carbon on the formation of carbide phases. From reduction experiments of chromite using carbon, CO or both as reductants, Xiao (2004) [69] concluded that solid carbon enhances the Boudouard reaction (r.8) by which CO_2 is converted to CO. Based on experimental results, Niayesh and Dippenaar (1992) [62] supported that the reduction of chromite by CO alone is not feasible, as the presence of fine solid carbon is necessary to maintain the low oxygen potentials in the gaseous phase during reduction. Kekkonen (1995) [11] supported that diffusion of CO_2 through the product layer was the limiting step when chromite is roasted in the presence of carbon in Ar atmosphere at temperatures ranging between 1420°C and 1595°C.

2.3.4. EFFECT OF PROMOTERS

With the aim of promoting chromite reduction, many investigations have studied the addition of fluxing agents, which may help achieving a good metal recovery with adequate furnace operation. The addition of silica was studied and is reported in bibliography [68,75,76,77]. Wang (2015) [77] suggested that silica and chromium may form a $CrO\text{-}SiO_2$ liquid phase which has a negative effect on the of chromium reduction.

Weber and Eric (2006) [76] concluded that the reduction was affected by the presence of silica at temperatures above 1400°C, but has no effect on the rate of iron metallisation. The effect of lime on the reduction of chromite ore was also studied by Ding (1997) and Wang (2015) [77,78], concluding that it can have a beneficial effect facilitating the reduction of chromite by promoting the diffusion of chromium cations. The same was found for Al_2O_3, while in the case of MgO addition, $MgCr_2O_4$ formation and poor chromium reduction were observed.

2.4. ALKALI ROASTING OF CHROMITE ORE

In this process, the extraction of chromium is achieved via roasting of the mineral with alkali salts (usually sodium carbonate). It is based on the conversion of Cr^{3+} to Cr^{6+} and combination with the alkali to form water soluble chromates. Roasting of chromite ore with alkali salts in oxidising atmosphere is the main process used for manufacturing of chromium chemicals.

As mentioned before in this report, the main drawback of the process is the generation of chromite ore processing residue (COPR) which contains hazardous hexavalent chromium and therefore represents a serious risk for the environment. With the aim of minimising waste generation, many investigations have focused on the optimization of the process parameters in order to maximize chromium extraction [17,26,28,29,32,79,80,81].

The parameters affecting the degree of extraction include chromite ore composition, roasting temperature and time, oxygen potential, the use of fillers and the origin and quantity of gangue materials present in the ore.

The traditional roasting process uses soda-ash (Na_2CO_3) as alkali. Chromite ore, soda-ash, filler materials and lime (when applicable) are mixed and fed into a hearth furnace or rotary kiln, where they are roasted for 4 hours at temperatures ranging between 1100°C and 1200°C [2]. Under these conditions, chromium is oxidized to Cr^{6+} state, which then solubilizes in water in the form of alkali chromate (e.g. Na_2CrO_4).

$$FeCr_2O_4\,(s) + 2\,Na_2CO_3\,(s) + \frac{7}{4}\,O_2\,(g) \rightarrow 2\,Na_2CrO_4\,(s) + \frac{1}{2}\,Fe_2O_3\,(s) + 2CO_2\,(g) \qquad (r.9)$$

The three main reactions occurring during soda-ash roasting are:

$$FeCr_2O_4\,(s) + \frac{1}{4}O_2\,(g) \rightarrow Cr_2O_3\,(s) + \frac{1}{2}\,Fe_2O_3\,(s) \qquad (r.10)$$

$$Cr_2O_3\,(s) + Na_2CO_3\,(s) + \frac{3}{2}\,O_2\,(g) \rightarrow 2\,Na_2Cr_2O_4\,(s) + CO_2\,(g) \qquad (r.11)$$

$$Na_2Cr_2O_4\,(s) + Na_2CO_3\,(s) + \frac{3}{2}O_2\,(g) \rightarrow 2\,Na_2CrO_4\,(s) + CO_2\,(g) \qquad (r.12)$$

Sodium chromate formed during roasting is selectively leached out with water from the roasted sample. The residue after water leaching is a Fe and Mg-rich phase which also contains trapped hexavalent chromium. Part of the COPR generated can be recycled back into the process as filler material. The rest is treated with acid prior to landfilling in order to reduce residual hexavalent chromium into trivalent chromium, which is less toxic and hazardous for the environment.

However, remaining Cr^{6+} it is usually present in the solid waste in varying concentrations [8,27]. This residue needs to be landfilled, which inevitably represents a hazardous source of hexavalent chromium, being this considered highly toxic and hazardous for human beings and the environment [30].

Sodium carbonate solution is converted to sodium dichromate by sulfuric acid treatment [82], following reaction (r.13), and further crystallisation. Sodium dichromate is the raw material employed for the manufacturing of the rest of chromium-containing chemicals.

$$2\,Na_2CrO_4\,(s) + H_2SO_4\,(aq) + H_2O\,(l) \rightarrow Na_2Cr_2O_7\cdot 2H_2O\,(aq) + Na_2SO_4\,(s) \tag{r.13}$$

The predominance diagram presented in Figure 2-7 confirms that the formation of sodium chromate is possible at 1100°C. A schematic diagram of the manufacturing process of chromium chemicals from chromite ore based on alkali roasting and water leaching can be seen in Figure 2-8.

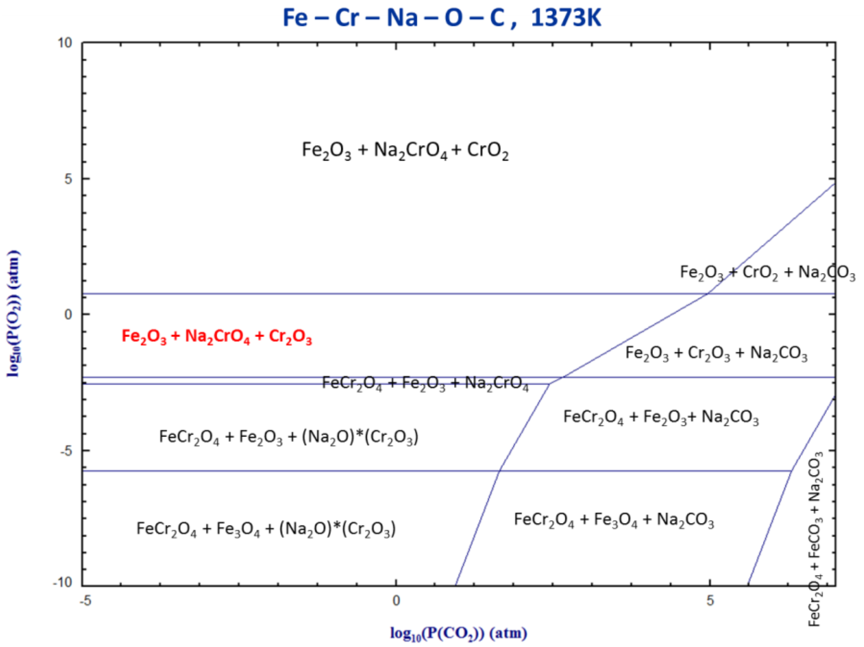

Figure 2-7. Predominance area diagram of the Fe-Cr-Na-O-C system at 1273 K (1000°C). Represented using FactSage 6.4 software [46].

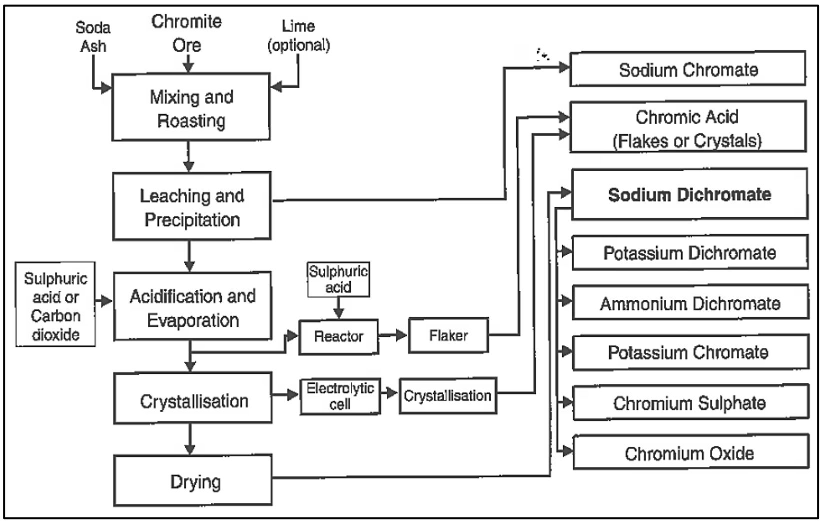

Figure 2-8. The manufacturing of chromium chemicals by soda-ash roasting (Maliotis (1996) [2]).

Much research work has been carried out in attempt to optimize the process parameters of alkali roasting of chromite ore and establish the kinetics and the mechanisms of the reaction [28,29,32,34,83]. Maximizing the yield of sodium chromate has been the main challenge for both economic and environmental aspects associated with the manufacturing of chromium compounds from by alkali roasting of chromite.

Some research was carried out with the aim of studying the roasting of chromite ore at different temperatures in oxidising atmosphere using NaOH and KOH as alkali salts. The results are presented and discussed in Chapter 6.

2.4.1. LIME-BASED AND LIME-FREE ALKALI ROASTING OF CHROMITE

The development of the lime-based process in 1845 was a significant breakthrough in the treatment of chromite ores by alkali roasting [44]. This was the main process used at industrial scale until the 1960s. The lime-based alkali roasting process aimed to solve some technical problems of the traditional soda-ash roasting process, in order to improve its efficiency. The addition of lime ($CaCO_3$) enables the neutralization of silica by forming silicates, enhancing the oxygen diffusion and reducing the amount of alkali consumed. On the other hand, the formation of highly volatile calcium chromate ($CaCrO_4$) contributes to air-bone Cr^{+6} pollution and reduces the process efficiency [84]. Afterwards, the lime-free process was developed, being able to eliminate the environmental problems associated with $CaCrO_4$. Nowadays, the lime-free technology has been industrially adopted in most developed countries as an alternative to a dolomite-based process. However, it is limited to ores with silica content lower than 1% [2], because of its negative effect on the oxygen transport at the reaction interface. High silica in the ore has an adverse effect on alkali roasting mainly due to: (a) higher consumption of sodium due to sodium silicates formation and, (b) highly viscous liquid phase formation which hinders the oxygen diffusion [28].

Previous authors [79] observed the changes on the physical and chemical properties of the reaction mixture when lime was present. The porosity of the mixture increases when lime is added, thus enhancing the oxygen transport during roasting. The same authors reported that $Mg(Al,Cr)_2O_4$ phase was present when roasting without lime, whereas in the presence of lime this phase could be broken. The main disadvantage of the lime process is the formation of calcium chromate ($CaCrO_4$) depending on the amount of soda-ash and lime in the charge [85]. Calcium chromate is a volatile alkaline compound with high toxicity [84] and hazardous for the environment. Therefore, due to environmental restrictions imposed to chromium chemical producers, the use of lime in the alkali roasting of chromite ore has been progressively eliminated since approximately 1960 [44]. Nowadays, the lime-free process has been adopted by all main producers.

The application of this process depends mainly on the mineralogy of the ore and origin of gangue materials, especially silicate compounds found together with chromite ore. For the efficient application of the lime-free process silica needs to be lower than 1% due to its negative effect on chromite roasting, as explained before.

Darrie (2001) [44] summarised the evolution of alkali roasting of chromite indicating the main changes in the process (TABLE 2-5). The main difference between processes is the presence or absence of lime and the kiln size. It can be seen in the table that the process evolved from batch to continuous. Sodium carbonate has been widely used as alkali source, with sodium hydroxide being also used in some cases.

TABLE 2-5. Sodium dichromate process evolution [44].

Generation	1st	2nd	3rd	4th	5th
Process flow	Batch	Batch	Continuous	Continuous	Continuous
Process type	Lime	Lime	Lime	No lime	No lime
Kiln size kT/y	< 1000	5000	10000	20000	75000
Introduced	Pre 1920	1930-1940	1950’s	1960’s	1980’s

2.4.2. PREVIOUS INVESTIGATIONS ON THERMODYNAMICS, KINETICS AND REACTION MECHANISM OF THE LIME-FREE ALKALI ROASTING OF CHROMITE

2.4.2.1. Thermodynamics of chromite roasting with different alkali salts

The thermodynamics of the alkali roasting of chromite ore with different alkali salts have been studied by different authors [26,29,86,87]. An investigation on the thermodynamics of the roasting with sodium carbonate was carried out by Qi (2011) [87], and the different phases that may be potentially formed were discussed. They concluded that sodium carbonate reacts not just with chromite spinels ($FeCr_2O_4$ and $MgCr_2O_4$) to form Na_2CrO_4 but also with the rest of spinel members ($MgFe_2O_4$, $MgAl_2O_4$, $FeAl_2O_4$) and silica to form intermediate compounds such as $NaFeO_2$, $NaAlO_2$ and Na_2SiO_3. It was found that further reaction of these intermediate compounds with chromite to form sodium chromate is possible. Magnesium is also able to combine with Fe and Si to form $MgFe_2O_4$ and $MgSiO_3$. Antony (2006) [29] studied the thermodynamics of the lime-free alkali roasting of Indian chromite ores and determined that the roasting process can be applied to these type of chromites but the extraction yield is limited to about 65%.

The thermodynamics of the roasting with KOH were studied by Sun (2007) [17]. They corroborated that thermal reaction alone is not able to decompose chromite and therefore reaction with alkali is necessary. In this study, the free energy values of chromite spinel decomposition with sodium and potassium carbonates and hydroxides were compared and it was concluded that the tendency to react with the ore is higher for hydroxides than for carbonates, and also higher for potassium than sodium (KOH > NaOH > K_2CO_3 > Na_2CO_3).

2.4.2.2. Kinetics and reaction mechanism of roasting with sodium carbonate

Tathavadkar et al. [28,29,32] performed a thorough analysis of the reaction rate and mechanism of the roasting of chromite ore with soda-ash, and studied the influence of temperature, oxygen partial pressure and charge composition. South African, Indian and Chinese chromites with different chemical composition were tested. They pointed out the differences between the reaction mechanism with and without silica [28]. When silica is present in a significant amount, there is formation of a liquid phase rich in alkali in which chromite dissolves completely, whereas in the absence of silica, Cr^{3+} ions diffuse towards the reaction zone where reaction with sodium takes place. Iron (Fe^{2+}/Fe^{3+}) and Mg^{2+} cations diffuse in the same direction forming a $MgFe_2O_4$-rich rim surrounding the unreacted chromite ore particle. This has an important influence on the extraction efficiency, which is higher for ores with low silica content. The main phases found in the process residue after extracting water soluble compounds by water leaching were: unreacted chromite depleted in iron with $Mg(Al,Cr)_2O_4$ in the centre of the particle, and magnesium spinel phases $Mg(Al,Fe)_2O_4$ in the outer part [32].

The process is considered to be controlled by diffusion and can be described by the Ginstling and Brounshtein (GB) equation [29,32]. This is applicable to the treatment of both South African and Indian chromites.

In a kinetic study of Indian chromite alkali roasting carried out by Antony (2006) [29], it was concluded that the diffusion of Cr^{3+} and Na^+ is the rate-limiting step when temperature is low (700°C to 900°C) whereas at high temperature (above 900°C) the diffusion of gaseous species controls the rate of reaction. Tathavadkar (2003) [28] reported a conversion efficiency of 85%, 68%, and 45% by alkali roasting of South African, Indian, and Chinese chromite ores with 0.97 wt.%, 0.89 wt.% and 5.96 wt.% SiO_2, respectively. The high SiO_2 wt.% of the Chinese ore explains the low recovery percentages. The conversion efficiency values achieved by Antony (2006) [29] were 65% and 60% for two different Indian ores with similar silica content (0.89wt.%-0.92wt.% SiO_2). The authors also explained the key role played by the binary Na_2CrO_4–Na_2CO_3 molten phase formed during alkali roasting. The oxygen transport is obstructed by this liquid phase decreasing the formation of sodium chromate [32].

They highlighted the significant effect of gangue minerals and ore composition in the properties of the binary Na_2CrO_4–Na_2CO_3 liquid phase [28], which ultimately affects the extraction yield of chromium during alkali roasting of chromite ore.

2.4.2.3. Chromite ore treatment with potassium hydroxide at low temperature

A new process was developed by the Institute of Process Engineering in the Chinese Academy of Sciences, Beijing, based on potassium hydroxide treatment at low temperature (300°C) [80,81,86]. Authors claimed that 99% recovery of chromium without any additives could be achieved. Zheng (2006) [81] calculated a higher free energy change in the reaction conditions compared to the roasting with soda-ash. The energy consumption is also lower due to operation at low temperature and the exothermic nature of the reaction.

Sun (2007) [17] applied this process for the treatment of Vietnamese chromite and carried out a study of the thermodynamics and kinetics of the decomposition of the ore in molten KOH. The analysis of reacted samples proved that the spinel structure can be broken by KOH and water-soluble potassium chromate is formed and subsequently extracted with water. The decomposition was found to be thermodynamically favourable with exothermic reactions taking place; which corroborated results from previous publications [81].

2.5. PRODUCTION OF CHROME METAL FROM CHROME OXIDE

An important application of chromium metal is on the manufacturing of gas turbines engines for aircrafts, natural gas engines and electrical power generation [43]. Superalloys, based on iron, cobalt, and nickel, are employed for the fabrication of this turbines due to their strength provided by the formation of carbides and intermetallic precipitates. These alloys contain high levels of chromium metal which increases the quality and mechanical properties of the material. The purity of the chromium metal required for the manufacturing of superalloys is high in order to obtain good behaviour against fatigue and creep and avoid component failures [43].

The main methods for production of Cr metal are the ***trivalent chrome-alum bath electrolyte method***, and the ***chromic-acid electrolyte method***. Both methods require chromium(III) oxide (Cr_2O_3) for the production of the metal. Sodium chromate, produced by alkali roasting of chromite ore in oxidative atmosphere, is used for the manufacturing of Cr_2O_3. The treatment of the by-products generated by the alkali roasting process increases the cost of production of the metal and has important environmental.

2.6. REDUCTIVE ALKALI ROASTING

Although there is extensive literature about carbothermic reduction of chromite ores in the presence of additives (including sodium carbonate), the extraction of chromium oxide from chromite ore by alkali reduction followed by magnetic separation has not been studied before. As explained in section 2.3, the aim of previous research on chromite ore reduction has been to enhance the formation of Fe-Cr alloy by using additives, but never to separate iron from chromium by forming $NaCrO_2$ and metallic Fe in the presence of Na_2CO_3 and solid carbon in argon atmosphere.

Some investigations have studied the reductive alkali roasting of other minerals like ilmenite [88,89,90], however, the literature on that area still very limited. Moharty and Smith (1993) [88] studied the effect of alkali metal carbonates on the reduction of synthetic ilmenite at temperatures up to 1200°C using graphite. The kinetics and mechanism of the reaction were studied when the amount of catalyst in the reduction mixture was 5 wt.%. They found that alkali carbonates are able to increase the rate and extent of reduction compared to reduction carried out in the absence of additives. The additives tested were sorted from higher to lower catalytic activity obtaining the following sequence: $CaCO_3 > Rb_2CO_3 > Li_2CO_3 > K_2CO_3 > Na_2CO_3$.

Few years later, El-Tawil (1996) [89] also investigated the alkali reduction of ilmenite with carbon at a temperature ranging from 1000°C to 1200°C, but in this case just sodium carbonate was tested as catalyst. Iron metallization percentages of up to 85% were achieved with 20% of sodium carbonate addition with respect to the ore quantity. Significant crystallographic changes were observed when reduction was carried out in the presence of sodium carbonate as a consequence of ions diffusion within the crystal structure of ilmenite. Sodium carbonate promoted the reduction of iron by increasing the carbon gasification rate. In fact, previous literature claimed that the addition of various alkali salts may enhance the Boudouard reaction promoting in this way the reduction process [91]. An increase of the metallic iron particle size and the formation of a porous structure were reported [89].

The crystal growth of metallic iron particles has also been reported by Guo (2010) [90]. The application of a magnetic separation step after reduction of ilmenite using alkali metal additives was studied with the aim of the separating metallic iron from a non-magnetic TiO_2-rich material. They reported a 90% TiO_2 recovery achieving a 75%-rich TiO_2 material when ilmenite was roasted in reducing atmosphere at 1100°C for 3 hours and 5% additives.

Apart from ilmenite, recent investigations have been also carried out on alkali reduction of iron ores in the presence of sodium carbonate followed by magnetic separation [92,93].

They observed that sodium carbonate promoted the breakage of the ore structure which enhanced the reduction of iron.

They found that it was possible to improve the separation between phosphorus and iron by magnetic separation, increasing dephosphorization of the ore by 26% when sodium carbonate was present. The formation of aluminium silicate phosphorus phases, which aids in the fracture of the mineral structure [92,93], was observed and the growth of iron particles due to the presence of sodium carbonate was confirmed once again. The improvement of alumina separation from iron ores by carbothermic reduction using Na_2CO_3 followed by magnetic separation has very recently been reported (Chun, Long et al. 2015).

2.7. SPECIFIC OBJECTIVES

Based on the literature survey presented, the specific objectives of the research project are the following:

- Characterise the chromite ores that will be used as raw materials in the research project to determine the chemical composition and nature of the mineral phases present by different characterisation techniques.
- Develop improved understanding of the reactions of chromite mineral under different chemical potentials, temperatures and in the presence of reaction reagents (such as alkali salts and activated charcoal) by using thermodynamics, phase equilibria and phase transformation studies.
- Study the effect of the experimental parameters and the use of different feedstocks (S.A chromite, Brazilian chromites and COPR) and alkali salts on the formation of metallic iron and $NaCrO_2$ during reduction of chromite with alkali and carbon.
- Perform a kinetic study on the reduction of chromite ores in the presence of alkali and activated charcoal and study the mechanism of reduction.
- Study the treatment of chromite reduced samples by magnetic separation, water leaching, and alkali leaching. The characterisation of the main streams obtained along the process is required; and the effect of acid leaching parameters, including acid use, time, temperature and acid concentration, on the purity of the material obtained needs to be studied.
- Design the process flowsheet for maximum Cr_2O_3 recovery with minimum waste generation, energy consumption and water utilisation. Perform estimated mass and energy balances of the different stages and the overall process. Characterise the waste produced to ensure the absence of Cr^{6+} in solid and liquid by-products or waste material.

Chapter 3

MATERIALS AND METHODS

Chapter content

Chapter 3 describes the chromite ores and rest of chemical reagents used in the experimental part of the study, as well as the experimental procedures employed in the different sets of tests. It also includes a description of the characterisation techniques used and the sample preparation protocols.

Chapter conclusions

South African and Brazilian chromite ores have been used as raw materials for the experiments performed. The rest of reagents required are mainly alkali salts, activated charcoal and different organic and inorganic acids. The atmosphere of the experiments was controlled by using air, argon or CO_2 *gases. A simple experimental arrangement, including batch reduction experiments, magnetic separation and leaching set-ups was required for most of the experiments. A thermogravimetric equipment was also used for thermal analysis of sample mixtures.*

The characterisation of the samples was carried out by different techniques, including: XRPD (phase analysis), SEM-EDX (microstructure analysis and elemental composition), XRF (chemical composition of solids), EPMA (chemical composition of solids), AAS (elemental composition of liquid samples), UV-vis (oxidation state of ions in solution). Sample preparation protocols were established and followed for each of the techniques.

3.1. MATERIALS

South African chromite ore (S.A. chromite) was the main mineral sample used for the study of the reductive and oxidative alkali roasting. In order to study the effect of silica content on the reactions, two additional ores of Brazilian origin, namely Brazilian chromite ore E4 and Brazilian chromite ore E5, were also used in some of the experiments. A detailed characterisation of the chromite ores is presented in Chapter 4.

The list of chemicals used during the different experiments is given below.

✓ Solids/Powders: sodium carbonate (Na_2CO_3, M_W = 105.98 g/mol), activated charcoal (C, M_W = 12.01 g/mol), sodium hydroxide 98% (NaOH, M_W = 40 g/mol), sodium bicarbonate ($NaHCO_3$, M_W = 84.01 g/mol), sodium bisulphate ($NaHSO_4$, M_W = 120.06 g/mol), aluminium oxide gamma 99.97% (Al_2O_3, M_W = 101.96 g/mol), iron(III) oxide (Fe_2O_3, M_W = 159.69 g/mol), chromium(III) oxide 98+% (Cr_2O_3, M_W = 151.99 g/mol), magnesium oxide 99+% (MgO, M_W = 40.31 g/mol), silica oxide (SiO_2, M_W = 60.08 g/mol), calcium oxide (CaO, M_W = 56.08 g/mol), potassium carbonate anhydrous (K_2CO_3, M_W = 138.21 g/mol), sodium chromate (Na_2CrO_4, M_W = 161.97 g/mol), lithium-borates binder for X-ray fluorescence sample preparation (66.67% $Li_2B_4O_7$, 32.83% $LiBO_2$ and 0.5% LiBr), oxalic acid anhydrous ($C_2H_2O_4$, M_W = 90.04 g/mol), citric acid anhydrous 99+% ($C_6H_8O_7$, M_W = 192.12 g/mol), L-Ascorbic acid ($C_6H_8O_6$, M_W = 176.12). All powders were anhydrous and of analytical grade.

✓ Liquids/Solutions: sulfuric acid 98% (H_2SO_4, M_W = 98.08 g/mol, d = 1.84 g/mL), nitric acid 70% (HNO_3, M_W = 63.01 g/mol, d = 1.42 g/mL), hydrochloric acid 37% (HCl, M_W = 36.46 g/mol, d = 1.2 g/mL), acetic acid glacial $\geq$ 99.85% ($C_2H_4O_2$, M_W = 60.05 g/mol, d = 1.05 g/mL), DL-Lactic acid 85+% ($C_3H_6O_3$, M_W = 90.08 g/mol, d = 1.2 g/mL), L-(+)-Tartaric acid 99% ($C_4H_6O_6$, MW = 150.09 g/mol, d = 1.76 g/mL) and AAS standards of Cr, Fe, Al, Mg, Na, Si, Ca of concentration 1000 mg/L.

✓ Gases: argon gas (Ar), carbon dioxide gas (CO_2).

3.2. EXPERIMENTAL SETUP

3.2.1. THERMOGRAVIMETRIC ANALYSIS

Thermogravimetric analysis (TGA) was carried out with the purpose of studying the weight change that occurs when the sample is heated under different temperature conditions (isothermal and non-isothermal experiments) and oxygen potentials. Thermogravimetric data was used in phase decomposition studies and to analyse the rate of reaction as a function of temperature during the kinetic study.

For TGA experiments, between 1-2 grams of the reaction mixture was weighed and transferred into an alumina crucible. The alumina crucible containing the sample was suspended from a Sartorius microbalance and introduced in a silica tube (0.5 L volume) which was fitted inside an electrically-heated furnace (FIGURE 3-1). The furnace could be raised up or lowered down using a driving mechanism which allowed to adjust the position of the crucible inside the furnace. The furnace controller was used to set the temperature program required for each experiment. During non-isothermal experiments the temperature was ramped from room-temperature to 1050°C at a constant rate of 5°C/min, whereas isothermal experiments were carried out at a constant temperature.

The samples analysed consisted on chromite ore, chromite ore and activated charcoal mixture, or a homogeneous mixture of chromite, Na_2CO_3 and activated charcoal in the corresponding weight ratio. The 4-decimal places microbalance (sensitivity of 0.1 mg) provided accurate reading of the sample weight every 10 seconds, allowing the record of weight change data against time and temperature throughout the different experiments. A thermocouple located next to the crucible was used to measure the temperature, which was continuously recorded using a MyPClab data logger.

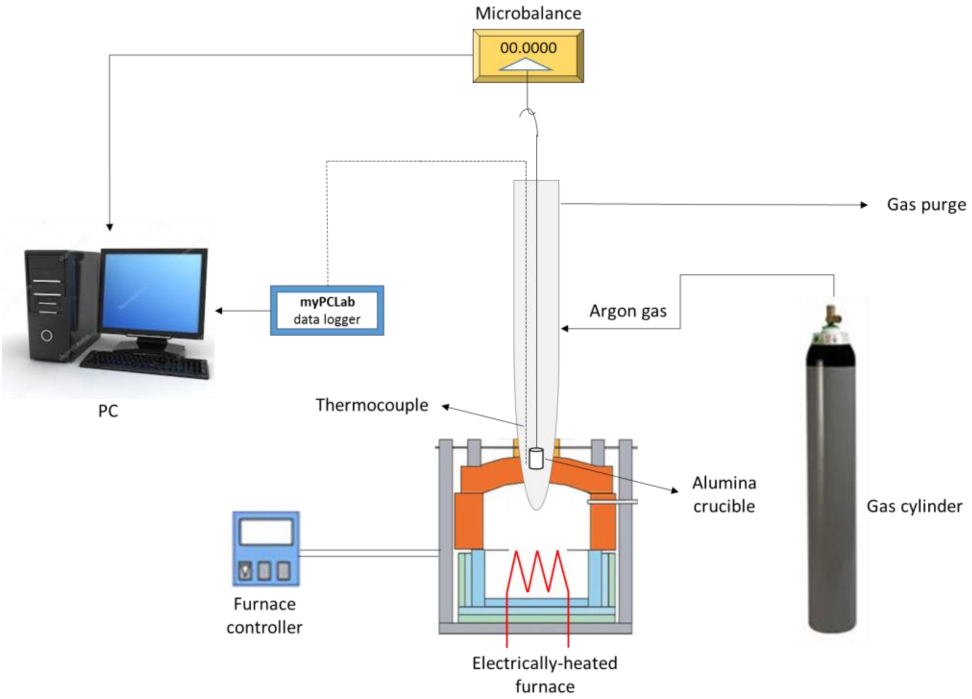

FIGURE 3-1. Schematic diagram of the thermogravimetric analyser.

Compressed air or argon gas was continuously passed through the silica tube in order to maintain an oxidising or reducing atmosphere, respectively, depending on the test. The argon gas used was passed through a purifier to remove any possible moisture, the pressure was adjusted to 1 bar, and a flowmeter located between the pressure regulator and the silica tube was used to control the flow of gas, which was set at 0.6 Lmin^{-1}.

3.2.2. TUBE FURNACE EXPERIMENTS IN CONTROLLED ATMOSPHERE

The TGA experiments described above were carried out only for small samples (< 2g). For larger samples, the experiments were carried out in a tube furnace. Samples for batch tube furnace experiments were prepared by thoroughly mixing with a mortar and pestle the as-received ore with the corresponding reagents and weight ratios depending on the experiment. The temperature in the experiments was in the range of room-temperature to 1100°C, and the time was minimum 15 minutes and maximum 6 hours.

Isothermal roasting in reductive/oxidative conditions was carried out in an electrically-heated furnace controlled by a SFL programmable temperature-controlling device. Samples were placed in an alumina crucible which was introduced in the preheated furnace with the aid of a silica cradle. For reduction experiments, the crucible was covered with a graphite lid to prevent oxidation of the sample during cooling after the completion of the experiment. An alumina liner with a volume of approximately 1.9 L was fitted inside the furnace with the purpose of protecting the interior of the furnace and the heating elements from the atmosphere created in the reaction chamber.

For reduction experiments, the reaction chamber was continuously purged with argon gas in order to maintain an oxygen-free atmosphere and prevent oxidation of the samples during the process. The pressure was adjusted to 2 bar using the pressure regulator, the argon gas flow was set to 2 L/min and the off-gases were directed to an extraction hood. Oxidative roasting experiments were carried out in air atmosphere, and therefore the same experimental set-up, except for the argon gas arrangement, was employed.

At the end of the experiment, the cradle holding the alumina crucible with the sample was taken out of the furnace and cooled to room-temperature. For non-oxidising experiments, the crucible containing the sample was covered with a bigger crucible during cooling to prevent oxidation. After cooling, reduced samples were ground for 30 minutes in a mortar grinder Retsch® RM200 before analysis or further treatment as minor sintering occurs during reduction. Samples treated in oxidising atmosphere partially melted at the reaction temperatures due to the presence of alkali reagents and were therefore water leached directly from the crucible.

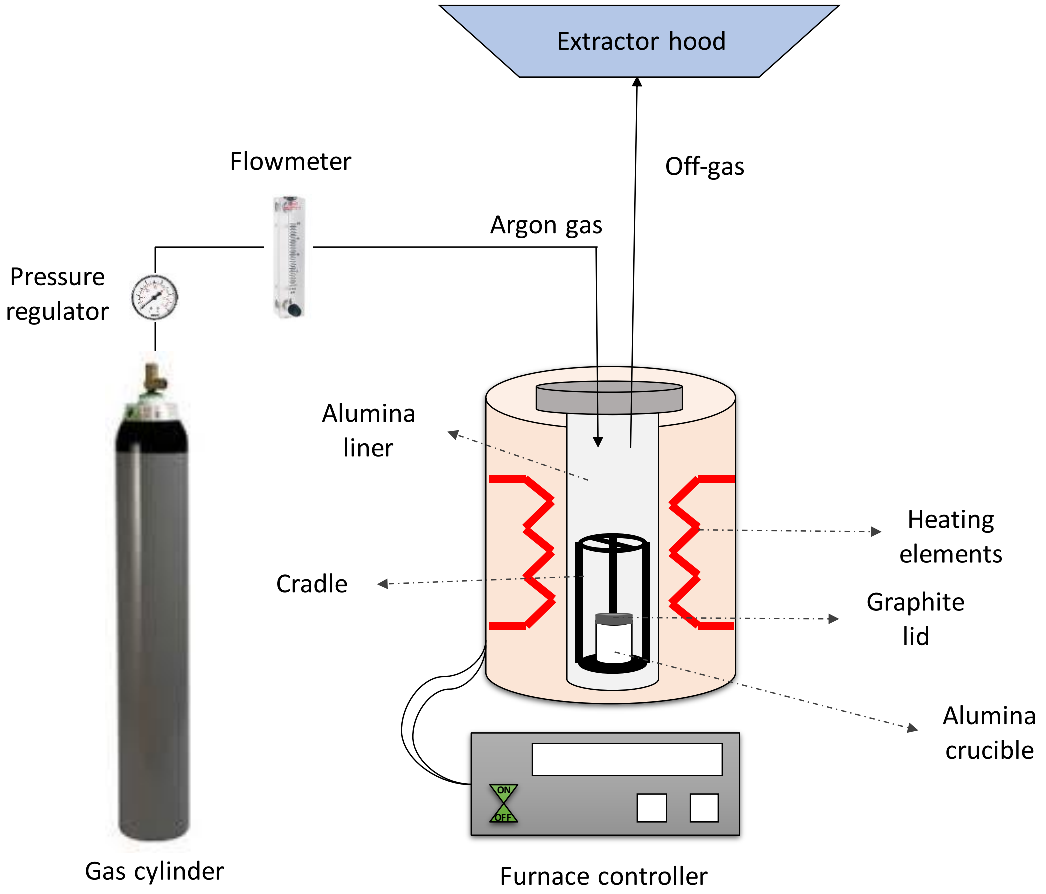

FIGURE 3-2. Schematic diagram of tube furnace experiments set-up.

3.2.3. PROCESSING OF ALKALI ROASTED SAMPLES

Roasted chromite samples were leached in water with the purpose of selectively separating chromium by extracting the highly water-soluble alkali chromate (Na_2CrO_4, K_2CrO_4) into solution. The leaching was carried out by adding distilled water directly to the crucible containing the sample. The crucible was introduced in a beaker to prevent any leaking of the chromate solution and they were placed in a Stuart® UC152 hot plate in order to maintain the temperature at approximately 50-60°C during leaching. Samples were water leached for 2 hours at $pH \approx 12$ and continuously stirred at 500 rpm using a magnetic stirrer.

Leached samples were subsequently filtered using Whatman® cellulose filters obtaining an alkali chromate solution and a solid processing residue containing the insoluble phases which remained in the filter. Filter papers and solid residues were then dried in a drying oven at 80°C. The weight of the powder residue was obtained by subtracting the weight of the filter (measured before leaching) to the final weight of the dried filter paper containing the residue.

Leached solutions were analysed by atomic absorption spectroscopy, while the solid powder residues were characterised by X-ray powder diffraction and scanning electron microscopy including X-ray spectroscopy analysis.

3.2.4. PROCESSING OF ALKALI REDUCED SAMPLES

Part of the reduced samples obtained were further treated by magnetic separation and leaching as described below.

3.2.4.1. Magnetic separation

The purpose of magnetic separation is to physically separate the magnetic Fe-rich fraction from the Cr-rich non-magnetic fraction. The magnetic separator used was a Wet Test Chute from Master Magnets Ltd, equipped with a Strontium ferrite magnet system. Magnetic separation was carried out by placing the ground reduced sample on to the magnetic separator and spraying the sample with warm water to wash-off the non-magnetic fraction. Water soluble components such as $NaAlO_2$ and unreacted Na_2CO_3 dissolve in water during the separation, while the magnetic fraction remains on the separator, as shown in FIGURE 3-3. Part of the sodium was also leached out from sodium chromite contained in the non-magnetic fraction. The non-magnetic fraction, containing mainly $NaCrO_2$, silicates, magnesium oxide and calcium carbonate, was collected in a beaker and allowed to settle down. The solution was afterwards decanted and sent to the CO_2 bubbling stage for alumina separation and sodium carbonate recovery.

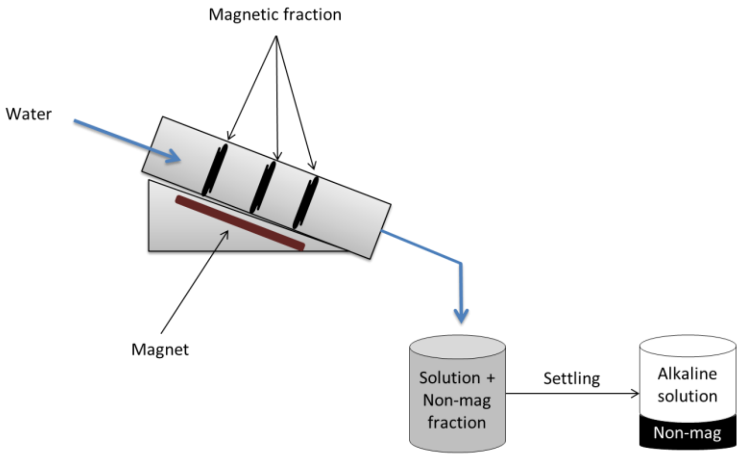

FIGURE 3-3. Schematic diagram of magnetic separation of reduced samples.

In order to improve the efficiency of this stage, a two-step magnetic separation is carried out. As it can be seen in FIGURE 3-4, reduced ground samples are subjected to a first magnetic separation step obtaining the magnetic fraction (1) and the non-magnetic fraction (1). The magnetic fraction (1) was re-ground and subjected to a second step of magnetic separation. The magnetic fraction (2) corresponds to the final magnetic fraction obtained. Both the 1st and 2nd non-magnetic fractions are combined to give the final non-magnetic material, which will be further treated in order to extract Cr_2O_3.

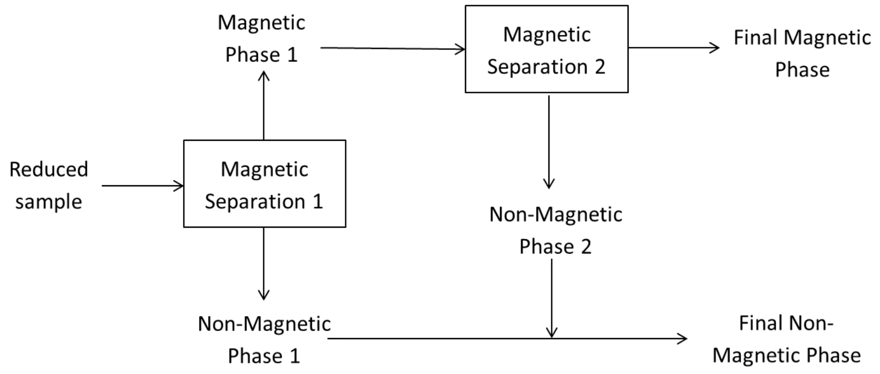

FIGURE 3-4. Schematic diagram of the double magnetic separation process.

3.2.4.2. Water leaching of non-magnetic fraction

The non-magnetic fraction obtained by magnetic separation was leached in water in order to extract any remaining water-soluble compounds into solution. In particular Na^+ which could be later recovered as Na_2CO_3 and recycled back into the process. Any residual sodium aluminate that did not dissolve during magnetic separation is also leached out at this stage.

The non-magnetic fraction samples were placed in a pyrex beaker and water was added up to a solid:liquid ratio of 1:100 g/mL. The beaker was sited in a Stuart® UC152 hot plate were the sample was leached during 1.5 hours with continuous stirring at 500 rpm. A FiveGo Mettler Toledo pH meter was employed for any required pH measurements and to maintain the temperature at 50°C during water leaching. The leached sample was filtered using Whatman® cellulose filters at the end of the experiment. The alkaline leachate obtained was combined with the alkaline solution from the magnetic separation step and reserved for the posterior recovery of alkali. The leach residue was dried with the filter in a drying oven at 80^{o}C and subsequently weighted and analysed by X-ray diffraction, secondary electron microscopy and X-ray fluorescence.

3.2.4.3. Acid leaching of water leached residues

The powder residues obtained after water leaching were subsequently leached in acid media with the aim of removing the remaining sodium ions from the partially leached sodium chromite ($Na_{1-x}CrO_2$) phase, yielding Cr_2O_3. The remaining iron and any water insoluble silicates present in the non-magnetic fraction may be removed at this stage in order to obtain an enriched Cr_2O_3 precipitate.

The effect of acid concentration and solid: liquid ratio was studied by performing the leaching of water leach samples with sulphuric acid (H_2SO_4). The kinetics of sulphuric acid leaching were also investigated by leaching tests at different temperatures. Leaching experiments using a wide range of organic and inorganic acids were carried out in order to compare the results with H_2SO_4 results and determine the most efficient acid.

Water-leached samples were leached in an acid solution for 1.5 hours, with continuous stirring and at 50°C, unless otherwise stated. The experimental set-up used for acid leaching was identical to that employed for water leaching. Solid:liquid ratios and acid concentrations used in the different leaching experiments varied from 1:30 g/mL to 1:150 g/mL and 0.05M to 0.5M, respectively. Leaching kinetic experiments were carried out at room-temperature, 50°C and 80°C, with a total volume of 1.5 litres and solid:liquid ratio of 1:100 g/mL. Small aliquots of constant volume (15 mL) were taken at different intervals of time using a plastic syringe. The pH of the solution was also measured simultaneously using a FiveGo Mettler Toledo pH meter, which was also used to maintain the temperature constant during the experiment. Each aliquot was subsequently filtered obtaining a leachate solution and a solid sample which were subsequently analysed.

After filtering and drying the acid leached residues in a drying oven at 80°C, the solid precipitates were finally heated in oxidising atmosphere at 800°C for 1 hour in an ELITE chamber furnace in order to burn any remaining carbon in the samples. The weight of the precipitates was measured before and after carbon burning. The final Cr_2O_3-rich materials obtained were characterised by X-ray powder diffraction, secondary electron microscopy and X-ray fluorescence. Leachate solutions were analysed by atomic absorption and/or UV-vis spectrometry.

3.2.4.4. Sodium carbonate and alumina recovery from alkaline solutions

The solutions obtained during wet magnetic separation and water leaching are highly alkaline and contain mainly sodium and alumina in solution, with minor amounts of silica also present. With the aim of recovering sodium as Na_2CO_3, these solutions were combined and subjected to bubbling with CO_2 gas. CO_2 bubbling was carried out in a 1 litre vessel covered with a lid which made the system air-tight.

The lid had three apertures through which the gas was bubbled using a silica tube adapter and the off-gas was directed to the extraction hood (see experimental set-up in Figure 3-5). The CO_2 bubbling was carried out at 50°C during 1.5 hours with a CO_2 flow rate of 1 L/min.

During CO_2 bubbling, alumina (Al_2O_3) was precipitated and recovered by filtration. The alumina precipitate was separated, dried at 80°C and analysed by X-ray diffraction and X-ray fluorescence. Sodium carbonate was recovered from the remaining solution by evaporation, and for that, the solution was transferred to a pyrex beaker which was placed in a hot plate and heated until all water was evaporated. The result was a Na_2CO_3-rich solid precipitate which was recovered from the beaker and weighted. The Na_2CO_3 recovered was analysed and can be recycled back into the alkali reduction stage.

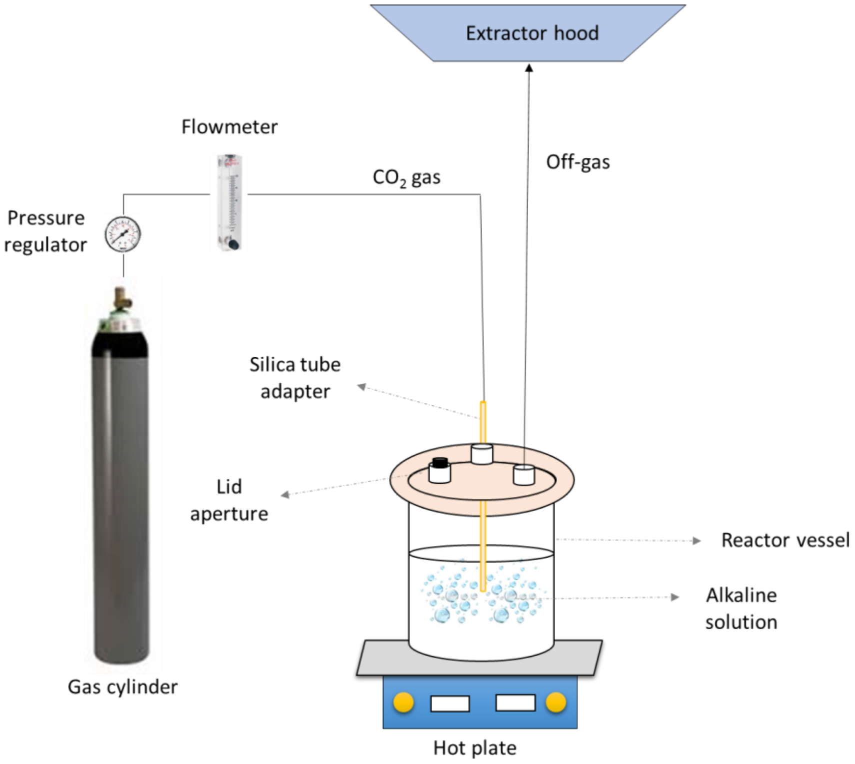

FIGURE 3-5. Experimental set-up of the CO_2 bubbling experiments.

3.3. CHARACTERISATION TECHNIQUES

Samples obtained from both alkali roasting and alkali reduction experiments were characterised by different analytical techniques. Powder samples were characterised by X-ray powder diffraction (XRPD), X-ray fluorescence (XRF) and scanning electron microscopy (SEM) including energy dispersive X-ray spectrometry (EDX). Chromite samples were also analysed by electron probe micro-analysis (EPMA) and their density was measured by a pycnometer (or density bottle). Liquid samples, on the other hand, were analysed by Atomic Absorption Spectroscopy (AAS) and Ultraviolet-visible spectroscopy (UV-vis). A more detail description and technical details of the different analyses are presented below.

3.3.1. X-RAY POWDER DIFFRACTION

3.3.1.1. Basic principles of operation

The most common way of producing X-rays is based on the fact that, when a particle of small mass and high kinetic energy collides with a material, part of that energy is transformed into X-rays [94]. Electrons are commonly used for bombarding the material, and the device used for this is known as X-ray tube. X-ray tubes have a tungsten filament working as cathode and a copper anode with a metal plate which can be made of different elements (Cu, W, Cr, Ag, Co, etc.). Electrons are produced by applying a high voltage through the filament, and then concentrated into an electron beam which is used to bombard the target anode. The incident beam is able to ionize electrons from the K-shell of the atoms of the target material, giving as a result the emission of X-rays as the vacancies created are filled with electrons of higher orbitals [94]. The intensity and wavelength of the resulting light can be adjusted by controlling the amount of current and voltage of the electrons. The wavelength of the X-ray beam will be dependent on the energy of the resulting light.

- Bragg’s law

In 1913, Bragg observed that crystalline solids are able to diffract X-rays, giving as a result diagrams characterised by quite sharp peaks in certain directions. In order to explain this phenomenon, Bragg supposed that the crystal was formed by parallel planes of atoms separated by a distance *d*. A diffracted beam is then produced as a result of a constructive interference between the rays scattered by atoms arranged in these planes.

The planes produced a mirror reflection of X-rays and the path difference between two reflected rays by adjacent planes will be equal to two times the interplanar distance times the sin of the angle θ, as shown in FIGURE 3-6b. Bragg's law is hence formulated as [95]:

$$2 \cdot \mathrm{d} \cdot \sin\theta = \mathrm{n} \cdot \lambda \qquad \text{(eq.2)}$$

This is the essential condition for diffraction to occur, where *n* (order of diffraction) is an integer number which represents the number of wavelengths contained in the rays' path difference. For each value of *n*, there will be a value for the angle of incidence that satisfies the condition, provided that λ and *d* are constant values. The diffraction angle (2θ) is the one usually measured experimentally and it corresponds to the angle between the incident and diffracted beams.

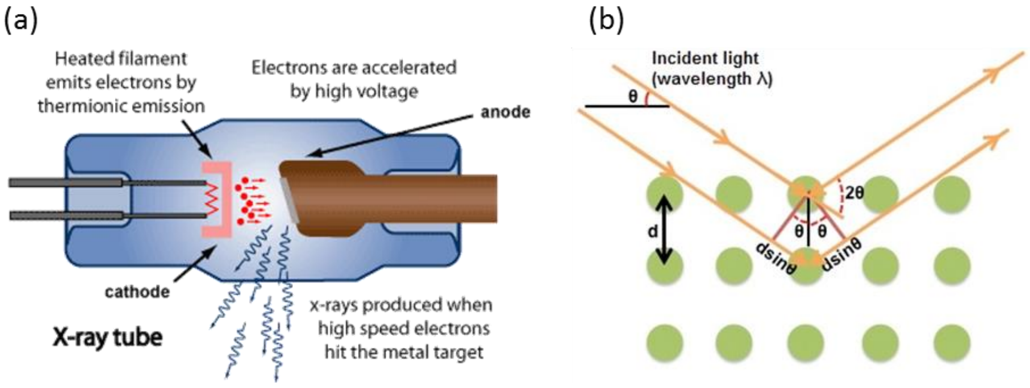

FIGURE 3-6. a) Schematic representation of production of X-rays in an X-ray tube [96] and b) Bragg's Law reflection: constructive interference between diffracted X-rays satisfying Bragg's condition [97].

3.3.1.2. Sample preparation and analysis details

X-ray powder diffraction (XRPD) was used for characterisation of treated and untreated powder samples. Samples were prepared for XRPD by grinding using a mortar and pestle until a fine and homogeneous powder was obtained. The samples were then placed in the appropriate sample holder and analysed by XRPD using a Philips X'Pert X-ray diffractometer. Samples were analysed using Cu-Kα radiation (λ = 0.15417 nm), a step size of 2θ = 0.0334225° and over an angle 2θ with a maximum range of 5° to 85°. This range was chosen taking into account the position (2θ) of the main peaks of the compounds present in the different samples. X'Pert HighScore Plus database software was used for phase-identification of the XRPD patterns.

3.3.2. RIETVELD ANALYSIS

Rietveld analysis was performed on some of the X-ray powder diffraction patterns with the aim of studying the change of the crystallographic parameters of the phases present in chromite samples treated at different temperatures and under different oxygen potentials.

The X-ray scattering patterns of a material depend on the crystal structure of the phases present, which determine the position and intensity of the diffraction peaks. Diffraction peaks are created by constructive interference of X-rays which are scattered by a family of planes (hkl), which only show a diffraction peak at specific diffraction angles according to Bragg's law (eq.4) [94]. The planes d-spacing (d_{hkl}) is related to the lattice parameters of the unit cell, and therefore, any changes in average atomic distances will influence the diffraction peak position as a consequence of a change on d_{hkl}. The intensity of the diffraction peaks depends on the atoms located in the atomic planes, their exact position indicated by the fractional coordinates and the interaction of the X-rays with the atom's electrons; being the efficiency of the scattering quantified by the scattering factor F. The vibration of an atom due to its thermal energy also affects the scattering factor, which decreases with increasing atom vibration about its lattice site.

Considering all the above, the Rietveld method is based on the refinement of certain parameters to optimize the model function and minimise the difference between the intensities in the experimental X-ray diffraction pattern ($y_{o,i}$) and intensities of the pattern calculated ($y_{c,i}$) considering crystallographic and instrumental parameters [98,99]. This difference can be expressed by $\Sigma_i w_i(y_{C,i}-y_{O,i})^2$, where the weight ($w_i$) is $1/\sigma^2(y_{O,i})$. Therefore, Rietveld analysis begins with starting values of the lattice parameters, the atomic position and occupancies and the thermal vibrations of the different atoms in a phase. The starting values can be obtained from the available crystallographic databases and are refined by the Rietveld method in order to minimize the difference between the calculated and experimental diffraction pattern. The result of the analysis is an accurate value of lattice parameter, atomic positions and occupancies and thermal parameters for each phase present in the material under analysis. Quantitative phase analysis can also be performed based on the refinement data obtained. Rietveld refinement requires quality diffraction data of the sample and the identification of all phases present in the sample.

3.3.2.1. Sample preparation and analysis details

S.A. chromite samples were treated at temperatures ranging from 100°C to 1050°C, under oxidising (air) and oxygen-free (argon and argon plus carbon powder) atmospheres. Experimental X-ray diffraction patterns of these samples were obtained using Cu-Kα radiation with a wavelength of $\lambda = 0.15417$ nm, over a range of 2θ between 5° and 85°, with a step size of $2\theta = 0.02473932$ and a scan speed of 2 s/°.

General Structure Analysis System (GSAS) [100] software package and the EXPGUI graphical interface were employed to perform Rietveld analysis for the refinement of crystal structures in the different samples.

The crystal structure data of the different phases was obtained from the Crystallography Open Database [101]. The refinement of the lattice parameters, atom coordinates, site occupancies and isotropic thermal parameters (u_{iso}) of the atoms in a phase was carried out for every sample under study. The zero point and the scale factor –a parameter that adjusts the net intensity of the pattern– were refined simultaneously. A polynomial function type 1 with 20 terms was used to fit the pattern background, while the peaks' shape was modelled by two profile functions (profile functions 3 and 4). The same starting values of the different parameters were used for the analysis of all diffraction patterns (TABLE 3-1), and the parameters were refined in the same order so as to obtain consistent and comparable results.

TABLE 3-1. Starting values of parameters refined by Rietveld analysis.

				Site occupancies				
Phase	a=b=c	α=β=γ	Oxygen (xyz)	f_{Fe}	f_{Mg}	f_{Cr}	f_{Al}	U_{iso}
$(Fe,Mg)(Cr,Al)_2O_4$	8.2787	90^{o}C	0.2627	0.51	0.49	0.73	0.27	0.025

		Peak profile parameters (for profile function 3)							
Zero	Scale factor	Gu	Gv	Gw	Gp	Lx = Ly	stec = ptec = sfec	Lxx	Peak cutoff
0.01	1	0.5	-0.5	0.5	0	0	0	0	0.0001

The fractional coordinates (x, y, z) of the cations in the spinel phase are equal to (0.5, 0.5, 0.5) for Cr^{3+} and Al^{3+} in octahedral sites, and (0.125, 0.125, 0.125) for Fe^{2+} and Mg^{2+} in tetrahedral sites. These are general atom positions and hence were not refined. S/L and H/L parameters, which are related to certain distances in the instrument, were fixed at $0.5 \cdot 10^{-2}$ and $0.5 \cdot 10^{-3}$, respectively.

Two main constrains were introduced:

- $f_{Fe} + f_{Mg} = f_{Cr} + f_{Al} = 1$. For some of the samples, $f_{Fe} + f_{Mg}$ was left unrestricted.
- The U_{iso} of atoms occupying the same site (tetrahedral or octahedral in the case of chromite spinel) are equal.

The discrepancy between the observed and calculated diffraction patterns may be expressed by the weighted profile R-factor (R_{wp}), which can be calculated by (eq.3) [98,99].

$$\mathrm{R}_{wp} = \sqrt{\frac{\sum_i w_i \cdot (y_{c,i} - y_{o,i})^2}{\sum_i w_i \cdot (y_{o,i})^2}} \qquad \text{(eq.3)}$$

In (eq.3), $y_{c,i}$ and $y_{o,i}$ are the intensity values calculated and observed, respectively, and w_i stands for the weight equal to $1/\sigma^2(y_{O,i})$. R_{wp} was used as an indicator of the goodness of fit, and the analysis was considered completed once further refinement of the crystallographic and instrument parameters do not lead to any significant improvement of the R_{wp}. Values of R_{wp}(%) below 5% were considered acceptable.

3.3.3. SCANNING ELECTRON MICROSCOPY

Scanning electron microscopy is a non-destructive characterisation technique widely used for the examination of materials in many scientific applications. The topography of the surface of the specimen may be analysed by scanning of an electron beam over the surface and acquisition of an image from the secondary electrons emitted [102]. The composition of individual particles or features can be determined when SEM is combined with energy-dispersive X-ray microanalysis (EDX).

Scanning electron microscopy (SEM) including Energy-dispersive X-ray spectrometry (EDX) was used to study the microstructure and obtain elemental maps and chemical composition of the mineral samples.

3.3.3.1. Basic principles of operation

In scanning electron microscopes, an electron beam is produced by the electron gun, being electrons emitted by heating at high temperature a tungsten filament acting as cathode. A positive voltage is applied to a metal plate (anode) so that the electron beam is concentrated and forced to flow towards the anode [102].

The electron beam subsequently passes through a system of one or more apertures and electron lenses which produce a thin beam of electrons. The electron beam is deflected at different points along the path, which allows the beam to move over the surface and scan the specimen by the use of scan coils, being the scanning of the viewing screen and the scanning of the beam on the specimen synchronised. The magnification of the image corresponds to the ratio of the size of the screen and the size of the scanned area. High magnifications, showing details down to 25 Å may be achieved by decreasing the size of the area under scanning.

The energy carried by the accelerated electron beam is dissipated when the beam decelerates in the solid sample [103]. Various signals, such as secondary electrons, backscattered electrons, diffracted backscattered electrons, photons, visible light and heat, are produced as a result of the interaction of the scanning beam with the sample, as illustrated in FIGURE 3-7. These signals can be collected by different detectors and used to observe and analyse the sample surface.

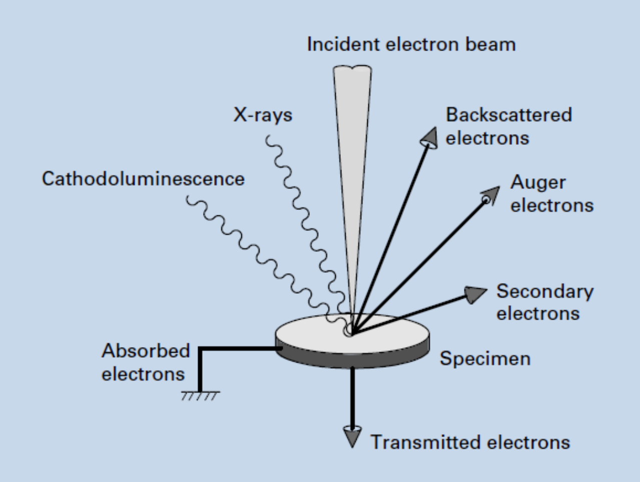

FIGURE 3-7. Emission of different electrons and electromagnetic waves from the specimen as a result of the incident electron beam [102].

Secondary electron and backscattered electron images are the most common types of electron images; used for morphology and topography analysis, and for phase identification, respectively. Secondary electrons have low energy, and therefore the electrons emitted are those generated at the surface, which makes secondary electrons very sensitive to surface features [102]. Secondary electrons are used to examine the topography of a specimen by using the difference in the number of secondary electrons emitted which is dependent on the incidence angle of the electron beam, which produces a difference in the brightness of the sample surface.

Backscattered electrons are sensitive to the composition, as the emission of backscattered electrons increases with increasing atomic number of the atoms in the sample. The higher the atomic number of the atom, the brighter it appears in the SEM image; and therefore, backscattered electron images are a very powerful method for differentiating phases present in a sample and studying their distribution within the specimen under analysis. Backscattered images have been widely used in the present study for characterisation of mineral samples obtained from the different stages of the process, and have been very useful for gaining a better understanding of the phases present and hence of the chemistry of the process.

The penetration of the incident electrons depends on the accelerating voltage, being the penetration depth higher with increasing voltage. A higher accelerating voltage may cause overlapping of any structural features inside the sample with the surface structures, therefore a lower accelerating voltage is recommended for a clearer surface image. The absorbed electrons, shown in FIGURE 3-7, need to be dissipated by assuring the conductivity of the sample, otherwise, charging of the sample occurs affecting the microscopy image. For this reason, an important part of the sample preparation is the coating of the sample, which consist on the deposit of a thin layer of conductive material on the sample surface to ensure that the electrons do not remain in the specimen and flow through the sample stage.

- Energy-dispersive X-ray microanalysis

Energy-dispersive X-ray microanalysis (EDX) may be used to complement scanning electron microscopy for determination of the composition of the sample under analysis. This technique is based on the generation of characteristic X-rays produced for each element in a mineral as a result of the interaction of an electron beam with the specimen.

A voltage pulse is generated when the X-rays are captured by and X-ray detector, being the size of the pulse proportional to the energy of the X-rays. A spectrum of the X-ray energies can be obtained, and by analysing this spectrum it is possible to determine the different elements in the sample. Elemental distribution maps, elemental line profiles and point ID for analysis of chemical composition.

3.3.3.2. Sample preparation and analysis details

Samples were ground with a mortar and pestle, until they were completely homogeneous, and placed in a plastic mould where they were mounted with a mixture of Epofix resin and hardener (6:1). Once the resin had hardened, mounted samples were removed from the mould and grinded using silicon carbide papers of different grade (P240-P4000) and a Buehler MetaSeru® 250 grinder-polisher. Finally, graphite paint was applied, and they were coated with platinum in order to prevent charging of the samples during the analysis. SEM analysis was performed using Carl Zeiss Evo MA 15 and HITACHI SU8230 scanning electron microscopes. The accelerating voltage used was 20kV.

3.3.4. X-RAY FLUORESCENCE

3.3.4.1. Principles of X-ray fluorescence

In X-ray fluorescence, the sample is exposed to X-rays produced by an X-ray tube [104]. The atoms of the elements in the irradiated specimen can absorb energy in form of photons, and as a result, it is possible to eject an electron from its atomic orbital if the energy of the incident photon is greater than the bounding energy of the electron to the atom nuclei. If the electron is ejected from an inner orbital then a different electron from an outer orbital can relocate to the lower orbital so that the initial configuration is restored [104]. The difference in energy between the two orbitals is released as a photon.

The photons emitted are the characteristic fluorescent X-ray radiation of the element, and since the energy difference between two atomic orbitals of an atom is characteristic of each element, which can be then identified by measuring the energy of the radiation emitted (FIGURE 3-8).

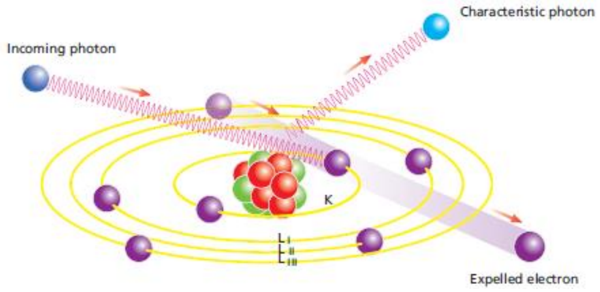

FIGURE 3-8. Product of characteristic radiation [104].

The quantity of an analyte present in a sample is related to the peak intensity. The X-ray fluorescent lines are observed as peaks, and the peak intensities depend on the count rate of a particular element determined by the number of photons emitted per unit of time. Light elements can have a lower number of fluorescent photons emitted, and hence it is more difficult to quantify them in a sample. The quantitative elemental composition of a sample is therefore calculated by identifying the energy of the X-ray peaks and the count rates of this energy lines.

In summary, XRF is a non-destructive, efficient technique for the quantitative analysis of all types of samples and with analytes concentrations starting from ppm level.

3.3.4.2. Sample preparation and analysis details

X-ray fluorescence (XRF) was employed for analysing the chemical composition of solid samples. XRF sample preparation started with the grinding of the samples until a fine powder was obtained, followed by heating at 900°C in oxidising atmosphere for the determination of the loss of ignition. Each sample was subsequently mixed with a lithium borate-based binder in a weight ratio of 95% binder and 5% sample and total weight of the mixture equal to 7 grams. The mixture was placed in a zirconium crucible (V = 30 mL, h = 32 mm, d_o = 40.5 mm and straight wall), which was fitted in a Katanax® K1 Prime fusion furnace. A temperature program was set during which the mixture is first heated until fused (T ≈ 1050 °C), mixed by automatic swinging of the crucible in the furnace, and finally poured on to a mould. The program finishes with the cooling of the mould and sample until approximately 70°C - 80°C. The result was a fused bead which was used for the analysis.

The analysis was carried out in a ZSX Primus II multi-element wavelength dispersive X-ray fluorescence spectrometer with the ZSX Primus II software. A fully-quantitative program was developed using a series of standards, which allowed to obtain calibration curves for the different analytes and to take into account the effects of the sample matrix. The analytes included in the program were Cr, Al, Fe, Mg, Na, Si and Ca. The standards were prepared by mixing pure oxides of the analytes of interest (excepting Na, which was added as Na_2CO_3) in different weight ratios; and their corresponding fused beads were obtained following an identical procedure than that used for the rest of samples.

Quantitative analysis by XRF is not influenced by the oxidation state of the elements, and the results are reported as oxides independently of the phases present in the sample.

3.3.5. ATOMIC ABSORPTION SPECTROSCOPY

Atomic absorption spectroscopy (AAS) is a characterisation technique able to quantify the concentration of different analytes in a sample by measuring the absorption of electromagnetic radiation by the atoms of the elements present. This technique was employed for analysis of liquid samples obtained during the alkali reduction process.

3.3.5.1. Principles of atomic absorption spectroscopy

When electromagnetic radiation is directed to a substance, part of it can be absorbed and increase the energy of the atoms. Electrons in the atoms get excited as a consequence of the energy gain, which depends on the wavelength of the electromagnetic radiation, and are able to reach higher energy levels within the atoms orbital.

Atoms of a particular element are able to absorb light of a particular wavelength, and this is the principle of atomic absorption spectroscopy, where light emitted by excited atoms of the element under analysis is passed through the sample in gaseous state [105]. In order to obtain a gaseous sample, the liquid sample is atomised in a burner with the aid of an oxidant gas mixture. The lamp acting as light source in atomic absorption spectrometers consists of a cathode of the corresponding element and an anode made of tungsten.

The reduction in intensity of the radiation after interacting with the sample is measured, as part of it is absorbed by the atoms of this element present in the sample [106]. The amount of radiation absorbed is directly proportional to the concentration of the analyte in the sample, and thus a calibration curve absorbance versus concentration can be obtained by measuring the absorption of standard solutions of known concentration.

Atomic absorption spectroscopy is commonly used for the analysis of the chemical composition of a sample as it is a highly sensitive technique which provides accurate results and the analysis requires a very small amount of sample.

3.3.5.2. Sample preparation and analysis details

Atomic absorption spectroscopy was used for the analysis of liquid samples obtained from the treatment of the reduced and roasted chromite ore samples.

Liquid samples were first diluted with distilled water up to a total volume of 100 mL in a volumetric flask, using a dilution ratio of 1:50 or 1:100 depending on the sample. For the calculation of the calibration curve, a bulk solution containing a known concentration of the analytes under study was prepared. The concentration of the bulk depended on the maximum concentration of each analyte expected in each batch of samples. For the preparation of the bulk solutions standard solutions of concentration 1000 µg/L of the different analytes and distilled water were used. Cr, Fe, Na, Al, Mg, Ca and Si hollow cathode lamps were used for AAS analysis. Fe, Na, Si, Ca and Mg were analysed using an air-acetylene flame, while N_2O gas was also required for analysis of Cr and Al. The software reported the concentration of the analytes in the sample as mg/L.

3.3.6. THERMODYNAMIC COMPUTATIONS

Thermodynamic computations were carried out using HSC [107] and FactSage 6.4 [46] thermodynamic databases. HSC was mainly employed for calculating free Gibbs energy, whereas FactSage was preferred for the computation of predominance area diagrams, E_h-pH diagrams, equilibrium calculations and phase diagrams.

FactSage combines different pure substances and solution databases for the performance of thermodynamic calculations. In this case, the calculations were carried out using the following databases: FactPS, SGPS, FToxid, FTsalt and FTmisc. The software offers various options for the representation of the results depending on the application required.

3.3.7. DENSITY DETERMINATION

The density of the three chromite ores was measured by using a density bottle or pycnometer. The specific gravity of the ore is the ratio of the mass of a known volume of dry solids in the presence of air to the mass of an equal volume of water. The density can be then calculated by equation (eq.4):

$$\mathrm{d} = \frac{\mathrm{W}_2 - \mathrm{W}_1}{(\mathrm{W}_2 - \mathrm{W}_1) - (\mathrm{W}_3 - \mathrm{W}_4)} \qquad \text{(eq.4)}$$

where W_1 is equal to the mass of the empty bottle, W_2 the mass of the bottle and dry ore, W_3 the mass of bottle, ore and water and W_4 is the mass of the bottle filled with water. The ore samples were dried at 100°C before being subjected to the density analysis.

The empty and dry bottle including the stopper (W_1) was weighted in a 3 decimal places microbalance. Approximately 1 gram of ore was transferred to the bottle and the exact weight of bottle and sample (W_2) was taken. Distilled water was then added to the bottle until completely full, making sure that any entrapped air bubbles are removed, and the mass of bottle, soil and water was measured (W_3). Finally, the bottle was emptied, thoroughly washed and dried before filling it up with only distilled water. The bottle full of water was weighted (W_4).

3.3.8. OTHER CHARACTERISATION TECHNIQUES USED

3.3.8.1. Ultraviolet-visible spectroscopy (UV-vis)

UV-vis spectroscopy was used to determine the oxidation state of chromium in aqueous solution. A series of Cr^{3+} and Cr^{6+} standard solutions of known concentration were prepared and analysed to obtain calibration curves. The aqueous samples were diluted with distilled water (if necessary) to ensure that the analytes under study were in the range of the calibration curves. Distilled water and a solution of sulfuric acid were used as the blank solutions required for the base line of the equipment. Absorption (A) versus wavelength (λ) data was recorded and plotted. The UV-vis patterns obtained were analysed by comparing with existing literature.

3.3.8.2. Electron probe micro-analysis (EPMA)

Electron probe micro-analysis (EPMA) is a non-destructive analytical technique able to provide very accurate quantitative elemental analysis of solid samples. The fundamentals of EPMA are the same that those of SEM, with the added ability to acquire compositional information by energy-dispersive spectroscopy. EPMA was used to analyse the composition of the chromite phase in the three different chromite ores used in this research project. The sample preparation was identical to that for SEM analysis, but due to the accuracy of the technique, finer grinding (0.25 µm) was required. This was achieved by using a combination of silicon carbide papers and polishing liquids of different grade.

Chapter 4

CHARACTERISATION OF CHROMITE ORES

Chapter content

Three different chromite ores were used in the experimental part of this investigation. The characterisation of the chromite ores was carried out by using XRPD, EPMA, SEM-EDX and XRF analytical techniques. Phase mapping analysis of the Brazilian chromite ore was performed using SEM with Mineralogic Mining software attached. The results obtained for each chromite are presented and compared in this chapter.

Chapter conclusions

The S.A. chromite is a chemical grade ore of composition 44.66% Cr_2O_3*, 24.56* Fe_2O_3*, 10.94 MgO, 14.43* Al_2O_3*, 3.82* SiO_2 *and 0.52* TiO_2*. The main phase present in the ore is chromite spinel with the stoichiometric formula* $(Fe_{0.56}Mg_{0.44})(Cr_{0.61}Al_{0.29}Fe_{0.08})_2O_4$ *as calculated from EPMA results; and the chemical composition of the chromite phase does not vary significantly from particle to particle. A Na-Al-Ca-silicate phase was also identified.*

In the case of the Brazilian ores, the content of silica is significantly higher, with 8.48 wt.% and 13.20 wt.% SiO_2 *in chromite E4 and chromite E5 respectively. In this case, chromite spinel is also the dominant phase, but a higher variety of silicates and gangue minerals can be found, including* $(Mg,Fe,Al)_6(Si,Al)_4O_{10}(OH)_8$, SiO_2, $NaCa_2Mg_5AlSi_7O_{22}(OH)_2$, $K_{0.7}Na_{0.4}Ca_{1.1}Al_{3.3}Si_{8.7}O_{24}(H_2O)_3$, $NaCa_2Mg_5AlSi_7O_{22}(OH)_2$, $Ca(Mg_{0.67}Fe_{0.33+2})(CO_3)_2$ and $(Mg_7Al_4(OH)_{22})_{0.09091}$. *Analysis using Mineralogic Mining tool suggested that the main mineral phases present in Br. chromite E4 are chromite spinel, dolomite and forsterite, which altogether account for more than 85% of the weight of the sample. SEM analysis indicated that the silicate gangue can be found embedded in the chromite particles.*

4.1. CHARACTERISATION OF SOUTH AFRICAN CHROMITE ORE

The overall chemical composition of the South African chromite ore used in most of the experiments was determined by XRF and is presented in TABLE 4-1. Other properties of the ore such as density, particle size, phase analysis and Cr:Fe ratio are also included in the table.

TABLE 4-1. Chemical composition (by XRF), density, particle size and phase analysis of the as-received South African chromite ore.

As-received South African chromite ore			
Chemical composition		**Density (g/cm^3)**	3.73
Cr_2O_3	44.66	**Particle size (μm)**	90-120
Fe_2O_3	24.56	**Phase analysis**	$(Fe,Mg)(Cr,Al)_2O_4$, $Ca_{11.5}Al_{23}Si_{25}O_{96}$ and SiO_2
MgO	10.94		
Al_2O_3	14.43	**Cr:Fe (from XRF)**	1.73:1
SiO_2	3.82		
TiO_2	0.52		
V_2O_5	0.32		
MnO	0.26		
CaO	0.42		

The S.A. chromite can be considered as chemical grade ore, as it has a high chromium concentration of 44.66% wt. Cr_2O_3 and relatively low silica content, 3.82% wt. SiO_2; although less than 1% wt. silica content is desirable for chemical grade chromites. According to the classification presented by Maliotis (1996) [2], the chromite could be also regarded as a high-iron chromite ore of metallurgical grade with a Cr:Fe weight ratio in the range of 1.5-2:1. The ore sample available has homogeneous particle size of approximately 106 μm. The density of the ore is 3.728 g/cm^3 and was determined following the procedure described in section 3.3.7.

Besides the main constituents of chromite spinel $(Fe,Mg)(Cr,Al,Fe)_2O_4$, minor quantities of Ti, V and Mn are present in the sample, which are expected to be located in octahedral positions substituting Cr^{3+} and Al^{3+} cations. Ca, however, is more likely to be found in the silicate phases present in the ore, as it will be discussed below.

The phase analysis was carried out by X-ray powder diffraction, and the XRPD pattern of the as-received chromite ore is shown in FIGURE 4-1. The experimental pattern was examined using the X'Pert HighScore Plus database software, and the results indicated that the predominant phase is chromite spinel with Fe^{2+} and Mg^{2+} cations occupying tetrahedral positions and Cr^{3+} and Al^{3+} cations in octahedral sites. The reference pattern available in the database that best matched the experimental data corresponds to a chromite spinel phase with the stoichiometric formula $(Fe_{0.52}Mg_{0.48})(Cr_{0.76}Al_{0.24})_2O_4$ and ICDD reference pattern number 01-070-6386. The reference pattern is shown in FIGURE 4-1 for comparison with the experimental XRPD data. Low-intensity peaks corresponding to silicate phases $Ca_{11.5}Al_{23}Si_{25}O_{96}$ were also identified.

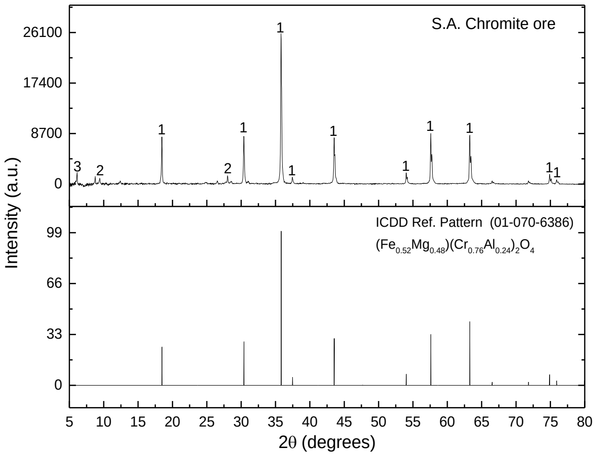

FIGURE 4-1. X-ray powder diffraction pattern of the as-received chromite ore (top) and ICDD reference pattern (01-070-6386) for the $(Fe_{0.52}Mg_{0.48})(Cr_{0.76}Al_{0.24})_2O_4$ spinel phase (bottom). 1 = $(Fe_{0.52}Mg_{0.48})(Cr_{0.76}Al_{0.24})_2O_4$ (01-070-6386), 2 = SiO_2 (01-073-3423), 3 = $Ca_{11.5}Al_{23}Si_{25}O_{96}$ (04-009-9842).

Based on the XRPD data, the crystallographic parameters of the chromite spinel phase were refined by Rietveld analysis using GSAS-EXPGUI software [100]. FIGURE 4-2 shows the observed XRPD data of S.A. chromite ore in black colour, the calculated pattern in red, the refined background in green and the difference plot in blue, all obtained by Rietveld refinement. The fitting of the calculated pattern is significantly good as it can be seen in FIGURE 4-2 by comparing the observed and calculated patterns superimposed. This is also confirmed by the goodness of fit obtained equal to Rp(%) = 2.70.

The chromite spinel phase has a faced-centered cubic lattice and the Rietveld refinement provided a figure for the lattice parameter of 8.306 Å. The site occupancies in tetrahedral and octahedral sites were also refined and the stoichiometric formula of the chromite phase obtained was $(Fe_{0.51}Mg_{0.49})(Cr_{0.68}Al_{0.32})_2O_4$. The crystallographic parameters obtained are presented in TABLE 4-2.

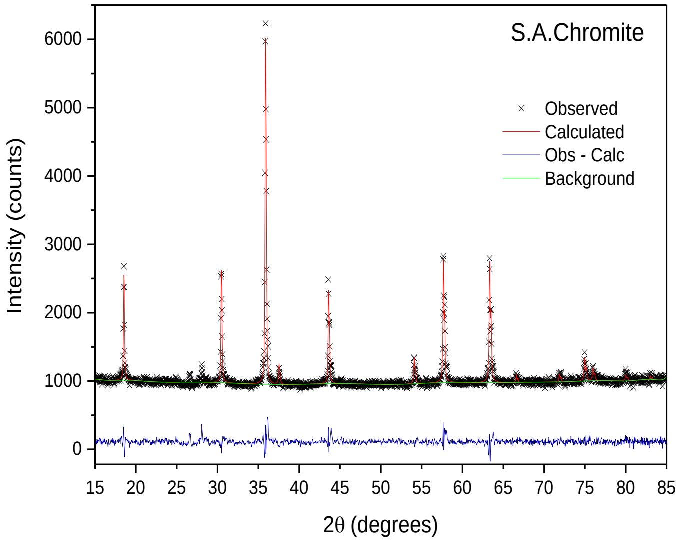

FIGURE 4-2. Comparison of observed XRPD pattern, calculated pattern, background and difference plot obtained by Rietveld refinement of S.A. chromite ore X-ray diffraction data.

TABLE 4-2. Crystallographic parameters of S.A. chromite ore calculated by Rietveld analysis. Rp(%) = 2.70.

Lattice/Space Group		Lattice parameter (Å)	
F-centered cubic/Fd-3m		8.306	
Octahedral sites		Tetrahedral sites	
Fraction Cr^{3+}	Fraction Al^{3+}	Fraction Fe^{2+}	Fraction Mg^{2+}
0.68	0.32	0.51	0.49

The composition of the chromite spinel phase present in the ore was analysed by electron probe micro-analysis (EPMA). The analysis of a number of random chromite particles by EPMA provided an accurate average chemical composition of the chromite phase expressed in weight percentage. All iron was initially reported as Fe^{2+} by this technique, and further calculation was required to distinguish between Fe^{2+} and Fe^{3+}, as both oxidation states of iron are possible in chromite spinel. The method used for the recalculation of the iron percentage, using uniquely EPMA data, is based on stoichiometric criteria and was described by Droop (1987) [108] in detail. The difference between the tabulated oxygen total and cation total –calculated taking into consideration the total cation charge and the total number of cations– and the observed values is attributable to the incorrect assumption that all the iron in chromite is present as Fe^{2+}. The number of Fe^{3+} ions present per X oxygens (F) may be calculated by the following expression (eq.5).

$$F = 2X \cdot (1 - \frac{T}{S}) \qquad \text{(eq.5)}$$

where T is the ideal number of cations per formula unit, and S is the observed cation total per X oxygens calculated assuming all iron to be in (2+)-state.

The chemical composition and ions per formula unit of the chromite phase, obtained by EPMA, were recalculated using the method by Droop (1987) [108] and are presented in TABLE 4-3.

TABLE 4-3. Chemical composition expressed as oxides and ions per formula unit of chromite phase analysed by EPMA (recalculated using the stoichiometric method by Droop (1987) [108]).

Composition (wt.%)	**Cr_2O_3**	**FeO**	**Fe_2O_3**	**MgO**	**Al_2O_3**	**TiO_2**	**V_2O_3**	**NiO**	**MnO**
	46.75	20.40	6.65	9.03	14.97	0.65	0.32	0.11	0.35
Ions per formula unit	Cr^{3+}	Fe^{2+}	Fe^{3+}	Mg^{2+}	Al^{3+}	Ti^{4+}	V^{3+}	Ni^{2+}	Mn^{2+}
	1.22	0.56	0.17	0.44	0.58	0.02	0.01	0.003	0.010

Using the results obtained from XRD-Rietveld and EPMA analysis, the stoichiometric formula of the chromite spinel in the S.A. ore was calculated obtaining the following:

- XRD-Rietveld → $(Fe_{0.51}Mg_{0.49})(Cr_{0.68}Al_{0.32})_2O_4$
- EPMA → $(Fe_{0.56}Mg_{0.44})(Cr_{0.61}Al_{0.29}Fe_{0.08})_2O_4$

The stoichiometric formulas obtained by the two methods are comparable. The formula obtained by EPMA is considered to be the closest to the real formula of the mineral because of the high accuracy provided by this technique. Minor constituents such as Ti, V and Mn were not taken into account in the formula. In the case of the stoichiometric formula obtained by XRD-Rietveld, all iron was assigned to tetrahedral sites and is reported as Fe^{2+}. Fe^{3+} was initially included in the refinement of the crystal structure, but a negative value of the octahedral site occupancy (fraction) for Fe was obtained, and accordingly, Fe^{3+} was excluded from the refinement. Nevertheless, XRD-Rietveld provides a stoichiometric formula in good agreement with EPMA results.

An important factor to consider in the characterisation of chromite ores is the presence of silica-based gangue minerals commonly associated with them, including enstatite ($MgSiO_3$), olivine ($(Mg,Fe)_2SiO_4$), talc ($Mg_3Si_4O_{10}(OH)_2$) or serpentine ($(Mg,Fe)_3Si_2O_5(OH)_4$), among others.

In this particular case, magnesium silicate with small amounts of dissolved iron and a complex Ca-Al-Na-silicate phase were identified in the ore, as shown in the backscattered SEM image and elemental mapping of the as-received S.A. chromite in FIGURE 4-3.

Low and high magnification backscattered SEM images of the as-received chromite ore are presented in FIGURE 4-4. The two phases can be clearly differentiated in these images: light grey particles (A, B, D) are chromite spinel particles, and darker grey particles (C) correspond to siliceous gangue minerals. The EDX-SEM elemental analysis of areas A-D is shown in TABLE 4-4, which suggest that the composition of chromite ore is consistent and does not vary significantly from one particle to another.

The gangue phase is composed of silica combined mainly with aluminium, calcium and a smaller proportion of Na, which agrees with elemental mapping results in FIGURE 4-3.

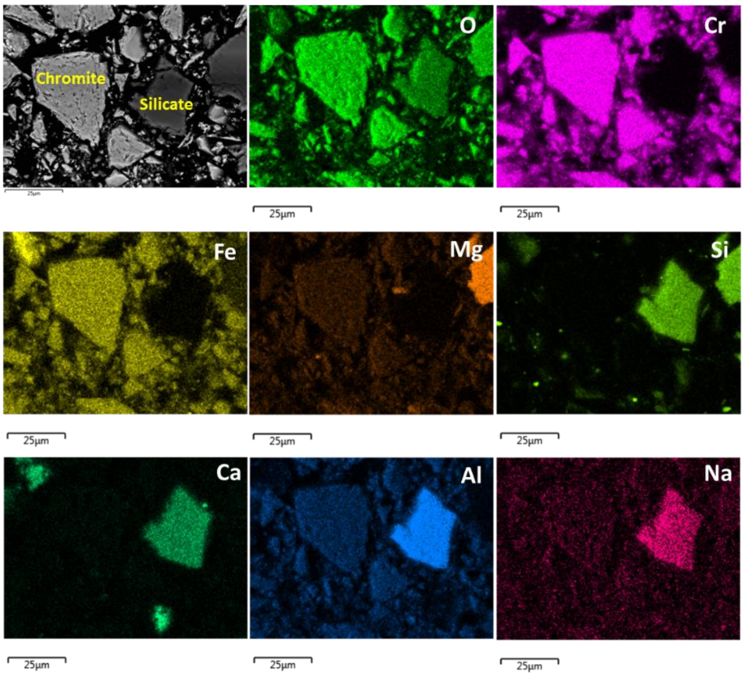

FIGURE 4-3. Backscattered scanning electron microscopy image (operating voltage = 20 kV) of the as-received chromite ore and elemental distribution map obtained by energy dispersive X-ray analysis (EDX).

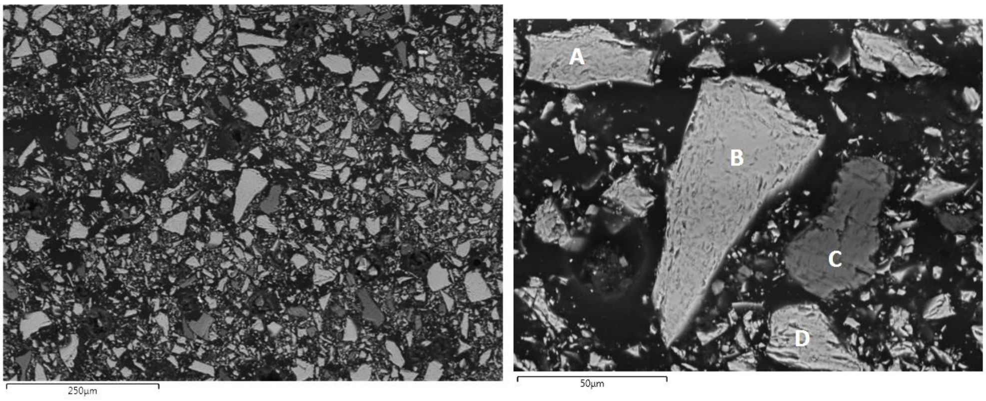

FIGURE 4-4. Backscattered scanning electron microscopy images of the as-received chromite ore: low magnification (left) and high magnification (right).

TABLE 4-4. Elemental composition of areas A to B in FIGURE 4-4 analysed by SEM-EDX.

%Wt	Cr	Fe	O	Mg	Al	Si	Ca	Na	Ti
A	36.8	21.8	27.3	5.8	7.9	-	-	-	0.5
B	36.7	22.8	26.6	5.7	7.7	-	-	-	0.5
C	0.6	0.4	41.0	-	18.9	24.3	13.0	1.8	-
D	37.1	22.4	25.8	6.2	8.0	-	-	-	0.4

The SEM-EDX analysis of two more particles in a different area of the sample confirms the results above. EDX spectra from particles 4 and 5 and their corresponding elemental composition are shown in FIGURE 4-5. The elemental composition of particle 4 indicates that this is an Al-Ca-Na silicate particle, while particle 5 is chromite with 35.2% wt.% Cr.

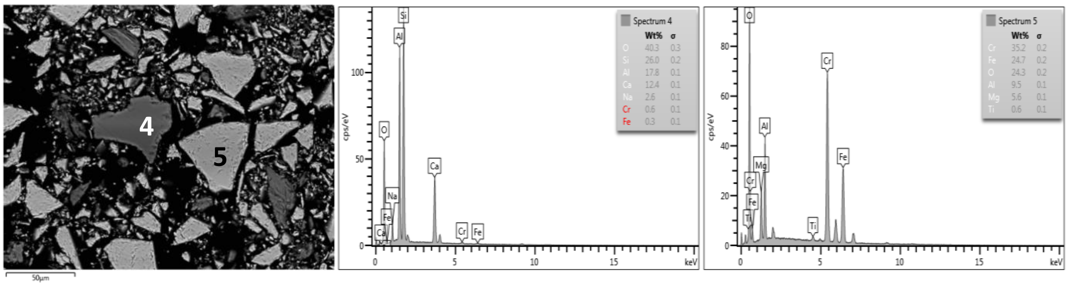

Spectrum 4

	Wt%	σ
O	40.3	0.3
Si	26.0	0.2
Al	17.8	0.1
Ca	12.4	0.1
Na	2.6	0.1
Cr	0.6	0.1
Fe	0.3	0.1

Spectrum 5

	Wt%	σ
Cr	35.2	0.2
Fe	24.7	0.2
O	24.3	0.2
Al	9.5	0.1
Mg	5.6	0.1
Ti	0.6	0.1

FIGURE 4-5. Backscattered SEM image of S.A. chromite ore and EDX spectra and elemental composition of particles 4 and 5.

4.2. CHARACTERISATION OF BRAZILIAN CHROMITES

The E4 and E5 chromite ore samples tested for alkali reduction have Brazilian origin. The XRF analysis of the ores, and the chemical composition and ions per formula unit of their corresponding chromite phases are presented in TABLE 4-5.

TABLE 4-5. Overall ore composition, and chemical composition and ions per formula unit of the chromite phase in the Brazilian E4 and Brazilian E5 chromite ores.

Overall composition of the ore analysed by XRF (wt.%)

Ore	Cr_2O_3	Fe_2O_3	MgO	Al_2O_3	SiO_2	CaO	TiO_2	MnO	Cr:Fe
Br.E4	44.32	14.29	15.05	16.15	8.48	1.34	0.24	-	3.03
Br.E5	39.20	14.32	15.24	14.71	13.20	2.76	0.22	0.19	2.68

Chemical composition of the chromite phase analysed by EPMA (wt.%)

Ore	Cr_2O_3	FeO	Fe_2O_3	MgO	Al_2O_3	TiO_2	V_2O_3	NiO	MnO
Br.E4	50.89	15.09	1.11	12.56	18.48	0.17	0.11	0.14	0.31
Br.E5	51.36	15.63	-	12.24	18.94	0.19	0.11	0.12	0.30

Ions per formula unit (4 oxygens) of the chromite phase analysed by EPMA (wt.%)

Ore	Cr^{3+}	Fe^{2+}	Fe^{3+}	Mg^{2+}	Al^{3+}	Ti^{4+}	V^{3+}	Ni^{2+}	Mn^{2+}	Cr:Fe
Br.E4	1.273	0.400	0.027	0.593	0.689	0.004	0.003	0.003	0.008	2.98
Br.E5	1.284	0.413	-	0.577	0.706	0.004	0.003	0.003	0.008	3.12

XRF analysis of the Brazilian E4 and E5 chromites shows that the ores have a Cr_2O_3 concentration of 44.32% wt. and 39.20% wt., respectively, and a Cr-to-Fe equal to 3.03 and 2.68. Based on this, the E4 chromite could be classified as refractory grade with high chromium, low aluminium and very high silica. Brazilian chromite E5 is similar in terms of Fe_2O_3% wt., MgO% wt. and Al_2O_3% wt, but it is less concentrated in Cr_2O_3 and has, on the other hand, higher SiO_2 content (13.2 wt.%). The EPMA analysis provided accurate composition of the chromite phase (excluding the silicate gangues). As in the case of S.A. chromite, the original results given by EPMA technique were recalculated to account for the presence of Fe^{3+} in the spinel structure, and the composition of the chromite phase is expressed both as oxides and ions per formula unit (TABLE 4-5). The differences between the Cr:Fe ratios calculated from XRF and EPMA results can be explained by the presence of iron also in the silicate-based gangues and not exclusively in the chromite phase.

If minor substituents (Ti, V, Ni and Mn) are not taken into account, the chromite spinel in Br.E4 has a formula of the following stoichiometry $(Fe^{2+}_{0.403}Mg_{0.597})(Cr_{0.640}Al_{0.347}\ Fe^{3+}_{0.013})_2O_4$. One of the main features of both Brazilian ores is the high amount of siliceous gangue minerals present, which in the case of the E4 chromite accounts for the 8.48% wt. of the total ore. This is a significantly high value taking into account that, as already mentioned in this document, chromite ores with less than 1 wt.% SiO_2 are the preferred feedstock for the production of sodium chromate by the alkali roasting process.

The XRPD experimental data obtained for the Brazilian ores are shown in FIGURE 4-6 along with the identification of the X-ray peaks and the phase analysis.

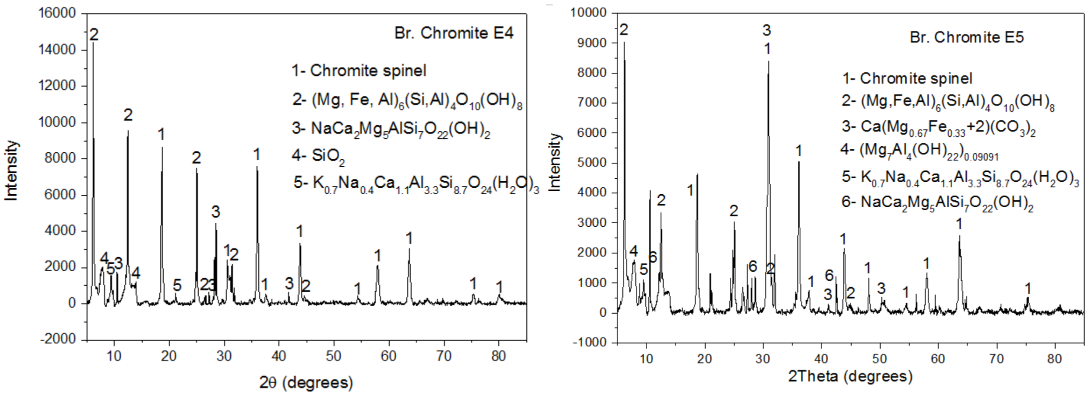

FIGURE 4-6. X-ray powder diffraction patterns and phase analysis of the as-received Brazilian chromite ores E4 and E5.

TABLE 4-6. Density and phase analysis of the Brazilian chromite E4 and E5 ores.

	Density (g/cm^3)	**Phase analysis**
Br. Chromite E4	3.898	$(Fe,Mg)(Cr,Al)_2O_4$, $(Mg,Fe,Al)_6(Si,Al)_4O_{10}(OH)_8$, SiO_2, $NaCa_2Mg_5AlSi_7O_{22}(OH)_2$, $K_{0.7}Na_{0.4}Ca_{1.1}Al_{3.3}Si_{8.7}O_{24}(H_2O)_3$
Br. Chromite E5	3.713	$(Fe,Mg)(Cr,Al)_2O_4$, $(Mg,Fe,Al)_6(Si,Al)_4O_{10}(OH)_8$, $Ca(Mg_{0.67}Fe_{0.33+2})(CO_3)_2$, $(Mg_7Al_4(OH)_{22})_{0.09091}$, $K_{0.7}Na_{0.4}Ca_{1.1}Al_{3.3}Si_{8.7}O_{24}(H_2O)_3$, $NaCa_2Mg_5AlSi_7O_{22}(OH)_2$

TABLE 4-6 summarises the particle size, density and phase analysis of the Brazilian chromites. These ores contain phases with a wide range of particle sizes, and therefore, they were ground down to a particle size of approximately 100-120 µm as preparation for the reduction experiments.

The phase analysis performed using XRPD experimental data showed that the main phase corresponds to chromite spinel which coexist in the ore body with a series of silicate phases as it can be seen in TABLE 4-6. XRPD peaks for $Mg,Fe,Al)_6(Si,Al)_4O_{10}(OH)_8$, $NaCa_2Mg_5AlSi_7O_{22}(OH)_2$, $K_{0.7}Na_{0.4}Ca_{1.1}Al_{3.3}Si_{8.7}O_{24}(H_2O)_3$ and free SiO_2 were identified in the chromite E4 pattern; whereas the XRPD pattern of the E5 ore shows diffraction peaks for $(Mg,Fe,Al)_6(Si,Al)_4O_{10}(OH)_8$, $NaCa_2Mg_5AlSi_7O_{22}(OH)_2$, $Ca(Mg_{0.67}Fe_{0.33+2})(CO_3)_2$, $(Mg_7Al_4(OH)_{22})_{0.09091}$ and $K_{0.7}Na_{0.4}Ca_{1.1}Al_{3.3}Si_{8.7}O_{24}(H_2O)_3$.

High magnification backscattered SEM images of the as-received Br. Chromite E4 sample are shown in FIGURE 4-7. Just by looking at the colour contrast between particles, it is obvious that the sample consists of a heterogeneous mixture of different phases, as it was also observed from the XRPD results. When focusing on individual particles, the sample contains particles with homogenous composition and particles where more than one phase can be differentiated. In general, brighter phases were identified as chromite spinel and darker phases as complex silicates. The backscattered SEM image shown in FIGURE 4-8 illustrates a chromite particle (bottom right), a silicate particle (top right) and a particle where both phases are present. The distribution of phases can be observed in the elemental mapping also shown in FIGURE 4-8.

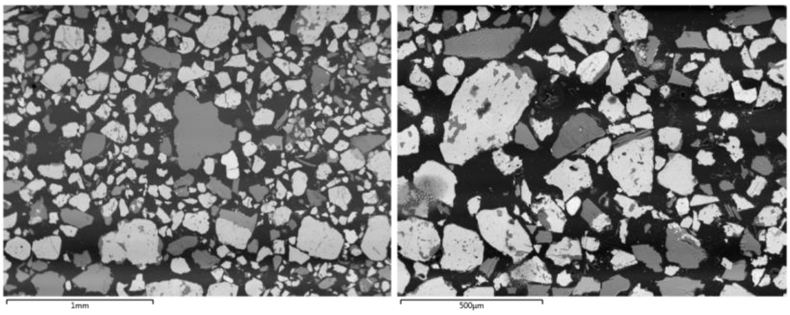

FIGURE 4-7. Low-magnification backscattered SEM images of a Brazilian chromite E4 sample.

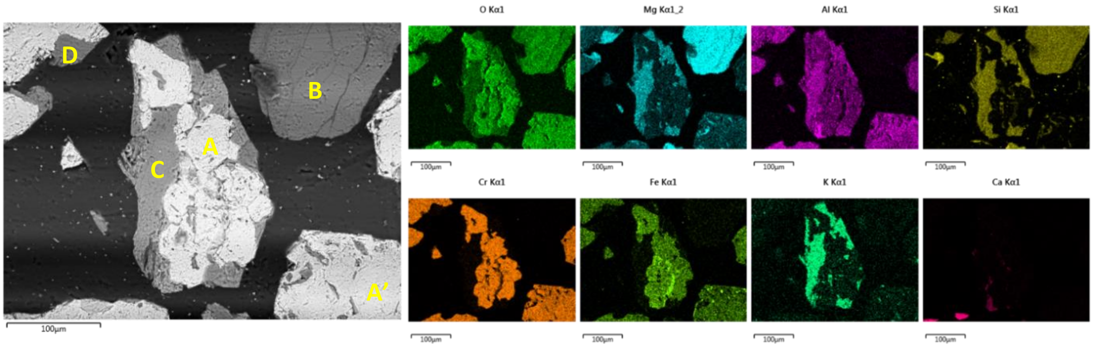

FIGURE 4-8. Backscattered SEM image and elemental mapping of Brazilian chromite E4 sample.

According to the elemental mapping, brighter areas labelled as A and A' in FIGURE 4-8 correspond to chromite spinel phase. Chromium is concentrated on this phase, but it is also found in minor concentrations in darker areas i.e. B, C and D, which correspond to silicate-based complex phases. FIGURE 4-8 illustrates two types of silicates i.e. a K-Mg-Al silicate (areas D and C) and a magnesium silicate (area B). Complex silicates present in this ore vary in composition along the particles, as it can be seen in TABLE 4-7 where EDX point analysis of areas A, B, C and D is presented with the corresponding calculated stoichiometric phases.

TABLE 4-7. EDX analysis of areas A-D in FIGURE 4-8. Values are expressed in wt%.

Are	Cr	Fe	Al	Mg	Si	K	Ti	O	Stoichiometric phase
A	48.9	16.9	6.0	4.5	-	-	-	23.8	$Fe_{0.62}Mg_{0.38}Cr_{1.63}Al_{0.37}O_4$
B	-	1.3	-	28.6	25.4	-	-	44.8	$Mg_{1.3}Fe_{0.02}SiO_3$
C	2.8	1.5	9.5	15.8	23.2	10.4	1.0	35.8	$K_{0.33}Cr_{0.06}Al_{0.42}Mg_{0.78}SiO$
D	2.9	1.9	11.5	23.1	18.6	-	-	41.9	$Mg_{1.44}Al_{0.65}Cr_{0.08}SiO_4$

The similarities between the microstructure of the two Brazilian chromite ores are significant, with chromite spinel and complex silicates as the principal phases constituting the Brazilian chromite E5. However, one of the main differences is the higher content of silicate phases in this ore compared to the E4 chromite, and this can be readily observed in the SEM images of different magnification of the Brazilian chromite E5 sample in FIGURE 4-9.

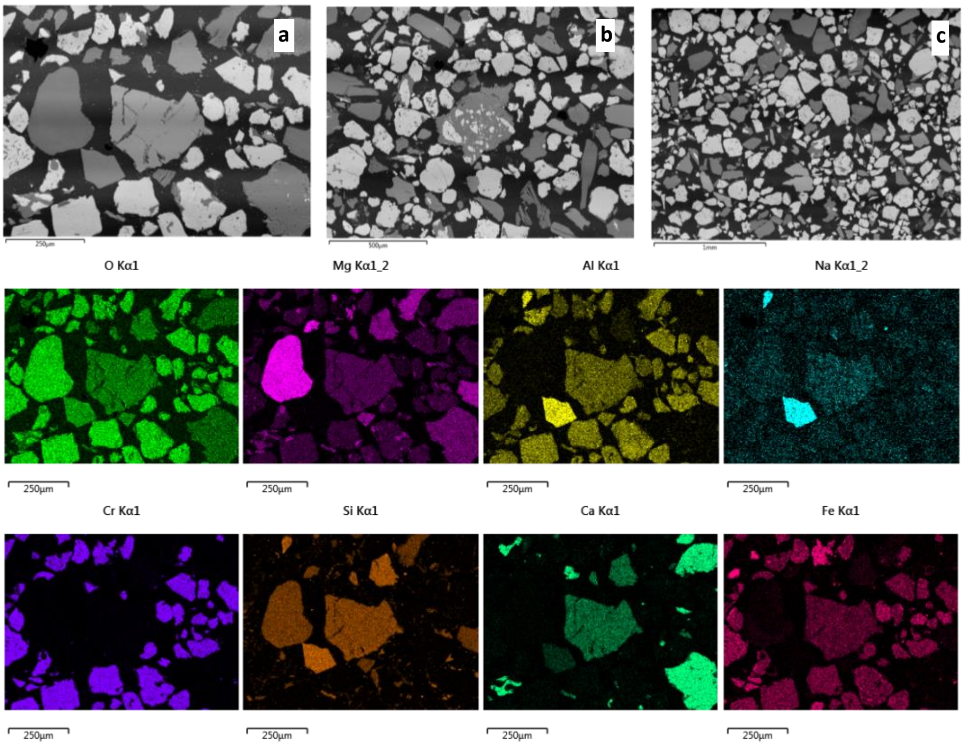

FIGURE 4-9. Backscattered SEM images of Br. chromite E5 and elemental mapping of image a.

The elemental EDX mapping of micrograph (a) is also shown in this figure. In this case, the main silicate phases identified are $MgSiO_3$, an Al-Na-Ca-silicate and a complex silicate containing Mg, Al, Na, Ca and Fe. Generally, the chromite phase and the silicate gangues are found in individual particles, but FIGURE 4-9 shows that there is also possible to find entrapment of the silicate gangue within the chromite phase in some of the particles (micrographs a and b).

4.2.1. ANALYSIS OF BR. CHROMITE E4 ORE USING ZEISS MINERALOGIC MINING SYSTEM

The analysis of the Brazilian chromite E4 using Zeiss Mineralogic Mining system installed in SEM equipment was carried out by collaboration with CarlZeiss (Cambridge, UK). The Mineralogic Mining application allows the identification of mineral phases in a sample using EDX and the illustration of the results as a map where each phase is associated to a particular colour. The possible phases present, named as mineral classes, need to be defined beforehand by the user, and the software analyses and classifies every particle in the corresponding mineral class. Particles that do not fall under any of the mineral classes defined are classified as unidentified particles; and they are shown in grey by the software allowing the addition of new possible mineral classes and the progressive improvement of the analysis of a certain sample.

In this case, 16 different mineral classes were identified and added to the analysis. A backscattered SEM image of the whole area of the sample was obtained and the phase identification of the image was performed obtaining a Mineralogic colour map. The software allowed to report the results of both the backscattered image and the Mineralogic map as montage images, and these are shown in FIGURE 4-10. The main target minerals found in this sample, and their weight(%), area (%), particle size and average composition are listed in TABLE 4-8. The results show that approximately 65 wt.% is chromite ore, while the 31.9 wt.% correspond to dolomite and a mixture of different silicate minerals, namely forsterite, quartz, albite and a Ca-Mg-(Fe) silicate. The remaining contains small traces of other minerals and the unidentified particles (which account for the 7% of the area).

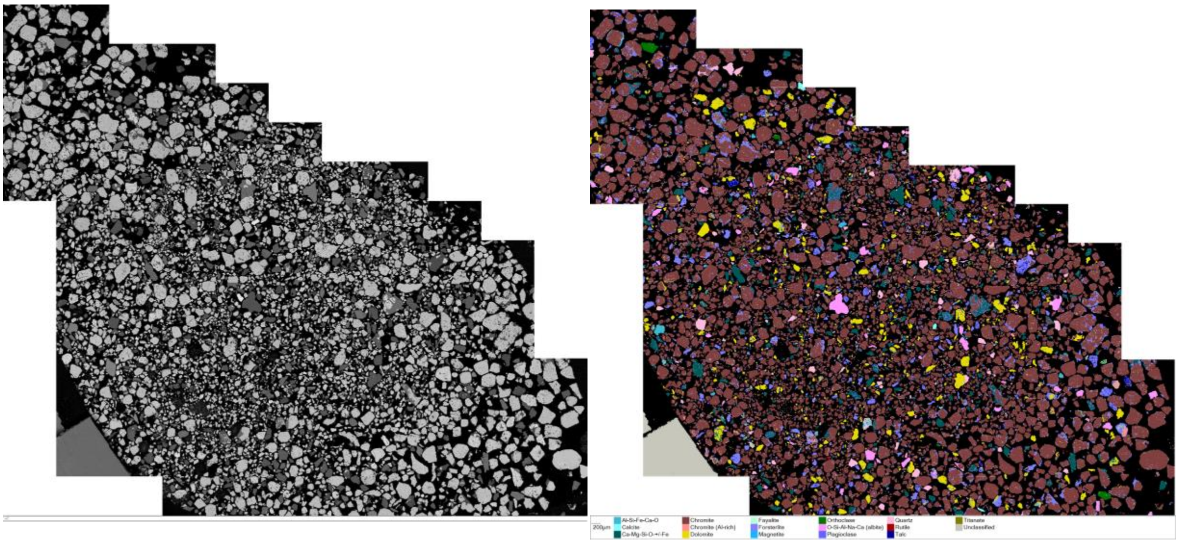

FIGURE 4-10. Backscattered scanning electron microscopy and Mineralogic phase map montage images of the Brazilian chromite ore E4.

TABLE 4-8. Weight (%), area (%), average composition and grain size of the main target minerals identified in the Brazilian chromite E4 ore.

Target Mineral	Wt %	Area %	Average Composition	Grain Size (µm)
Chromite	65.718	69.170	Cr 52.36; Fe 18.84; Al 12.42; Mg 8.52; O 7.86;	92.6
Dolomite	12.605	4.655	O 51.07; Ca 33.16; Mg 15.1; Fe 0.37; Si 0.3;	49.35
Forsterite	7.879	8.293	Si 34.5; O 30.94; Mg 29.01; Cr 3.63; Fe 1.91;	24.70
Ca-Mg-Si-O+/-Fe	4.881	5.138	O 36.92; Si 31.88; Mg 13.95; Ca 12.81; Fe 3.47; Cr 0.96;	42.73
Quartz	4.334	1.721	Si 55.33; O 44.55; Fe 0.12; K 0;	28.66
O-Si-Al-Na-Ca	1.546	1.628	O 40.51; Si 36.93; Al 13.48; Na 6.38; Ca 2.71;	75.13
Talc	0.689	0.725	O 47.87; Si 28.34; Mg 23.78;	16.33
Magnetite	0.361	0.380	Fe 78.99; O 20.99; Ti 0.03;	13.98
Rutile	0.137	0.032	Ti 58.94; O 41.06;	21.86
Fayalite	0.007	0.007	Fe 53.8; O 33.04; Si 13.08; Cr 0.08;	10.46

The analysis of the sample also provided the list of traces minerals and additional assay data showing the elemental distribution between the different mineral classes. A more detail explanation of the analysis carried out can be seen in Appendix 3.

Chapter 5

THERMODYNAMIC STUDY AND THERMAL DECOMPOSITION ANALYSIS

Chapter content

Chapter 5 aims to present the main thermodynamic aspects related with the alkali reduction of chromite ore and the phase transformations taking place at different temperatures and chemical potentials. Gibbs free energy calculations and a phase equilibria study have been performed and compared for the alkali roasting of chromite in reducing and oxidising atmosphere. Isochronal and isothermal thermogravimetric experiments of chromite ore under different chemical potentials were performed, and the samples were characterised by XRPD and Rietveld refinement.

Chapter conclusions

The ΔG of formation of the metallic oxides present in chromite were calculated (300°C to 1300°C) and the following sequence was obtained from highest to lowest stability: $MgO > Al_2O_3 > Cr_2O_3 > FeO > Fe_3O_4 > Fe_2O_3$*. The Ellingham diagram computed indicates that the temperatures required to reduce* FeO *and* Cr_2O_3 *with carbon are 725°C and 1250°C, respectively. The decomposition tendency of magnesiochromite in reducing atmosphere is lower than that of ferrochromite; and ΔG calculations confirmed that* $MgCr_2O_4$ *is harder to decompose also under oxidising conditions. The predominance area diagram for the Fe-Cr-Na-O-C system showed that metallic Fe and* $NaCrO_2$ *co-exist at 1050°C for a certain range of partial pressures of* CO/CO_2*, and under these conditions the instability of* Cr^{6+} *is assured. Thermal analysis indicated that the decomposition of chromite in* $NaCrO_2$ *and Fe starts from 800°C, and the phases can be observed in XRPD patterns at 1000°C and 1050°C. Texture analysis suggested that the Fe formed has a preferential orientation in the [110] direction. In air atmosphere, exsolution of* Fe_2O_3 *can be observed when heating at 900°C and above. In argon atmosphere, and in the presence of carbon, no phase decomposition was observed.*

5.1. THERMODYNAMIC STUDY

5.1.1. GIBBS FREE ENERGY CALCULATIONS

A process is considered spontaneous when there is a decrease of the system free energy which occurs without the assistance of any external energy (from the 2nd law of thermodynamics) [109]. The Gibbs free energy (ΔG) is the variable used to evaluate whether a reaction is spontaneous or not, and for a chemical reaction at constant temperature and pressure, the free energy can be calculated as:

$$\Delta G = \Delta H - T \cdot \Delta S \qquad \text{(eq.6)}$$

where T is the temperature in kelvin degrees and ΔS is the change in entropy. A negative value of ΔG indicates that the reaction occurs spontaneously, while a reaction with a positive value of free energy is considered non-spontaneous. At equilibrium, the energy of the system is constant and therefore ΔG is equal to 0. It is also important to bear in mind the fact that any prediction made considering only thermodynamic factors does not take into account the kinetics of the reaction; which can be not favourable if the reaction has, for instance, an elevated activation energy.

In order to gain a better understanding of the reaction chemistry of the reductive alkali roasting process, a discussion of the possible reactions taking place and the calculation of their free energy values has been carried out as a function of temperature and considering different alkali metal sources. The compounds in the reactions shown in this chapter are considered to be in solid form unless otherwise stated.

The effect of the oxygen potential has also been studied by considering the reaction chemistry of chromite under reducing atmosphere in the absence of alkali (carbothermic reduction of chromite), and under oxidising atmosphere in the presence of alkali (alkali roasting of chromite).

5.1.1.1. Free energy formation of pure oxides

The plot of the standard Gibbs free energy change (ΔG) of the formation reactions of Fe, Cr, Mg and Al oxides (shown in reactions (r.14) to (r.19)) against temperature –commonly known as Ellingham diagram- is presented in FIGURE 5-1. The calculations were carried out using HSC 5.1 software [107]. The formation of CO from the oxidation of solid carbon following reaction (r.20) was also included in the figure for comparison purposes.

$\frac{4}{3}$ Cr + O_2(g) → $\frac{2}{3}$ Cr_2O_3 (r.14)

$\frac{4}{3}$ Al + O_2(g) → $\frac{2}{3}$ Al_2O_3 (r.15)

2 Mg + O_2(g) → 2 MgO (r.16)

2 Fe + O_2(g) → 2 FeO (r.17)

4 Fe_3O_4 + O_2(g) → 6 Fe_2O_3 (r.18)

4 FeO + O_2(g) → 2 Fe_2O_3 (r.19)

2 C + CO_2(g) → 2 CO(g) (Boudouard reaction) (r.20)

The positive slope of the ΔG-T plots for reactions (r.14) to (r.19) indicates that the respective oxides are stable at low temperature; whereas at high temperature the oxides become unstable and can be reduced to the metallic form, or in the case of reactions (r.18) and (r.19), to an oxide of iron with lower oxidation state. As stated by equation (eq.6), the slope of the lines correspond to the change in entropy, ΔS, which is positive and has very similar values for all the reactions in FIGURE 5-1. According to FIGURE 5-1, the metallic oxides in reactions (r.14) to (r.19) can be sorted from highest to lowest stability in the temperature range of 300°C to 1300°C according to the following sequence: MgO > Al_2O_3 > Cr_2O_3 > FeO > Fe_3O_4 > Fe_2O_3. Reaction (r.20) known as Boudouard reaction, shows the tendency of solid carbon to form CO gas. The slope of the line is negative, indicating that this reaction is favoured at higher temperatures. If the ΔG versus T line of the Boudouard reaction falls below the line of a specific oxide at a given temperature, then it is possible to reduce the oxide to its metallic form –or to an oxide with lower oxidation number– using solid carbon as reducing agent.

According to this, the minimum temperature required to reduce FeO to metallic Fe by carbon is 725°C (where the oxide line and the Boudouard reaction line intersect), and the one for reduction of Cr_2O_3 to Cr is approximately 1250°C. In the case of MgO and Al_2O_3 the minimum temperature required is above 1600°C, confirming the high stability of these two oxides at high temperatures.

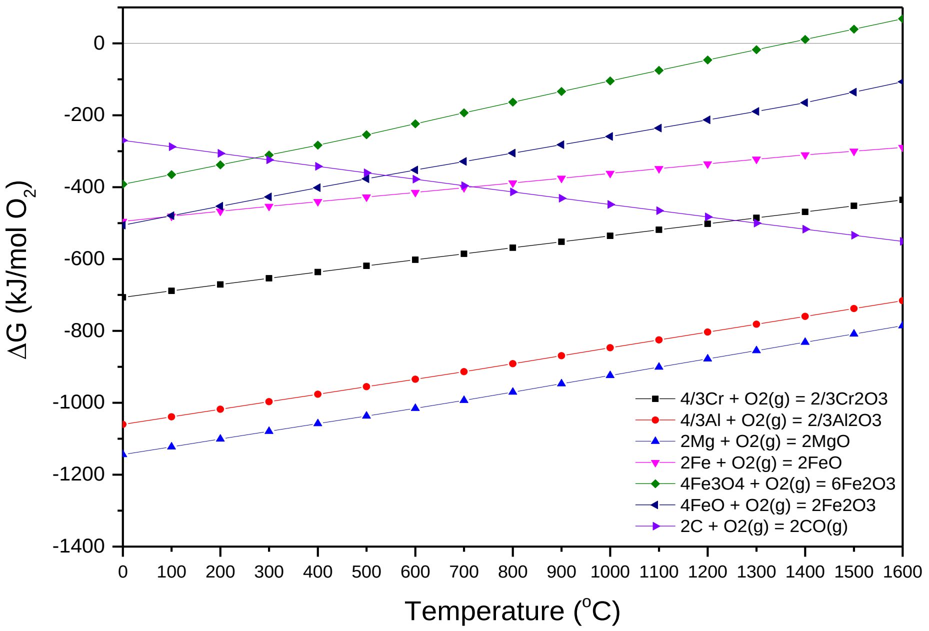

FIGURE 5-1. Free energy versus temperature curves for reactions (r.14) to (r.19). Data was computed using HSC 5.1 software [107].

5.1.1.2. Reaction of spinel members with solid carbon

Ferrochrome is produced by smelting chromite ore in submerged-arc furnaces with pre-reduction of the ore in a rotary kiln. The reducibility of the different components in chromite with solid carbon has been studied by computations of the standard free energy of reactions (r.21) to (r.26), which have been plotted against temperature in FIGURE 5-2.

$FeCr_2O_4 + 4 C \rightarrow Fe + 2 Cr + 4 CO (g)$ (r.21)

$FeCr_2O_4 + C \rightarrow Fe + Cr_2O_3 + CO (g)$ (r.22)

$Cr_2O_3 + 3 C \rightarrow 2 Cr + 3 CO (g)$ (r.23)

$MgCr_2O_4 \rightarrow MgO + Cr_2O_3$ (r.24)

$FeAl_2O_4 + C \rightarrow Fe + Al_2O_3 + CO (g)$ (r.25)

$MgFe_2O_4 + 3 C \rightarrow 2 Fe + MgO + 3 CO (g)$ (r.26)

Reduction of iron oxide in $FeCr_2O_4$ to form metallic iron starts at significantly lower temperature than the reduction of chromium. The plot shows that reduction of iron is feasible at temperatures of about 1000°C, while formation of Cr by reduction of Cr_2O_3 with solid carbon is not thermodynamically favourable below 1250°C.

This is beneficial for the alkali reduction process carried out at a maximum temperature of 1050°C, as it is possible to reduce iron oxide to its metallic form at this temperature, but the reduction of chromium and hence its incorporation into the metallic phase is not thermodynamically favourable.

When comparing chromium-containing spinels ($FeCr_2O_4$ and $MgCr_2O_4$), the decomposition tendency of ferrochromite in Fe and Cr_2O_3 (r.22) is slightly higher than that of magnesiochromite when it decomposes to MgO and Cr_2O_3 oxides (r.24). This was previously reported by Xiao (2001) [110], who studied the reducibility of chromite with CO by plotting the reactions of the different components as function of CO_2/CO gas against temperature.

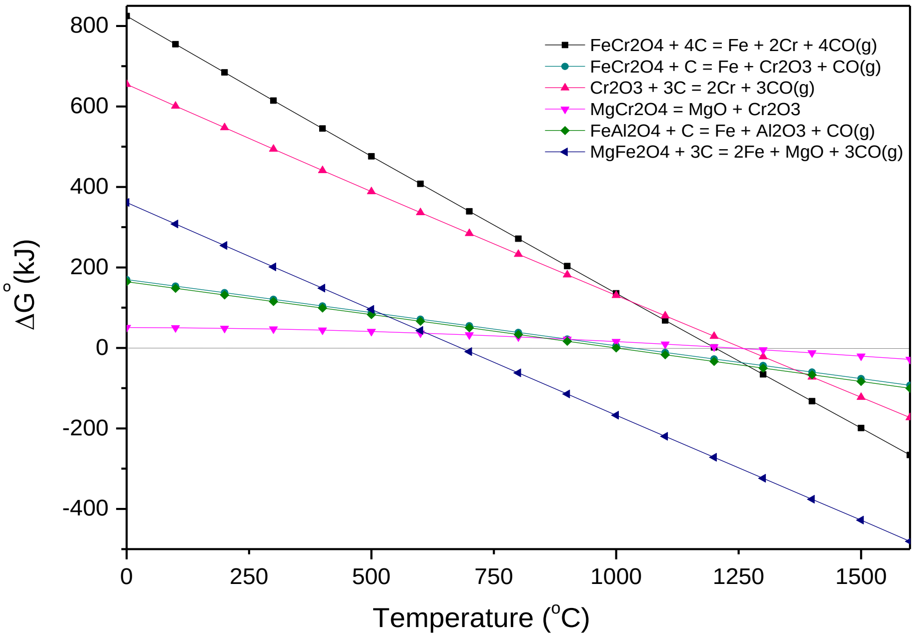

FIGURE 5-2. ΔG versus temperature plot of reactions (r.21) to (r.26). Computed using HSC 5.1 [107].

5.1.1.3. Reaction of spinel members with alkali under oxidising atmosphere

The aim of the alkali roasting of chromite in oxidising atmosphere is to oxidise Cr^{3+} to Cr^{6+}, which reacts with Na_2O to form sodium chromate (Na_2CrO_4). As Na_2CrO_4 is highly water-soluble, it can be extracted from the roasted samples by water leaching. The reactions of the different spinel members with Na_2CO_3 in oxidising atmosphere are shown in reactions (r.27) to (r.32) below. Since silicates are present in the chromite ore and have a significant negative effect on the oxygen diffusion during the oxidation reaction of chromite, reaction (r.33) showing the formation of sodium silicate (Na_2SiO_3) from SiO_2 has been included for comparison.

$$FeCr_2O_4 + 2\ Na_2CO_3 + \frac{7}{4}\ O_2\ (g) \rightarrow \frac{1}{2}\ Fe_2O_3 + 2\ Na_2CrO_4 + 2\ CO_2\ (g) \qquad (r.27)$$

$$MgCr_2O_4 + 2\ Na_2CO_3 + \frac{3}{2}\ O_2\ (g) \rightarrow MgO + 2\ Na_2CrO_4 + 2\ CO_2\ (g) \qquad (r.28)$$

$$FeAl_2O_4 + Na_2CO_3 + \frac{1}{4}\ O_2\ (g) \rightarrow \frac{1}{2}\ Fe_2O_3 + 2\ NaAlO_2 + CO_2\ (g) \qquad (r.29)$$

$$MgAl_2O_4 + Na_2CO_3 \rightarrow MgO + 2\ NaAlO_2 + CO_2\ (g) \qquad (r.30)$$

$$MgFe_2O_4 + Na_2CO_3 \rightarrow MgO + 2\ NaFeO_2 + CO_2\ (g) \qquad (r.31)$$

$$Fe_3O_4 + \frac{3}{2}\ Na_2CO_3 + \frac{1}{4}\ O_2\ (g) \rightarrow 3\ NaFeO_2 + \frac{3}{2}\ CO_2\ (g) \qquad (r.32)$$

$$SiO_2 + Na_2CO_3 \rightarrow Na_2SiO_3 + CO_2\ (g) \qquad (r.33)$$

The Gibbs free energy (ΔG) of the reactions (r.27) to (r.33) was computed as a function of temperature and plotted in the range of 0°C to 1600°C.

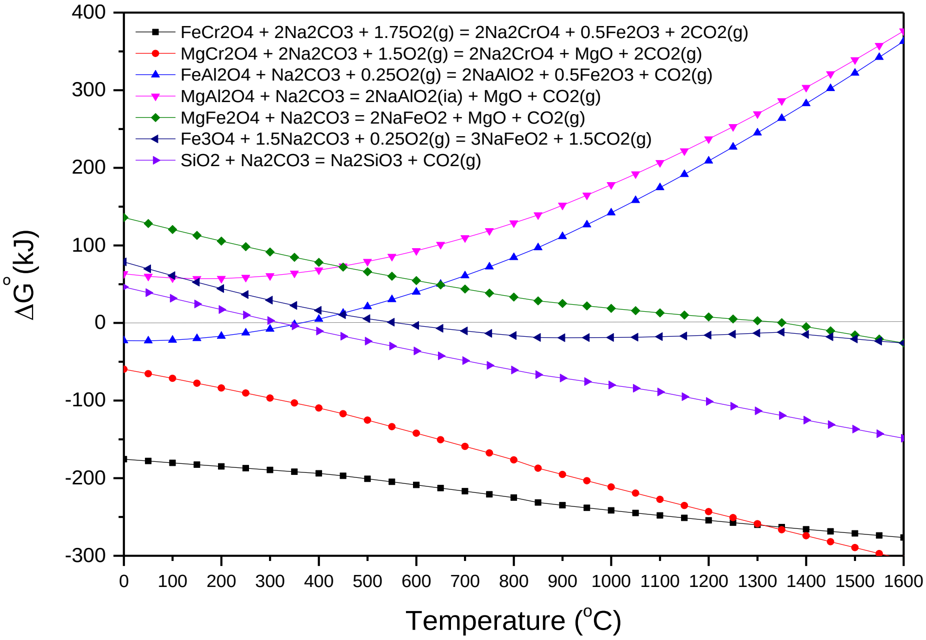

FIGURE 5-3. Free energy versus temperature curves for reactions (r.27) to (r.33). Data was computed using HSC 5.1 software [107].

Chromate phases are preferentially formed compared to the rest of alkali compounds, which favours the extraction of chromium from chromite spinel. Free energy calculations show the preference of chromium-based spinel members ($FeCr_2O_4$ and $MgCr_2O_4$) to decompose and form Na_2CrO_4 and the corresponding oxide (Fe_2O_3 or MgO). This is beneficial for the alkali roasting of chromite ore since it maximises the formation of the alkali chromate which is subsequently extracted by water leaching.

Theoretically, formation of $NaAlO_2$ is thermodynamically not favourable as reactions (r.29) and (r.30) exhibit positive values of ΔG, however, $NaAlO_2$ has previously been identified experimentally in alkali roasting experiments of chromite with sodium carbonate [33,34]. Tathavadkar (2001) [32] suggested the presence of other alkali compounds apart from Na_2CrO_4 ($NaAlO_2$, $NaFeO_2$ and Na_2SiO_3) during roasting of chromite with excess Na_2CO_3 and highlighted its adverse effect on oxygen diffusion by decreasing the eutectic temperature of the Na_2CO_3-Na_2CrO_4 binary liquid. Qi (2011) [87] explained the thermodynamics of chromite roasting with Na_2CO_3 and proved the formation of alkali compounds during roasting, suggesting that they may act as intermediate compounds that can further react with chromite spinels to form sodium chromate.

Below 1300°C, the Gibbs energy values for $FeCr_2O_4$ reactions are more negative than those for $MgCr_2O_4$ reactions. This indicates that $MgCr_2O_4$ spinel phase is more stable than $FeCr_2O_4$ and thus harder to decompose below 1300°C. Sun (2007) [86] explained the difference between the reactivity of iron and magnesium chromites in oxidising atmosphere taking into account the changes in the crystal structure due to the $Fe^{2+} \rightarrow Fe^{3+}$ oxidation step.

Oxidation experiments of S.A. chromite ore using different alkali hydroxides of sodium and potassium have been carried out and are presented in this manuscript. The reaction chemistry of the roasting of chromium-containing spinels using either NaOH or KOH as alkali source is summarised by reactions (r.34) to (r.37).

$$FeCr_2O_4 + 4\,NaOH + \frac{7}{4}\,O_2\,(g) \rightarrow \frac{1}{2}\,Fe_2O_3 + 2\,Na_2CrO_4 + 2\,H_2O\,(g) \qquad (r.34)$$

$$FeCr_2O_4 + 4\,KOH + \frac{7}{4}\,O_2\,(g) \rightarrow \frac{1}{2}\,Fe_2O_3 + 2\,K_2CrO_4 + 2\,H_2O\,(g) \qquad (r.35)$$

$$MgCr_2O_4 + 4\,NaOH + \frac{3}{2}\,O_2\,(g) \rightarrow MgO + 2\,Na_2CrO_4 + 2\,H_2O\,(g) \qquad (r.36)$$

$$MgCr_2O_4 + 4\,KOH + \frac{3}{2}\,O_2\,(g) \rightarrow MgO + 2\,K_2CrO_4 + 2\,H_2O\,(g) \qquad (r.37)$$

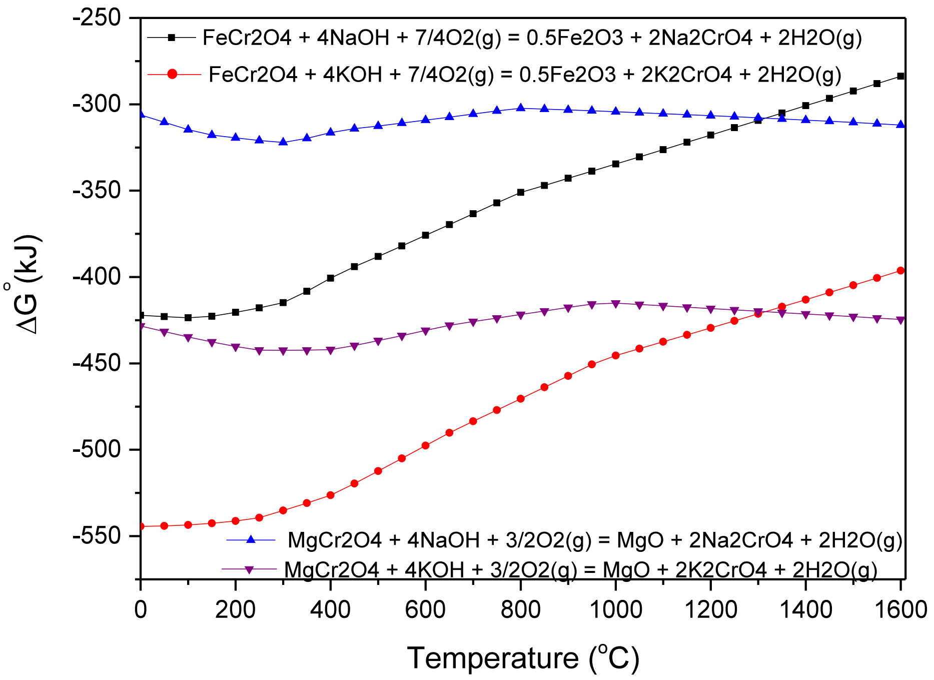

FIGURE 5-4. Comparison of free energy vs temperature curves for reactions (r.34) to (r.37). Computed using HSC 5.1 software [107].

According to FIGURE 5-4, the Gibbs energy values for KOH reactions (r.35) and (r.37), are more negative than the values for NaOH reactions (r.34) and (r.36), implying that the formation of K_2CrO_4 in oxidizing atmosphere is more favourable. Both sodium and potassium hydroxides do not only react with chromite spinels but also combine with other spinel members and silicate impurities as shown in reactions (r.38) to (r.47).

$$FeAl_2O_4 + 2\,NaOH + \frac{1}{4}\,O_2(g) \rightarrow \frac{1}{2}\,Fe_2O_3 + 2\,NaAlO_2 + H_2O(g) \qquad (r.38)$$

$$FeAl_2O_4 + 2\,KOH + \frac{1}{4}\,O_2(g) \rightarrow \frac{1}{2}\,Fe_2O_3 + 2\,KAlO_2 + H_2O(g) \qquad (r.39)$$

$$MgAl_2O_4 + 2\,NaOH \rightarrow MgO + 2\,NaAlO_2 + H_2O(g) \qquad (r.40)$$

$$MgAl_2O_4 + 2\,KOH \rightarrow MgO + 2\,KAlO_2 + H_2O(g) \qquad (r.41)$$

$$Fe_3O_4 + 3\,NaOH + \frac{1}{4}\,O_2(g) \rightarrow 3\,NaFeO_2 + \frac{3}{2}\,H_2O(g) \qquad (r.42)$$

$$Fe_3O_4 + 3\,KOH + \frac{1}{4}\,O_2(g) \rightarrow 3\,KFeO_2 + \frac{3}{2}\,H_2O(g) \qquad (r.43)$$

$$MgFe_2O_4 + 2\,NaOH \rightarrow MgO + 2\,NaFeO_2 + H_2O(g) \qquad (r.44)$$

$$MgFe_2O_4 + 2\,KOH \rightarrow MgO + 2\,KFeO_2 + H_2O(g) \qquad (r.45)$$

$$SiO_2 + 2\,NaOH \rightarrow Na_2SiO_3 + H_2O(g) \qquad (r.46)$$

$SiO_2 + 2\ KOH \rightarrow K_2SiO_3 + H_2O(g)$ (r.47)

By comparing ΔG values in FIGURE 5-4 and FIGURE 5-5, it is possible to deduce that Na_2CrO_4 and K_2CrO_4 are more stable than the rest of phases formed via alkali roasting, e.g. $NaAlO_2$, $NaFeO_2$, Na_2SiO_3, $KAlO_2$, $KFeO_2$ and K_2SiO_3. Note that ΔG figures for reaction (r.47) were not plotted as values are very positive (1343.97 kJ/mol, T = 1000°C) and therefore not comparable with the rest of reactions. Applying this to roasting of chromite with NaOH and KOH and considering the excess alkali used in this study, then sodium ferrite, sodium aluminate and sodium silicates are expected to be formed.

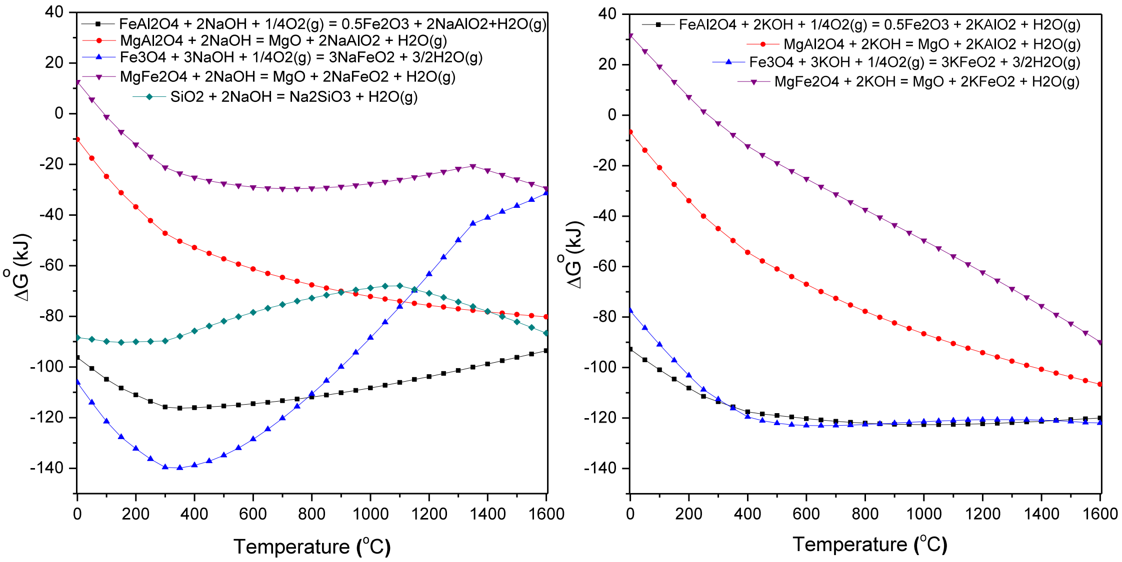

FIGURE 5-5. ΔG versus temperature plot of reactions (r.38) to (r.46). Computed using HSC 5.1 [107].

5.1.1.4. Reaction of spinel members with alkali under reducing atmosphere

When ferrochromite spinel ($FeCr_2O_4$) is treated with Na_2CO_3 and carbon at high temperature, metallic iron and sodium chromite are expected to be formed following reaction (r.48). However, as detailed in section 2.2.2, chromite mineral is a solid solution of different spinel members and therefore individual spinel members were considered for the computation of phase equilibria. Reactions of $FeCr_2O_4$, $MgCr_2O_4$, $FeAl_2O_4$, $MgAl_2O_4$, $MgFe_2O_4$ and Fe_3O_4 spinel members with Na_2CO_3 and carbon taking place during the alkali reduction are summarised in reactions (r.48) to (r.54). The Gibbs energy changes of these reactions against temperature were computed using HSC 5.1 software [107] and are plotted in FIGURE 5-6.

$FeCr_2O_4 + Na_2CO_3 + 2\ C \rightarrow Fe + 2\ NaCrO_2 + 3\ CO\ (g)$ (r.48)

$MgCr_2O_4 + Na_2CO_3 + C \rightarrow MgO + 2\ NaCrO_2 + 2\ CO\ (g)$ (r.49)

$$FeAl_2O_4 + Na_2CO_3 + 2\,C \rightarrow Fe + 2\,NaAlO_2 + 3\,CO\,(g) \qquad (r.50)$$

$$MgAl_2O_4 + Na_2CO_3 + C \rightarrow MgO + 2\,NaAlO_2 + 2\,CO\,(g) \qquad (r.51)$$

$$MgFe_2O_4 + Na_2CO_3 + C \rightarrow MgO + 2\,NaFeO_2 + 2\,CO\,(g) \qquad (r.52)$$

$$MgFe_2O_4 + 3\,C \rightarrow MgO + 2\,Fe + 3\,CO\,(g) \qquad (r.53)$$

$$Fe_3O_4 + 4\,C \rightarrow 3\,Fe + 4\,CO\,(g) \qquad (r.54)$$

$$SiO_2 + Na_2CO_3 + C \rightarrow Na_2SiO_3 + 2\,CO\,(g) \qquad (r.55)$$

Reaction (r.55) has also been included for comparison, as SiO_2 is present in the ore. FIGURE 5-6 shows that free energy values for reactions (r.48) to (r.54) are negative at temperatures above 800°C approximately. Comparing chromite spinels reactions above 900°C, reduction of $FeCr_2O_4$ to form metallic iron and $NaCrO_2$ is more thermodynamically favourable than reduction of $MgCr_2O_4$. However, the differences are not very significant in the temperature range of 950°C to 1100°C. The same tendency is observed in the case of reduction of aluminium-based spinel members, $FeAl_2O_4$ and $MgAl_2O_4$, in the presence of alkali and carbon.

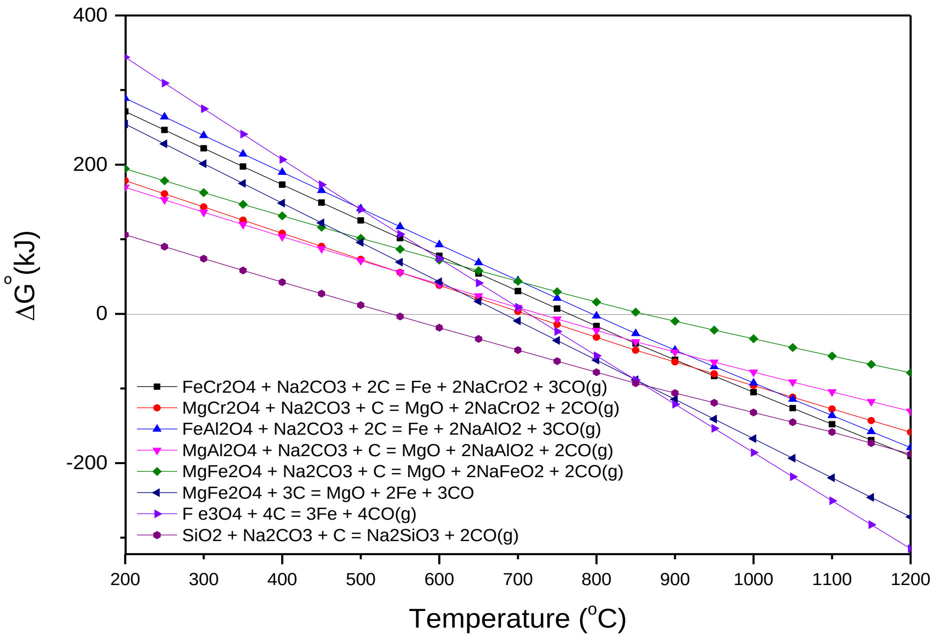

FIGURE 5-6. ΔG versus temperature plot of reactions (r.48) to (r.55). Computed using HSC 5.1 [107].

When comparing between pairs of chromium-based and aluminium-based spinel members, i.e. $FeCr_2O_4$ versus $FeAl_2O_4$ and $MgCr_2O_4$ versus $MgAl_2O_4$, it can be observed that reactions with chromium-based members show slightly lower values of ΔG than those of aluminium-based members, and this applies to the entire range of temperatures shown in the plot.

It can be therefore deduced that formation of $NaCrO_2$ is thermodynamically more favourable than $NaAlO_2$, but since the difference in free energy values is small, both are expected to form during alkali reduction. Sodium ferrite is however less stable under alkaline reducing conditions, and hence $NaFeO_2$ is not an expected reaction product. The formation and stability of $NaCrO_2$, $NaAlO_2$ and $NaFeO_2$ phases ultimately depends on the oxygen partial pressure and the activity of Na_2CO_3.

The formation of both $NaCrO_2$ and $NaAlO_2$ is desirable for the alkali reduction process, as $NaCrO_2$ can be separated from metallic Fe by magnetic separation to subsequently extract Cr_2O_3, and $NaAlO_2$ is solubilised during magnetic separation and water leaching yielding an alkaline solution which can be further treated to recover Na_2CO_3 and Al_2O_3. On the contrary, $NaFeO_2$ is undesirable since it would affect negatively to the later separation of iron by magnetic separation.

The addition of other sodium salts to the alkali reduction of chromite has been tested and the results are presented in this document. Reactions of $FeCr_2O_4$ with NaOH, $NaHCO_3$ and $NaHSO_4$ in the presence of carbon are shown in reactions (r.56) to (r.58). Free energy calculations for potassium salts were also performed with the aim of comparing with sodium salts. Gibbs energy values of reactions (r.59) to (r.61) are also plotted in FIGURE 5-7.

$FeCr_2O_4 + 2\,NaOH + C \rightarrow Fe + 2\,NaCrO_2 + CO\,(g) + H_2O\,(g)$ (r.56)

$FeCr_2O_4 + 2\,NaHCO_3 + 3\,C \rightarrow Fe + 2\,NaCrO_2 + 5\,CO\,(g) + H_2O\,(g)$ (r.57)

$FeCr_2O_4 + 2\,NaHSO_4 + 3\,C \rightarrow Fe + 2\,NaCrO_2 + 3\,CO\,(g) + H_2O(g) + 2\,SO_2(g)$ (r.58)

$FeCr_2O_4 + K_2CO_3 + 2\,C \rightarrow Fe + 2\,KCrO_2 + 3\,CO\,(g)$ (r.59)

$FeCr_2O_4 + 2\,KOH + C \rightarrow Fe + 2\,KCrO_2 + CO\,(g) + H_2O\,(g)$ (r.60)

$FeCr_2O_4 + 2\,KHCO_3 + 3\,C \rightarrow Fe + 2\,KCrO_2 + 5\,CO\,(g) + H_2O\,(g)$ (r.61)

Comparing the free energy values of reactions (r.56) to (r.61) with reaction (r.48), shown in FIGURE 5-7, it can be observed that between 900°C and 1100°C reactions of chromite with Na_2CO_3 and NaOH have approximately the same free energy values, while values for $NaHCO_3$ and $NaHSO_4$ are significantly more negative. From ΔG plots, it can be concluded that the reactivity of the four sodium salts tested at temperatures around 1050°C follows the sequence $NaHSO_4 > NaHCO_3 > Na_2CO_3 \approx NaOH$.

Potassium salts show a similar behaviour than sodium salts, with potassium bicarbonate having higher reactivity than both potassium hydroxide and carbonate. Reactions with potassium have slightly more negative free energy values than sodium reactions if $NaOH/KOH$, Na_2CO_3/K_2CO_3 and $NaHCO_3/KHCO_3$ pairs of reactions are compared.

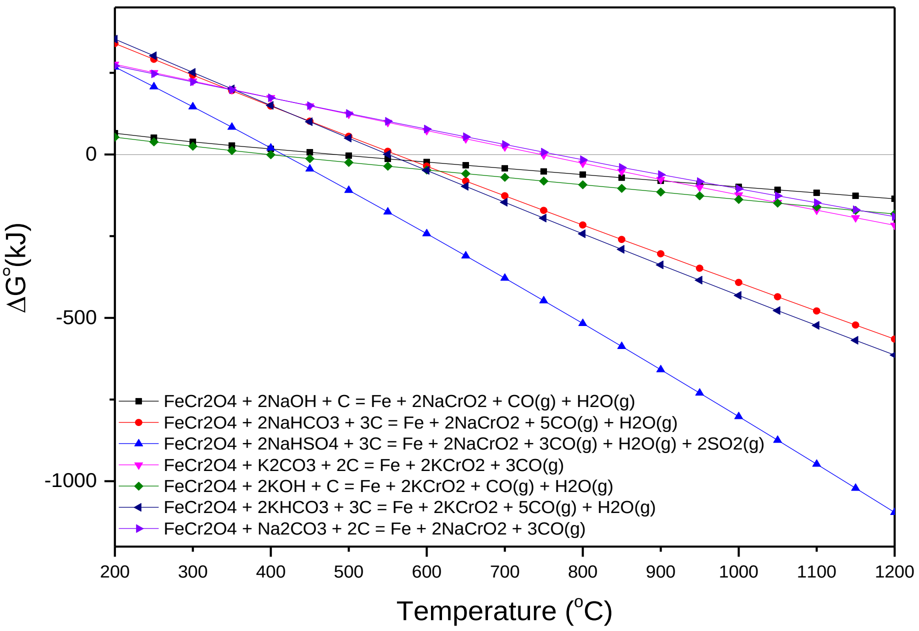

FIGURE 5-7. ΔG versus temperature plot of reaction (r.56) to (r.61) compared to reaction (r.48). Computed using HSC 5.1 software [107].

5.1.2. PREDOMINANCE DIAGRAMS, PHASE DIAGRAMS AND EQUILIBRIUM CALCULATIONS

Predominance area diagrams were computed in order to predict the behaviour of chromite under different reaction conditions and the expected products of reaction. FactSage© software package [46] was used for computation of 2-metal and 3-metal predominance area diagrams for systems including different elements.

For predominance area computation, the *Predom* module in FactSage© was used. This module allows the calculation and plotting of isothermal predominance area diagrams using available compound databases. Predominance diagrams were calculated at a constant temperature, with a maximum of three metal elements present and with the possibility of including three non-metals elements. After selecting the components of the diagram, the axes of the diagram were selected from a list of variables, which included the activity or partial pressure of the non-metal elements selected for the diagram or compounds resulting from the combination of them. It is also possible to select the state (gases, liquids and solids) of the possible species presented in the diagram.

The phases formed during the reductive roasting of chromite in the presence of sodium carbonate and solid carbon, as a function of the partial pressures of CO and CO_2 (axis of the diagram), are compared below by computation of the corresponding predominance diagrams.

Since all experiments were carried out at atmospheric pressure, and the main gas products expected in the reaction chamber are CO and CO_2, an isobar curve at a total pressure $P_{total} = P_{CO} + P_{CO2} = 1$ atmosphere has been plotted in each diagram.

A red dot has also been included in the predominance diagrams representing the theoretical gas composition in the reaction chamber during an alkali reduction experiment as a function of the reaction charge. The coordinates of the point, namely P_{CO2} and P_{CO}, have been calculated using equilibrium data computed by FactSage 6.4. [46]. A charge of 100 g of chromite ore, 70 g of Na_2CO_3 and 12 g of solid carbon was used for the purpose of the simulation. The products obtained in equilibrium, including both the gas and solid components, are shown in TABLE 5-1.

TABLE 5-1. Equilibrium products corresponding to the theoretic alkali reduction of chromite (100 g) with Na_2CO_3 (100g) and carbon (30 g) at 1050ºC. Computed using FactSage 6.4 [46].

Reactants			wt.(g)	Products	wt.(g)	mol	
Chromite			**100**	**Gas**	**45.71**	**1.64**	**%mol**
	Component	**Wt.(%)**		CO	44.04	1.573	96.09
	Cr_2O_3	44.66	44.66	CO_2	0.35	0.008	0.5
	FeO	18.99	18.99	Na	1.29	0.056	3.4
	Fe_2O_3	6.19	6.19	Others	0.03	0.003	0.01
	MgO	10.94	10.94	**Solid**	**135.22**	**1.32**	**%wt.**
	Al_2O_3	14.43	14.43	$NaCrO_2$	62.87	0.294	46.49
	SiO_2	3.82	3.82	Fe	19.09	0.342	14.12
Na_2CO_3			**70**	$NaAlO_2$	23.20	0.283	17.16
Carbon			**12**	MgO	10.94	0.271	8.09
				Na_4SiO_4	11.70	0.063	8.65
				Na_2CO_3	7.42	0.070	5.49

A maximum number of three metals are allowed in a single diagram, and therefore, the systems computed correspond to individual $FeCr_2O_4$, $FeAl_2O_4$, $MgCr_2O_4$ and $FeAl_2O_4$ spinel members in chromite with sodium as alkali element and solid carbon as reducing agent at a temperature of 1050ºC. The equilibrium data of chromite ore reduction under these reaction conditions may be explained on the basis of the Fe-Cr-Na-O-C, Fe-Al-Na-O-C, Mg-Cr-Na-O-C and Mg-Al-Na-O-C predominance area diagrams in FIGURE 5-8 and FIGURE 5-9.

In the case of Fe^{2+} containing spinels ($FeCr_2O_4$ and $FeAl_2O_4$), the predominance area diagrams in FIGURE 5-8 show the possibility of decomposing the spinel structure into metallic iron and $NaMO_2$ oxide (where M = Cr or Al). In the Fe-Cr-Na-O-C system, metallic Fe co-exists with $NaCrO_2$ at 1050ºC (1323 K) for a certain range of partial pressures of CO and CO_2 represented by area 4. At these temperatures and under reductive conditions, $NaCrO_2$ is stable thereby ensuring the instability of chromium in (6+)-state.

The dot corresponding to the expected gas composition in the reaction chamber during an alkali reduction experiment with the charge composition given in TABLE 5-1, and at 1050°C, confirms the formation of metallic Fe and $NaCrO_2$ during alkali reduction at the conditions stated.

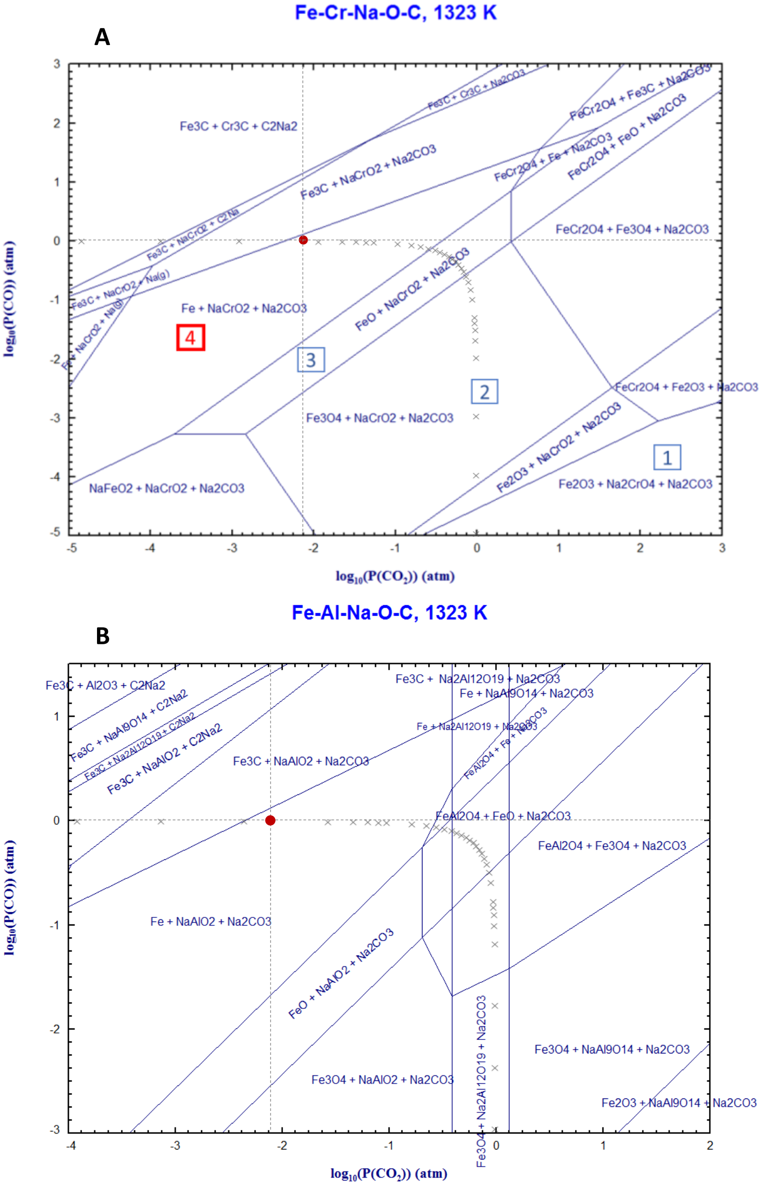

FIGURE 5-8. Predominance diagrams of the Fe-Cr-Na-O-C and Fe-Al-Na-O-C systems at 1323K (1050°C) computed using FactSage 6.4. [46].

Reduction of iron oxide takes place by shifting the equilibrium condition corresponding to area [1] to area [4] following the sequence shown in reaction (r.62), resulting in the decrease of the P_{CO2} value.

$Fe_2O_3 \rightarrow Fe_3O_4 \rightarrow FeO \rightarrow Fe$ (r.62)

The same conclusions can be obtained from the diagram of the Fe-Al-Na-O-C system, where Fe and $NaAlO_2$ coexist at certain ranges of P_{CO2} and P_{CO} and are expected as reaction products.

Even though an oxygen-free atmosphere is required for the reduction of iron oxides, the P_{CO} needs to be controlled in order to avoid formation of cementite (Fe_3C), which is stable at high reducing potentials, and maintain iron in metallic form. In practice, this could be achieved by adjusting the amount of solid carbon in furnace burden. Similarly, the formation of alkaline compounds of iron such as $NaFeO_2$ should be avoided by regulating the excess alkali present in the reaction mixture, as previously mentioned.

In general, the formation of any non-magnetic Fe-bearing compounds is undesirable as it affects negatively to the physical separation of iron carried out by the magnetic separation of reduced samples.

The predominance area diagrams for the Mg-Cr-Na-O-C and Mg-Al-Na-O-C systems illustrated in FIGURE 5-9 show the phase equilibria of magnesium containing spinels members in chromite, i.e. $MgCr_2O_4$ and $MgAl_2O_4$, in the presence of sodium and carbon at 1050°C. According to the predominance area diagrams, the decomposition of these spinels under reducing conditions would lead to the formation of MgO and $NaMO_2$ (where M = Cr and Al) under a wide range of CO and CO_2 partial pressures.

The effect of temperature on the diagram boundaries has been studied by superimposing the predominance diagrams of the Fe-Cr-Na-O-C system at 800°C, 900°C, 1000°C and 1050°C. For simplification of the diagram, only the area of interest, where Fe and $NaCrO_2$ coexist, is shown. The diagram shows how lower partial pressures of CO_2 are required when the working temperature decreases from 1050°C to 800°C. This means that more severe reducing conditions are required to decompose chromite at lower temperatures compared to higher temperatures, which is represented in the diagram by the shifting of the area boundary lines towards lower values of P_{CO2} and a shrinkage of the $Fe+NaCrO_2+Na_2CO_3$ coexistence area.

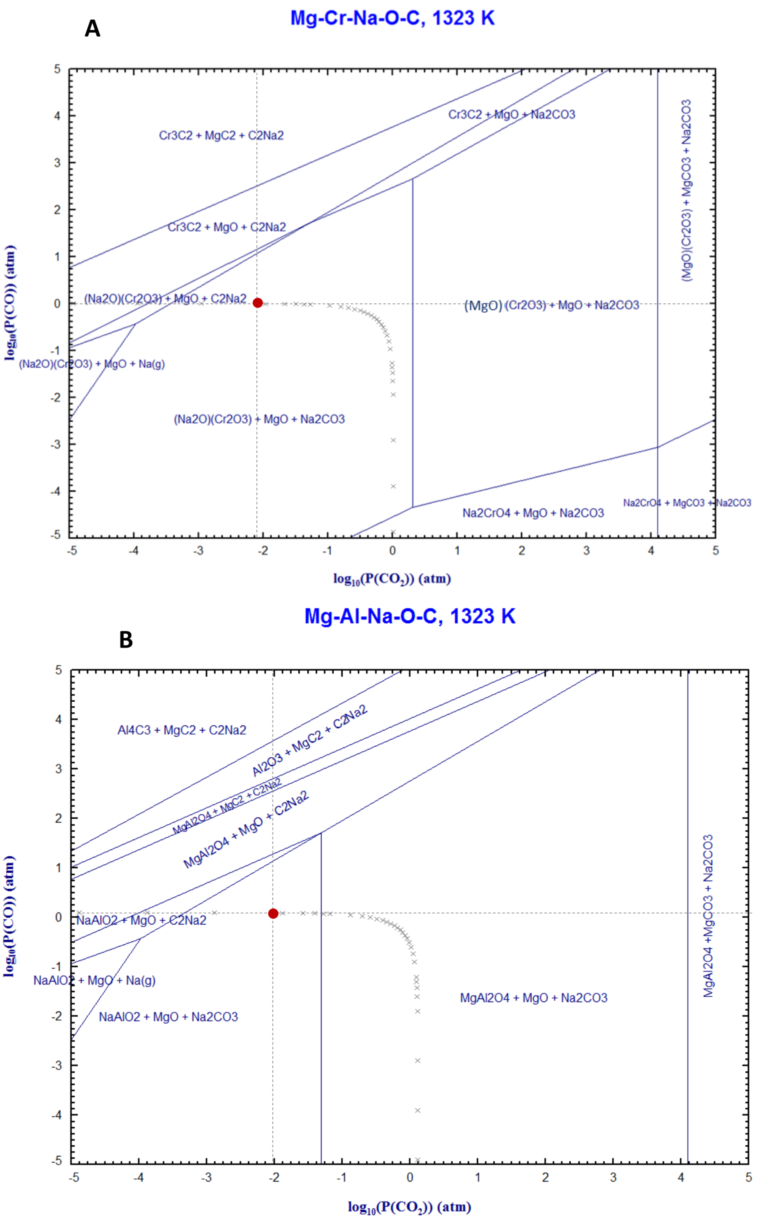

FIGURE 5-9. Predominance diagrams of the Mg-Cr-Na-O-C and Mg-Al-Na-O-C systems at 1323K (1050°C) computed using FactSage 6.4. [46].

The effect of temperature on the alkali reduction of chromite can also be observed in the phase diagram in FIGURE 5-11. The phase diagram of the Cr_2O_3-Fe_2O_3-Na_2CO_3-C system, with a mol ratio of $Cr_2O_3/(Cr_2O_3+Fe_2O_3+C) = 0.192$ and $Fe_2O_3/(Cr_2O_3+Fe_2O_3+C) = 0.118$, and at a constant total pressure of 1 atmosphere was calculated using FactSage 6.4. [46]. The diagram shows the phases in equilibrium as a function of temperature, in kelvin degrees, and the activity of the alkali ($\log_{10}a[Na_2CO_3]$) in the reaction mixture.

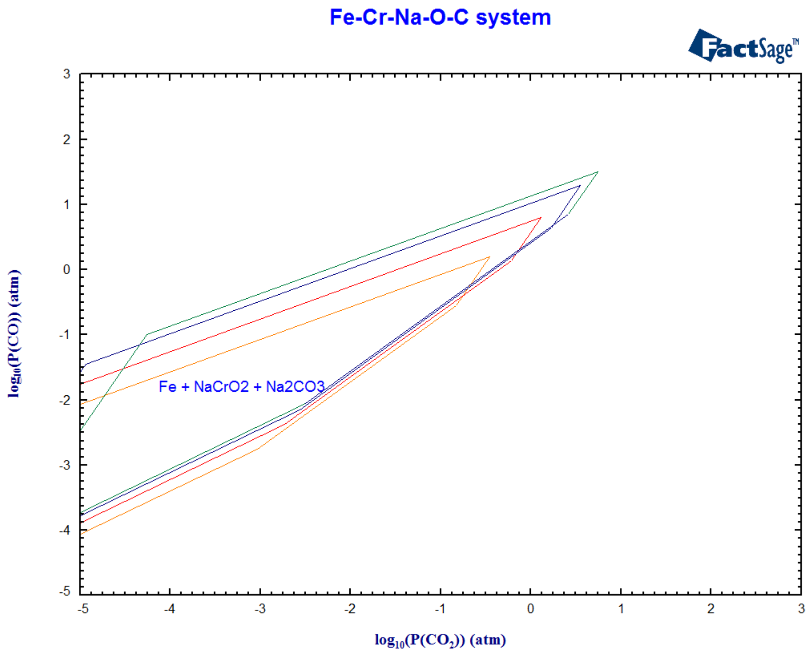

FIGURE 5-10. Superimposed predominance diagram of the Fe-Cr-Na-O-C system at different temperatures (green 1050°C, blue 1000°C, red 900°C and orange 800°C) showing the coexistence of Fe, $NaCrO_2$ and excess Na_2CO_3 as a function of the partial pressures of CO and CO_2. Computed using FactSage6.4.[46].

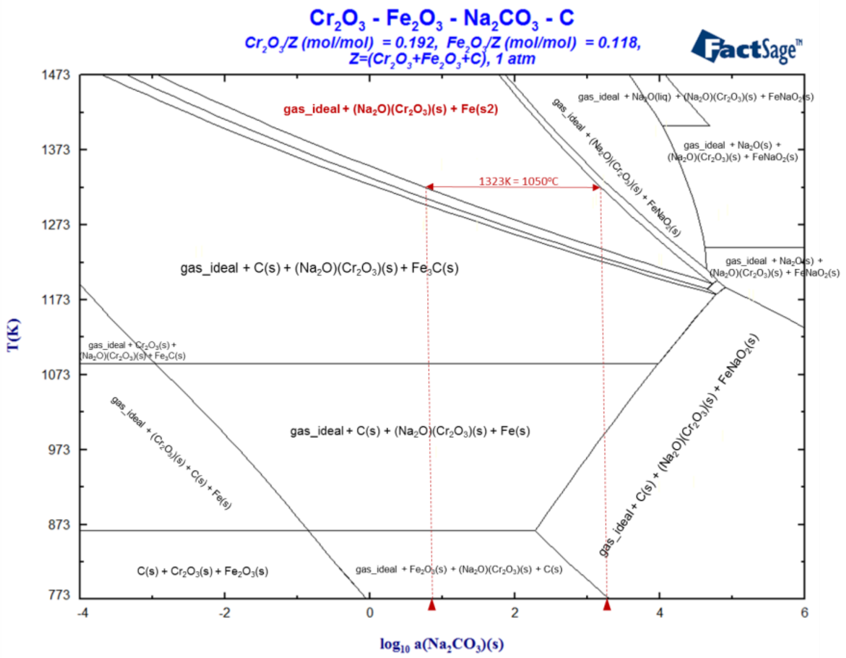

FIGURE 5-11. Phase diagram of the Cr_2O_3-Fe_2O_3-Na_2CO_3-C system at 1 atm as a function of the temperature and the $\log_{10}$ of the activity of Na_2CO_3. Computed using FactSage 6.4. [46].

The area highlighted in bold comprises the desired products of reduction, solid $NaCrO_2$ and Fe, in equilibrium with the ideal gas. A horizontal line was drawn in the area of interest for a possible reaction temperature of 1050°C with the aim of determining the required range of Na_2CO_3 activity in the reactants mixture. Based on this, the activity of alkali at this particular temperature, expressed in a logarithm scale, needs to be in the range of $0.86 < \log_{10}a_{Na2O3} < 3.30$ so as to obtain all chromium as $NaCrO_2$ and all iron in metallic form. The amount of alkali required to fully decompose ferro-chromite into Fe and $NaCrO_2$ decreases as the temperature of the system increases. If the activity of the alkali is lowered, iron coexists with sodium chromite in the form of iron carbide (Fe_3C) and metallic iron is not the stable phase. On the other hand, if the activity of Na_2CO_3 is higher, $FeNaO_2$ can be formed impeding the formation of the metal phase. The formation of either Fe_3C or $FeNaO_2$ is undesirable since it would affect negatively the physical separation of iron by magnetic separation, and therefore it is important to maximise the formation of metallic iron during the alkali reduction stage.

5.2. THERMAL DECOMPOSITION STUDIES

5.2.1. HEATING OF CHROMITE ORE UNDER DIFFERENT CHEMICAL POTENTIALS

The progressive heating of S.A. chromite ore samples under controlled atmosphere was carried out in the thermogravimetric analysis equipment described in Section 3.2.1. The purpose of this study was to obtain a through characterisation of the S.A. chromite by determining the phases formed when chromite is heated, either itself or in the presence of carbon and alkali, and under oxidising (air) or chemically-neutral (argon) atmosphere.

The chromite samples or corresponding mixtures were placed in an alumina crucible and heated from room temperature up to 1050°C at a constant heating rate of 5°C/min under different chemical potentials as detailed below:

- ***Set of experiments PDS1.*** S.A. chromite heated under air atmosphere.
- ***Set of experiments PDS2.*** S.A. chromite heated under Ar atmosphere.
- ***Set of experiments PDS3.*** Mixture of S.A. chromite and activated charcoal in a chromite:C weight ratio of 1:0.2 heated under Ar atmosphere.
- ***Set of experiments PDS4.*** Mixture of S.A. chromite, Na_2CO_3 and activated charcoal in a chromite:Na_2CO_3:C weight ratio of 1:0.8:0.2 heated under Ar atmosphere.

During non-isothermal analysis, temperature and weight were monitored and logged with time for the entire heating experiment. The results are shown in FIGURE 5-12, where the percentage weight loss is plotted against temperature for the different mixtures tested.

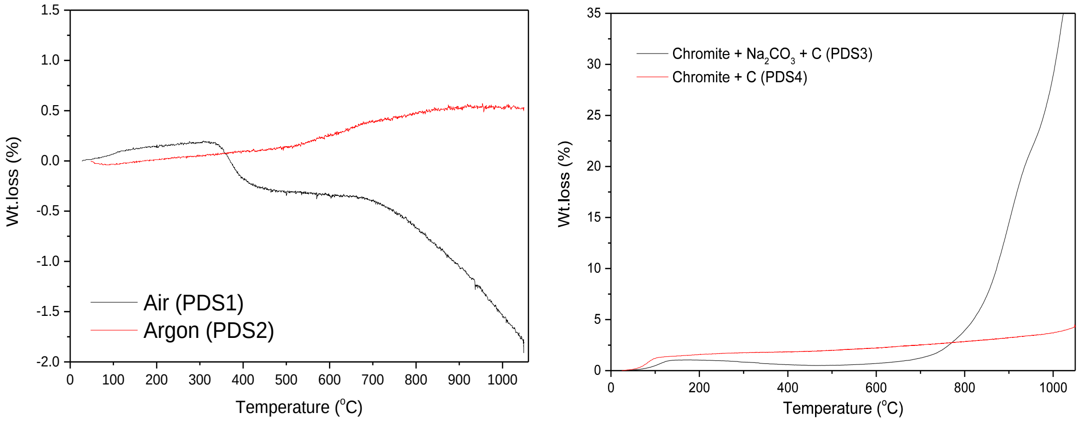

Figure 5-12. Weight loss (%) versus temperature TGA curves of S.A. chromite in air, S.A. chromite in Ar, S.A. chromite and solid carbon in argon and S.A. chromite, Na_2CO_3 and solid carbon mixture in Ar.

When S.A. chromite is heated in argon atmosphere, the samples experienced almost no weight loss until a temperature of 600°C, after which there is a slightly higher weight loss step until 1050°C. On the other hand, the sample heated in air shows a first regime of slight weight loss from 100°C to approximately 350°C, which is due to the loss of moisture from the chromite sample. This is followed by a weight gain attributed to the oxidation of FeO to Fe_2O_3 on the chromite spinel lattice [111].

The heating of the chromite ore and carbon mixture show a total weight loss of 4.2%. In this case, the loss of weight starts at 100°C and is progressive until the maximum temperature of 1050°C. Fe_2O_3 in the ore reduces to FeO in the presence of carbon as reducing agent leading to the weight loss observed in the isochronal TGA curves. Reduction of FeO to metallic iron can also take place under reducing atmosphere, but may not be complete at the temperatures under study [62,67]. In the presence of alkali and under reducing atmosphere, the weight loss observed is significantly higher than in the rest of the cases. The TGA curve reaches a maximum of 35% wt. loss at 1050°C, as seen in Figure 5-12. The significant weight loss starts around 700°C and is consequence of the decomposition of Na_2CO_3 [112]. Since there is a significant excess Na_2CO_3 in the reaction mixture, the weight loss observed is high accordingly. As shown in Figure 5-1, the reduction of FeO to metallic iron by solid carbon occurs above 725°C yielding CO gas and therefore a weight loss in the sample. The gasification of the solid carbon used as reducing agent also takes place following the Boudouard reaction (r.20) and also accounts for part of the weight loss observed.

Isothermal heating experiments at different temperatures ranging from 100°C to 1050°C were also performed in batch experiments in the electrically-heated furnace. The samples collected at different temperatures were analysed by XRPD and are shown in Figure 5-13.

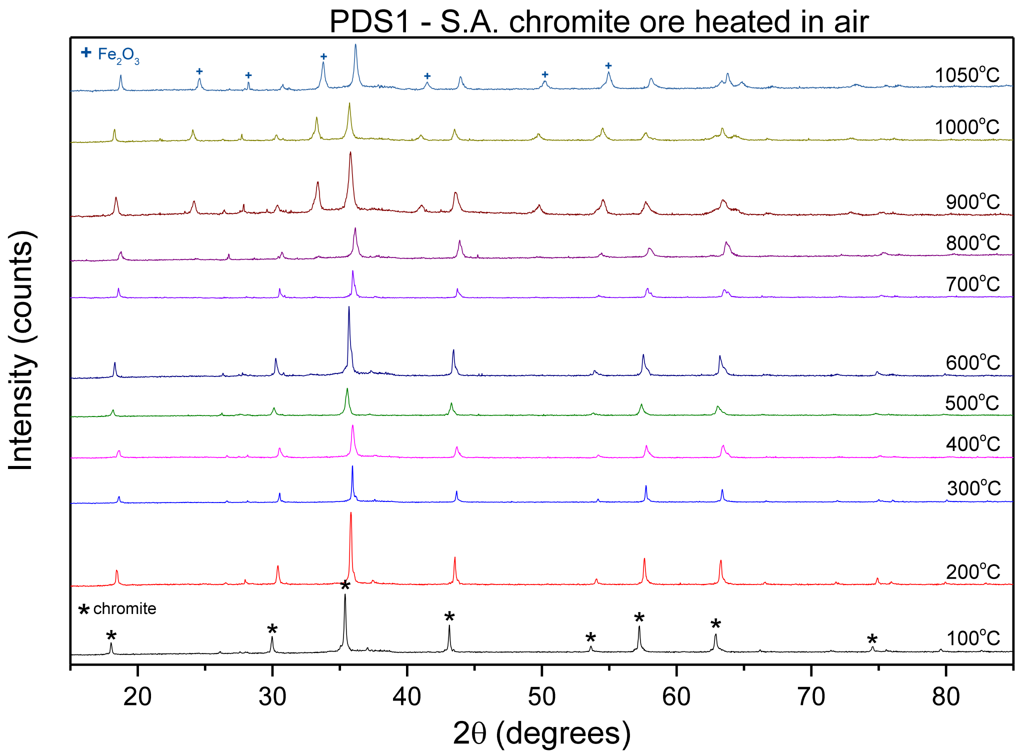

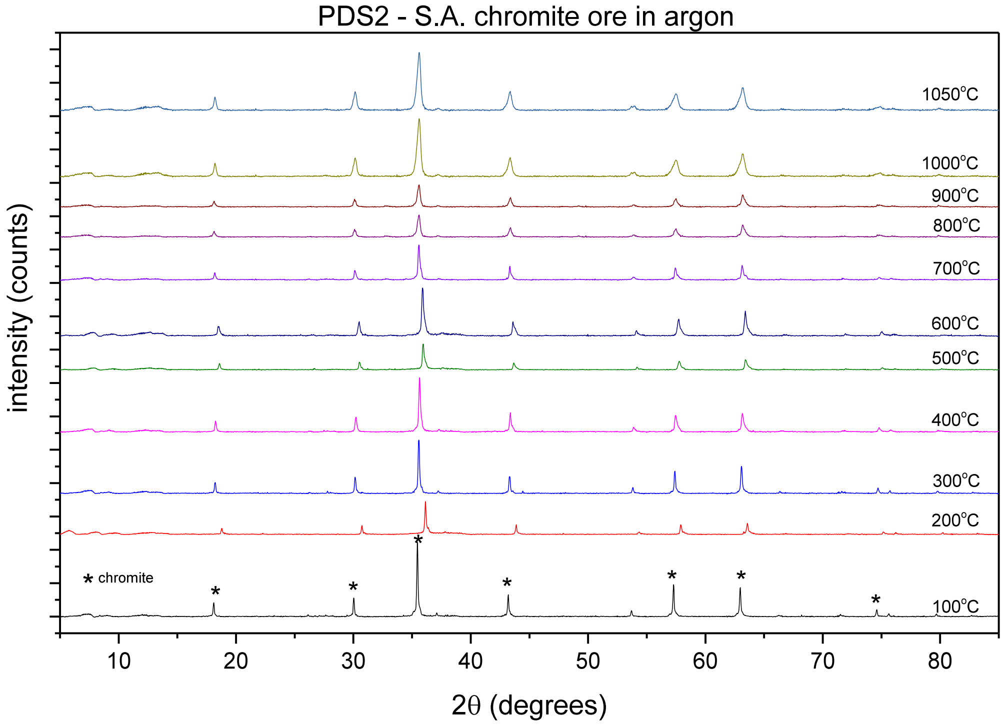

FIGURE 5-13. X-ray powder diffraction patterns of S.A. chromite ore isothermally heated in air atmosphere, heated in argon atmosphere, mixed with activated charcoal in a wt. ratio of chromite:C = 1:0.2 and heated in Ar atmosphere, and mixed with Na_2CO_3 and activated charcoal in a wt. ratio of chromite:Na_2CO_3:C = 1:0.8:0.2 and heated in Ar atmosphere; at 100°C, 200°C, 300°C, 400°C, 500°C, 600°C, 700°C, 800°C, 900°C, 1000°C and 1050°C.

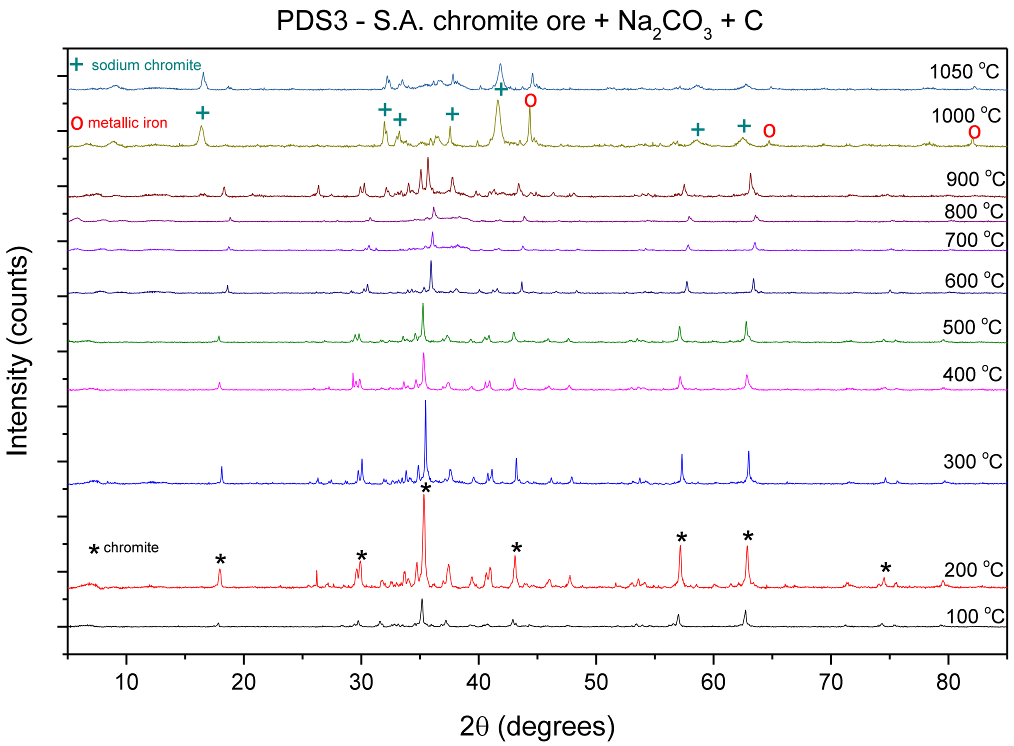

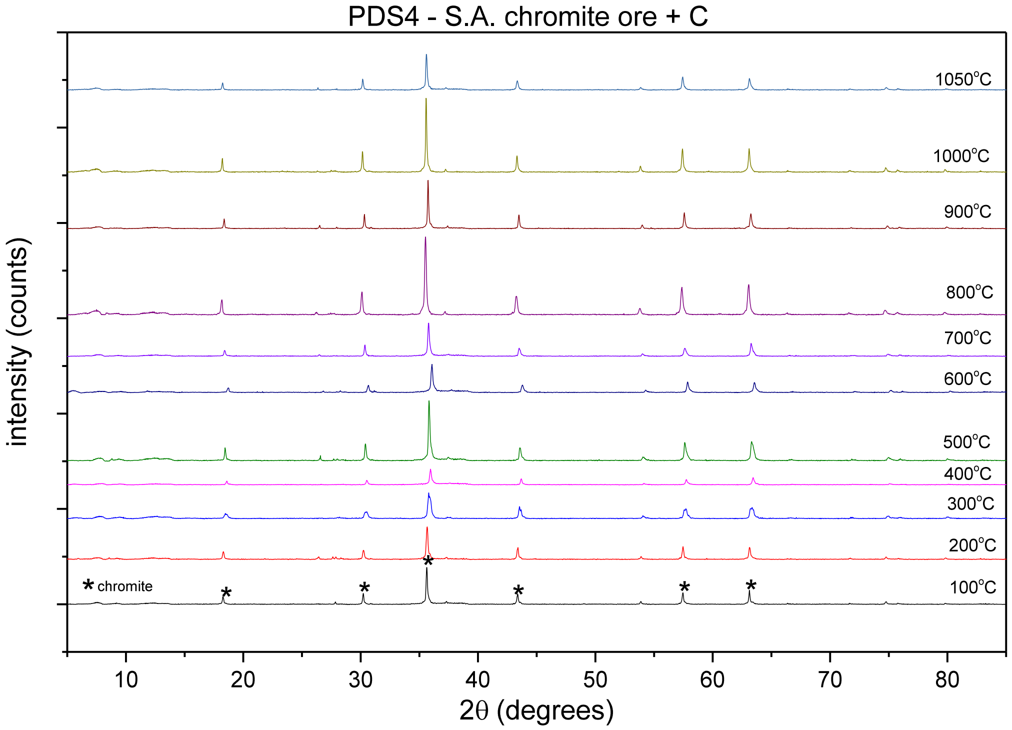

FIGURE 5-13 (CONTINUED). X-ray powder diffraction patterns of S.A. chromite ore isothermally heated in air atmosphere, heated in argon atmosphere, mixed with activated charcoal in a wt. ratio of chromite:C = 1:0.2 and heated in Ar atmosphere, and mixed with Na_2CO_3 and activated charcoal in a wt. ratio of chromite:Na_2CO_3:C = 1:0.8:0.2 and heated in Ar atmosphere; at 100°C, 200°C, 300°C, 400°C, 500°C, 600°C, 700°C, 800°C, 900°C, 1000°C and 1050°C.

The weight gain observed in the thermogravimetric curves of chromite heated in air was explained by the oxidation of FeO in the chromite spinel to form hematite (Fe_2O_3). This is confirmed by the XRPD patterns, where peaks for Fe_2O_3 can be observed at patterns for temperatures of 900°C and above. Below 900°C, no phase transformation is observed and only peaks for chromite spinel phase were identified. In argon atmosphere, however, the oxidation of FeO does not take place, and only the chromite spinel phase can be observed in the XRPD patterns at all temperatures.

In reducing atmosphere in the absence of alkali, metallisation of Fe is not observed. Only chromite spinel is observed in XRPD patterns of PDS4 experiments (chromite+C) and no phase transformation is observed. On the contrary, in the presence of alkali (PDS3 experiments in FIGURE 5-13) $NaCrO_2$ and metallic Fe start forming at moderate temperatures, and these phases can be identified in XRPD patterns after heating at 1000°C and 1050°C. This confirms that the presence of alkali leads to the formation of sodium chromite and the formation of metallic Fe is achieved at lower temperature than that required for the carbothermic reduction in the absence of alkali. Other phases such as unreacted Na_2CO_3 and MgO are observed in XRPD patterns at lower and higher temperatures, respectively.

The effect of temperature on the alkali reduction of chromite can also be observed in the phase diagram in FIGURE 5-11. The phase diagram of the Cr_2O_3-Fe_2O_3-Na_2CO_3-C system, with a mol ratio of $Cr_2O_3/(Cr_2O_3+Fe_2O_3+C) = 0.192$ and $Fe_2O_3/(Cr_2O_3+Fe_2O_3+C) = 0.118$, and at a constant total pressure of 1 atmosphere was calculated using FactSage 6.4. [46]. The diagram shows the phases in equilibrium as a function of temperature, in kelvin degrees, and the activity of the alkali ($\log_{10}a[Na_2CO_3]$) in the reaction mixture.

5.2.2. RIETVELD ANALYSIS

The Rietveld analysis of the XRPD patterns shown in the previous section was carried out in order to identify any significant changes or trends followed with increasing temperature in the lattice parameters or the site occupancies of the chromite spinel structure.

Fully identified XRPD patterns are required in order to perform Rietveld analysis using GSAS software. This means that all phases present need to be identified including all peaks present in the sample. This difficulted the Rietveld analysis of the XRPD patterns of the set of experiments PDS3 (corresponding to the heating experiments of the mixture of chromite, Na_2CO_3 and activated charcoal) due to the complexity of the patterns.

As the temperature increases, the formation of new phases in low quantity in the first stages of reduction leads to the formation of numerous small peaks difficult to include in the refinement. In the rest of experiments, chromite spinel (space group Fd-3m) was de main phase present, with formation of hematite (Fe_2O_3, space group R-3c) in some of the samples.

The XRPD patterns of the rest of samples at different temperatures were refined by the Rietveld method using GSAS software, and the samples are presented in FIGURE 5-14. The complete set of data obtained by this analysis, including lattice parameter, elemental site occupancies, oxygen coordinate of the spinel structure, thermal coefficients of tetrahedral and octahedral sites and the corresponding goodness of fit of each refinement; was tabulated and can be found in Appendix 1.

When chromite ore with no additives was heated in air atmosphere, there was a shrinkage of the spinel lattice indicated by the 0.6 % decrease of the lattice parameter from 8.31 to 8.26 Å. The occupancies were refined by keeping the relation $F_{Cr}+F_{Al} = 1$ and leaving the F_{Mg} and F_{Fe} free for refinement. The restriction of $F_{Cr}+F_{Al} = 1$ had to be maintained, otherwise the refinement model could not be converged. F_{Cr} and F_{Al} occupancies vary between the values of 0.7 and 0.3 respectively, but no clear trend was observed. The occupancy of Mg in the as-received chromite was calculated as 0.49, and it remains nearly constant as the temperature of heating increases. However, due to the oxidation of FeO to Fe_2O_3 and its segregation from chromite, the tetrahedral site occupancy of Fe in the spinel decreases from 0.51 to 0.33.

When chromite is heated in argon atmosphere, the lattice parameter also shows a decreasing trend with increasing temperature, bus its value oscillates more than in the case of air atmosphere, and the trend is not that clear. Furthermore, from a temperature of 800^{o}C onwards, an increase of the lattice parameter is observed. In this case, no significant phase transformation was observed in heated samples at different temperatures. Similar results were obtained for samples of chromite and activated charcoal heated isothermally at various temperatures.

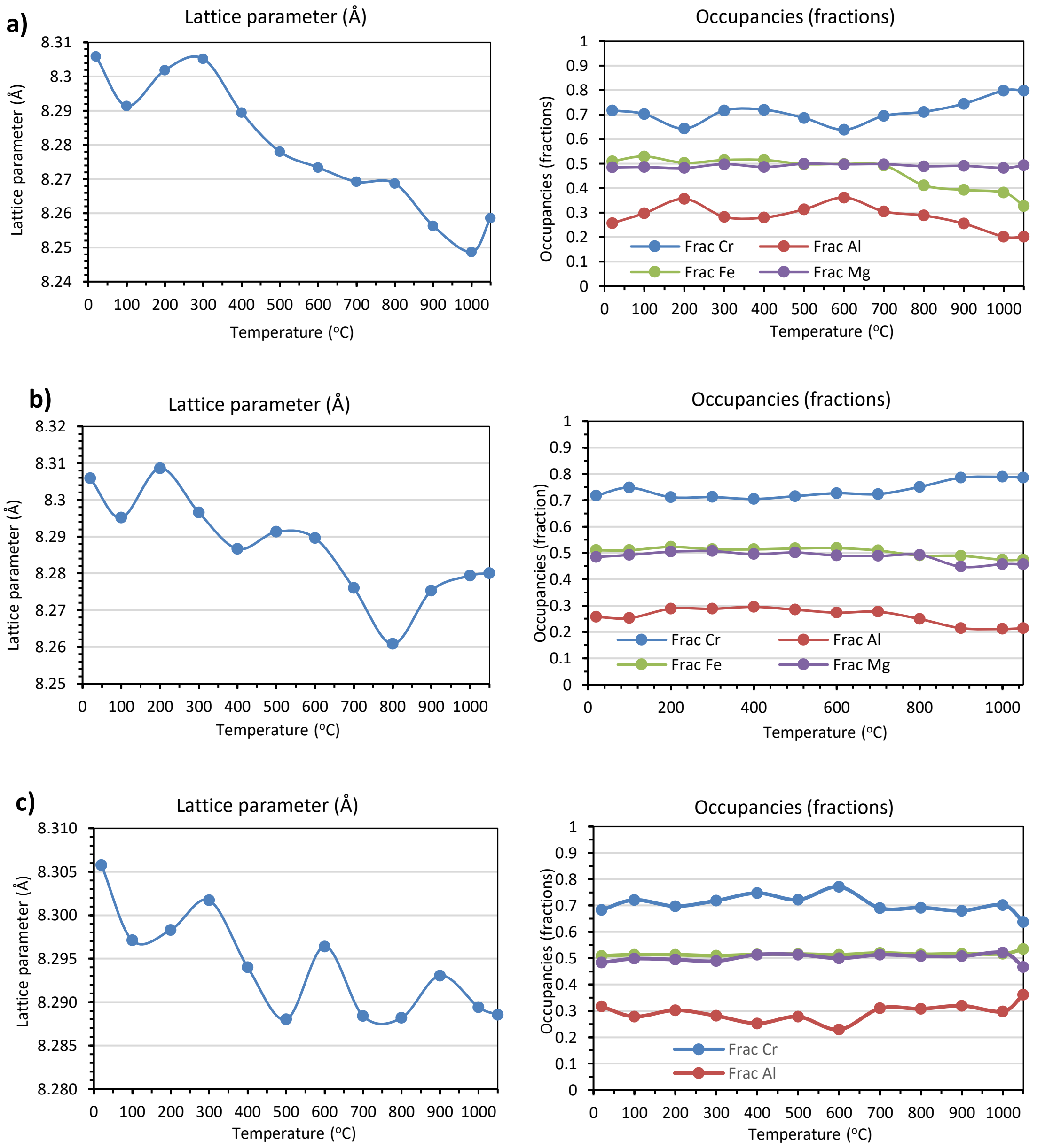

FIGURE 5-14. Lattice parameter and sites occupancies of the chromite spinel phase in samples heated isothermally in: a) heated air atmosphere, b) heated in argon atmosphere and c) mixed with activated charcoal in a wt. ratio of chromite:C = 1:0.2 and heated in Ar atmosphere; at 100°C, 200°C, 300°C, 400°C, 500°C, 600°C, 700°C, 800°C, 900°C, 1000°C and 1050°C.

5.2.3. ANALYSIS OF S.A. CHROMITE SAMPLES REDUCED IN THE PRESENCE OF Na_2CO_3

Samples of chromite heated in the presence of activated charcoal and sodium carbonate at 1000-1050°C were analysed by SEM obtaining high magnification images. Images in FIGURE 5-15 show the formation of metallic iron in the early stages of reduction. The diffusion of Na^+ ions can also be observed in the formation of a darker grey border around the particle in image b.

Part of the small needle-shape particles of metallic Fe seem to form in parallel directions, which suggests that the growth of Fe happens along preferential directions. The formation of the metal phase also takes place along the cracks that appear within the chromite particles as a result of the reaction of Cr_2O_3 and Al_2O_3 with Na_2O and therefore the decomposition of the chromite structure to form the products of reduction. A closer image of one of these metallic needles is shown in image c in FIGURE 5-15.

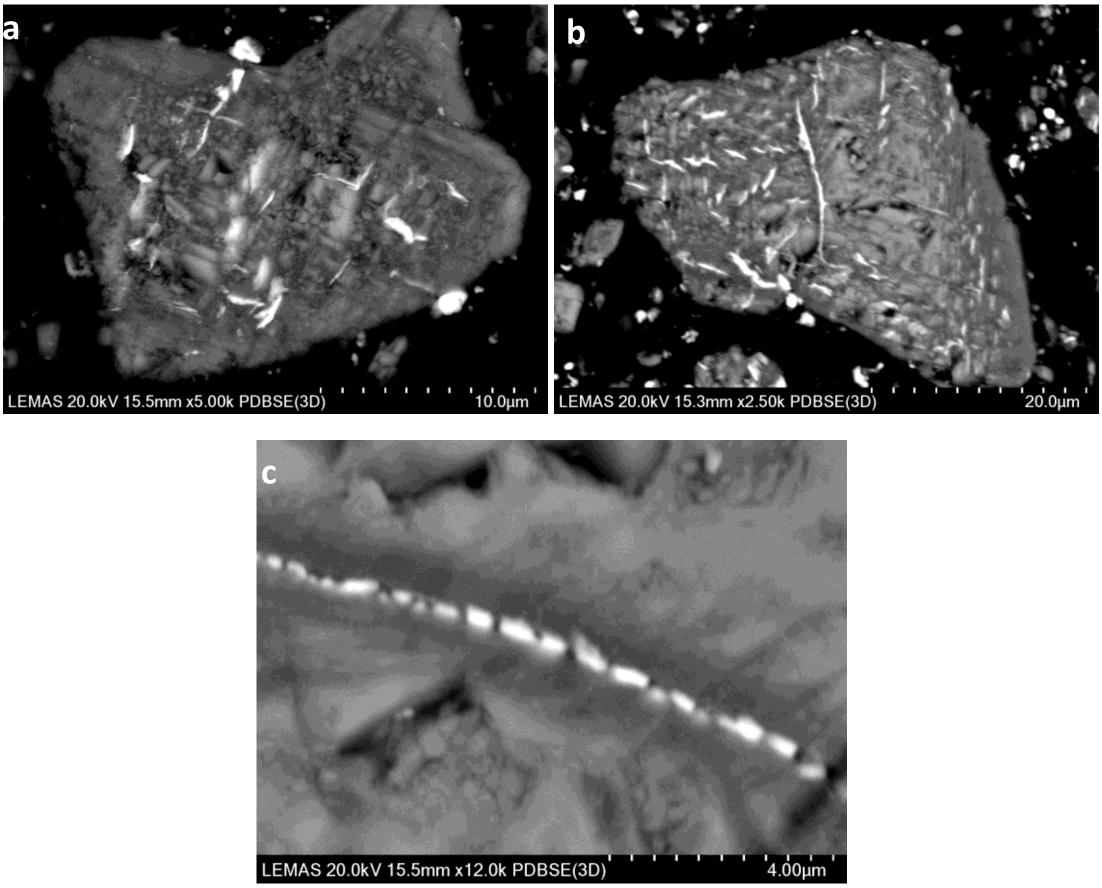

FIGURE 5-15. Backscattered SEM images of chromite ore reduced with Na_2CO_3 and C for 30 minutes at 1000-1050°C obtained using HITACHI scanning electron microscope.

Texture analysis was performed with the aim of determining if the needle-shape metallic Fe was preferentially formed in any particular crystallographic direction during reduction. The analysis was carried out using G-SAS software. G-SAS allows the Rietveld refinement of XRPD patterns including a MD Preferred Orientation tool which is able to identify any preferred orientations in the phase under refinement. In this case, the XRPD pattern analysed was a magnetic fraction obtained by reduction of S.A. chromite ore with Na_2CO_3 and charcoal at 1050°C, for 2.5 hours and chromite:Na_2CO_3:charcoal weight ratio of 1:1:0.2, followed by wet magnetic separation.

A magnetic sample was chosen for this because the peaks for metallic Fe on this sample are the main peaks of the pattern with higher intensity and therefore is easier to refine. In the XRPD of the reduced samples various phases are present, and it is therefore more complex to perform the refinement of the Fe phase. The fitting of the Fe phase was carried out by refining the lattice parameter of the cubic phase and other parameters such as the scale factor, isotropic thermal parameters, background parameters and peak shape parameters using profile function 3. A preliminary good fit was obtained with a Rp(%) = 1.66. The texture analysis tool included in GSAS-EXPGUI was then used to identify any preferred orientations in the metallic Fe formed by using the MD and SH functions. FIGURE 5-16 shows the fitting obtain by Rietveld refinement. Refinement using the SH function did not provide a clear preferential orientation of the sample. However, the refinement by the MD function provide the results shown in FIGURE 5-17, which suggested that the Fe metallic phase has higher preferential orientation on the [110] direction. The Rp(%) obtained when refining on the [110] direction was 1.6, compared to an Rp(%) = 1.75 when refining on the [211] direction. This indicates that metallic Fe may be forming preferentially on the [110] direction thereby yielding the needle-shape structures observed by SEM analysis and already presented and discussed on this document.

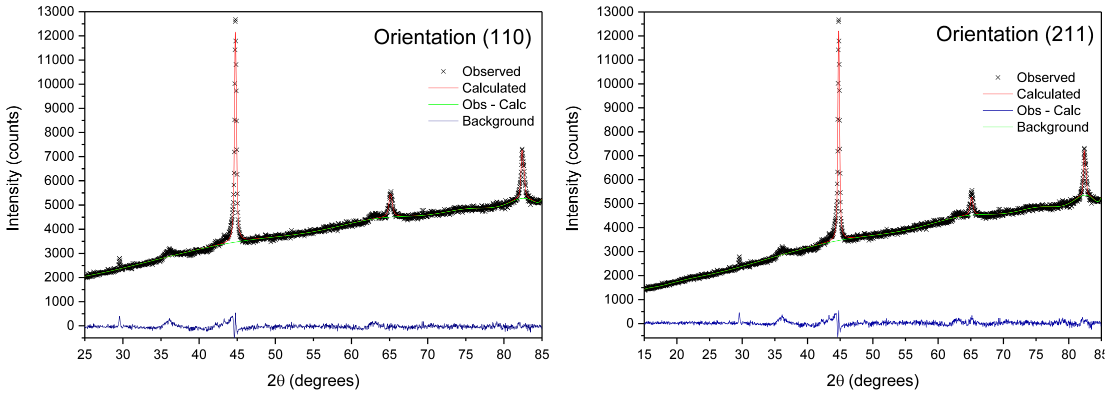

FIGURE 5-16. Observed XRPD pattern, calculated pattern, calculated background and difference plot obtained by Rietveld refinement of the XRPD data of a magnetic fraction.

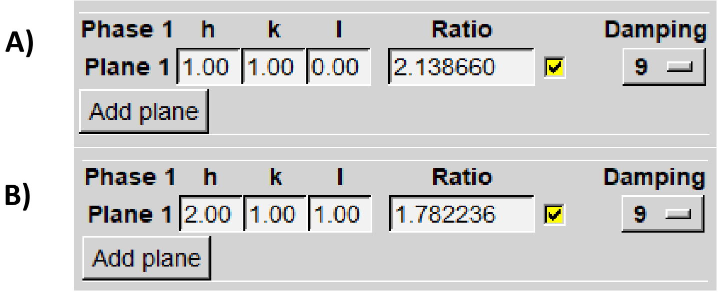

A)

Phase 1 h k l Ratio Damping
Plane 1 1.00 1.00 0.00 2.138660 ☑ 9

B)

Phase 1 h k l Ratio Damping
Plane 1 2.00 1.00 1.00 1.782236 ☑ 9

FIGURE 5-17. GSAS-EXPGUI preferential orientation results.

Chapter 6

ALKALI ROASTING OF CHROMITE ORE IN OXIDISING ATMOSPHERE

Chapter content

The physical chemistry of the alkali roasting of S.A. chromite ore in oxidative atmosphere was studied. Roasting experiments with NaOH/KOH at different reaction temperatures and times were performed, followed by water leaching for Na_2CrO_4 *extraction. The processing residues were characterised by XRPD and SEM. The influence of the alkali ratio on the chromium extraction yield is also analysed in this chapter, and the results obtained with both hydroxides are compared. Sample characterisation and thermodynamic analysis, including phase diagrams, equilibrium calculations and computation of liquidus curves, are combined to study the formation of the molten salt phase and its effect on the* Na_2CrO_4 *extraction yield.*

Chapter conclusions

At low temperature (400°C) the recovery of chromate in solution was higher for chromite roasted with KOH than with NaOH. However, at high temperatures (700°C and 1000°C) the recoveries were similar for both hydroxides. Around 95% Na_2CrO_4/K_2CrO_2 *yield was achieved when chromite was roasted with NaOH/KOH at 1000°C for 2 hours and water leached.*

Equilibrium data showed the need of a Cr_2O_3*:MOH ratio higher than the stoichiometric in order to fully decompose the chromite spinel phase and confirmed that formation of alkali ferrites, aluminates and silicates is possible and may influence the properties of the molten salt. The reaction mechanism with different alkali ratios was discussed based on experimental results and thermodynamic data. The main phases found in water leached residues were partially-reacted chromite,* Fe_2O_3*, MgO and complex silicates. Sodium chromate was not present in water leached residues as shown by XRPD and SEM results, which suggests high efficiency of the leaching step. It was shown that the addition of excess alkali increases the extraction of the alkali chromate, but it also generates a higher volume of molten phase, leading to lower reaction rates as it represents an obstacle to the pore diffusion of oxygen.*

6.1. EFFECT OF TEMPERATURE ON THE ALKALI ROASTING OF CHROMITE

Chromite ore was roasted with excess NaOH or KOH in air atmosphere at three different temperatures, 400°C, 700°C and 1000°C, and with a weight ratio of chromite:MOH = 1:1. Roasted samples were water-leached for 2 hours at 60°C, as described in the procedure in section 3.2.3. FIGURE 6-1 shows the E_H-pH diagram for the Fe-Na-Cr system in water at 50°C computed using FactSage 6.4 software [46]. The striped area illustrates the conditions during the water leaching stage where Na^+ and CrO_4^{2-} ions are found in solution, leaving behind a solid residue containing insoluble phases (mainly Fe_2O_3, MgO and insoluble silicates). Water-leached residues were analysed by XRF in order to quantify the residual chromium and the results are summarised in TABLE 6-1.

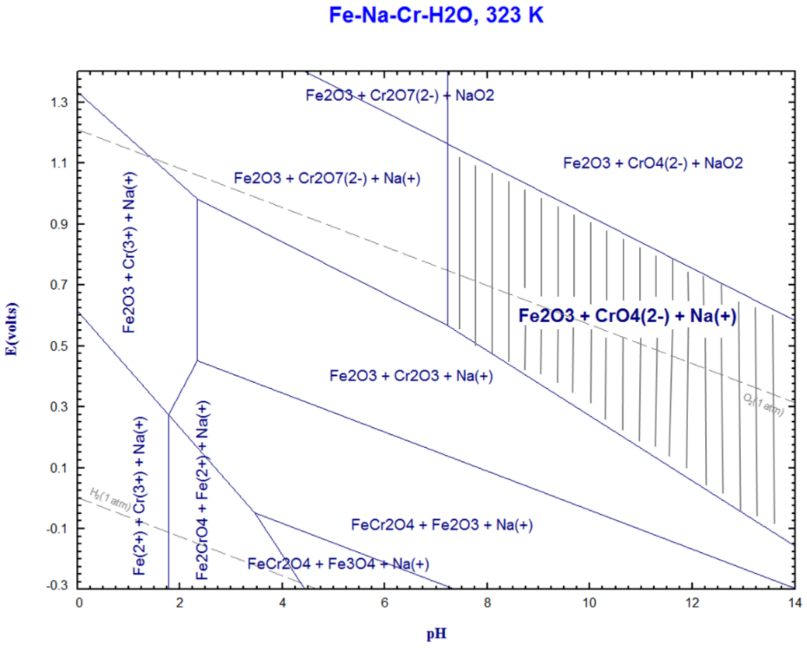

FIGURE 6-1. EH-pH diagram for the Fe-Na-Cr-H_2O system at 50°C (323K) computed by FactSage 6.4 [46].

TABLE 6-1. Wt.% Cr_2O_3 in the water leached residues after roasting of chromite with NaOH or KOH at different temperatures. Samples were analysed by XRF.

Chromium left in the solid residues after water leaching (wt.% Cr_2O_3)			
Chromite + NaOH		**Chromite + KOH**	
400°C	46.3	400°C	39.7
700°C	24.7	700°C	24.5
1000°C	3.65	1000°C	3.73

It can be seen in TABLE 6-1 that chromite spinel does not undergo significant decomposition when roasted with alkali at 400°C. Potassium hydroxide seems to be more reactive than sodium hydroxide at low temperature. However, above 400°C small differences in the extraction yield were found which justify the use of sodium hydroxide because of its lower price. In FIGURE 6-2a, a backscattered SEM image of a water leached residue after chromite roasting with KOH at 400°C is presented, from which it is apparent that chromite particles remained unreacted.

When the reaction is carried out at 700°C, the percentage of chromium in the residue is still significantly high (24.7 wt.% Cr_2O_3 for NaOH and 24.5 wt.% Cr_2O_3 for KOH), indicating that the chromite structure was not completely decomposed at this temperature. Looking at the structure of the residue particles after roasting of chromite with KOH at 700°C and water leaching, presented in FIGURE 6-2b, an unreacted chromite core (bright phase) surrounded by the reaction layer (darker phase) is observed. The Shrinking-core model has been applied to the chromite roasting by previous authors [80].

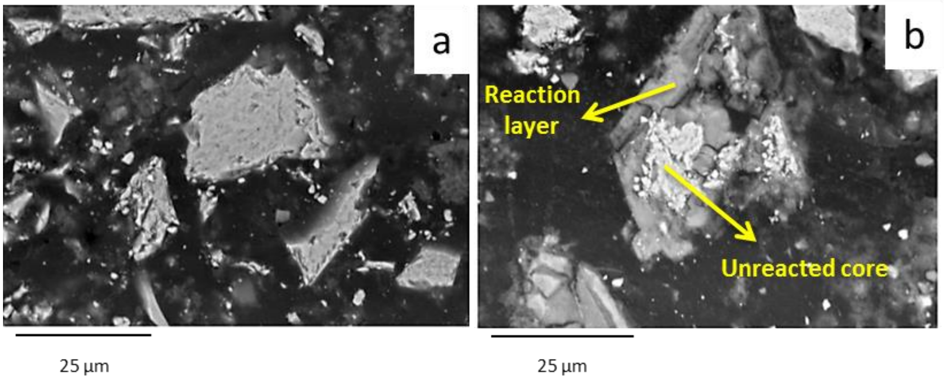

FIGURE 6-2. Backscattered SEM images of water leached residues after roasting of chromite ore with KOH at a) 400°C and b) 700°C.

At 1000°C, chromite ore reacted with alkali to a significant extent, and most chromium was extracted as sodium or potassium chromate by water leaching. The wt.% of Cr_2O_3 decreased from 48.8% in the as-received chromite sample to 3.65% and 3.73% in the water leached residues after roasting with sodium and potassium hydroxides, respectively.

During alkali roasting, the Cr^{3+} cations diffuse towards the reaction zone where they combine with Na^+/K^+ to form water-soluble chromate compounds (Na_2CrO_4, K_2CrO_4), which are subsequently extracted during water leaching. Aluminium is also leached out in the form of water-soluble alkali aluminates ($NaAlO_2$, $KAlO_2$). Consequently, the remaining residue after water leaching is Fe and Mg-rich.

A backscattered SEM image of a water leached residue after chromite roasting with NaOH at 1000°C is shown in FIGURE 6-3a. Tathavadkar (2003) [28] described how Mg^{2+} cations diffuse outwards from the chromite structure during the soda-ash roasting of South African chromite, occupying voids in the Fe-rich phase surrounding the unreacted core and promoting the formation of magnesioferrite ($MgFe_2O_4$).

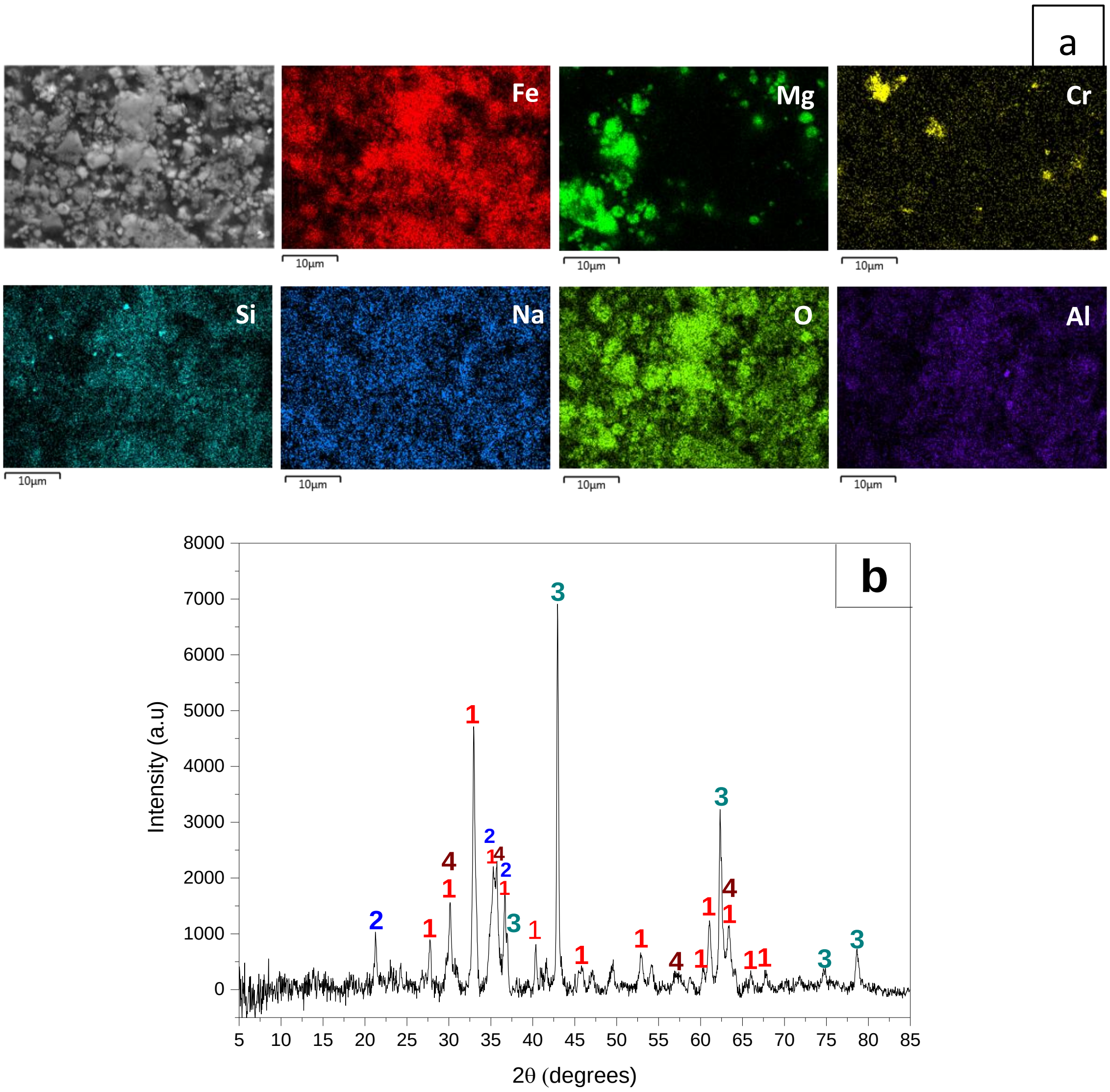

FIGURE 6-3. (a) Backscattered SEM image and elemental mapping, (b) XRPD pattern of water leached residue after roasting with NaOH at 1000°C. [1=Fe_2O_3, 2=$Na_{1.15}Al_{1.15}Si_{0.85}O_4$, 3=$MgO$, 4=$MgFe_2O_4$].

The XRPD pattern of the water leached residue after roasting at 1000°C, in FIGURE 6-3b, confirms the presence of $MgFe_2O_4$, however, Fe_2O_3 and MgO phases can also be found separately. SEM elemental mapping of the same sample presented in FIGURE 6-3a clearly shows Fe_2O_3 and MgO phase segregation. This may be explained by the excess alkali present during the roasting reaction, which leads to water-soluble $NaFeO_2$ formation.

Reaction (r.63) shows the formation of $NaFeO_2$ by reaction of $MgFe_2O_4$ with NaOH. The Gibbs energy value for this reaction at 1000°C, computed using HSC 5.1 software [107], is -27.6 kJ per mol of $MgFe_2O_4$ reacted, which indicates that $MgFe_2O_4$ may react with excess alkali to form MgO and water-soluble $NaFeO_2$ when roasting is carried out at 1000°C.

$$MgFe_2O_4\ (s) + 2\ NaOH\ (s) \rightarrow MgO\ (s) + 2\ NaFeO_2\ (s) + H_2O(g) \qquad \text{(r.63)}$$

During water leaching, the separation of $NaFeO_2$ into NaOH and Fe_2O_3 takes place, followed by precipitation of iron oxide which remains in the residue, as described by previous authors [25]. The main phases found in the residue after water leaching are MgO, Fe_2O_3, $MgFe_2O_4$ and sodium aluminium silicate, as confirmed by the XRPD pattern in FIGURE 6-3b. Some free silica is also observed, as apparent from the elemental mapping (FIGURE 6-3a).

6.2. CHROMIUM EXTRACTION WITH TIME DURING ALKALI ROASTING

Chromite ore samples were roasted with NaOH and KOH at 1000°C for different periods of time between 15 minutes and up to 2 hours, and subsequently water leached for 2 hours at 60°C. The weight ratio chromite:MOH was kept constant at 1:1 (equivalent to a molar ratio of Cr_2O_3:MOH = 1:7.8). The XRF analysis of the water-leached residues was used to calculate the extraction yield according to the equation (eq.7) below. Chromium extraction profiles are presented in FIGURE 6-4.

$$\text{Extraction yield (\%)} = \frac{\text{Cr in solution}}{\text{Cr in chromite}} \cdot 100 = \frac{\text{Cr in chromite-Cr in residue}}{\text{Cr in chromite}} \cdot 100 \qquad \text{(eq.7)}$$

During the early stages of reaction, extraction kinetics are slower for NaOH compared with KOH reaction, as shown in FIGURE 6-4, which might be due to extensive fracture of particles caused by K^+ ions. The fractured surface area is larger with K^+ ions than with Na^+ ions, [26]. Eventually, the two extraction curves converge, and the final chromium extraction is quite similar for both hydroxides yielding slightly above 95% extraction efficiency after roasting at 1000°C for 2 hours.

A SEM micrograph and line-scan analysis of a water-leached sample previously roasted with NaOH at 1000°C for 30 minutes can be seen in FIGURE 6-5a. After 30 minutes of reaction, a clearly defined reaction layer can be differentiated from the unreacted chromite core. The reaction product is composed of two distinct phases, an inner layer surrounding the unreacted core and an outer layer.

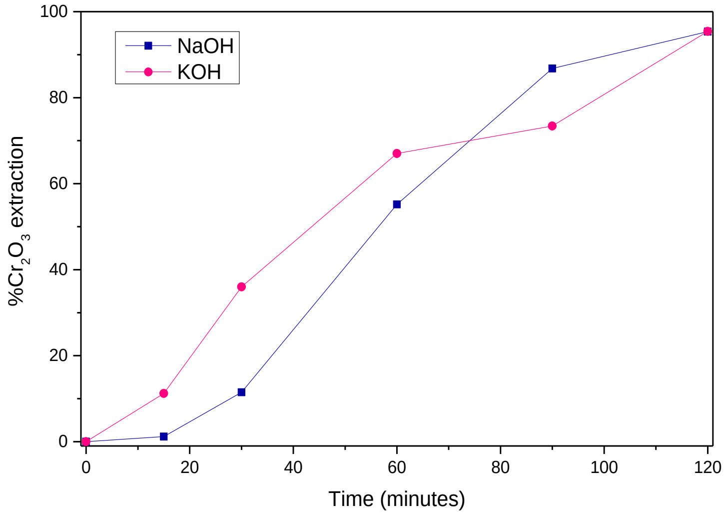

FIGURE 6-4. Influence of time over chromium extraction yield for samples roasted at 1000°C (Cr_2O_3:MOH = 1:7.8) and water leached at 60°C.

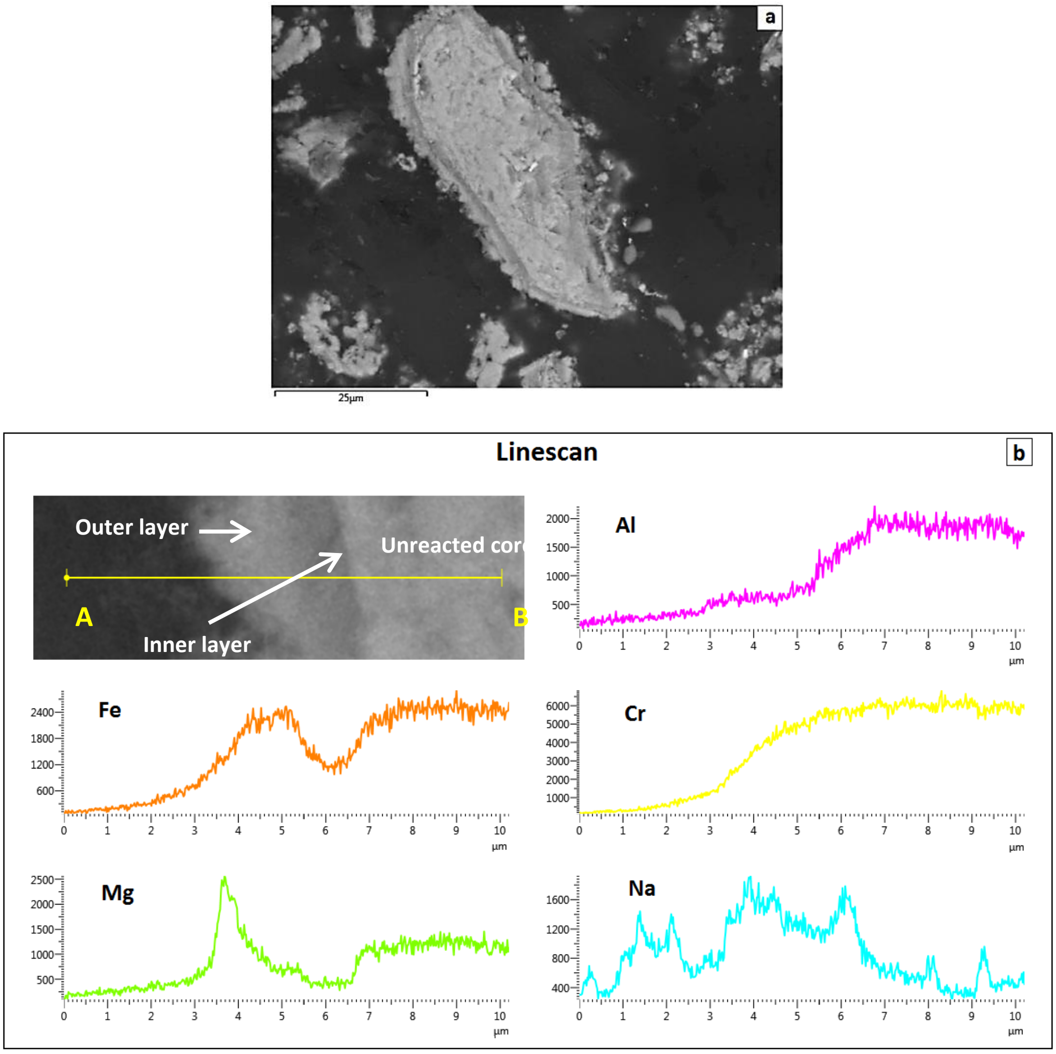

FIGURE 6-5. a) Backscattered SEM image of a residue particle after chromite roasting with NaOH at 1000°C for 30 minutes and water leaching and b) line-scan analysis from points A-B.

The difference in colour intensity of the two rings indicates that there is a difference in chemical composition between them, which was confirmed by line scan and chemical analysis of the particle using EDX. The chemical composition of the three distinct areas indicated in FIGURE 6-5b was also analysed by SEM-EDX and is presented in TABLE 6-2.

Line scan in FIGURE 6-5b shows how both chromium and aluminium concentrations progressively decrease as you move towards the reaction interface, where reaction with alkali forms water-soluble Na_2CrO_4 and $NaAlO_2$. In the first stages of the reaction, the oxidation of Fe^{2+} present in the chromite spinel to Fe^{3+} occurs, via voids generated in the spinel structure as a consequence of this oxidation process [111]. These structural vacancies promote the diffusion of Cr^{3+} outwards the chromite grain. Iron diffuses from the chromite spinel structure to the reaction layer, where it can mainly be found in the outer ring and not in the inner one as seen in the Fe line scan graph in FIGURE 6-5b. Magnesium is present in the outermost part of the reaction layer and is likely to combine with iron to form $MgFe_2O_4$.

This agrees with the elemental analysis shown in TABLE 6-2, where it can be seen how Fe and Mg are more concentrated in the outer layer than in the inner one. The results show that the wt.% of chromium in the inner layer is higher, which can be due to the relatively lower concentration of Fe and Mg.

TABLE 6-2. Elemental composition of unreacted core, inner and outer product layers indicated in FIGURE 6-5b analysed by SEM-EDX.

wt.%	Cr	Fe	O	Mg	Al	Si	Ca	Na	Ti
Unreacted core	32.7	19.7	31.4	6.8	9	-	-	-	0.4
Inner layer	45.3	12.7	25.5	1.6	6.8	-	0.2	7.5	0.5
Outer layer	31.7	22.6	23.6	6.0	2.3	0.6	0.6	12.4	0.3

6.3. ROLE OF LIQUID PHASE ON THE OXIDATIVE ROASTING OF CHROMITE ORE

The parameters affecting the degree of chromium extraction by alkali roasting in oxidising conditions include chromite ore composition, roasting temperature and time, oxygen potential and the origin and quantity of gangue materials present in the ore. Another important factor which is known to have a critical effect on the roasting reaction is the formation of an alkaline molten phase containing chromium.

The formation of the alkali-rich liquid during the roasting of chromite is an important step in controlling the overall chemical reaction, which depends on the pore diffusion of oxygen.

Tathavadkar (2001) [33] previously described the key role played by the binary Na_2CrO_4–Na_2CO_3 molten phase formed during alkali roasting of chromite ore with sodium carbonate. The liquid phase mainly consists on the formation of an eutectic mixture at 928 K between Na_2CO_3 and Na_2CrO_4 with a 62.5 wt.% sodium chromate. It was pointed out that the ore composition and gangue materials have a significant effect on the properties of the binary Na_2CrO_4–Na_2CO_3 liquid phase, which ultimately affects the extraction yield of chromium. In this set of experiments, alkali hydroxides, namely NaOH and KOH, are used for the roasting of chromite ore, and therefore an M_2CrO_4-MOH molten phase, where M represents the alkali metal (Na or K), is expected to form. When roasting with sodium or potassium hydroxide, the main reaction taking place is shown below in (r.64):

$$2\ FeCr_2O_4\ (s) + 8\ MOH\ (l) + 7/2\ O_2(g) \rightarrow 4\ M_2CrO_4\ (l) + Fe_2O_3\ (s) + 4\ H_2O(g) \qquad \text{(r.64)}$$

Since chromite ore also contain iron, alumina and gangue minerals including silicates, reaction of alkali with these elements will yield new complexes which are likely to alter the chemical composition of the liquid phase. Thermodynamic analysis of the possible reactions of sodium/potassium hydroxides with the different elements of the ore (see equations (r.34) to (r.47)) shows that besides the formation of alkali chromate, formation of alkali ferrite ($NaFeO_2$, $KFeO_2$), alkali aluminate ($NaAlO_2$, $KAlO_2$) and alkali silicate (Na_2SiO_3, K_2SiO_3) is also possible during roasting depending on the alkali available [24]. Previous authors [28,87] also described the formation of alkali compounds, which were identified either as intermediates of reaction or final products after roasting of chromite with Na_2CO_3. Tathavadkar (2003) [28] reported that the formation of $NaAlO_2$, $NaFeO_2$ and Na_2SiO_3 during roasting of chromite with Na_2CO_3 leads to a change in both the physical and chemical properties of the liquid phase.

The liquid phase generated acts as coating, filling the pores on the surface of the non-reacted or partially-reacted chromite particles during the oxidation reaction with alkali metal hydroxides, as shown in FIGURE 6-6. During roasting in the presence of alkali, there is diffusion of Na^+ through the liquid phase towards the reaction zone [34] and diffusion of gaseous species. The roasting reaction is considered to be controlled by diffusion and can be described by the Ginstling and Brounshtein (GB) equation [29,32]. In a kinetic study of alkali roasting of Indian chromite [29], it was concluded that the diffusion of Cr^{3+} and Na^+ is the rate-limiting step when temperature is low (700°C to 900°C), whereas at higher temperatures (above 900°C) the diffusion of gaseous species controls the rate of reaction.

The presence of the molten salt layer impedes the overall kinetics of sodium chromate formation when roasting at 1000°C by decreasing the rate of gas diffusion (rate-limiting step) through the molten salt towards the reaction interface, where trivalent chromium is oxidised and formation of sodium chromate takes place in the presence of O_2 by reaction between Cr^{6+} and Na^+ [32,33]. At a fixed temperature, the obstruction of the oxygen transport is more significant with increasing volume and proportion of the liquid phase in the reaction mixture.

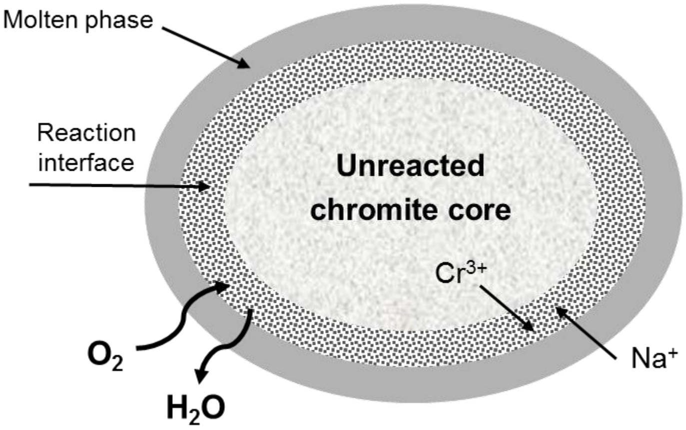

FIGURE 6-6. Schematic representation of a partially-reacted chromite particle and molten salt phase formed during roasting with alkali in oxidising conditions.

Tathavadkar (2003) [28] pointed out the importance of the viscosity of the molten phase, as this is the property which mainly affects the thickness of the liquid layer and its resistance to the transport of gaseous species. In the case of roasting with Na_2CO_3, the viscosity of the Na_2CO_3–Na_2CrO_4 molten salt mixture was found to be highly dependent on the roasting temperature and the composition of the initial charge [33].

It has been demonstrated that the presence of silica leads to the formation of sodium silicate compounds which drops the activity of alkali metal ions (Na^+, K^+) and increase the viscosity of the liquid phase [28]. The differences between the reaction mechanism with and without silica are significant, and hence the yield of sodium chromate extraction strongly depends on the amount of silica present in the ore. When sodium silicate dissolves into the liquid phase, sodium ferrite and aluminate tend to dissolve too, and the result is the formation of a highly-viscous liquid rich in alkali, in which chromite dissolves completely forming a complex Na-Cr-Fe-Al-Si-Mg-O liquid at high temperature [33]. This is the reason why the presence of silica in the ore has a strong negative influence on the extraction efficiency of chromate, which is higher for ores with low silica content.

The reaction mechanism of the roasting of chromite was studied using Cr_2O_3:hydroxide molar ratios of 1:3.2, 1:4, 1:6, 1:8 and 1:10, which correspond to 80%, 100%, 150%, 200% and 250% of the stoichiometric hydroxide amount needed to convert all Cr^{3+} contained in the ore to water soluble alkali chromate (Na_2CrO_4 or K_2CrO_4). Relevant phase diagrams and equilibrium calculations are also computed with the aim of determining the different phases formed during roasting and their effect on the properties of the liquid phase, the rate of diffusion of oxygen to the reaction interface and, ultimately, the extraction efficiency of chromium.

6.3.1. THERMODYNAMIC CONSIDERATIONS

The effect of the alkali ratio on the oxidation reaction was studied by performing roasting experiments using five different Cr_2O_3:MOH molar ratios (where M = Na or K) of 1:3.2, 1:4, 1:6, 1:8 and 1:10. It was mentioned before that the analysis of the Gibbs free energy of the roasting of chromite with NaOH/KOH indicated that both hydroxides can be consumed by alumina and silica to form alkali aluminates and alkali silicates [24]. This makes it necessary to increase the amount of alkali above the stoichiometric, by taking into account the alumina and silica content of the ore. Iron oxide may also react with Na^+/K^+ to form $NaFeO_2/KFeO_2$, only if alkali is in excess.

Formation of alkali ferrites can be seen in FIGURE 6-7. The computed phase diagrams for the $NaOH\text{-}Cr_2O_3\text{-}Fe_2O_3\text{-}Al_2O_3\text{-}O_2$ and $KOH\text{-}Cr_2O_3\text{-}Fe_2O_3\text{-}Al_2O_3\text{-}O_2$ systems were calculated by using FactSage 6.4 software [46] including FactPS, FToxid, FTsalt and FTmisc databases. The diagrams indicate the phases coexisting in equilibrium at 1000°C as a function of the partial pressure of oxygen, $Pp(O_2)$, and the activity of MOH. Both diagrams show that the partial pressure of oxygen required to form the alkali chromates (M_2CrO_4) decreases as the concentration of MOH increases; implying that, from a thermodynamic point of view, chromate formation will be enhanced by the presence of excess hydroxide.

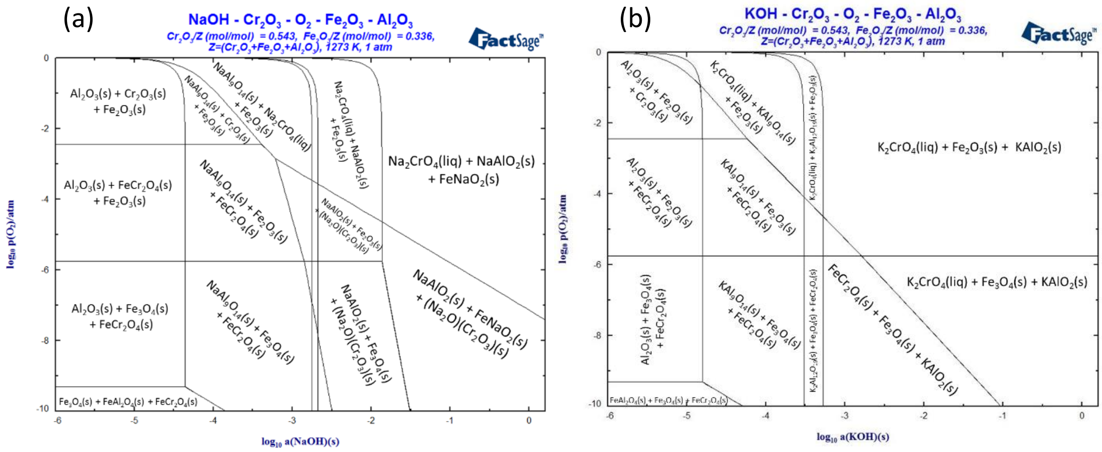

FIGURE 6-7. Phase diagrams of the a) Cr_2O_3-Fe_2O_3-Al_2O_3-NaOH-O_2 and b) Cr_2O_3-Fe_2O_3-Al_2O_3-KOH-O_2 systems. Computed using FactSage 6.4 [46].

It should be noticed that $NaFeO_2$ appears in FIGURE 6-7a for certain conditions of Pp(O_2) and NaOH activity, whereas $KFeO_2$ does not exist in FIGURE 6-7b under comparable conditions. This is due to a lack of thermodynamic data for this compound in the software's database.

However, $KFeO_2$ is expected to form if there is an excess of KOH, since the reaction for the formation of $KFeO_2$ by combination of Fe_2O_3 and KOH at 1000°C has a significantly large negative value of Gibbs energy, which is equal to ΔG_f = -1129.88 kJ per mol of reacted Fe_2O_3 at 1000°C (calculated using HSC 5.1 software [107]).

Under conditions of high activity of the alkali compound and low partial pressure of oxygen, oxidation of Cr^{3+} to Cr^{6+} is not achieved leading to formation of alkali phases containing trivalent chromium, such as $NaCrO_2$ and $KCrO_2$; as it can be seen in FIGURE 6-7a where $(Na_2O)(Cr_2O_3)$ is found at the bottom right-hand corner of the diagram. However, $(K_2O)(Cr_2O_3)$ is not present in FIGURE 6-7b for comparable conditions of a(KOH) and Pp(O_2), which may be explained due to the lack of $KCrO_2$ data in the FactSage 6.4 database. In this study, experiments were carried out in air and therefore the partial pressure of oxygen is Pp(O_2) = 0.21 atm and log(Pp(O_2)) = -0.68. Hence, the reaction takes place at the top of the phase diagram where the pressure of oxygen is theoretically sufficient for oxidation of chromium to (6+)-state, and $NaCrO_2$ and $KCrO_2$ are not expected to be found at equilibrium.

Phase equilibria conditions were also computed for the roasting of chromite and the five different alkali ratios tested experimentally by using FactSage 6.4 [46]. In TABLE 6-3 below, the moles of the different phases in equilibrium after roasting 50g of chromite with the corresponding alkali amount at 1000°C are compared. As the experiments were carried out in air atmosphere, it was assumed that there was excess oxygen available.

TABLE 6-3. Equilibrium data calculated for the roasting of 50g of chromite with five different ratios of NaOH/KOH (1:3.2, 1:4, 1:6, 1:8, 1:10) at 1000°C in oxidising conditions.

Alkali	**Cr_2O_3:MOH**	**Phases in equilibrium (moles)**					
NaOH	1:3.2	Na_2CrO_4(liq) 0.24410	Fe_2O_3 0.09781	$MgAl_2O_4$ 0.02668	Mg_2SiO_4 0.01236	$NaAlSiO_4$ 0.01680	$(MgO)(Cr_2O_3)$ 0.03584
NaOH	1:4	Na_2CrO_4 (liq) 0.31425	Fe_2O_3 0.09780	$MgAl_2O_4$ 0.03368	Mg_2SiO_4 0.02643	$NaAlSiO_4$ 0.00274	$(MgO)(Cr_2O_3)$ 0.00068
NaOH	1:6	Na_2CrO_4 (liq) 0.31579	Fe_2O_3 0.01938	MgO 0.08722	$FeNaO_2$ 0.15686	$Na_6Si_2O_7$ 0.01458	$NaAlO_2$ 0.07010
NaOH	1:8	Na_2CrO_4 (liq) 0.31579	NaOH (liq) 0.24330	MgO 0.08722	$FeNaO_2$ 0.19563	Na_4SiO_4 0.02917	$NaAlO_2$ 0.07010
NaOH	1:10	Na_2CrO_4 (liq)	NaOH (liq) 0.558800	MgO 0.087221	$FeNaO_2$ 0.19563	Na_4SiO_4 0.029167	$NaAlO_2$ 0.070098
KOH	1:3.2	K_2CrO_4 (liq) 0.24805	Fe_2O_3 0.09781	$MgAl_2O_4$ 0.03060	$MgSiO_4$ 0.01138	$KAlSi_2O_6$ 0.00890	$(MgO)(Cr_2O_3)$ 0.03387
KOH	1:4	K_2CrO_4 (liq) 0.31489	Fe_2O_3 0.09781	$MgAl_2O_4$ 0.03432	$MgSiO_4$ 0.02623	$KAlSi_2O_6$ 0.00147	$(MgO)(Cr_2O_3)$ 0.00036
KOH	1:6	K_2CrO_4 (liq) 0.31579	KOH (liq) 0.13960	MgO 0.08722	Fe_2O_3 0.09781	K_2SiO_3 (liq) 0.02917	$KAlO_2$ 0.07010
KOH	1:8	K_2CrO_4 (liq) 0.31579	KOH (liq) 0.45520	MgO 0.08722	Fe_2O_3 0.09781	K_2SiO_3(liq) 0.02917	$KAlO_2$ 0.07010
KOH	1:10	K_2CrO_4 (liq) 0.31579	KOH (liq) 0.77070	MgO 0.08722	Fe_2O_3 0.09781	K_2SiO_3(liq) 0.02917	$KAlO_2$ 0.07010

The comparison of equilibrium data in TABLE 6-3 and FIGURE 6-7a and b confirms that it is necessary to have excess alkali in order to extract all Cr^{3+} in the form of water soluble chromate. When the stoichiometric amount of alkali is added, part of the chromium remains unreacted as $MgCr_2O_4$, since some sodium and potassium are consumed in the formation of alkali aluminosilicates ($NaAlSiO_4$, $KAlSiO_4$). However, when excess alkali is added, the magnesiochromite phase cannot be observed in the reaction product. Based on equilibrium calculations, the majority of chromium is extracted as Na_2CrO_4 when the Cr_2O_3:NaOH molar ratio is 1:6 (150% of the stoichiometric amount), and therefore, a further increase of the amount of alkali in the charge does not necessarily mean an improvement of the chromium extraction yield. These observations were also found to be consistent with results for KOH.

Part of the alumina reacts to form $MAlSiO_4$ and the rest remains unreacted as $MgAl_2O_4$ when roasting with the stoichiometric alkali ratio, but when the ratio is increased from 1:4 to Cr_2O_3:MOH = 1:6 or above, the alumina combines with Na^+/K^+ to form sodium or potassium aluminate ($MAlO_2$). The oxides of iron and magnesium separate out by forming the respective single oxide phases (MgO, Fe_2O_3) or they may be also found combined as magnesioferrite ($MgFeO_2$). When excess alkali is high (molar ratio Cr_2O_3:MOH = 1:6 or higher), iron forms $MFeO_2$, as mentioned above.

TABLE 6-3 shows the state of the difference phases (solid or liquid), which allows to predict the composition of the molten salt phase. The liquid phase is mainly composed of M_2CrO_4 and unreacted MOH, however, as it can be seen in TABLE 6-3, alkali silicates form when alkali is in excess (Cr_2O_3:MOH molar ratios of 1:6, 1:8 and 1:10). Particularly, if K_2SiO_3 forms during roasting, it will be present in the liquid as it melts below 1000°C (melting point of K_2SiO_3 = 976°C), leading to an increase in the viscosity of the molten phase [33]. The amount of alkali added will determine the volume of the liquid phase generated and its compositional properties for governing the intergranular fluid flow in the chromite matrix.

Eutectic diagrams for the binary systems composed by MOH or M_2CrO_4 and different alkali compounds ($MAlO_2$, M_2SiO_3, $M_2Si_2O_5$) were plotted with the aim of comparing the temperature and composition of the eutectic points of the two-component mixtures. The liquidus curves for binary phase diagrams were calculated by using the Clausius-Clapeyron relation [113], shown in equation (eq.10), in which the liquidus temperature (T) of the binary mixture is dependent on the molar composition (x_i), by assuming that the mixture forms an ideal solution.

$$-\ln x_i = \frac{\Delta H_{fi}}{R} \cdot \left(\frac{1}{T} - \frac{1}{T_{fi}}\right) \qquad \text{(eq.8)}$$

Equation (eq.8) allows the calculation of the theoretical liquid curves for the binary systems as a function of the heat of fusion (ΔH_f) and the melting point (T_f) of each component. The thermodynamic data required was obtained from Perry (2016) [114] and HSC 5.1 software [107]. R is the gas constant equal to 8.31 $Jmol^{-1}K^{-1}$. The computed diagrams are presented in Figure 6-8, where the eutectic point of each binary system is located at the intersection of the liquidus curves of the two components.

It can be seen in FIGURE 6-8a and FIGURE 6-8c that the binary mixtures M_2CrO_4– MOH (where M is either Na or K) have the lowest temperature eutectic points with low molar fraction of the alkali chromate; 560 K – 8.2% Na_2CrO_4 and 645 K – 6.8% K_2CrO_4, respectively. The eutectic KOH – K_2CrO_4 mixture at 633 K and 7.8% K_2CrO_4 was previously reported in the literature [115,116], which is comparable with the values obtained theoretically.

The calculated eutectic temperature of the Na_2CrO_4 – NaOH mixture (560K) is significantly lower than the value for the Na_2CrO_4 – Na_2CO_3 system (928 K), which was reported in a previous study by Tathavadkar (2003) [28]. It was also described on that study how the presence of other alkali compounds in the liquid phase contributes to the decrease of the eutectic temperature of the mixture, causing an increase of the liquid phase present which is detrimental for the overall oxygen transport [28].

The respective Na_2CrO_4 and K_2CrO_4 liquidus curves show that the liquidus temperature increases as the molar fraction of the alkali chromate increases, which indicates that the liquidus temperature raises as sodium hydroxide is consumed and sodium chromate is formed. NaOH and KOH form low temperature eutectics not only with the chromates but also with the rest of alkali compounds. This is shown in Figure 6-8b and Figure 6-8d, where it can also be observed that the eutectic temperatures of the binary mixtures containing NaOH are lower than those for the binary systems containing KOH.

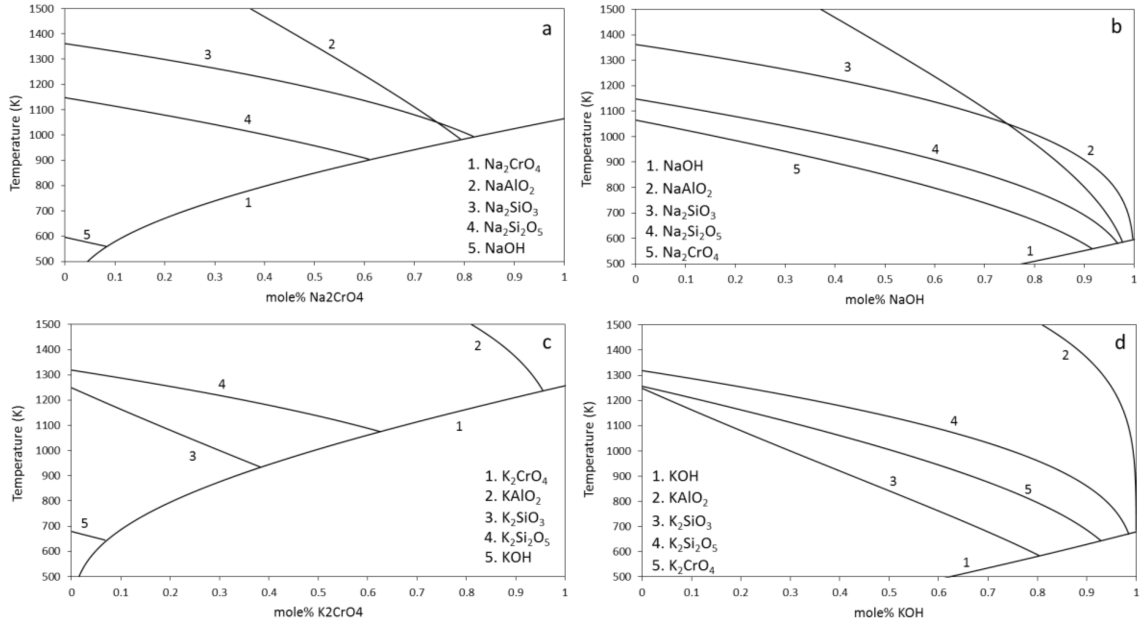

Figure 6-8. Liquidus curves for the A) Na_2CrO_4 and $NaAlO_2$/Na_2SiO_3/$Na_2Si_2O_5$/NaOH; B) K_2CrO_4 and $KAlO_2$/K_2SiO_3/$K_2Si_2O_5$/KOH; C) NaOH and $NaAlO_2$/Na_2SiO_3/$Na_2Si_2O_5$/Na_2CrO_4; D) KOH and $KAlO_2$/K_2SiO_3/$K_2Si_2O_5$/K_2CrO_4 binary systems.

6.3.2. REACTION MECHANISM AND PHASE ANALYSIS

The mechanism of the overall reaction may be analysed by combining the equilibrium data in Figure 6-7 and Table 6-3 with experimental results. In Figure 6-9, the X-ray powder diffraction data for leached residues after roasting of chromite with NaOH/KOH are compared for different stoichiometric molar ratios of Cr_2O_3:MOH (1:4, 1:6 and 1:8).

Leached residues contain the insoluble phases, while the alkali chromate and the rest of the water-soluble phases are extracted during leaching.

Equilibrium data shown in Table 6-3 indicates that, for roasting of chromite with the stoichiometric Cr_2O_3:alkali molar ratio, $MgAl_2O_4$ and $MgCr_2O_4$ spinel-type phases are in equilibrium. Experimental results demonstrate that these phases are present in the core of the partially-reacted particles and are found as a complex Mg-Fe-Cr-Al-O spinel with a certain stoichiometry, which in fact corresponds to the initial chromite ore phase depleted in Fe^{2+}/Fe^{3+} species. In the XRPD patterns of the residue samples in Figure 6-9, the complex spinels $Mg_{0.74}Cr_{0.96}Fe_{0.26}Al_{1.04}O_4$ and $MgCr_{0.2}Fe_{1.8}O_4$ can be found when roasting with the stoichiometric amount of NaOH, and $Mg(Fe_{0.5}Al_{0.5})_2O_4$ and $MgCrAlO_4$ were present when roasting with KOH. The depletion of iron was observed in the backscattered SEM images by analysing elemental mappings of particles from water-leached residues after roasting with the stoichiometric alkali ratio. The results are presented in Figure 6-10 and Figure 6-11 for NaOH and KOH, respectively, where it can be observed that all remaining chromium is in form of partially-reacted chromite spinel.

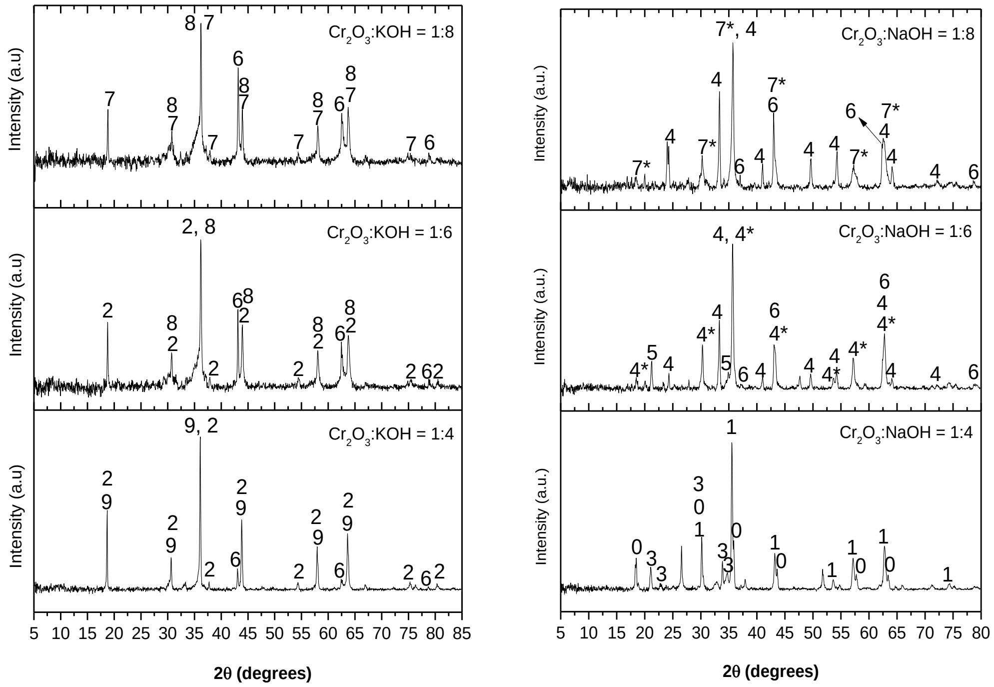

Figure 6-9. XRPD patterns of leached residues after roasting of chromite with different molar ratios of KOH and NaOH at 1000°C for 2 hours. Cu-Kα radiation was used (λ = 1.5418 Å). (0. $Mg_{0.74}Cr_{0.96}Fe_{0.26}Al_{1.04}O_4$, 1. $MgCr_{0.2}Fe_{1.8}O_4$, 2. $Mg(Fe_{0.5}Al_{0.5})_2O_4$, 3. $Na_2Mg(SiO_4)$, 4. Fe_2O_3 (hematite, rhombohedral), 4*. Fe_2O_3 (cubic), 5. SiO_2, 6. MgO, 7. $MgFe_2O_4$, 7*. $MgCr_2O_4$, 8. $Fe_{2.3}Si_{0.7}O_4$, 9. $MgCrAlO_4$).

The edge of the particles, where chromite is in contact with oxygen, is richer in iron oxides. In agreement with the equilibrium data presented in TABLE 6-3, Fe^{3+} seems to diffuse out first and remain at the edge of the partially reacted particles. This is evident in FIGURE 6-10, in which a rim of $MgFe_2O_4$ may be seen. It can also be observed in the microstructure how in some areas iron and magnesium phase-separate into the corresponding single oxide phases. Silica is mainly combined with Na^+ and Al^{3+} when roasting with NaOH (FIGURE 6-10), however, when roasting with KOH iron oxide is preferentially found as an insoluble complex K-Fe-Si-O phase, which can clearly be seen in the elemental mapping in FIGURE 6-11.

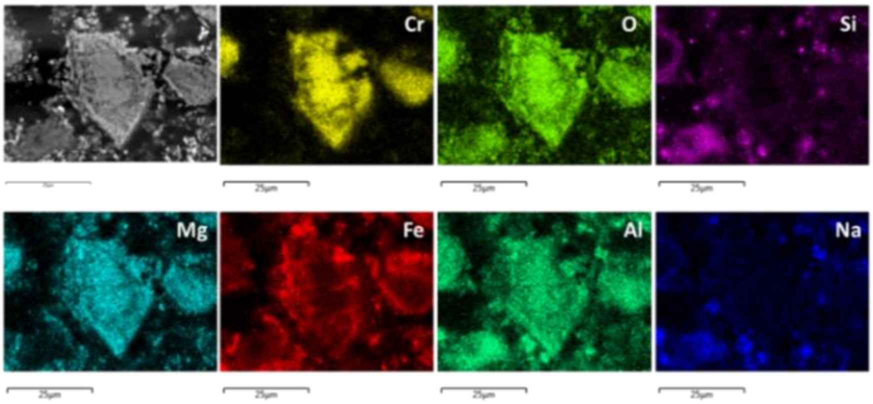

FIGURE 6-10. Backscattered SEM image and elemental distribution map obtained from energy dispersive X-ray analysis (EDX) of a leached residue particle after roasting of chromite with NaOH (Cr_2O_3:NaOH = 1:4, T = 1000°C, t = 2 hours, operating voltage = 20 kV).

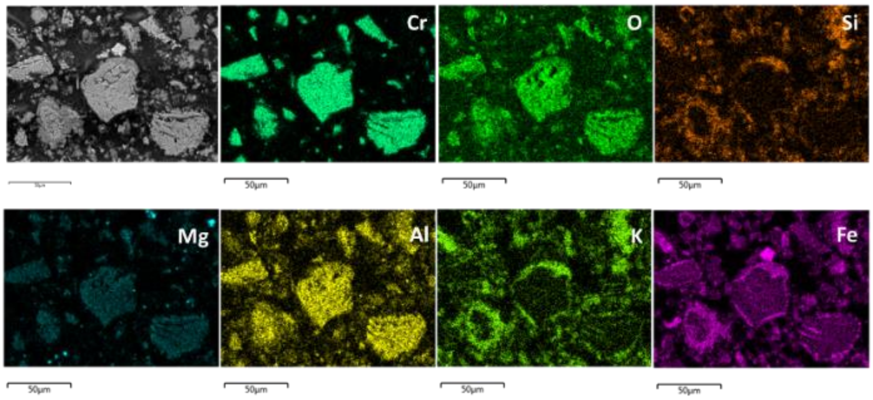

FIGURE 6-11. Backscattered SEM image and elemental distribution map obtained from energy dispersive X-ray analysis (EDX) of a leached residue particle after roasting of chromite with KOH (Cr_2O_3:KOH = 1:4, T = 1000°C, t = 2 hours, operating voltage = 20 kV).

When the molar ratio is increased to Cr_2O_3:KOH = 1:8, the water-leached residue is mainly composed of a Fe_3O_4-rich spinel phase which contains K and Si dissolved in it, which may correspond to the $Fe_{2.3}Si_{0.7}O_4$ phase identified in the XRPD patterns of FIGURE 6-9. This can be also seen in FIGURE 6-12, where a backscattered SEM image of a water-leached residue sample after roasting at 1000°C with Cr_2O_3:KOH = 1:8 is presented. Spectra at different areas were obtained by EDX and allow a comparison between the particle at the centre (spectra A and B) which corresponds to the Fe-K-Si-O phase; and the particle of unreacted chromite which can be seen at the left of the image (spectrum C).

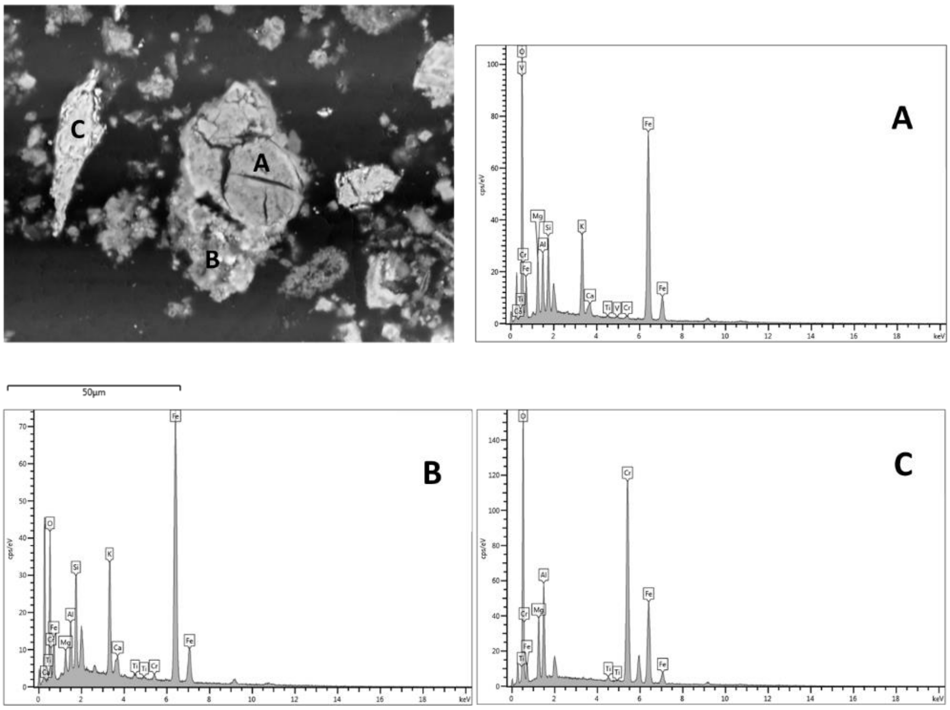

FIGURE 6-12. Backscattered SEM image and EDX spectra (A, B and C) of a leached residue particle after roasting of chromite with KOH (Cr_2O_3:KOH = 1:10, T = 1000°C and t = 2 hours, operating voltage = 20kV).

6.3.3. EFFECT OF THE ALKALI RATIO ON THE EFFICIENCY OF SODIUM CHROMATE EXTRACTION

The concentration of chromium in the solutions obtained from the water leaching stage was analysed by AAS technique. The values of %Cr extraction for each experiment, shown in FIGURE 6-13, were calculated by using equation (eq.7).

Excess alkali is expected to increase the extraction yield of chromium as a result of the following: a) equilibrium data in TABLE 6-3 shows the need for having higher Cr_2O_3:MOH than the stoichiometric in order to fully decompose the chromite spinel phase; b) excess alkali is necessary for neutralisation of alumina and silica and; c) phase diagrams in FIGURE 6-7 show that as the MOH concentration in the charge increases, the $Pp(O_2)$ required to form M_2CrO_4 decreases. This is in agreement with the experimental values of %Cr extraction presented in FIGURE 6-13, were the extraction of chromium increases with increasing Cr_2O_3:MOH molar ratio up to a value of 1:6. However, there is a decrease of the Cr^{6+} extraction when the molar ratio is increased above 1:6, which was predicted and may be explained by the fact that a higher amount of alkali in the charge increases the volume of molten salt phase present in the reaction mixture.

A higher volume of liquid represents an increase of the physical resistance to pore diffusion of gaseous species towards the reaction interface, and therefore, a decrease of the alkali chromate formation, as seen in FIGURE 6-13. The maximum sodium chromate extraction yields obtained were 91.1% and 88.51% when roasting chromite with NaOH and KOH (Cr_2O_3:MOH = 1:6), respectively.

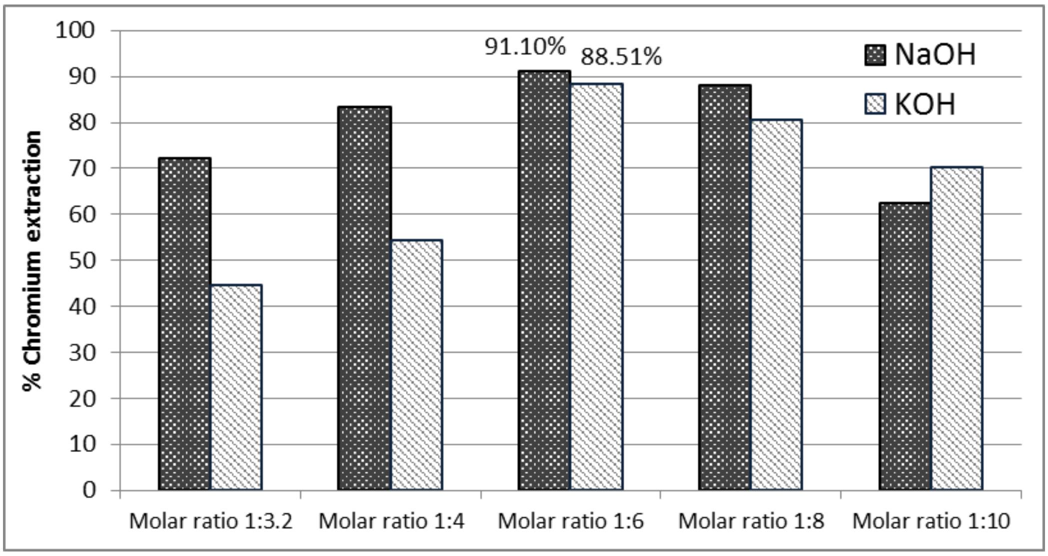

FIGURE 6-13. %Cr extraction after roasting of chromite at 1000°C with different Cr_2O_3:MOH ratios, followed by water leaching.

Chapter 7

REDUCTIVE ALKALI ROASTING OF CHROMITE ORES

Chapter content

The reductive alkali roasting of chromite ore is the key stage of the novel Cr^{6+}-free process. The physico-chemistry of the reduction reaction was studied by means of a number of batch reduction experiments in controlled oxygen-free atmosphere. The effect of process parameters, namely time, temperature, alkali ratio, carbon ratio, iron content and silica content, on the products of reaction and the microstructure of the reduced chromite was studied. XRPD and SEM-EDX were employed for characterisation of reduced samples. The kinetics of the reductive alkali roasting were studied by using experimental thermogravimetric data, and the mechanism of reduction was discussed based on the results presented.

Chapter conclusions

The effect of process parameters on the reduction of S.A. chromite ore including temperature, time, alkali ratio and carbon ratio was studied, and the best results were obtained for a chromite:Na_2CO_3:C weight ratio of 1:1:0.2, a temperature of 1050°C and a reduction time of 2.5 hours. The use of other sodium salts (NaOH, $NaHCO_3$, $NaHSO_4$) provided similar results to those achieved with Na_2CO_3. However, reduction with K_2CO_3 was not found successful since the metallic Fe did not form, and it is therefore needed to investigate further the reduction using potassium salts. Formation of $NaCrO_2$ was also achieved on the reduction of the Brazilian ores, but the metallisation of Fe observed was lower than in the case of S.A. chromite. Moreover, the alkali present reacted with silica forming complex silicate phases at high temperature.

The kinetic study suggests that the kinetics of the reaction can be described by the mixed model. The Ea of the reduction of S.A. and Brazilian chromite E4 are 217 kJ/mol and 205 kJ/mol for regime 1, and 211 kJ/mol and 177 kJ/mol for regime 2, respectively. The mechanism of the reductive alkali roasting has been discussed based on the experimental results presented.

7.1. FUNDAMENTALS OF ALKALI REDUCTION OF CHROMITE ORE

The alkali reduction of chromite ore in the presence of sodium carbonate (Na_2CO_3) and activated charcoal has been investigated. Chromite ores of different origin have been tested, and the effect of temperature, time, alkali addition and the use of other sodium salts such as NaOH, $NaHCO_3$ and $NaHSO_4$ have been studied and are presented in this chapter.

During alkali reduction, the iron oxide present in the spinel phase is reduced to metallic form (Fe), and the Cr_2O_3 in the ore reacts with Na_2CO_3 to form sodium chromite ($NaCrO_2$) as shown in (r.65).

$$FeCr_2O_4\ (s) + Na_2CO_3\ (s) + 2\ C\ (s) \rightarrow Fe\ (s) + 2\ NaCrO_2\ (s) + 3\ CO\ (g) \qquad (r.65)$$

As explained in the thermodynamic study in Chapter 5, the equilibrium reduction condition of chromite in the presence of alkali may be explained on the basis of the Na-Fe-Cr-O-C predominance area diagram reproduced in FIGURE 7-1.

It is apparent from this figure that metallic Fe co-exists with $NaCrO_2$ (area 4) at 1050°C (1323 K) for a range of partial pressures of CO and CO_2. Reduction of iron oxide takes place by shifting the equilibrium condition corresponding to area 1 to that in area 4, resulting in the decreasing value of $P(CO)_2$. $NaCrO_2$ is stable at these temperatures and reductive pressure conditions (high P(CO)), thereby ensuring that Cr^{6+} remains unstable. The partial pressure of CO_2 needs to be low for metallic iron to be formed. The formation of carbides is also possible, which has been reported before during carbothermic reduction of chromite in the absence of alkali salts [63,70,71].

Aluminium oxide from the ore also reacts with excess Na_2CO_3 to form water soluble sodium aluminate ($NaAlO_2$) as shown in (r.66). Part of the sodium may react with magnesium and silica to form complex sodium magnesium silicates. Magnesium oxide (MgO) and calcium carbonate ($CaCO_3$) may also present as products of reaction.

$$Al_2O_3\ (s) + Na_2CO_3\ (s) + C\ (s) \rightarrow 2\ NaAlO_2\ (s) + 2\ CO(g) \qquad (r.66)$$

The aim of the alkali reduction stage is to form an iron-rich metallic fraction and a non-metallic fraction containing sodium chromite, sodium aluminate and alkali silicates; which could be subsequently separated by magnetic separation. For an efficient magnetic separation, it is necessary to optimize the formation of metallic Fe by adjusting the operating parameters of the reduction process. The microstructure and phases present in reduced samples from the different experiments were characterised by XRPD and SEM techniques.

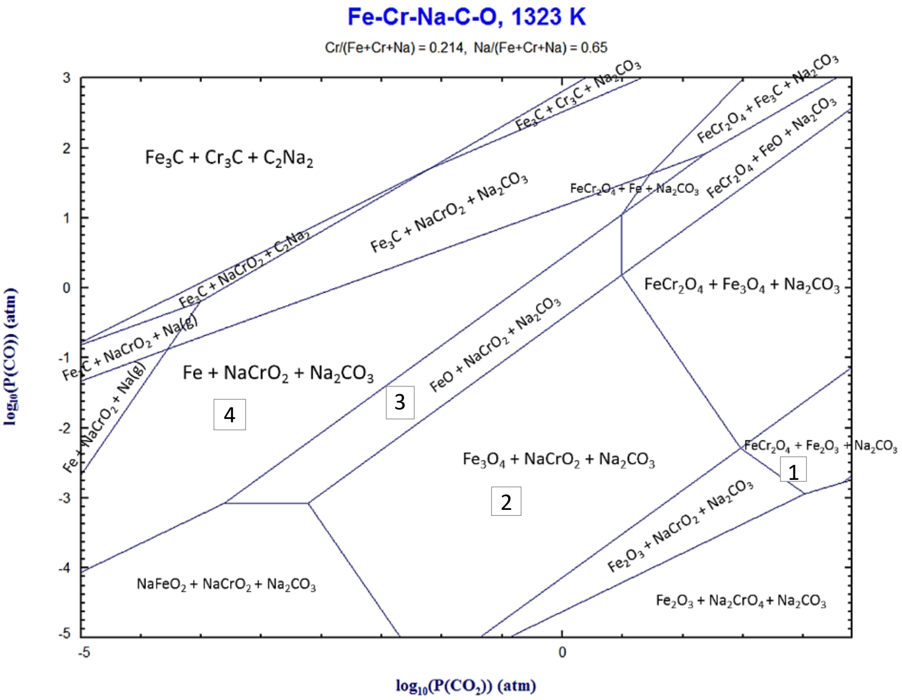

FIGURE 7-1. Predominance diagram of the system Na-Fe-Cr-O-C at 1323K (1050°C) calculated by Fact-Sage 6.4 software [46].

7.2. EFFECT OF PROCESS PARAMETERS ON THE CARBOTHERMIC REDUCTION OF S.A. CHROMITE ORE WITH SODIUM CARBONATE

7.2.1. EFFECT OF TEMPERATURE

Alkali reduction experiments were carried out at different temperatures in the range of 800°C to 1100°C. A weight ratio of chromite:Na_2CO_3:charcoal = 1:1:0.2 was used in this set of experiments. The reduction time was set up to 2.5 hours and argon gas with a flow rate of 2 L/min was used to maintain an inert atmosphere inside the furnace chamber. XRPD patterns of samples after reduction at different temperatures are presented in FIGURE 7-2.

At 800°C, unreacted chromite and sodium carbonate are the main phases present. Part of the iron oxide present in the ore was reduced at this temperature, but most of it is still forming part of the chromite spinel phase. Diffraction peaks of metallic Fe and $NaCrO_2$ have higher intensity at temperatures of 900°C and above, nevertheless, at 900°C unreacted chromite and sodium carbonate were still present. FIGURE 7-3a shows the microstructure of chromite particles after being reduced at 800°C and 900°C, respectively. In FIGURE 7-3b, the elemental mapping obtained by SEM-EDX indicates that the bright phase is metallic iron while the darker grey phase corresponds to partially reacted chromite phase. Therefore, no iron metal is present at 800°C while at 900°C the metallic phase can be identified.

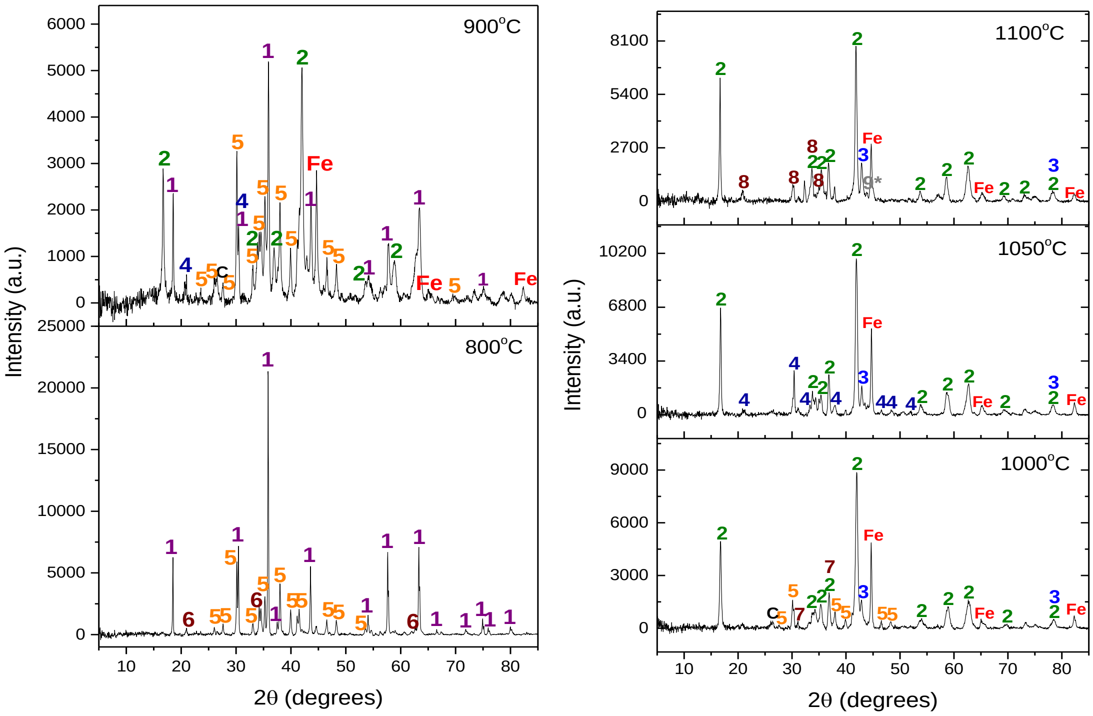

FIGURE 7-2. X-ray powder diffraction patterns of samples after reduction during 2.5 hours at temperatures 800°C, 900°C, 1000°C, 1050°C and 1100°C. Chromite: Na_2CO_3:charcoal weight ratio was constant and equal to 1:1:0.3 [1=$(Fe_{0.5}Mg_{0.5})(Cr_{0.73}Al_{0.27})_2O_4$, 2=$NaCrO_2$, 3=$MgO$, 4=$NaAlO_2$, 5=$Na_2CO_3$, 6=$Na_{0.87}Mg_{0.4}Al_{0.07}Si_{0.53}O_2$, 7=$(Fe,Mg)_2SiO_4$, 8=$Na_{1.8}Mg_{0.9}Si_{1.1}O_4$, 9*=$FeC_{0.045}$, Fe=metallic iron, C=carbon]

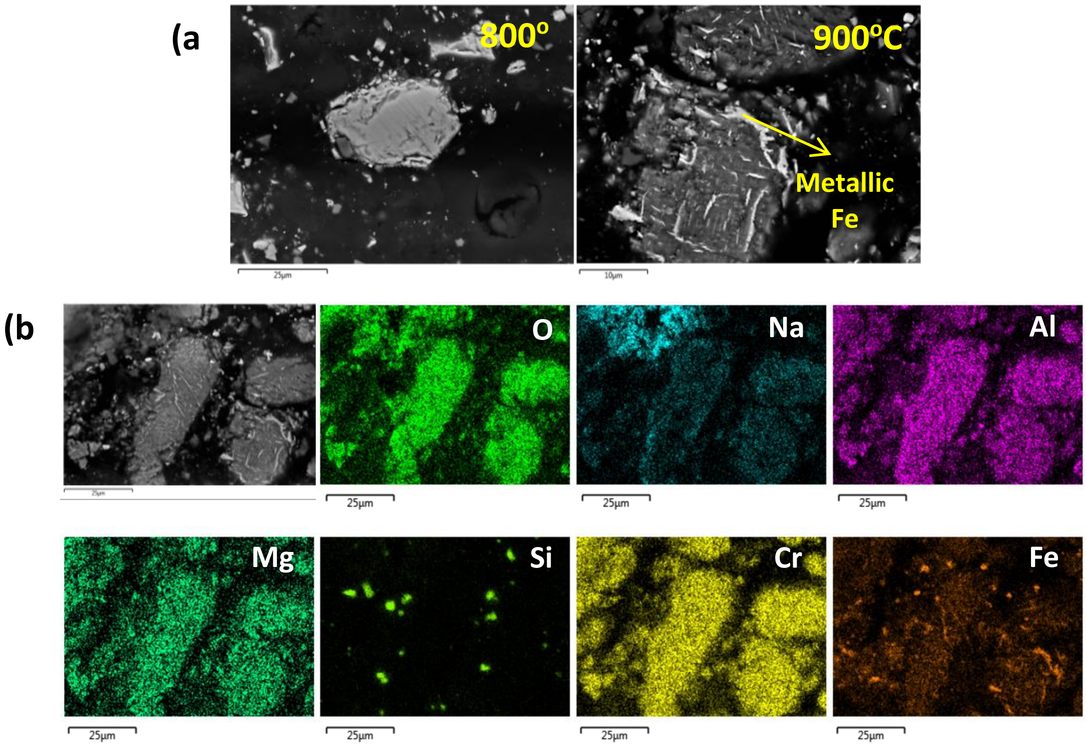

FIGURE 7-3. (a) Backscattered SEM images of chromite after reduction with Na_2CO_3 and activated charcoal at 800°C/900°C, and (b) Elemental mapping after reduction with Na_2CO_3 and C at 900°C.

FIGURE 7-3 shows how as iron reduction progresses, a Fe-rich metallic phase is developed in the form of fine needles trapped in the partially reacted chromite particles. At higher temperatures, the chromite phase could not be identified in the XRPD patterns FIGURE 7-2, being metallic Fe, $NaCrO_2$, $NaAlO_2$, MgO and complex silicates the major phases present. At 1050°C, most of the iron is in metallic form and larger Fe particles (bright phase) can be observed (FIGURE 7-4). Combining the phase analysis shown in FIGURE 7-2 and the elemental mapping in FIGURE 7-5, it can be concluded that darker grey particles are composed of Cr^{3+} and Al^{+3} combined with Na^{+} that diffuses inwards to form $NaCrO_2$ and $NaAlO_2$. Part of the magnesium oxide diffuses out to form a MgO-rich rim and the rest of it combines with silica to form complex silicates.

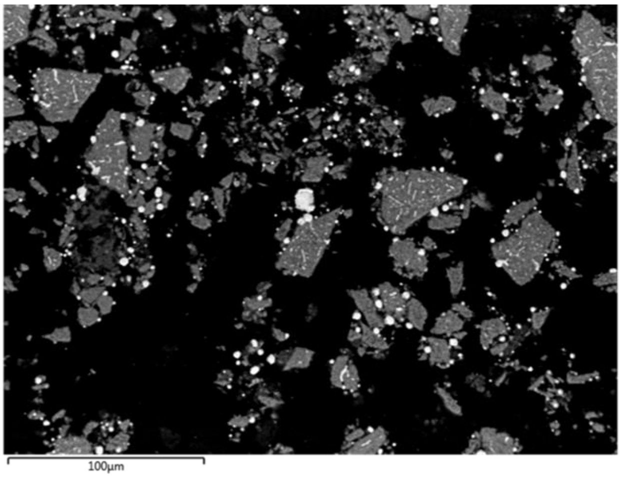

FIGURE 7-4. Backscattered SEM images of chromite particles after reduction with Na_2CO_3 and activated 0charcoal at 1050°C (weight ratio chromite:Na_2CO_3:C=1:1:0.2)

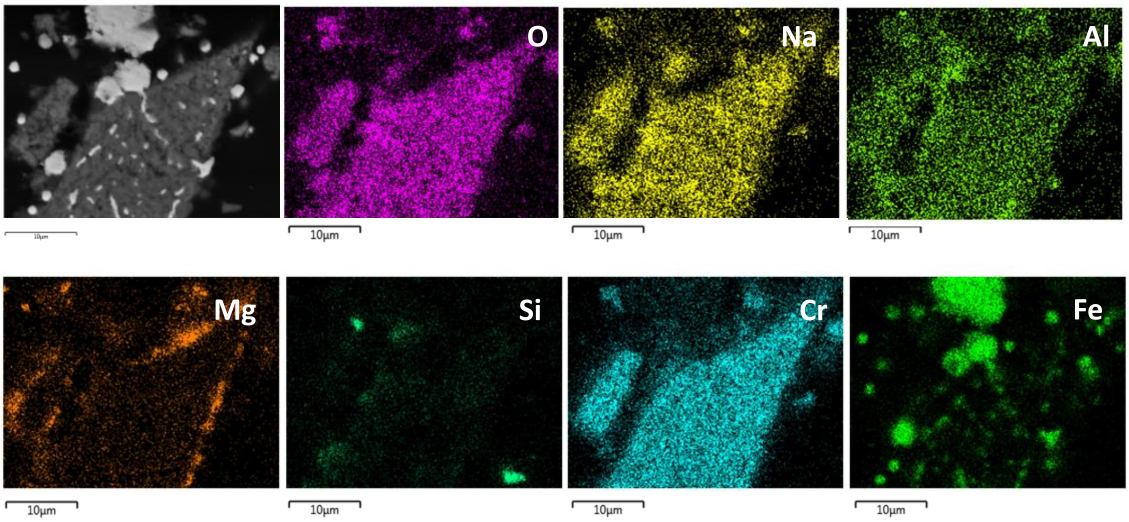

FIGURE 7-5. Elemental mapping of chromite sample reduced with carbon and sodium carbonate at 1050°C.

7.2.2. EFFECT OF TIME

The progress of the reaction has been studied by carrying out reduction experiments of chromite with Na_2CO_3 and activated charcoal at 1050°C during different reduction times (15 minutes, 30 minutes, 1 hour, 1.5 hours, 2.5 hours, 3.5 hours and 6 hours). The charge mixture had a weight ratio of chromite:Na_2CO_3:charcoal = 1:1:0.2 and the argon flow rate was set up at 2 L/min. XRPD patterns of reduced samples are presented in FIGURE 7-6.

XRPD peaks for metallic iron can be observed after 15 minutes of reaction, which indicates that reduction of iron oxide in chromite to metallic form occurs rapidly at a temperature of 1050°C. This was also reported in previous investigations [12] of carbothermic reduction of chromite for ferrochromium production at high temperatures (1350°C-1500°C). It is confirmed by the SEM analysis of the sample after only 15 minutes reduction presented in FIGURE 7-7.

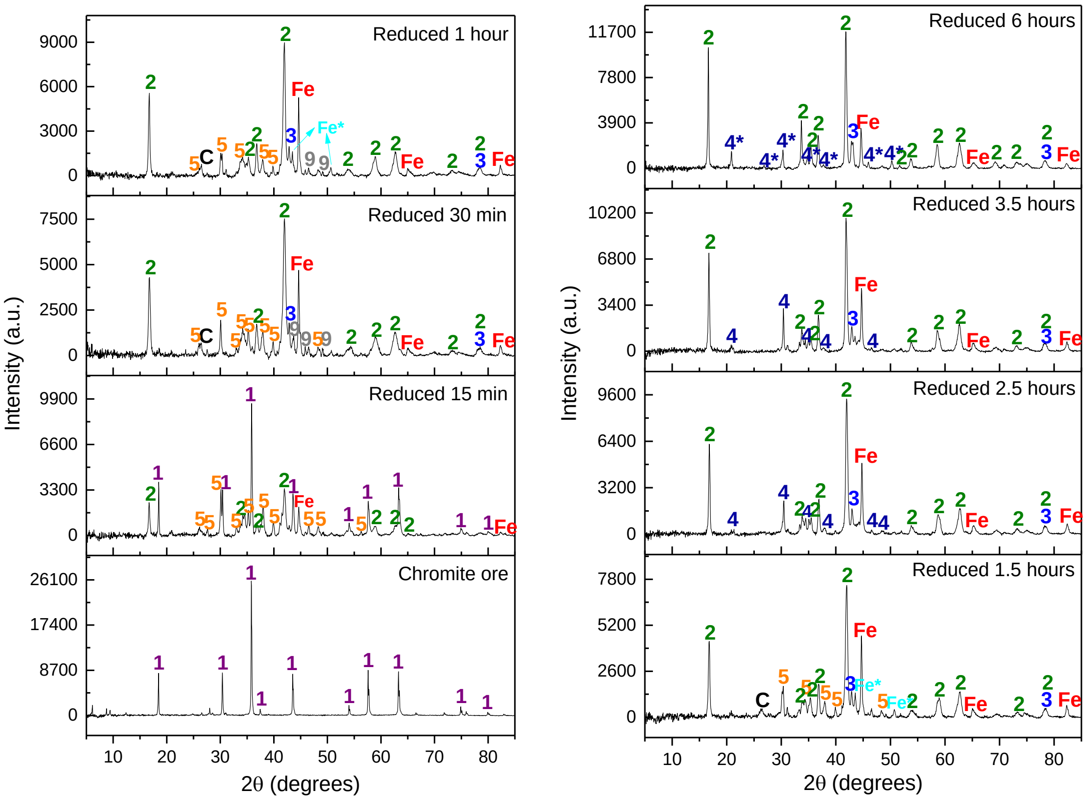

FIGURE 7-6. X-ray powder diffraction patterns of as-received chromite and reduced samples after reduction at 1050°C with weight ration chromite:Na_2CO_3:charcoal=1:1:0.2 for different times (15 minutes, 30 minutes, 1 hour, 1.5 hours, 2.5 hours, 3.5 hours and 6 hours). [1=$(Fe_{0.5}Mg_{0.5})(Cr_{0.73}Al_{0.27})O_4$, 2=$NaCrO_2$, 3=MgO, 4=$NaAlO_2$, 4*=$Na_{1.95}Al_{1.95}Si_{0.05}O_4$, 5=$Na_2CO_3$, 9=$Fe_3C$, Fe/Fe*=α/γ metallic iron, C=carbon]

As reaction proceeds, metallic iron appears in the form of fine needles inside chromite particles, and it can be observed in FIGURE 7-7 how iron particles start clustering and growing with time. Eventually, they may separate from reacted chromite and form round metallic particles, which is the preferred form for subsequent magnetic separation. The metallic iron predominantly formed during reduction is ferrite (α-Fe), however, formation of austenite (γ-Fe) can be observed at 1 and 1.5 hours. The differentiation of α-Fe and γ-Fe is feasible by XRPD technique since both phases are allotropes of metallic iron with different crystal structure. The possible crystal structures of metallic iron as a function of the temperature and at standard pressures have been summarised in TABLE 7-1. According to the table, FCC γ-Fe is the allotrope formed at the operating temperatures, between 950°C and 1050°C. However, since samples where cooled by just exposing them to ambient temperature, γ-Fe should transform to BBC α-Fe during the cooling process. α-Fe is the predominant and desirable form since it has the best magnetic properties; and therefore, any γ-Fe or paramagnetic α-Fe should be avoided so as to improve the efficiency of the succeeding magnetic separation stage.

TABLE 7-1. Allotropes of metallic Fe as a function of temperature at standard pressures [117].

Allotrope	Temperature stability range	Crystal structure	Magnetic properties
Ferrite (α-Fe)	Room T – 771°C	Body-centred cubic	Ferromagnetic
Ferrite (α -Fe)	771°C – 912°C	Body-centred cubic	Paramagnetic
Austenite (γ-Fe)	912°C – 1394°C	Face-centred cubic	Non-magnetic

Not all metallic iron is able to separate even after 6 hours reaction, being some of it still trapped in the internal cracks formed in the reacted chromite particles. This negatively affects the efficiency of magnetic separation due to $NaCrO_2$ particles being retained with the magnetic fraction as a consequence of iron staying trapped inside, which makes it more difficult to separate magnetic and non-magnetic phases.

Formation of $NaCrO_2$ can be also seen after 15 minutes of reaction. After 30 minutes, unreacted chromite cannot be identified in XRPD pattern in FIGURE 7-6. When reduction is carried out during 2.5, 3.5 or 6 hours, the main phases present are $NaCrO_2$, Fe, MgO and $NaAlO_2$. Based on this, 2.5 hours has been chosen as the optimum roasting time.

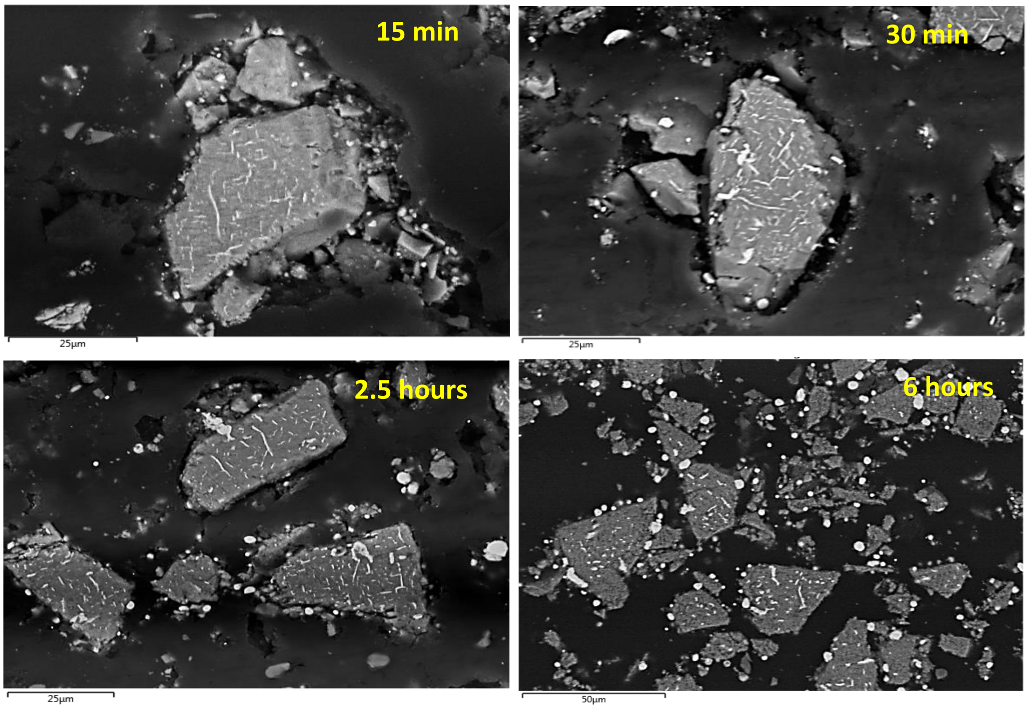

FIGURE 7-7. Backscattered SEM images of chromite after reduction with Na_2CO_3 and activated charcoal at 1050°C during 15 min, 30 min, 2.5 hand 6 h (wt. ratio chromite:Na_2CO_3:C = 1:1:0.2).

7.2.3. EFFECT OF Na_2CO_3 RATIO

According to equations (r.48) to (r.51) the stoichiometric amount of Na_2CO_3 needed to form $NaCrO_2$ and $NaAlO_2$ is 4.61 g of sodium carbonate for every 10 g of chromite ore, taking into account that the wt.% of Cr_2O_3 and Al_2O_3 in the ore are 44.60% and 14.43%, respectively. This represents a stoichiometric weight ratio of chromite:Na_2CO_3 equal to 1:0.46. However, sodium oxide also reacts with silica to form complex silicates and therefore excess sodium oxide is required. Different chromite:Na_2CO_3 ratios were tested, keeping the chromite:charcoal ratio constant to 1:0.2, and temperature, time and argon flow at 1050°C, 2.5 h and 2 L/min. Reduced samples were characterised by XRPD (FIGURE 7-8).

For reduction with weight ratios of chromite:Na_2CO_3 equal to 1:0.46 and 1:0.50, sodium chromite and metallic iron were formed. However, in the XRPD pattern in FIGURE 7-8 it can be seen that peaks for $MgCr_2O_4$/$MgFe_2O_4$ spinels have high intensity. The spinel phase did not react to a high extent and can be due to lack of sodium oxide as part of it is consumed by silica to form complex Na and Mg silicates. The formation of carbides is also observed in these two samples. For higher ratios, the spinel phase is not present, and for chromite:Na_2CO_3=1:1 the main phases present are Fe, $NaCrO_2$, $NaAlO_2$ and MgO. Thus, the results indicate that excess Na_2O promotes the formation of sodium chromite and helps the segregation of phases.

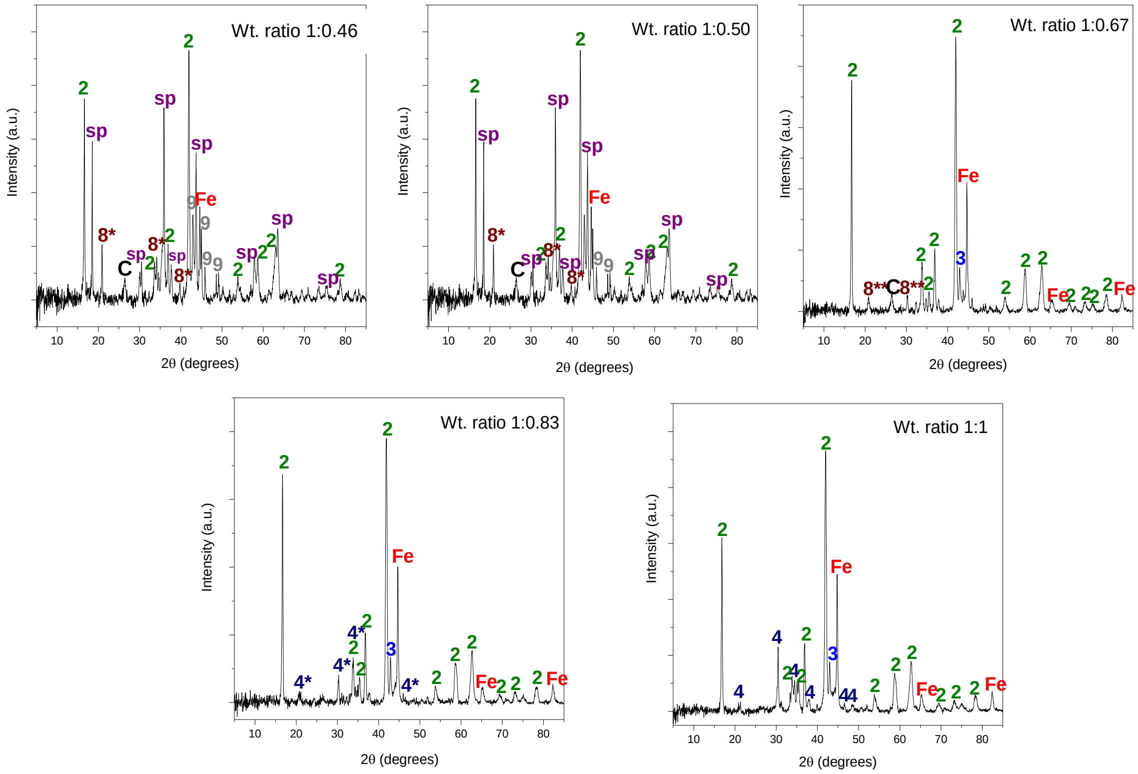

Figure 7-8. X-ray powder diffraction patterns of chromite samples after reduction at 1050ºC for 2.5 hours using different chromite:Na_2CO_3 weight ratios (1:0.46, 1:0.5, 1:0.67, 1:0.83 and 1:1). Chromite:charcoal weight ratio was kept constant at 1:0.2. [sp= $MgCr_2O_4$/$MgFe_2O_4$, 2=$NaCrO_2$, 3=MgO, 4=$NaAlO_2$, 4*=$Na_{1.95}Al_{1.95}Si_{0.05}O_4$, 8*= $Na_2Mg_2Si_2O_7$, 8**= $Na_2Mg_2Si_2O_7$, 9=Fe_3C, Fe=metallic iron, C=carbon]

The SEM images of chromite samples reduced with chromite:Na_2CO_3 weight ratios of 1:0.46, 1:0.67 and 1:1 are presented in Figure 7-9. Areas a-e were analysed by SEM-EDX so as to compare the chemical composition of the iron-rich metallic phase formed in samples reduced with different chromite:Na_2CO_3 weight ratios. Results presented in Table 7-2 show that Cr can dissolve into metallic Fe, being the wt.% of Cr lower as the amount of Na_2CO_3 in the initial mixture increases. This means that excess Na_2CO_3 is also necessary if the concentration of Cr in the metallic alloys needs to be minimised. Even in the case of the highest chromite:Na_2CO_3 weight ratio tested, the overall wt.% of Cr in iron metal found is 3%-5%.

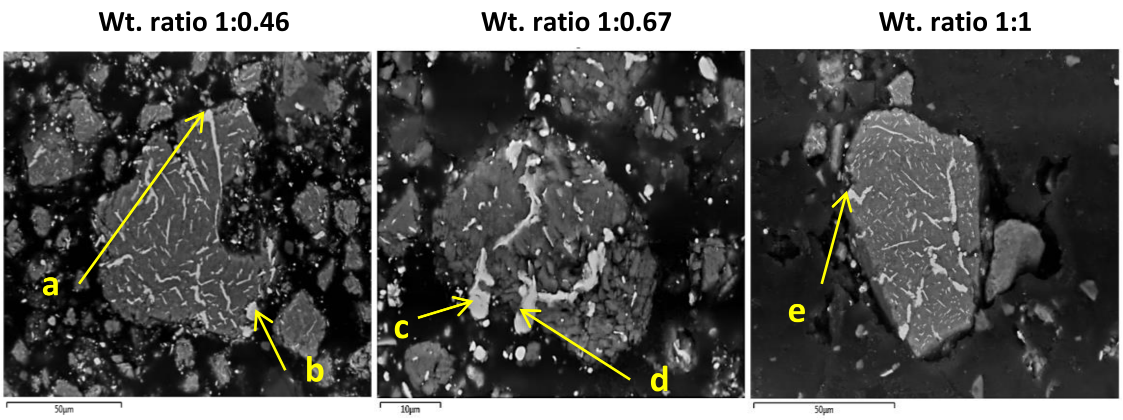

FIGURE 7-9. Backscattered SEM images of reduced chromite samples at 1050°C for 2.5 hours with three different chromite:Na_2CO_3 weight ratios (1:0.46, 1:0.67 and 1:1). Chromite:charcoal wt. ratio = 1:0.2.

TABLE 7-2. Chemical composition of areas a-e in FIGURE 7-9 analysed by SEM-EDX

	a	**B**	**c**	**d**	**e**
Chromite:Na_2CO_3 wt. ratio	1:0.46		1:0.67		1:1
wt.% Fe	87.2	84.6	95.9	95.7	95.2
wt.% Cr	12.8	15.4	4.1	4.3	4.8

The mass balance experiments shown in Chapter 9 were carried out using a weight ratio of chromite:Na_2CO_3:charcoal equal to 1:1:0.2 considering the results presented in this section. However, the excess sodium oxide corresponding to this weight ratio is considerably high, and therefore further optimization of the Na_2CO_3 amount required for reductive alkali roasting is needed.

7.2.4. EFFECT OF ACTIVATED CHARCOAL RATIO

The effect of carbon on the reduction of chromite in the presence of sodium carbonate was studied by carrying out reduction experiments with different chromite:charcoal weight ratios. The weight ratio of chromite:Na_2CO_3 was constant for all the experiments and equal to 1:1, temperature was fixed at 1050°C and samples were reduced for 2.5 hours. Weight ratios of chromite:charcoal equal to 6:4, 6:3, 6:2.5, 6:2, 6:1.8, 6:1.5, 6:1 and 6:0.5 were tested. XRPD patterns of the reduced samples are presented in FIGURE 7-10.

The reduction of iron is not complete when a chromite:charcoal weight ratio of 6:0.5 is used. However, when this ratio is increased up to 6:2, a better iron reduction is achieved.

This was also confirmed by SEM analysis. Above 6:2, the formation of metallic iron starts decreasing again. This might be due to an alteration of the CO/CO_2 ratio. The formation of $NaCrO_2$ is observed for all different ratios, and the formation of Na and Mg silicates and (Ca,Mg)CO_3 increases when the ratio of carbon is high (6:2 and above). According to the results obtained, the chromite:charcoal weight ratio should be in the range of 6:1.2 to 6:1.5.(corresponding to a ratio of 1:0.2 to 1:0.25).

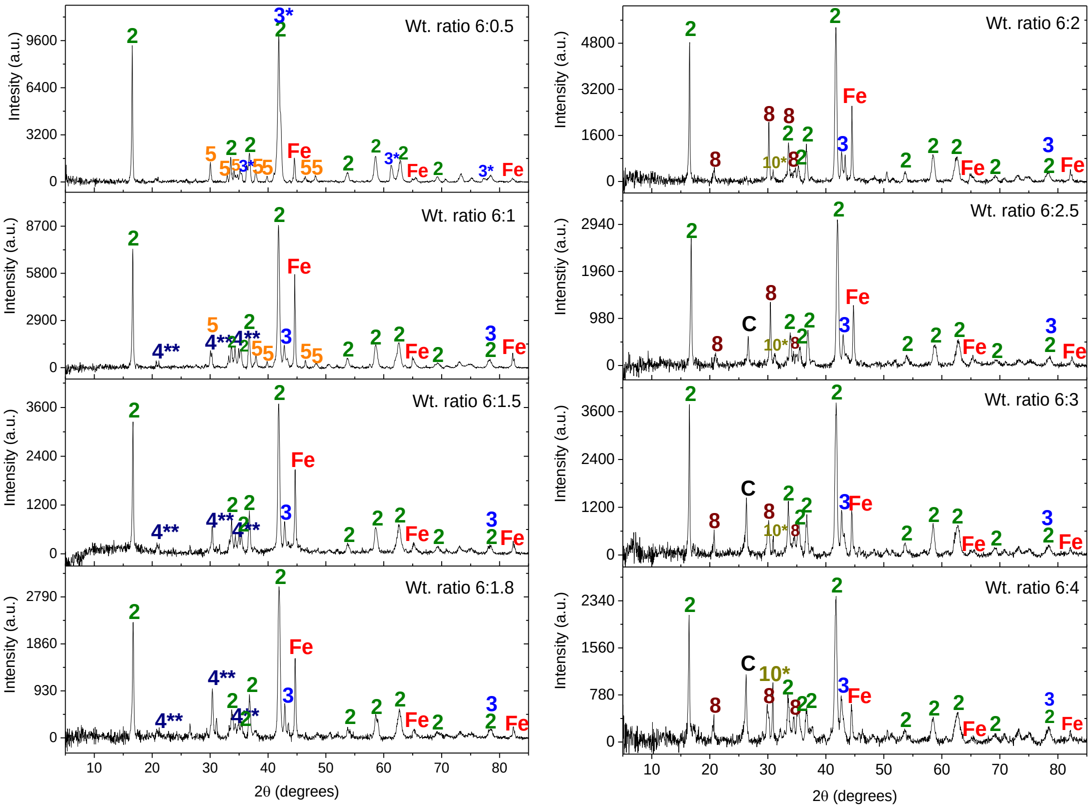

FIGURE 7-10. X-ray powder diffraction patterns of chromite samples after reduction at 1050°C for 2.5 hours using different chromite:charcoal weight ratios. Chromite:Na_2CO_3 weight ratio = 1:1 [2=$NaCrO_2$, 3=MgO, 3*=(Mg,Fe)O, 4**=$Na_{1.5}AlSiO_{4.25}$, 5=Na_2CO_3, 8= $Na_{1.8}Mg_{0.9}Si_{1.1}O_4$, 10*=(Ca,Mg)CO_3, Fe=iron, C=carbon]

7.2.5. EFFECT OF A FINAL HIGH TEMPERATURE STAGE

As it will be shown in Chapter 8, the main limitation of the magnetic separation of reduced samples is the entrapment of metallic iron particles in the $NaCrO_2$ phase. With the aim of increasing the size of the metallic phase and promote its segregation, an increase of the reaction temperature of the final stage of the reduction was studied. In this set of experiments, the reaction time was kept at 2.5 hours, with a reaction temperature of 1050°C during the first 1.5 hours and 1200 °C or 1300 °C during the last hour.

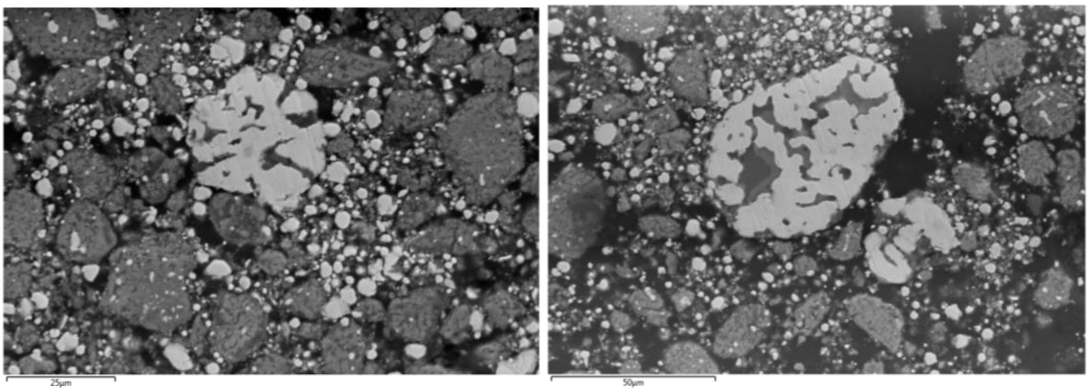

Figure 7-11. Scanning electron microscopy images of a S.A chromite ore sample reduced with Na_2CO_3 and carbon at 1050°C for 1.5 hours and 1200°C for 1 hour. The wt.ratio chromite:Na_2CO_3:C = 1:1:0.2.

SEM analysis in Figure 7-11 shows that the last high temperature stage at 1200°C achieved the growth of iron particles by promoting the clustering of the metallic phase. The effect of temperature can be observed in the size and shape of the metallic particles formed. The needle-type iron particles previously observed trapped in the fully-reacted chromite particles cannot be identified in this sample. Most of the particles present in the sample are now round-shaped, and few bigger particles of 25-50 μm were identified.

An identical behaviour can be observed in the sample heated at 1300°C as seen in Figure 7-12 and Figure 7-13. Bigger rounded particles were formed in this sample and a greater separation of the metallic phase is clear. Furthermore, the non-magnetic phase containing the $NaCrO_2$ formed presents segregation of two different phases. Elemental mapping and point ID analysis using EDX were carried out in order to identify the phases formed during the higher temperature stage, and the results are shown in Figure 7-14.

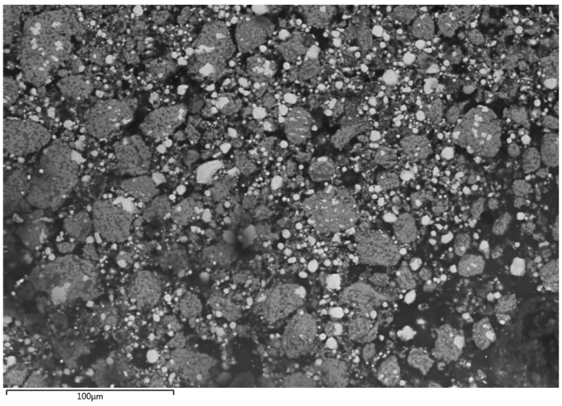

Figure 7-12. Scanning electron microscopy image of a S.A chromite ore reduced with Na_2CO_3 and carbon at 1050°C for 1.5 hours and 1300°C for 1 hour. The wt.ratio chromite:Na_2CO_3:C = 1:1:0.2.

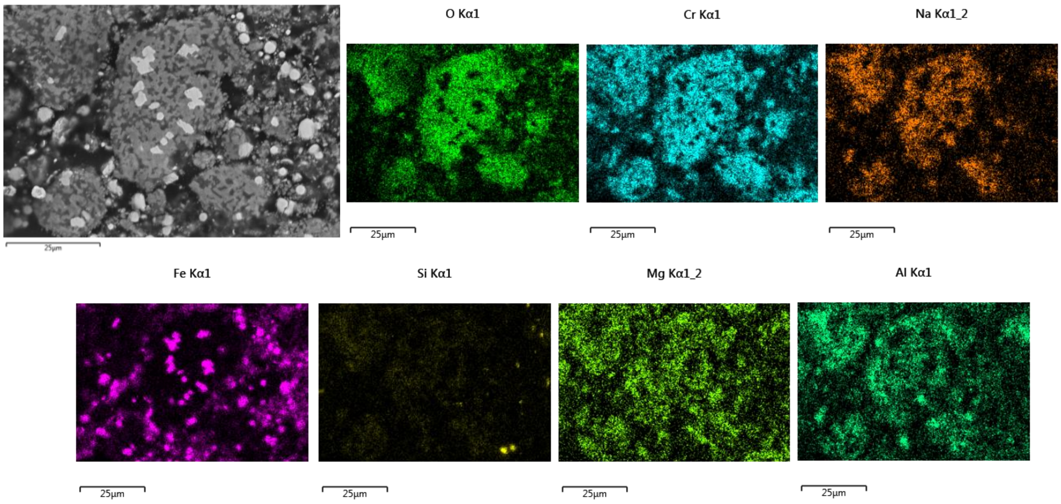

FIGURE 7-13. Scanning electron microscopy image and elemental mapping of a S.A chromite ore reduced with Na_2CO_3 and carbon at 1050°C for 1.5 hours and 1300°C for 1 hour. The chromite:Na_2CO_3:C weight ratio used was 1:1:0.2.

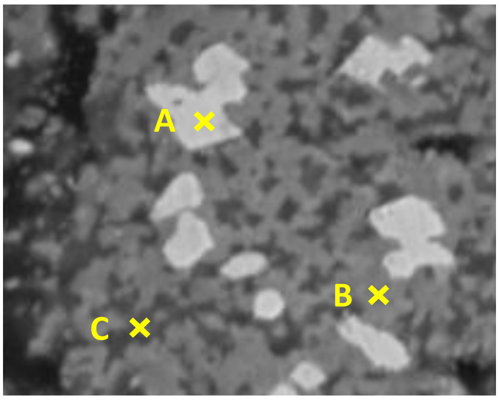

Wt.%	A	B	C
Cr	4.2	48.5	28.8
Fe	95.7	7.9	3.3
O		24.6	29.9
Al		3.5	15.3
Mg		6	3.0
Na		6.8	13.1
Si	0.2		5.4

FIGURE 7-14. Zoomed-in area of the backscattered SEM image in FIGURE 7-13, and point&ID EDX analysis of points A, B and C.

The higher magnification image in FIGURE 7-14 illustrates the phase segregation mentioned before. Point A corresponds to the metallic phase rich in Fe (95.7 wt.%) which also contains 4.2 wt.% Cr and traces of Si (0.2 wt.%). Point B and C are the non-magnetic phases. Chromium is more concentrated in particle B; while particle C is richer in aluminium and contains 5.4 wt.% silica.

The growth of magnetic particles and the phase segregation observed may improve the efficiency of magnetic separation and decrease the intensity of grinding. Separation of magnetic and non-magnetic fractions will be shown in a following chapter.

7.3. CARBOTHERMIC REDUCTION OF SOUTH AFRICAN CHROMITE ORE IN THE PRESENCE OF DIFFERENT ALKALI SALTS MIXTURES

Addition of mixtures of Na_2CO_3 and different sodium salts (NaOH, $NaHCO_3$ and $NaHSO_4$) were tested during reduction of chromite with activated charcoal. All reduction experiments were carried out at 1050°C during 2.5 hours in argon atmosphere (2 L/min).

7.3.1. Na_2CO_3 AND NaOH MIXTURES

Mixtures of 25% NaOH, 50% NaOH and 75% NaOH with Na_2CO_3 were used. Reduced samples were analysed by XRPD and the patterns obtained are presented in FIGURE 7-15. The chromite:alkali:charcoal used was 1:1:0.2. XRPD patterns show that the main phases obtained after reduction are metallic iron, sodium chromite, sodium aluminate and magnesium oxide.

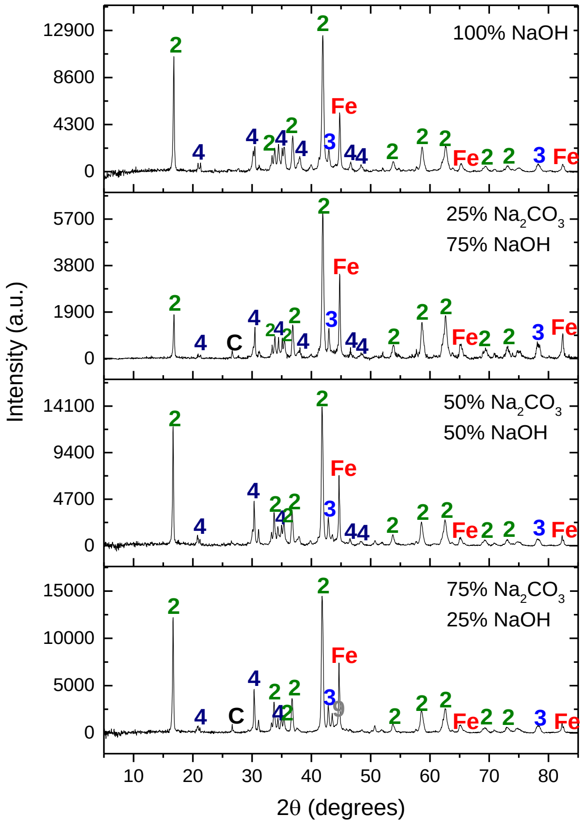

FIGURE 7-15. XRPD patterns of reduced chromite at 1050°C for 2.5 hours using mixtures of Na_2CO_3 and $NaHCO_3$ as alkali source. Weight ratio of chromite:alkali:charcoal = 1:1:0.2. [2=$NaCrO_2$, 3=MgO, 4=$NaAlO_2$, 9=Fe_3C, Fe=metallic iron and C=carbon]

According to the thermodynamic study presented in Chapter 5, free energy values for alkali reduction with Na_2CO_3 and NaOH are very similar and XRPD results show that there are not significant differences between reduced samples when NaOH is added. Reduced samples were also analysed by SEM but no differences were found in the microstructure of the particles compared to samples roasted using just Na_2CO_3. This differs to what it was observed in previous investigations of oxidative alkali roasting of chromite [26], which indicated that replacement of Na_2CO_3 by NaOH has beneficial effects in the chromium extraction yield, when treating chromite with alkali in oxidising atmosphere.

7.3.2. Na_2CO_3 AND $NaHCO_3$ MIXTURES

In this set of experiments, Na_2CO_3 was replaced by $NaHCO_3$ in different weight proportions, obtaining mixtures of 10% $NaHCO_3$, 25% $NaHCO_3$ and 50% $NaHCO_3$ with Na_2CO_3. An experiment using just $NaHCO_3$ as alkali source was also carried out, and for all samples the weight ratio chromite:alkali:charcoal was equal to 1:1:0.2. The XRPD analysis of the reduced samples was carried out and the patterns obtained can be seen in FIGURE 7-16.

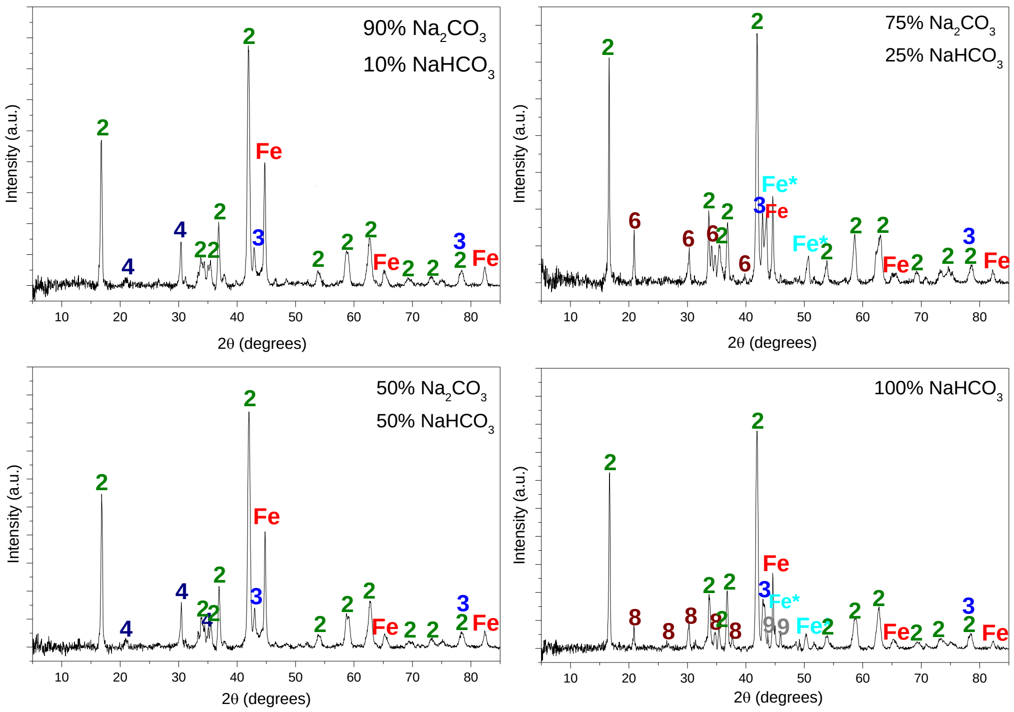

FIGURE 7-16. X-ray powder diffraction patterns of chromite samples after reduction at 1050°C for 2.5 hours using mixtures of Na_2CO_3 and $NaHCO_3$ as alkali source. Chromite:alkali:charcoal = 1:1:0.2. [2=$NaCrO_2$, 3=MgO, 4=$NaAlO_2$, 6=$Na_{0.87}Mg_{0.4}Al_{0.07}Si_{0.53}O_2$, 8= $Na_{1.8}Mg_{0.9}Si_{1.1}O_4$, 9=$Fe_3C$, Fe/Fe*=α/γ metallic iron].

When using mixtures with 10% and 50% $NaHCO_3$, the XRPD patterns were very similar with clear peaks for iron, $NaCrO_2$, $NaAlO_2$ and MgO. The formation of γ-iron can be observed in two of the samples. Na-Al-Mg complex silicates were observed when roasting with a mixture of 25% $NaHCO_3$ + 75% Na_2CO_3 and with just 100% $NaHCO_3$. Looking at SEM images in FIGURE 7-17, when $NaHCO_3$ is present the formation of metallic iron occurs in the manner explained before. The metallic phase appears and remains trapped inside sodium chromite particles. However, reduction with $NaHCO_3$ is thermodynamically more favourable than Na_2CO_3 and thus, the addition of sodium bicarbonate should be investigated in more detail.

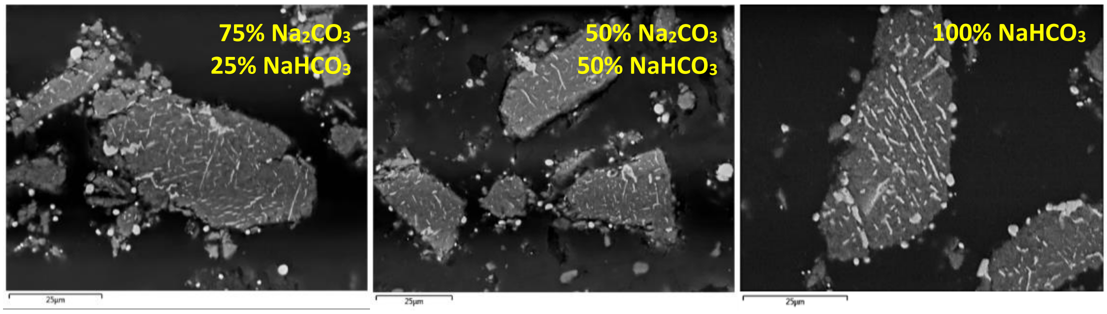

FIGURE 7-17. Backscattered SEM images of reduced chromite at 1050°C for 2.5 hours with different Na_2CO_3 and $NaHCO_3$ mixtures. Chromite:alkali:charcoal weight ratio was kept constant at 1:1:0.2.

7.3.3. Na_2CO_3 AND $NaHSO_4$ MIXTURES

The effect of $NaHSO_4$ on alkali reduction of chromite was tested using mixtures of Na_2CO_3 and $NaHSO_4$ as alkali source. Experiments with 10%, 25% and 50% $NaHSO_4$ mixtures were carried out and pure $NaHSO_4$ was also tested. Reduced samples were analysed by XRPD, and the results are presented in FIGURE 7-18. The weight ratio chromite:alkali:charcoal was equal to 1:1:0.2. In this case, the addition of $NaHSO_4$ has a significant effect on the phases formed during reduction, being this effect more negative as the quantity of $NaHSO_4$ in the mixture increases. FIGURE 7-18 shows that with increasing $NaHSO_4$ ratio in the mixture the intensity of metallic iron decreases, while the intensity of a spinel phase identified as $MgFe_2O_4$ gets stronger.

When just $NaHSO_4$ is added, the formation of both metallic iron and sodium chromite is very poor, being the main phase found $Fe_{0.42}Mg_{0.58}Cr_{1.52}Al_{0.48}O_4$. However, with low additions of $NaHSO_4$, especially with a mixture of 90% Na_2CO_3 + 10% $NaHSO_4$, the formation of iron seems to be favoured. In backscattered SEM images in FIGURE 7-19, it can be observed the formation of larger metallic iron particles in the presence of $NaHSO_4$.

This means that sulphur might promote the growth of metallic iron and therefore have a beneficial effect on later magnetic separation. The effect of sodium bisulfate needs to be further understood with the aim of enhancing the growth of iron so that magnetic separation is more efficient and less intensive grinding is needed.

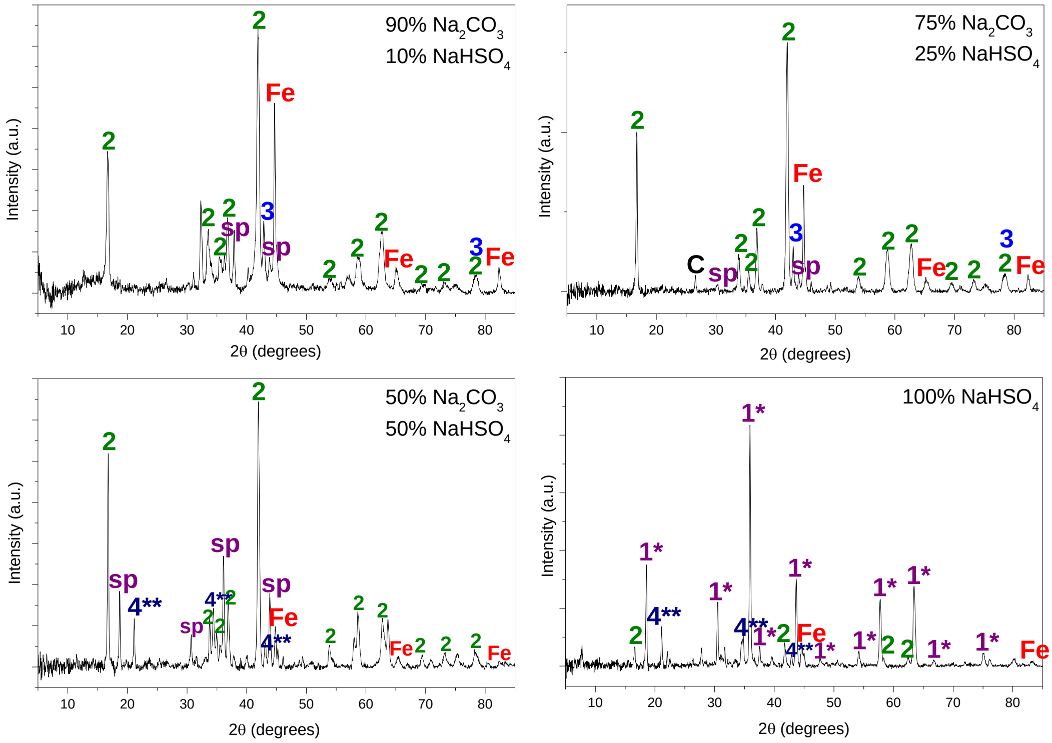

FIGURE 7-18. X-ray powder diffraction patterns of chromite samples after reduction at 1050°C for 2.5 hours, with chromite:charcoal=1:0.3 and using mixtures of Na_2CO_3 and $NaHSO_4$ as alkali source [sp=$MgFe_2O_4$, 1*=$Fe_{0.42}Mg_{0.58}Cr_{1.52}Al_{0.48}O_4$, 2=$NaCrO_2$, 3=MgO, 4**=$Na_{1.5}AlSiO_{4.25}$, Fe=metallic iron and C=carbon]

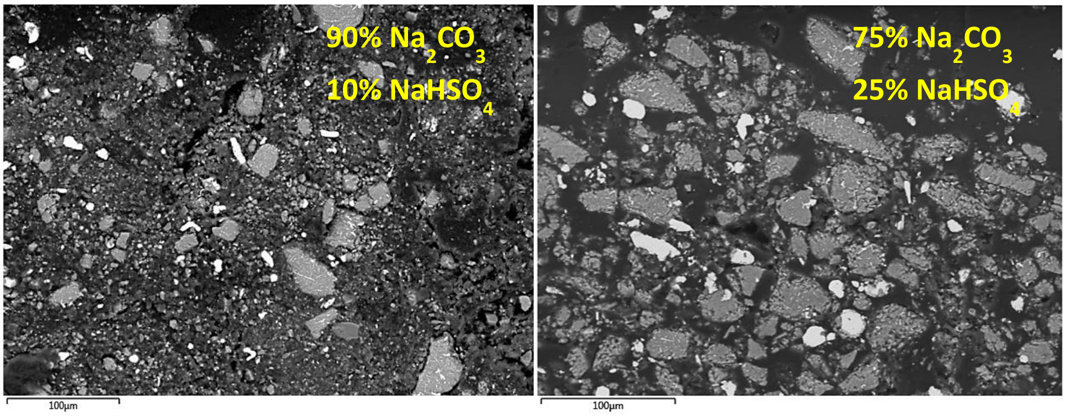

FIGURE 7-19. Backscattered SEM images of reduced chromite samples at 1050°C for 2.5 hours with different Na_2CO_3 and $NaHSO_4$ mixtures. Chromite:charcoal weight ratio was kept constant at 1:0.2

7.3.4. CARBOTHERMIC REDUCTION OF CHROMITE WITH POTASSIUM CARBONATE

Studies on the alkali roasting of chromite and ilmenite ores in oxidative atmosphere [24,25,118] have reported that potassium salts have similar behaviour to that of sodium salts. The physical-chemistry was compared, and it was reported similar extraction yield with both type of salts.

Alkali reduction experiments with potassium carbonate were carried out at the same experimental conditions than the experiments with Na_2CO_3 and following the same reduction procedure. Reductive roasting of S.A. chromite ore with K_2CO_3 and activated charcoal was performed at 1050°C, for 2.5 hours and using the stoichiometric, 150% the stoichiometric and 200% the stoichiometric K_2CO_3 addition. The XRPD patterns of reduced samples are shown in FIGURE 7-20.

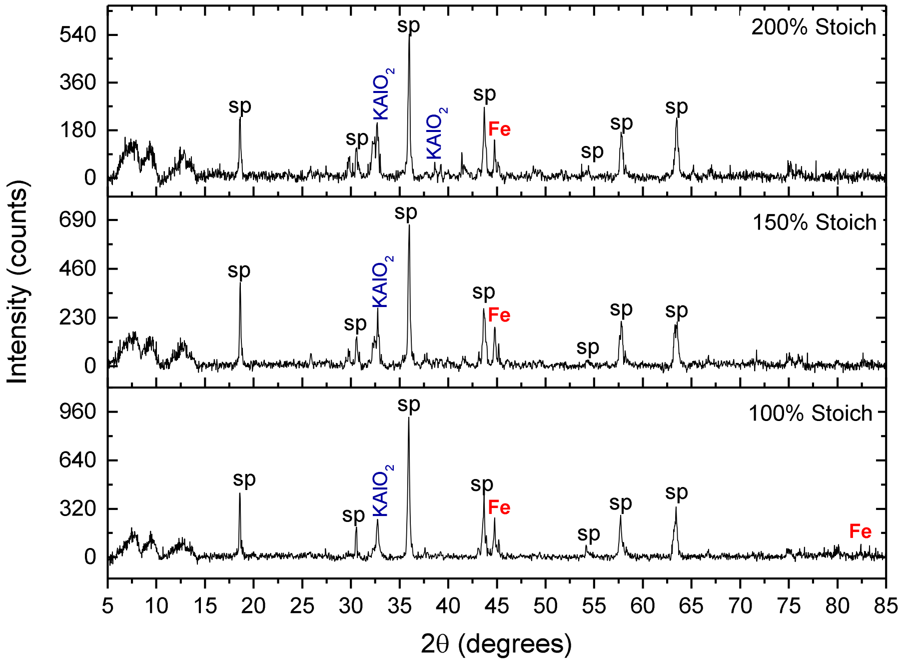

FIGURE 7-20. XRPD patterns of S.A. chromite ore reduced with K_2CO_3 and activated charcoal at 1050°C for 2.5 hours [sp=chromite spinel phase, Fe=metallic iron and $KAlO_2$].

The XRPD patterns show that the spinel was not fully decompose, and Cr^{3+} was not extracted from the chromite material as $KCrO_2$. $KAlO_2$ and metallic iron were formed, but the XRPD peaks for Fe have low intensity, which suggests that metallisation is not complete.

The reduced chromite samples were also characterised by SEM-EDX analysis. Lower and higher magnification images of a reduced sample can be seen in FIGURE 7-21.

The images show brakeage of the chromite ore particles by reaction with K_2CO_3. Image (b) shows how the chromite particles disintegrated into smaller particles. The SEM-EDX elemental maps show that partial reduction of iron took place, and iron appears more concentrated in some areas or particles. However, the Fe particles are very small and did not manage to cluster over the reaction time. Magnetic separation of this reduced sample was carried out, but no separation of magnetic and non-magnetic fractions was achieved. The different K_2CO_3 additions tested provided identical results.

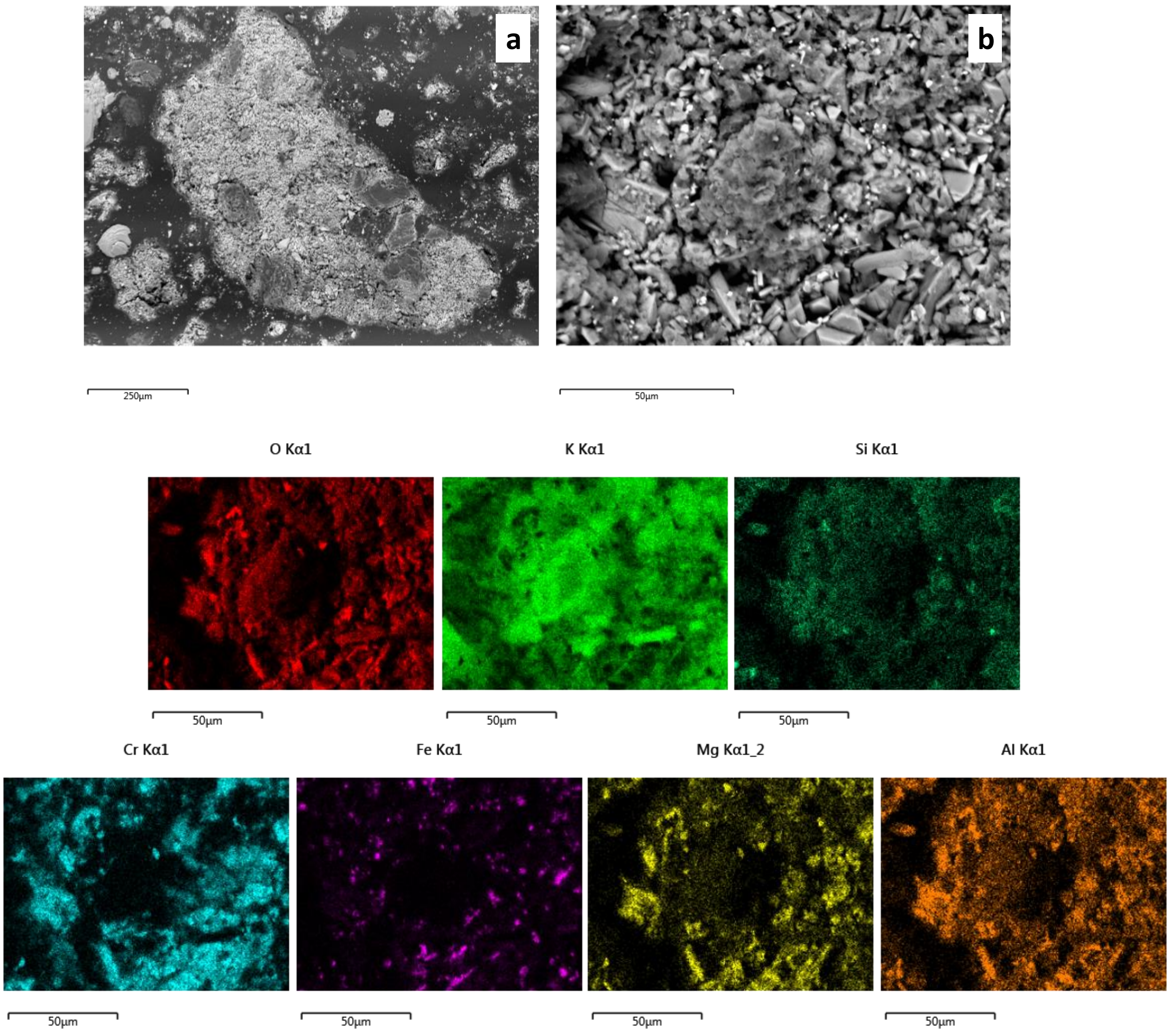

FIGURE 7-21. a) Lower and b) higher magnification backscattered SEM images, and EDX elemental mapping of a S.A. chromite reduced sample with K_2CO_3 and C in a weight ratio of chromite:K_2CO_3:C = 1:1:0.2. The sample was reduced at 1050°C for 2.5 hours.

7.4. CARBOTHERMIC REDUCTION OF HIGH SILICA BRAZILIAN CHROMITE ORES WITH SODIUM CARBONATE

The presence of silicate gangue minerals in chromite ores has an adverse effect on the extraction of chromium as sodium chromate solution by the oxidative alkali roasting route due to the following reasons:

(a) Decrease of the oxidation reaction rate due to formation of a viscous liquid phase which halts the diffusion of oxygen towards the reaction zone. $NaCr_2O_4$-Na_2CO_3-Na_2SiO_3 form a low temperature eutectic which results in the formation of a liquid phase that can envelop the chromite particles decreasing the oxygen transport and consequently the chromium oxidation rate [28,33].

(b) Higher consumption of sodium carbonate due to reaction with silica to form alkali silicates thereby reducing the availability of Na_2O to form Na_2CrO_4.

Therefore, the reduction of the extraction yield of sodium chromate is significant with increasing SiO_2-containing gangue in the ore.

Reduction of two high silica Brazilian ores has been carried out to study the effect of the silica content in the alkali reductive roasting. Brazilian chromite E4 (8.48 wt.% SiO_2) and Brazilian chromite E5 (13.20 wt.% SiO_2) have reduced with sodium carbonate and activated charcoal (chromite:Na_2CO_3:C weight ratio equal to 1:1:0.2) at a temperature of 1050°C for 2.5 hours, and the results are presented below.

7.4.1. CARBOTHERMIC REDUCTION OF BRAZILIAN CHROMITE E4

The Br. E4 ore contains 8.4 wt.% SiO_2, which is significantly high compared to the silica content of the South African ore. The reduction of this ore was carried out in the presence of Na_2CO_3 and activated charcoal in the weight ratio of 1:1:0.2, at 1050°C and for 2.5 hours. The stoichiometric chromite:Na_2CO_3 ratio was calculated as 1:0.48 taking into account the wt.% of Cr_2O_3 and Al_2O_3 in the ore and the reactions (r.65) and (r.66). The reduced sample was analysed by XRPD and the resultant experimental pattern is shown in FIGURE 7-22. The main phases identified in the reduced sample are similar to those formed during reduction of S.A. chromite ore, namely $NaCrO_2$, Fe and unreacted Na_2CO_3. In this case, peaks for MgO where not found, however, FeO was identified. A complex silicate compound, $Na_{0.87}Mg_{0.4}Al_{0.07}Si_{0.53}O_2$, was also present in the sample after reduction.

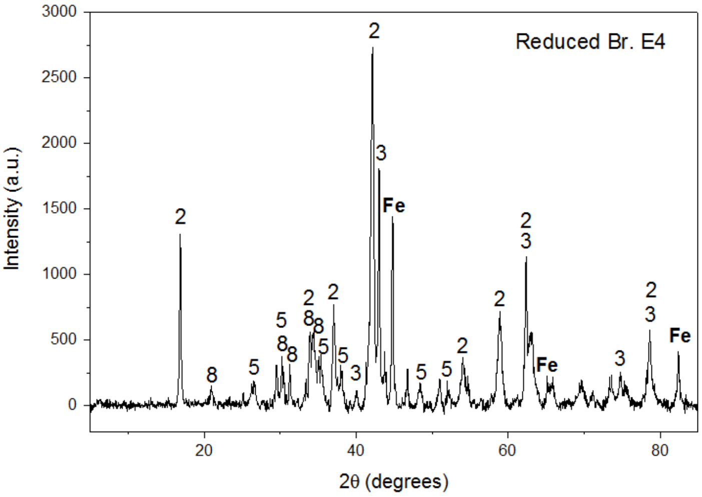

FIGURE 7-22. XRPD pattern of the reduced Brazilian chromite E4 with Na_2CO_3 and activated charcoal at 1050°C for 2.5 hours (weight ratio chromite:Na_2CO_3:C equal to 1:1:0.2). 2-$NaCrO_2$ (04-015-4350), 3- $Fe_{0.998}O$ (04-002-3667), 8- $Na_{0.87}Mg_{0.4}Al_{0.07}Si_{0.53}O_2$, 5- Na_2CO_3 (01-072-0628) and Fe (04-004-2482).

FIGURE 7-23 shows the SEM analysis of a reduced Brazilian chromite E4 sample and elemental mapping of a reduced particle. The high magnification SEM micrographs show that reduction took place and part of the iron oxides in the ore were reduced and formed a metallic phase. Extensive fracturing can be observed in the chromite particles, and SEM image C in FIGURE 7-23 is an example of that. The elemental mapping shows that Na^+ diffusion took place and a solid solution of $NaCrO_2$ and $NaAlO_2$ formed. Areas with higher concentration of magnesium are also observed, which suggest formation of MgO.

Most of the silica observed in the area analysed is concentrated in small SiO_2 particles, as shown in the elemental mapping in FIGURE 7-23. An example can be seen in the EDX analysis in FIGURE 7-24, in area E, with high concentration in Si. This suggests that in this case silica does not dissolve in the $NaCrO_2$/$NaAlO_2$ phase, but concentrates forming a SiO_2-rich phase.

The EDX chemical analysis on particles A to D shows how iron is distributed between the different phases in the reduced sample. The metallic phase contains approximately 75 wt.% Fe, being the remaining mainly Mg, Cr and O. Hence, the reduction seems incomplete, and the metallic iron-rich phase was not completely achieved. If these results are compared with the metallic phase obtained with the reduction of S.A chromite, which achieved an almost complete formation of metallic phase with at least 95 wt.% Fe, it can be concluded that the extent of reduction was lower in the case of reduction of the Brazilian chromite E4 ore. A possible explanation of the lower metallisation of Fe may be the lower activity of Na_2O due to the higher consumption of Na_2CO_3 by the silicate gangues present, which in the case of the Brazilian ores is significantly high.

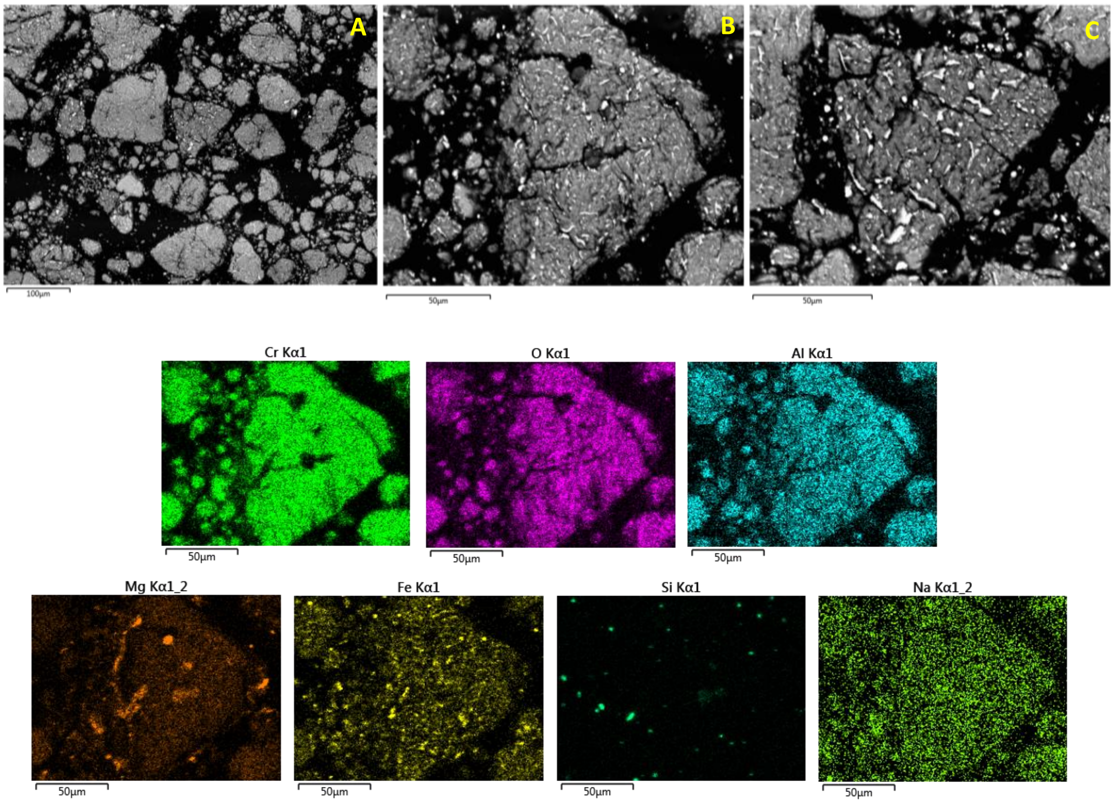

FIGURE 7-23. Backscattered SEM images (A, B and C) of Brazilian chromite E4 reduced (wt. ratio chromite:Na2CO3:C = 1:1:0.2) at 1050°C for 2.5 hours, and elemental EDX maps of micrograph B.

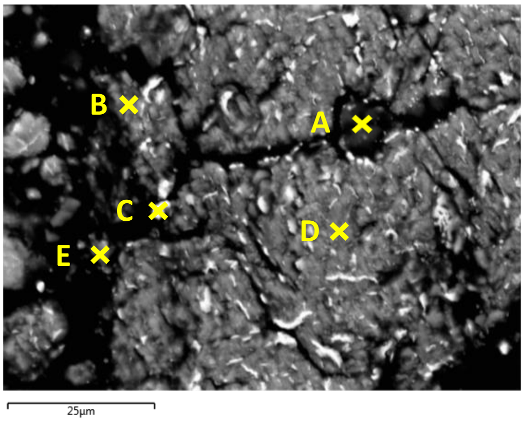

Wt.%	A	B	C	D	E
Cr	2.0	44.5	7.2	38.8	14.7
Fe	1.4	4.0	75.8	15.4	4.2
O	50.3	28.5	4.9	27.8	---
Al	6.7	10.0	1.2	9.0	1.7
Mg	19.4	9.3	10.7	5.2	4.9
Na	3.0	2.9	---	3.3	---
Si	16.9	---	---	---	73.9
Ca	0.3	0.8	0.2	0.4	0.6

FIGURE 7-24. Backscattered SEM image of a Brazilian chromite E4 sample reduced (chromite:Na_2CO_3:C = 1:1:0.2) at 1050°C and for 2.5 hours, and EDX elemental point analysis.

7.4.2. CARBOTHERMIC REDUCTION OF BRAZILIAN CHROMITE E5

The XRF analysis of the Brazilian chromite E5 presented in Chapter 4 shows that the ore contains 13.2 wt.% SiO_2, which is present in the form of different complex silicate phases, such as $(Mg,Fe,Al)_6(Si,Al)_4O_{10}(OH)_8$ and $NaCa_2Mg_5AlSi_7O_{22}(OH)_2$ (identified by XRPD). The stoichiometric amount of Na_2CO_3 required for the formation of $NaCrO_2$ and $NaAlO_2$ is 0.43g Na_2CO_3 per gram of Brazilian E5 ore.

The XPRD pattern in FIGURE 7-25 shows that $NaCrO_2$ was clearly formed, as well as MgO and $Na_2Mg(SiO_4)$. Metallic Fe is also present, but the intensity of the Fe peaks is lower than that observed in S.A. chromite ore reduced samples.

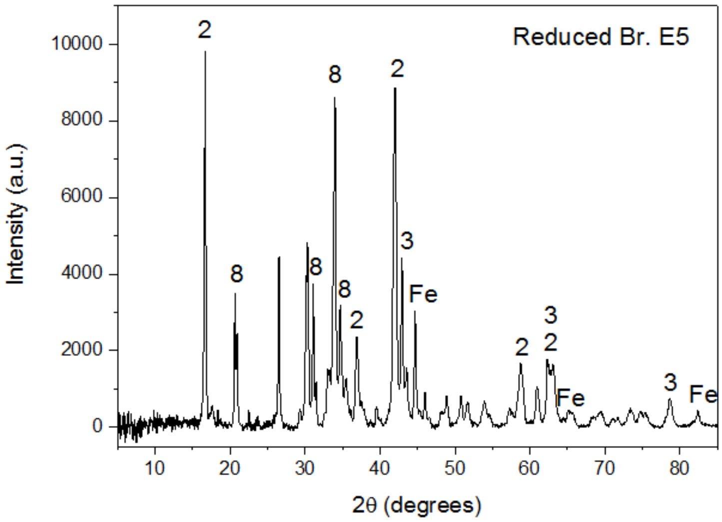

FIGURE 7-25. XRPD pattern of the reduced Brazilian E5 chromite with Na_2CO_3 and activated charcoal at 1050°C for 2.5 hours (chromite:Na_2CO_3:C = 1:1:0.2). [2=$NaCrO_2$, 3=MgO, 8=$Na_2Mg(SiO_4)$, and Fe].

The reduced sample of Br. Chromite E5 in FIGURE 7-26 confirms the partial reduction of the iron oxide. A metallic phase can be observed in brighter small particles embedded in the non-magnetic phase. The reduced particle in image B was analysed by elemental EDX mapping, where Fe can be seen in both the metallic and the non-magnetic phases. Segregation of a MgO-rich phase is also observed, as seen in previous examples with reduction of S.A. chromite and Brazilian chromite E4.

The Na EDX map illustrates the diffusion of Na^+ from the edges of the particle towards the centre, which is less concentrated in sodium than the borders. A Ca-Na-Mg-silicate phase was formed as a product layer surrounding the $NaCrO_2$-$NaAlO_2$ solid solution as a result of the alkali reduction process.

A similar microstructure was reported by Tathavadkar (2001) [33] on alkali roasting of high-SiO_2 Chinese ore in oxidising conditions. The author observed that a Na-Fe-Al-Cr-silicate phase was formed as a consequence of the dissolution of sodium carbonate, sodium chromate, sodium ferrite and sodium aluminate and sodium silicate and forming the liquid phase. The consumption of Na_2CO_3 in this case is also higher than in the S.A. chromite due to the high content of SiO_2, and therefore the alkali addition may need to be adjusted.

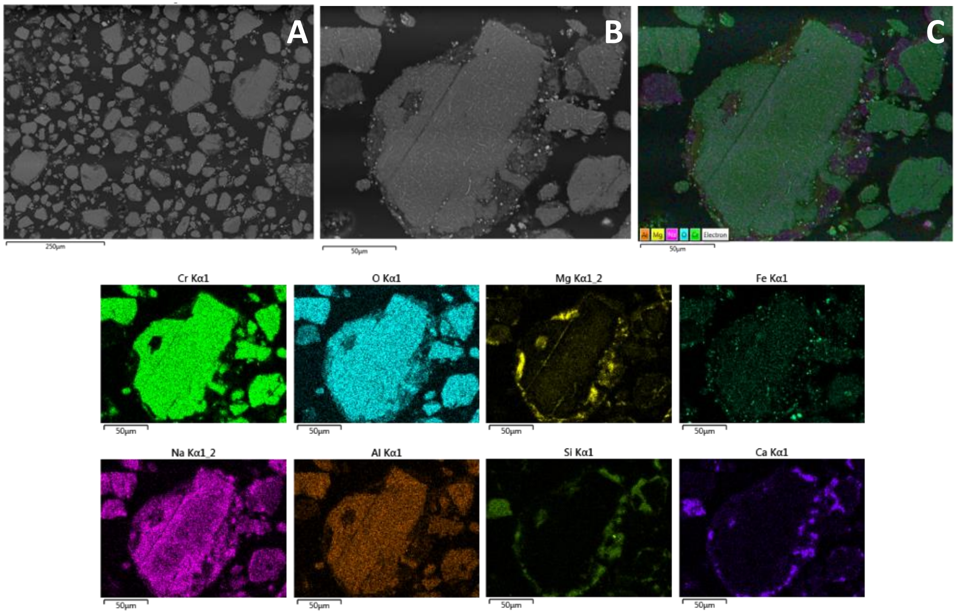

FIGURE 7-26. A and B: backscattered SEM images of Brazilian chromite E5 reduced with Na_2CO_3 and activated charcoal for 2.5 hours at 1050°C; C: EDX combined elemental mapping of image B; and single-element EDX mapping of image B.

7.4.3. EFFECT OF HIGH SILICA GANGUE MINERALS ON THE REDUCTIVE ALKALI ROASTING OF CHROMITE ORES

An investigation carried out by Tathavadkar [33] on the oxidative alkali roasting of different chromite ores reported less than 50 Na_2CrO_4 extraction after roasting at 1200°C and water leaching of Chinese ores with 6% SiO_2, whereas 95% extraction could be achieved with a South African ore with less than 1% SiO_2. The low efficiency of the oxidative alkali roasting route when processing > 1% SiO_2 chromite represents one of the main limitations of the oxidative route, as it creates a strong dependency on low silica ores (under 1 wt.% SiO_2). Under this consideration, the treatment of the high-SiO_2 Brazilian chromite ores used in this study by the oxidative alkali route would be both inefficient and highly waste-intensive due to the low chromate extraction and the high alkali consumption.

This highlights the need of studying the effect of silica on the reductive alkali roasting of chromite and determining if the novel reductive route is able to overcome this limitation.

In some of the SEM micrographs obtained of Brazilian chromite ores reduced with alkali and charcoal, a product layer formed by a complex silicate phase could be observed. The silicate phase was more clearly observed in the Brazilian chromite E5 reduced samples, which is expected due to the elevated amount of silica gangue present in this ore. By taking several EDX point ID, an average composition of the silicate phase which appeared enveloping chromite grains in Br. Chromite E5 reduced samples has been calculated and is equal to 20% wt. Si, 12.3% wt. Na, 9.4% wt. Mg, 9.8% wt. Ca, 2.8% wt. Al, 1.8% wt. Fe and 41.4% wt. O. This average composition can be expressed as the stoichiometric formula $Ca_{0.35}Mg_{0.55}Na_{0.75}(Fe,Al,Cr)_{0.25}SiO_{3.66}$, which approximates to the general orthosilicate formula $X^{+4}SiO_4$. The formation of the silicate phase may be one of the factors limiting the reduction of iron oxides by obstructing the CO/CO_2 gas transfer from the surface of the chromite particle to the core.

According to the average silicate phase composition calculated, Na_2O from the decomposition of Na_2CO_3 reacts to be part of the complex silicate, and hence the consumption of sodium oxide will increase as a function of the SiO_2 wt.% in the ore. This may also lower the activity of Na2O and limit the rate of metallisation. In this case, the amount of excess sodium carbonate expected to be consumed in the silicate phase is equal to 24.5% of the stoichiometric Na_2CO_3 required for the complete formation of $NaCrO_2$ and $NaAlO_2$. This means that the sodium carbonate consumed in the alkali reduction of Br. Chromite E5 is approximately 25% higher due to the presence of the gangue minerals.

7.5. KINETICS OF THE ALKALI REDUCTION OF S.A. CHROMITE ORE AND BRAZILIAN CHROMITE ORE E4

The kinetics of the reductive alkali roasting of S.A chromite ore and Brazilian E4 chromite ore with Na_2CO_3 and activated charcoal were studied based on thermogravimetric analysis. The kinetics results obtained are presented below and the reaction mechanism is discussed.

7.5.1. ISOTHERMAL THERMOGRAVIMETRIC TESTS

The degree of reduction (X) was calculated based on the thermogravimetric experimental data collected in isothermal experiments of alkali reduction at different temperatures. Experiments at temperatures of 800°C, 850°C, 900°C, 950°C, 1000°C and 1050°C were carried out with a chromite:Na_2CO_3:charcoal weight ratio of 1:1:0.2. The weight loss was recorded with time during each experiment (observed weight loss), and this data was used to calculate X following equation (eq.9).

$$X = \frac{\text{Observed weight loss (g)}}{\text{Theoretical weight loss (g)}} \qquad \text{(eq.9)}$$

The theoretical weight loss was determined by stoichiometric calculations based on the composition of the chromite ore, the alkali and carbon weight ratios in the reaction mixture, the initial weight of the sample and the weight loss expected from reactions (r.67) to (r.70) corresponding to the reduction of iron oxides and formation of sodium chromite and sodium aluminate.

$FeO (s) + C (s) \rightarrow Fe (s) + CO (g)$ (r.67)

$Fe_2O_3 (s) + 3 C (s) \rightarrow 2 Fe (s) + 3 CO (g)$ (r.68)

$Cr_2O_3 (s) + Na_2CO_3 (s) + C (s) \rightarrow 2 NaCrO_2 (s) + 2 CO (g)$ (r.69)

$Al_2O_3 (s) + Na_2CO_3 (s) + C (s) \rightarrow 2 NaAlO_2 (s) + 2 CO (g)$ (r.70)

If excess sodium carbonate is present in the reaction mixture, the weight loss due to the decomposition of Na_2CO_3 following reaction (r.71) needs to be taken into account. A detailed study of the thermal decomposition of sodium carbonate was carried out by Motzfeldt [112] and can be found in literature. The CO_2 evolved may then react with excess carbon to form CO gas as shown by the Boudouard reaction (r.20). The combination of reaction (r.71) and the Boudouard reaction results in reaction (r.72) shown below.

$Na_2CO_3 (s) \rightarrow Na_2O (s) + CO_2 (g)$ (r.71)

$Na_2CO_3 (s) + C (s) \rightarrow Na_2O (s) + 2 CO (g)$ (r.72)

Once the theoretical weight loss was determined, the degree of reduction was calculated substituting the theoretical weight loss in equation (eq.9), and the curves of (%)X versus time were plotted for the different temperatures and are shown FIGURE 7-27 and FIGURE 7-28.

It can be observed in the plot for S.A. chromite (FIGURE 7-27) that at temperatures of 800°C and 850°C, the degree of reduction shows a steady increase with time; whereas above 900°C, (%)X increases rapidly before it reaches a plateau where the reaction halts. Moreover, at temperatures of 900°C and above, a clear three-step reaction is observed, while at lower temperature this behaviour is not so apparent. At the higher temperature studied, 1050°C, the reaction occurred rapidly and achieved a maximum degree of reduction of approximately 92% after 30 min.

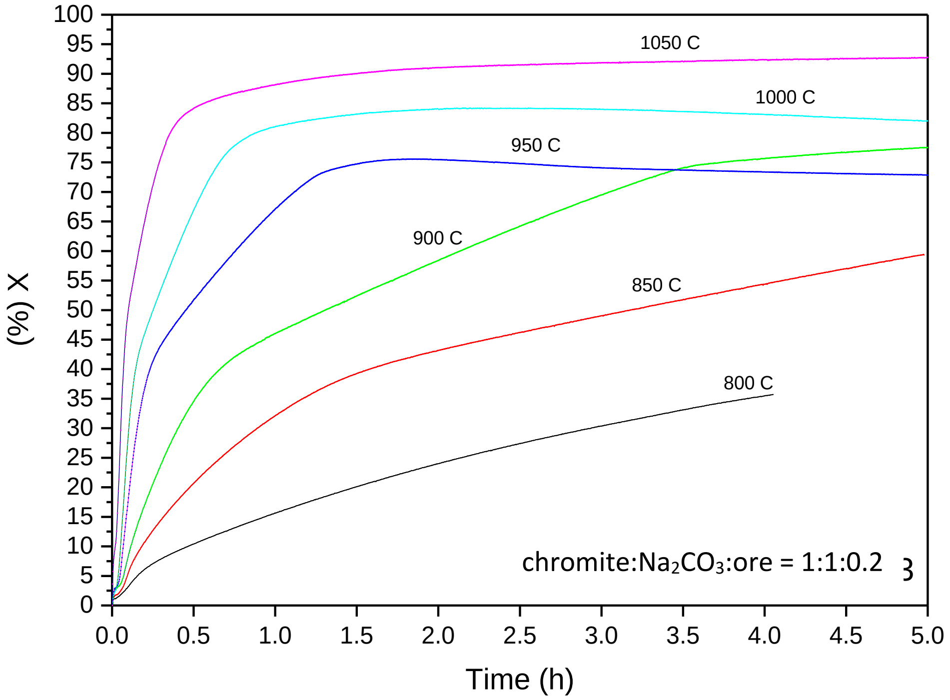

FIGURE 7-27. (%) Reduction vs time curves for the carbothermic reduction of S. A. chromite ore in the presence of Na_2CO_3 at constant temperatures (800°C, 850°C, 900°C, 950°C, 1000°C and 1050°C) with a chromite:Na_2CO_3:charcoal weight ratio of a) 1:1:0.2.

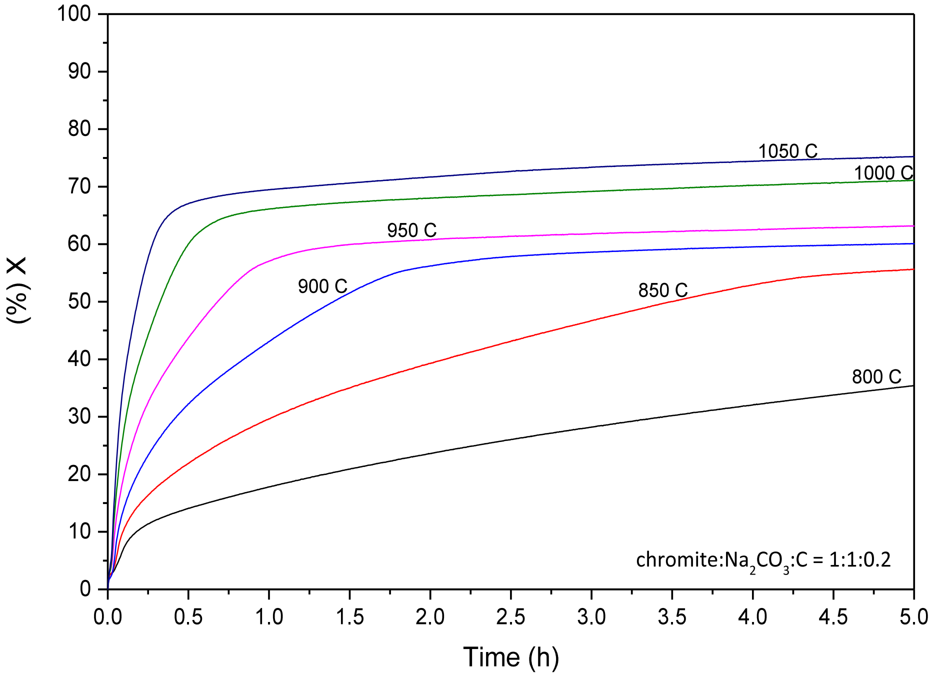

FIGURE 7-28. (%) Reduction vs time curves for the carbothermic reduction of Br. chromite E4 ore in the presence of Na_2CO_3 at constant temperatures (800°C, 850°C, 900°C, 950°C, 1000°C and 1050°C) with a chromite:Na_2CO_3:charcoal weight ratio of a) 1:1:0.2.

A similar type of curves is obtained for the reduction of Br. chromite E4, as shown in FIGURE 7-28. However, the maximum degree of reduction achieved in this case is approximately 75% at 1050°C. The degree of reduction in this case increases up to 66.8% after 30 minutes, and the curve then reaches a plateau where the rate of reaction decreases significantly.

7.5.2. DETERMINATION OF REACTION RATE AND ACTIVATION ENERGY

A kinetic study of the carbothermic reduction of chromite ore in the presence of Na_2CO_3 has been performed based on thermogravimetric experimental data. Kinetic models for diffusion-controlled and reaction-controlled solid-state reactions have been developed by different authors. In the case of the diffusion control model, where the rate-limiting step is the diffusion of gaseous species through the product layer, Ginstling and Brounshtein (1950) [119] (GB) proposed the following equation (eq.10):

$$1-\frac{2}{3}\cdot \mathrm{X}-(1-\mathrm{X})^{\frac{2}{3}}=\mathrm{k}\ \cdot \mathrm{t} \qquad \text{(eq.10)}$$

When the reaction at the particle interface is the rate-limiting step, the equation (eq.11) developed by Spencer and Topley (1929) [120] may be applied:

$$1-(1-\mathrm{X})^{\frac{1}{3}}=\mathrm{k}\ \cdot \mathrm{t} \qquad \text{(eq.11)}$$

A mixed kinetic control including both diffusion and reaction control can be also considered, in which case the kinetic equation would be the following:

$$(1-\frac{2}{3}\cdot \mathrm{X}-(1-\mathrm{X})^{\frac{2}{3}})+(1-(1-\mathrm{X})^{\frac{1}{3}})\ =\ \mathrm{k}\ \cdot \mathrm{t} \qquad \text{(eq.12)}$$

In equations (eq.10), (eq.11) and (eq.12), *X* stands for the fraction reacted or degree of reduction, *k* for the rate constant (h^{-1}) and *t* for the reaction time (h).

Experimental data from X versus time curves, in FIGURE 7-27 and FIGURE 7-28, were fitted to equations (eq.10), (eq.11) and (eq.12), for the GB, reaction and mixed model, respectively. The last section of the curves, where a plateau is reached, was not included in the fitting as the reaction is considered to stop when no weight loss is observed. FIGURE 7-29 shows the plots for the fitting to the different models as a function of time for the experimental data obtained at 800°C, 850°C, 900°C, 950°C, 1000°C and 1050°C. In the case of 800°C, the plots for the three models can be fitted to a straight line; whereas at 850°C and above, the GB model can be fitted with a single straight line but the ST and mixed models show two distinct regimes with different slopes. Even though the presence of two regimes can be observed in the results for both chromite ores, this effect is more pronounced for the S.A. chromite than in the Brazilian ore.

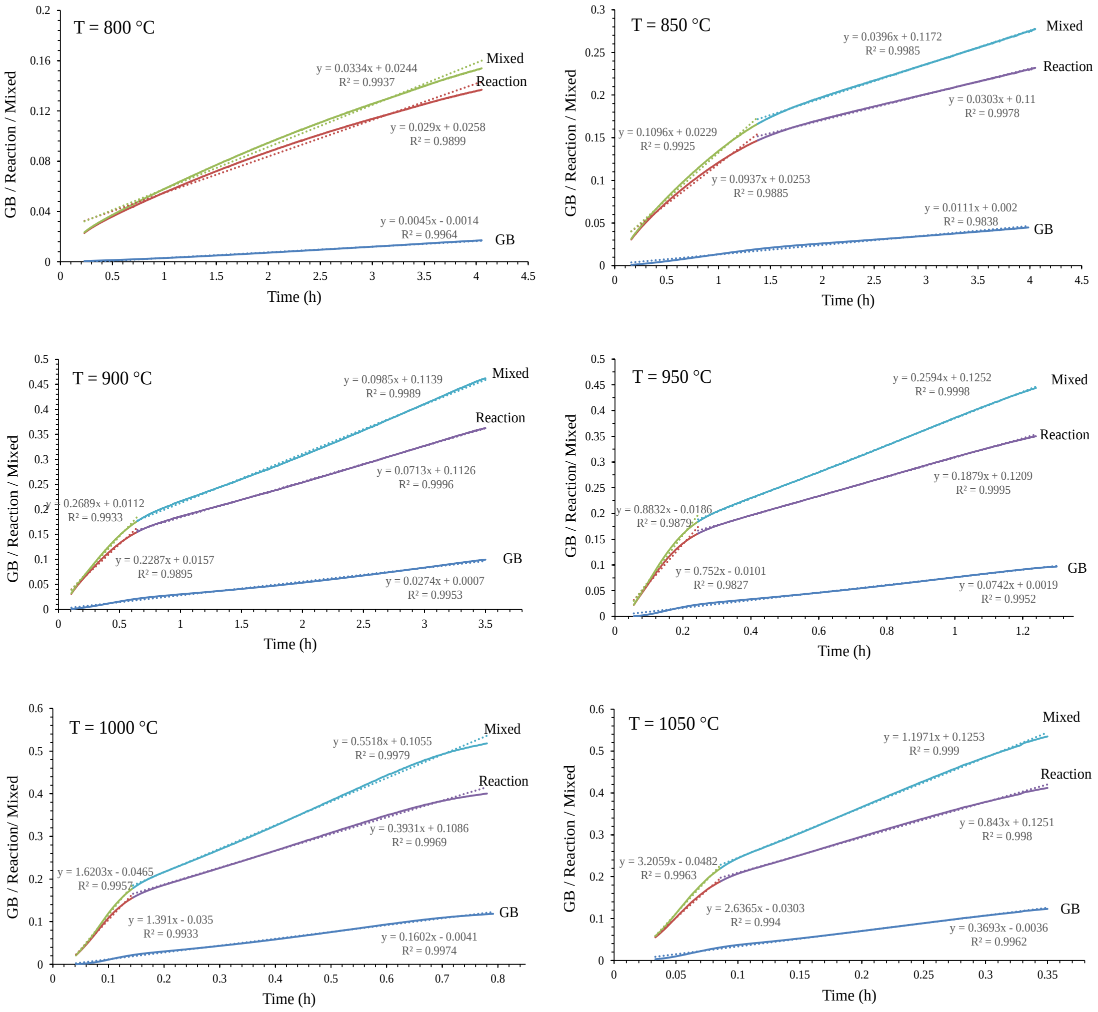

FIGURE 7-29. GB, reaction and mixed models' equations vs time from experimental TGA data collected with S.A. chromite at 800°C, 850°C, 900°C, 950°C, 1000°C and 1050°C (chromite:Na_2CO_3:C = 1:1:0.2).

TABLE 7-3. Rate constant and R-squared values of S.A. chromite ore obtained by fitting values of the degree of reduction vs time to the different rate equations of GB, ST and mixed models.

S.A. CHROMITE ORE		**GB**		**ST**				**MIXED**			
		Regime 1		**Regime 1**		**Regime 2**		**Regime 1**		**Regime 2**	
T (°C)	**T (K)**	**K**	**R²**	**K**	**R²**	**K**	**R²**	**K**	**R²**	**K**	**R²**
800	**1073**	0.0045	0.9964	0.0290	0.9899	0.0290	0.9899	0.0334	0.9937	0.0334	0.9937
850	**1123**	0.0111	0.9838	0.0937	0.9885	0.0303	0.9978	0.1096	0.9925	0.0396	0.9985
900	**1173**	0.0274	0.9953	0.2287	0.9895	0.0713	0.9996	0.2689	0.9933	0.0985	0.9989
950	**1223**	0.0742	0.9952	0.7520	0.9827	0.1879	0.9995	0.8832	0.9879	0.2594	0.9998
1000	**1273**	0.1602	0.9974	1.3910	0.9933	0.3931	0.9969	1.6203	0.9957	0.5518	0.9979
1050	**1323**	0.3693	0.9962	2.6365	0.9940	0.8430	0.9980	3.2059	0.9963	1.1971	0.9990
Mean			0.9942		0.9941		0.9896		0.9970		0.9931

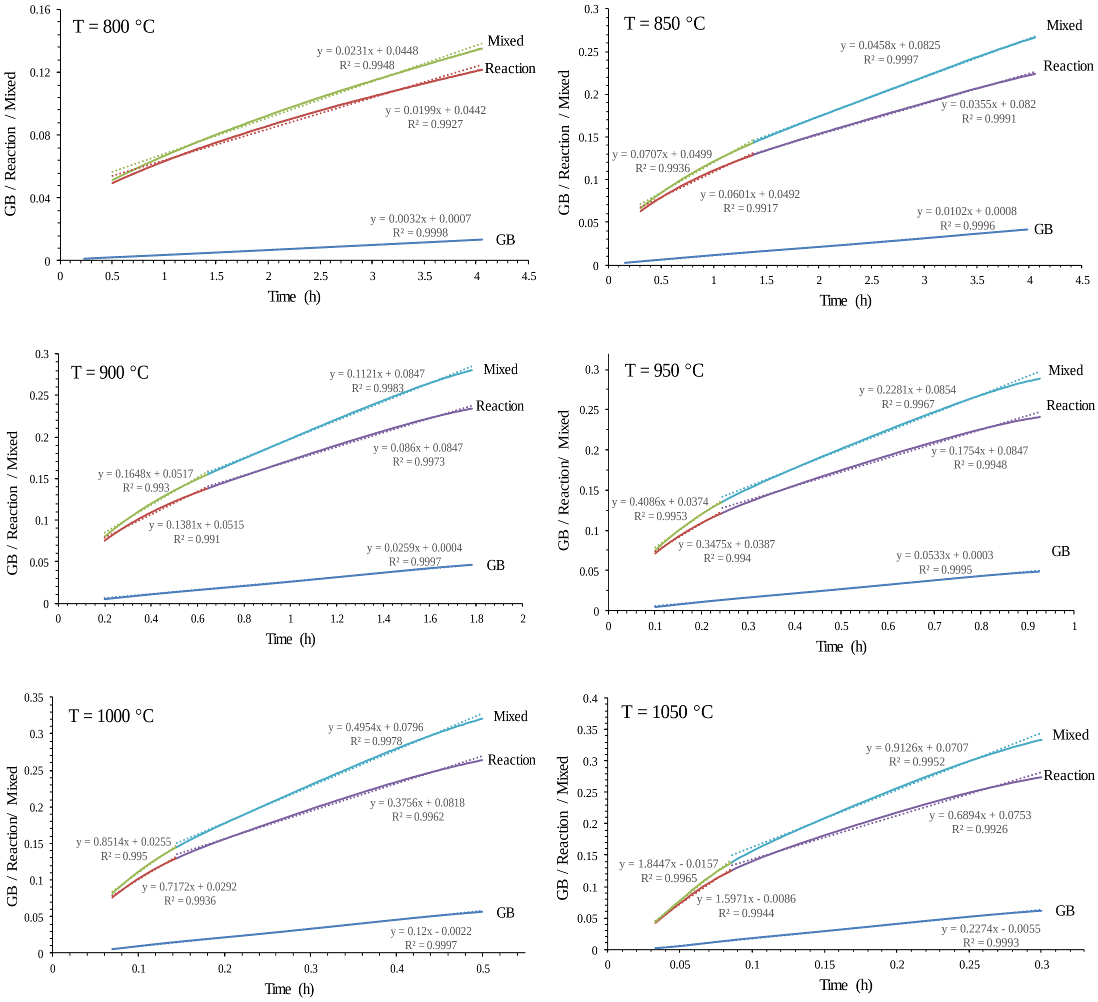

FIGURE 7-30. GB, reaction and mixed models' equations vs time from TGA data collected with Br. chromite E4 at 800°C, 850°C, 900°C, 950°C, 1000°C and 1050°C (chromite:Na_2CO_3:C = 1:1:0.2).

TABLE 7-4. Rate constant and R-squared values for Brazilian chromite E4 obtained by fitting values of the degree of reduction vs time to the different rate equations of GB, ST and mixed models.

BRAZILIAN Chr. E4		**GB**		**ST**				**MIXED**			
		Regime 1		Regime 1		Regime 2		Regime 1		Regime 2	
T (°C)	**T (K)**	**K**	**R^2**	**K**	**R^2**	**K**	**R^2**	**K**	**R^2**	**K**	**R^2**
800	**1073**	0.0032	0.9998	0.0199	0.9927	0.0199	0.9927	0.0231	0.9948	0.0231	0.9948
850	**1123**	0.0102	0.9996	0.0601	0.9917	0.0355	0.9991	0.0707	0.9936	0.0458	0.9997
900	**1173**	0.0259	0.9997	0.1381	0.9910	0.0860	0.9973	0.1648	0.9930	0.1121	0.9983
950	**1223**	0.0533	0.9995	0.3475	0.9940	0.1754	0.9948	0.4086	0.9953	0.2281	0.9967
1000	**1273**	0.1200	0.9997	0.7172	0.9936	0.3756	0.9962	0.8514	0.9950	0.4954	0.9978
1050	**1323**	0.2274	0.9993	1.5971	0.9944	0.6894	0.9926	1.8447	0.9965	0.9126	0.9952
Mean		-	0.9996	-	0.9929	-	0.9955	-	0.9947	-	0.9971

According to the models equations, the slope of each straight line corresponds to the rate constant (k), and the goodness of fit of each set of data to the corresponding straight line is given by the coefficient of determination R-squared (R^2). Identical data treatment was performed for all the temperatures, and the values obtained for k and R^2 for the fittings to the three models at the different temperatures for both S.A. and Brazilian E4 chromite ores are shown in TABLE 7-3 and TABLE 7-4.

Looking at the plots in Figure 7-29 and FIGURE 7-30, and the mean R-squared values in TABLE 7-3 and TABLE 7-4, the fitting of both the diffusion-controlled and reaction-controlled models to the experimental data is noticeably good, with R-squared values always above 0.98. This suggests that both reaction and diffusion have a significant effect on the rate of the reaction for both S.A. and Brazilian chromites. Therefore, the rate constants at different temperatures given by the mixed model -which also presents high values of R^2- will be considered for the determination of the activation energy of the global reaction.

The activation energy (E_a) of a reaction can be calculated by using the Arrhenius equation (v) shown below in (eq.13). The inverse of the temperature ($\frac{1}{T}$) in Kelvins against the natural logarithm of the rate constants obtained from the GB, reaction and mixed models, at the corresponding temperatures, were plotted (Figure 7-31); and the activation energy can be determined from the slope of the straight line which best fits the experimental points obtained.

$$\ln K = \ln A + \frac{E_a}{R} \cdot \frac{1}{T} \qquad \text{(eq.13)}$$

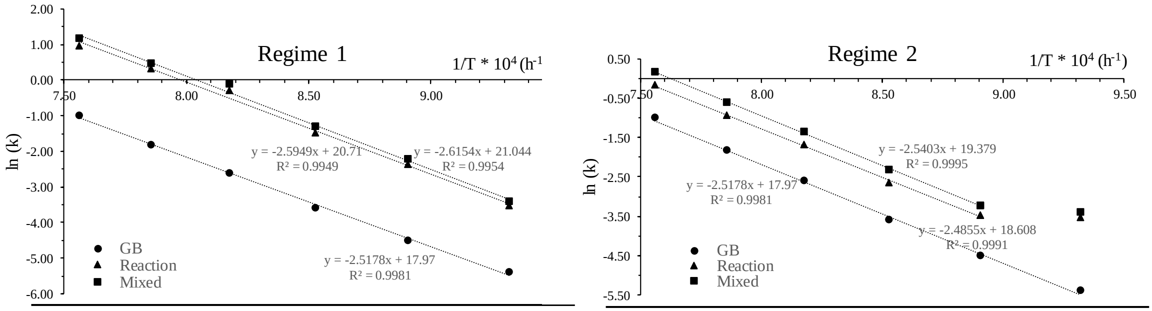

Regime 1						
$1/T *10^4$	K(GB)	ln(K)	K(Reac)	ln(K)	K(Mixed)	ln(K)
9.3197	0.0045	-5.4037	0.0290	-3.5405	0.0334	-3.3992
8.9047	0.0111	-4.5008	0.0937	-2.3677	0.1096	-2.2109
8.5251	0.0274	-3.5972	0.2287	-1.4753	0.2689	-1.3134
8.1766	0.0742	-2.6010	0.7520	-0.2850	0.8832	-0.1242
7.8555	0.1602	-1.8313	1.3910	0.3300	1.6203	0.4826
7.5586	0.3693	-0.9961	2.6365	0.9695	3.2059	1.1650
	STD error S	0.06	STD error S	0.09	STD error S	0.09

Regime 2						
$1/T *10^4$	K(GB)	ln(K)	K(Reac)	ln(K)	K(Mixed)	ln(K)
9.3197	0.0045	-5.4037	0.0290	-3.5405	0.0334	-3.3992
8.9047	0.0111	-4.5008	0.0303	-3.4966	0.0396	-3.2289
8.5251	0.0274	-3.5972	0.0713	-2.6409	0.0985	-2.3177
8.1766	0.0742	-2.6010	0.1879	-1.6718	0.2594	-1.3494
7.8555	0.1602	-1.8313	0.3931	-0.9337	0.5518	-0.5946
7.5586	0.3693	-0.9961	0.8430	-0.1708	1.1971	0.1799
	STD error S	0.06	STD error S	0.04	STD error S	0.03

FIGURE 7-31. Arrhenius plots of S.A. chromite ore reduction, where the natural logarithm of the rate constants obtained is plotted against the inverse of temperature for regimes 1 and 2.

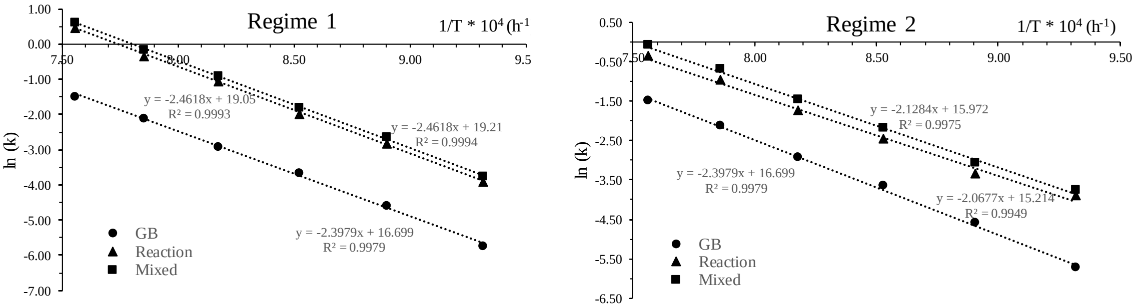

Regime 1

$1/T*10^4$	K(GB)	ln(K)	K(Reac)	ln(K)	K(Mixed)	ln(K)
9.3197	0.0032	-5.7446	0.0199	-3.9170	0.0231	-3.7679
8.9047	0.0102	-4.5854	0.0601	-2.8117	0.0707	-2.6493
8.5251	0.0259	-3.6535	0.1381	-1.9798	0.1648	-1.8030
8.1766	0.0533	-2.9318	0.3475	-1.0570	0.4086	-0.8950
7.8555	0.1200	-2.1203	0.7172	-0.3324	0.8514	-0.1609
7.5586	0.2274	-1.4810	1.5971	0.4682	1.8447	0.6123
	STD error S	0.05	STD error S	0.03	STD error S	0.03

Regime 2

$1/T*10^4$	K(GB)	ln(K)	K(Reac)	ln(K)	K(Mixed)	ln(K)
9.3197	0.0032	-5.7446	0.0199	-3.9170	0.0231	-3.7679
8.9047	0.0102	-4.5854	0.0355	-3.3382	0.0458	-3.0835
8.5251	0.0259	-3.6535	0.0860	-2.4534	0.1121	-2.1884
8.1766	0.0533	-2.9318	0.1754	-1.7407	0.2281	-1.4780
7.8555	0.1200	-2.1203	0.3756	-0.9792	0.4954	-0.7024
7.5586	0.2274	-1.4810	0.6894	-0.3719	0.9126	-0.0915
	STD error S	0.05	STD error S	0.07	STD error S	0.05

FIGURE 7-32. Arrhenius plots of Brazilian chromite E4 ore reduction, where the natural logarithm of the rate constants obtained is plotted against the inverse of temperature for regimes 1 and 2.

The constant rates at different temperatures given by the mixed model, which also presents high values of R^2, have been considered for the determination of the activation energy of the global reaction. The activation energies obtained for regimes 1 and 2 by the GB, reaction and mixed models are shown in TABLE 7-5. The values obtained by the mixed model will be used for comparison with other kinetic studies in literature.

TABLE 7-5. Activation energy values obtained for the alkali reduction of S.A. chromite ore.

	E_a (kJ/mol)	**REGIME 1**	**REGIME 2**
S.A. Chromite	GB	209±5	209±5
	Reaction	216±8	207±4
	Mixed	**217**±7	**211**±3
Brazilian chromite E4	**E_a (kJ/mol)**	**REGIME 1**	**REGIME 2**
	GB	199±5	199±5
	Reaction	205±3	172±3
	Mixed	**205**±2	**177**±3

According to the kinetic data summarised in FIGURE 7-31, FIGURE 7-32 and TABLE 7-5 the following observations can be obtained:

1 South African chromite ore. In the case of Regime 1, the Arrhenius plot for the three models shows a good fitting with R-square values above 0.99. For Regime 2, the values of the goodness of fit are similar to Regime 1; however, the Arrehnius plot for the reaction and mixed models follow a straight line with the exception of the point at 800°C, which was excluded from the fitting.

2. Brazilian chromite E4 ore. Both regimes can be fitted with the mixed model showing good fitting with all R-square values above 0.99. In both regimes, ln(k) values for all temperatures could be fitted to a straight line.

If a mixed model is considered, the values of E_a obtained for Regimes 1 and 2 are very similar in the case of the S.A. chromite ore, while a higher difference can be observed in the values for Br. Chromite E4 reduction. Note that the extent of reduction of the Brazilian ore (75%) was significantly lower than that achieved with South African chromite (92%). TABLE 7-6 was adapted from Wang et al., 2014 [70] and shows a compilation of previous findings on the kinetics of chromite reduction, using solid carbon or CO gas as reducing agent. The table includes, for each of the references, the controlling mechanism identified, the activation energy calculated and the addition of any additive. The main controlling mechanisms identified in most of the studies were nucleation, chemical reaction and gas/solid diffusion.

TABLE 7-6. Previous findings on the kinetics of chromite reduction. Adapted from Wang (2014) [70].

Reference	Additive	Controlling mechanism	E_a (kJ/mol)
[13]	None	Early stage: nucleation/chemical reaction Late stage: gas/solid diffusion	114 221
[63]	None	Low temperature: diffusion (1473-1523K) High temperature: nucleation (1573K)	---
[11]	None	Unreacted core with gas/solid diffusion	224
[73]	None	Diffusion of oxygen	57
[121]	None	Early stage: nucleation and growth Middle stage: phase boundary reaction Late stage: diffusion	270±10
[78]	CaO	Early stage: nucleation/chemical reaction Late stage: diffusion of Cr	139-161 410
[13]	SiO_2	Early stage: diffusion of ions Late stage: smelting of Cr	194 256
[75]	SiO_2	Early stage: nucleation/chemical reaction Late stage: not found	172
[122]	None	Low T: Pore diffusion+ interfacial reaction High T (>1520°C): Chemical reaction	420

The activation energy values calculated in this study for the reductive roasting of S.A. chromite in the presence of Na_2CO_3 are comparable to that obtained by Kekkonen (1995) [11], and Ding (1997) [13]. The authors studied the reduction kinetics of carbothermal and reduction with CO gas of chromite pellets in the temperature range of 1420°C to 1595°C and observed increasing reduction rate with increasing temperature. They used the unreacted core model to explain the mechanism of reduction and concluded that the diffusion of CO_2 in the product layer is the controlling step in the reduction of chromite and carbon pellets in argon atmosphere. The microstructure shown by Kekkonen (1995) [11] is similar to that observed in reduced samples in this study and shown in this chapter. The formation of round metallic particles can be observed in the reduced sample micrographs. Fine metallic-phase needles are also present in the chromite and carbon powder pellets reduced under Ar-atmosphere [11].

7.6. REACTION MECHANISM OF THE REDUCTIVE ALKALI ROASTING OF CHROMITE ORES

The mechanism proposed for the carbothermal reduction of chromite in the presence of Na_2CO_3 at 1050°C is summarised below. Some of the steps have been discussed based on experimental observations presented in this chapter and previous findings found in literature.

- ***Boudouard reaction*** *($C + CO_2 \rightarrow CO$)* ***and decomposition of Na_2CO_3*** *($Na_2CO_3 \rightarrow Na_2O + CO_2$)*.

During carbothermal reduction of chromite, the carbon gasification by the Boudouard reaction may be controlling the kinetics in the early stages of the process, as the replacement rate of the CO consumed on the reaction front depends on the rate of this reaction. If the Boudouard reaction is limiting the early stages of reduction a higher concentration of CO_2 is expected in the gas, and hence, this could be verified experimentally by continuous analysis of the gas outlet of the furnace [62]. The catalytic effect of alkali carbonates on the Boudouard reaction has been previously reported in literature [62,91,123], indicating that the presence of sodium carbonate might be increasing the rate of reduction.

- ***Diffusion of the gaseous reductant (CO) through the gas film around the chromite particle and*** **through the porous solid and cracks towards the reaction surface.**

This is expected to be a limiting factor of the reaction rate. The alkali present during reduction is, however, able to promote the breakage and cracking of the chromite particle and therefore the metallisation of $Fe^{2+/3+}$ by CO gas is increased.

In the case of high silica ores, the formation of a silicate product layer was observed, which could be limiting the CO transfer towards the reaction surface thereby hindering the reduction of Fe^{2+}/Fe^{3+}. The formation of metallic Fe spheres at the edges of the partially-reduced particles was reported as the rate limiting factor by Niayesh (1992) [62], as it can limit the diffusion of gases through the product-layer. In this case the formation of the metallic phase occurs first as needle-shape metallic Fe within the $NaCrO_2/NaAlO_2$ matrix, which later diffuses towards the edge or grows within internal cracks formed as a consequence of reduction. Rounded metallic particles are then formed at the border or in the cracks of the reduced particles in the last stages of the reaction. The metallic particles, however, tend to separate once in the surface of the particle and do not form a continuous rim. Therefore, this is not expected to be a limiting factor in this case.

- ***Adsorption of the gaseous reductant on the reaction surface.***
- ***Diffusion of Fe^{2+}/Fe^{3+} and O^{2-} through the vacancies of the structure and towards the reaction surface.***
- ***Chemical reaction on the reaction surface between the gaseous reductant and the oxygen in the chromite spinel lattice leading to metallisation of Fe.***

The reaction between CO and the oxygen from the lattice leads to the formation of CO_2 yielding $2e^-$, which are then responsible for the reduction of Fe^{2+} to metallic Fe^0. The reduction process is expected to create vacancies, which will increase the reactivity of chromite. Reaction could be a limiting factor, however, previous publications on the carbothermal reduction of chromite agreed on the fact that reduction of Fe_2O_3 and FeO occurs in first place [63,69,72,124], followed by the reduction of Cr_2O_3 once metallisation of iron is incomplete. In the case of alkali reduction of chromite, the presence of alkali minimises the formation of metallic Cr by forcing the equilibrium towards the formation of $NaCrO_2$ phase, and hence only a small fraction of chromium is metallised forming the Fe-Cr metallic alloy. The alloy has variable content of Cr metal depending on the temperature, time and content of alkali in the charge, as shown in section 7.2.3. Limited formation of Cr metal is an advantage of the alkali reduction over carbothermal reduction in the absence of alkali, as metallisation of Cr, which is the slow step, is not desired.

- ***Diffusion of sodium ions via the voids in the spinel structure towards the reaction surface and reaction with Cr^{+3} to form $NaCrO_2$.***

It was observed that the diffusion of Na^+ ions from the edges of the particle towards the centre occurs rapidly. Formation of $NaCrO_2$ can be observed after 15-30 minutes of reaction, as it was indicated by XRPD patterns presented in FIGURE 7-6. FIGURE 7-33 shows the SEM-EDX phase mapping of a S.A. chromite sample reduced with Na_2CO_3 for 30 minutes at 1050°C obtained by using Mineralogic Mining.

The progression of the $NaCrO_2/NaAlO_2$ phase can be observed in a lot of the particles, confirming the diffusion of Na^+ ions. In some bigger particles, Na^+ ions are present only in the rim, while the centre is still unreacted or partially-reacted chromite ore. By contrast, the formation of metallic Fe is not so obvious at this stage of reaction, as only few small areas concentrated in iron can be observed.

- ***Reaction of sodium oxide with Al^{+3} ions to form $NaAlO_2$.***
- ***Diffusion of Mg^{2+} ions through the vacancies in the spinel structure towards the outer rim of the chromite particle, and formation of MgO phase.***

Previous research carried out on the oxidative roasting of chromite ores studied the effect of Fe/Mg replacement on the extraction of chromium as Na_2CrO_4. It was found [125] that the replacement of Fe^{2+} by Mg^{+2} in the spinel structure has no significant effect on the chromium extraction. On the other side, Tathavadkar (2001) [33] found that the higher the fraction of Mg^{2+} in the chromite spinel, the lower is the extraction yield observed. The author concluded that there is a detrimental effect for chromite spinels rich in Mg.

As discussed in Chapter 5, the reduction of Mg-based spinels, namely $MgCr_2O_4$ and $MgAl_2O_4$, in the presence of Na_2CO_3 and charcoal is less thermodynamically favourable than that of Fe-base spinels ($FeCr_2O_4$, $FeAl_2O_4$). $MgCr_2O_4$ presents high stability at high temperatures and under reducing conditions and in the presence of alkali, which may be explained by the need of balancing between divalent and trivalent ions in the spinel lattice. The EPMA analysis of chromite ores indicated that Brazilian ores have a higher Mg wt.% in the spinel compared to the ore of South African origin. Brazilian chromite E4 contains 15.05 wt. % Mg, Brazilian chromite E5 15.24 wt.% Mg, while S.A. chromite ore has 9.03 wt.% Mg, as shown in TABLE 4-1 and TABLE 4-5. Therefore, the higher content of Mg in the Brazilian chromite spinels could be one of the reasons for the lower reduction extents obtained for these ores in the present study.

- ***Desorption of the gaseous reaction product (CO_2 gas) from the reaction surface.***
- ***Diffusion of the gaseous reaction product through the porous solid or cracks of the chromite particle, and diffusion through the gas film around the particle.***

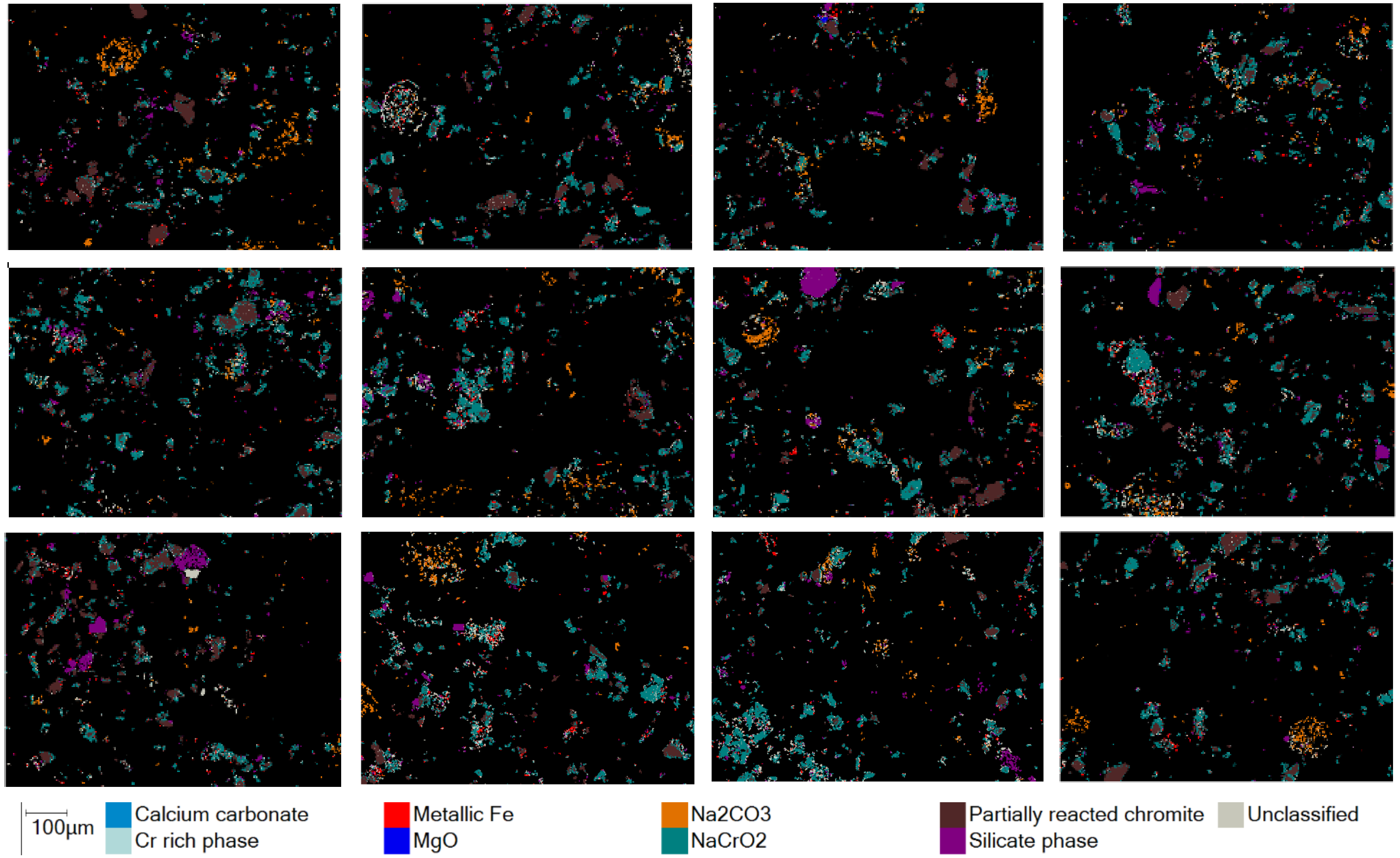

FIGURE 7-33. SEM-EDX phase mapping of a South African chromite ore reduced with Na_2CO_3 and activated charcoal (weight ratio chromite:Na_2CO_3:C = 1:1:0.2) at 1050°C for 30 minutes in an electrically-heated tube furnace. Map obtained using the Mineralogic Mining software attached to a ZEISS EVO scanning electron microscope.

Chapter 8

PRODUCTION OF Cr_2O_3-RICH MATERIAL FROM REDUCED SAMPLES

Chapter content

Reduced samples are subjected to magnetic separation in order to obtain a non-magnetic fraction enriched in $NaCrO_2$ *and depleted in iron. The magnetic and non-magnetic fractions were obtained and characterised, and the results are presented in this Chapter. The final* Cr_2O_3*-rich solid is produced by different leaching steps of the non-magnetic fraction in water and acid media. Different acids were tested during the acid leaching stage, and the effect of the leaching parameters on the purity of the final* Cr_2O_3*-rich product was studied and discussed.*

Chapter conclusions

The magnetic separation of reduced samples yielded magnetic and non-magnetic fractions which have different chemical composition depending on the parameters of alkali reduction stage. The extraction of Cr_2O_3 *into the non-magnetic fraction increased with increasing temperature and time of reduction. A non-magnetic fraction of 51.78 wt.%*Cr_2O_3 *was achieved after magnetic separation of samples reduced at* 1050^oC *for 2.5 hours and chromite:*Na_2CO_3*:C=1:1:0.2. The water leaching of the non-magnetic fraction achieved the extraction of 65.15 wt.% of the remaining* Na_2O *in the non-magnetic fraction and the results indicate that a 5% enrichment was attained by the water leaching step.*

Different organic and inorganic acids were tested, and the acid leached products obtained have a wt.%Cr_2O_3 *that increases in the following sequence: acetic<ascorbic<oxalic< tartaric <lactic<citric<phosphoric<hydrochloric<nitric<sulfuric. The best leaching results were achieved with* H_2SO_4 *with a concentration of 0.5M, a solid:liquid ratio equal to 1:100 g/mL, temperature of* 80^oC *and 2 hours leaching. Multiple-stage* H_2SO_4 *leaching increased the wt.%* Cr_2O_3 *from 81.01 wt.%, to 83.90 wt.% and 85.44 wt.% after two and three leaching steps, respectively.*

8.1. MAGNETIC SEPARATION OF THE REDUCED MATERIAL

8.1.1. CHARACTERIZATION OF MAGNETIC AND NON-MAGNETIC FRACTIONS

During alkali reduction, metallic iron and sodium chromite are formed. When reduced samples are subjected to magnetic separation (see FIGURE 3-3 and FIGURE 8-1), it is possible to separate a magnetic fraction rich in metallic phase and a non-magnetic fraction which ideally contains $NaCrO_2$, MgO, $CaCO_3$ and the alkali silicates formed. Magnetic separation is carried out with water and therefore $NaAlO_2$ and part of the water-soluble silicates are solubilized during this stage.

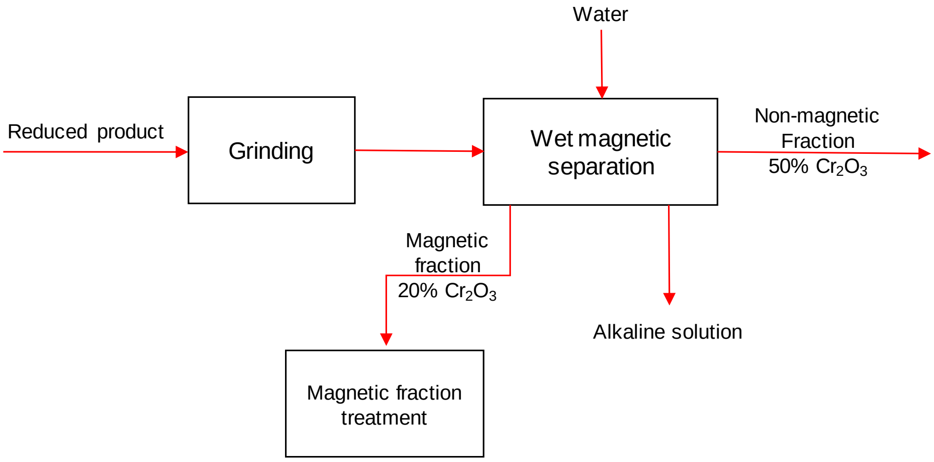

FIGURE 8-1. Sub-process flowsheet of the magnetic separation stage.

Since there is not formation of a liquid phase during reductive alkali roasting, the resultant reduced material is rather friable and does not require intensive crushing. However, grinding of reduced samples is needed before carrying out magnetic separation in order to liberate metallic iron from the reacted chromite particles. Grinding of reduced samples and 1st magnetic fractions for all samples was carried out in a mortar grinder Retsch® RM200 for 30 minutes. It is key for the process to determine the degree of grinding in order to optimise the magnetic separation stage and obtain maximum separation of $NaCrO_2$ in the non-magnetic fraction.

Reduced S.A. chromite samples were subjected to single or double magnetic separation stages and the X-ray powder diffraction patterns of the reduced sample, the 1st and 2nd magnetic fractions and the 1st and 2nd non-magnetic fractions are compared in FIGURE 8-2. A more detailed explanation of the procedure followed for magnetic separation can be found in section 3.2.4.1. The reduced material used was obtained by alkali reduction of S.A chromite ore with Na_2CO_3 and activated charcoal at 1050°C, for 2.5 hours and with a weight ratio chromite:Na_2CO_3:charcoal = 1:1:0.2.

The XRPD patterns in FIGURE 8-2 indicate that the magnetic fraction obtained after a single-step magnetic separation still contains significant amounts of $NaCrO_2$. This is due to the shape of the metallic iron particles formed during reduction, as already presented and discussed in Chapter 7. Since poor magnetic separation was achieved with a single grinding stage, an extra step of magnetic separation, was included. This consisted in further grinding of the magnetic fraction obtained for another 30 minutes in the mortar grinder and subsequent magnetic separation. This yielded a 2nd non-magnetic fraction rich in sodium chromite -which can be combined with the 1st non-magnetic fraction- and a 2nd magnetic fraction more enriched in metallic Fe. This is illustrated in FIGURE 8-2, where the peaks for $NaCrO_2$ and MgO are very low on the 2nd magnetic fraction pattern, and the main peak corresponds to Fe.

XRPD patterns for both non-magnetic fractions are not completely crystalline and peaks for sodium chromite could not been identified in these samples by this technique. This could be due to partial solubilisation of Na^+ thereby yielding non-stoichiometric compounds with the formula $Na_{1-x}CrO_2$. $CaCO_3$ and MgO can be seen in the non-magnetic fraction. Even though the amount of calcium in the ore is low, the intensity of calcium carbonate XRPD peaks is considerably high due to the high crystallinity of this phase.

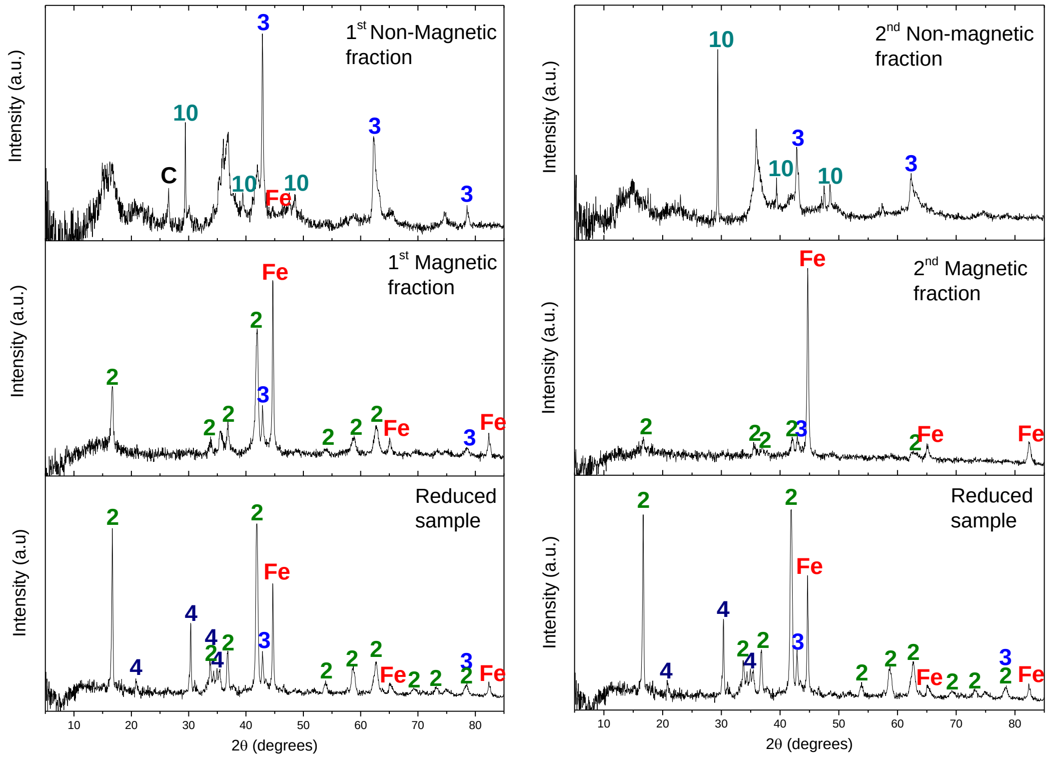

FIGURE 8-2. XRPD patterns of S.A. chromite reduced sample, magnetic and non-magnetic fractions. Reduction was carried out at 1050°C for 2.5 hours with chromite:Na_2CO_3:charcoal=1:1:0.2, followed by grinding and magnetic separation. [2=$NaCrO_2$, 3=MgO, 4=$NaAlO_2$, 10=$CaCO_3$, Fe=metallic iron and C=carbon]

The magnetic fraction contains residual sodium chromite, and the SEM analysis shows that this is due to entrapment of Fe in $NaCrO_2$ particles and sintering between both phases (FIGURE 8-3). After the second grinding and separation of the first magnetic fraction, the content of $NaCrO_2$ decreases significantly. This can be confirmed by looking at the backscattered SEM images of magnetic fractions in FIGURE 8-3, where the concentration of metallic iron particles is higher in the 2nd magnetic fraction compared to the 1st magnetic fraction. Therefore, double grinding and magnetic separation are required for improving the efficiency of the separation. The effect of the particle size of reduced samples on the efficiency of magnetic separation needs to be further investigated.

In FIGURE 8-4 and FIGURE 8-5, SEM images and elemental mapping of non-magnetic fraction are presented, respectively, confirming the presence of the sodium chromite phase which could not be identified by XRPD analysis. First and second non-magnetic fractions are combined for further treatment. The compositions of the final magnetic fraction and the combined non-magnetic are shown in TABLE 8-1. The magnetic fraction is rich in iron (71.20 wt% Fe_2O_3), and its main impurity is Cr_2O_3 which accounts for the 21.1 wt.%. On the other hand, the non-magnetic fraction is enriched in Cr_2O_3 (50.2 wt.%) and its main impurities are Fe_2O_3, Al_2O_3, MgO, SiO_2, Na_2O and CaO with concentrations ranging between 4.34 and 13.3 wt.%.

The proportion of magnetic fraction, non-magnetic fraction and alkali solution obtained after magnetic separation with respect to the reduced sample is approximately 17.50 wt.%, 42.30 wt.% and 40.20 wt.%, respectively.

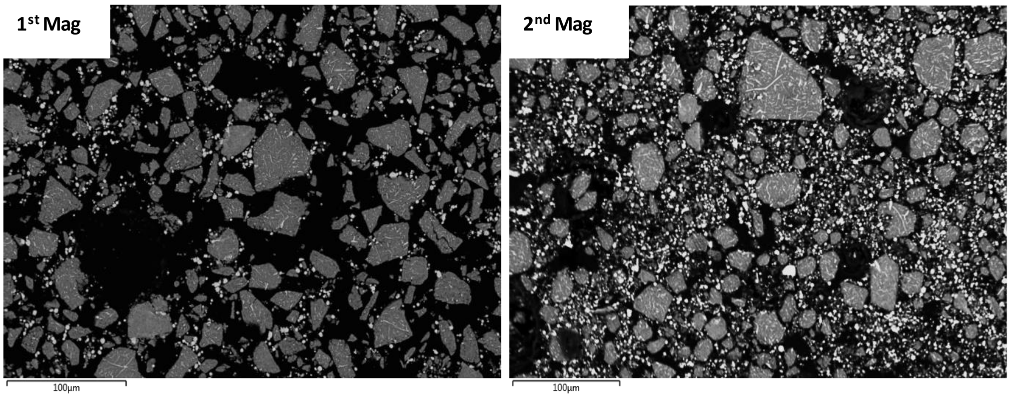

FIGURE 8-3. Secondary electron microscope (SEM) images of 1st and 2nd magnetic fractions obtained after two step magnetic separation. Chromite was reduced with Na_2CO_3 and charcoal (1050°C, 2.5 h).

The solution obtained after magnetic separation is highly alkaline due to:

a) Partial solubilisation of $NaCrO_2$, yielding non-stoichiometric phases ($Na_{1-x}CrO_2$)
b) Solubilisation of the $NaAlO_2$ formed during reduction
c) Solubilisation of the excess Na_2CO_3

The recovery of sodium as Na_2CO_3 is important from both the environmental and economic point of view, and therefore the alkaline solution is treated for alkali recovery as shown in the following chapter (Chapter 9).

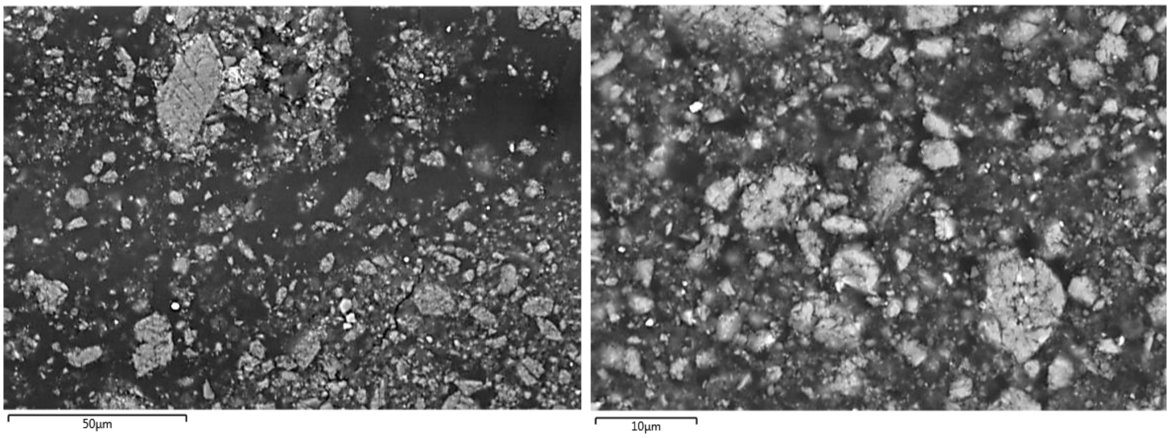

FIGURE 8-4. Secondary electron microscope (SEM) images of combined non-magnetic fractions obtained after two step magnetic separation. Chromite was reduced with Na_2CO_3 and charcoal (1050°C for 2.5 h).

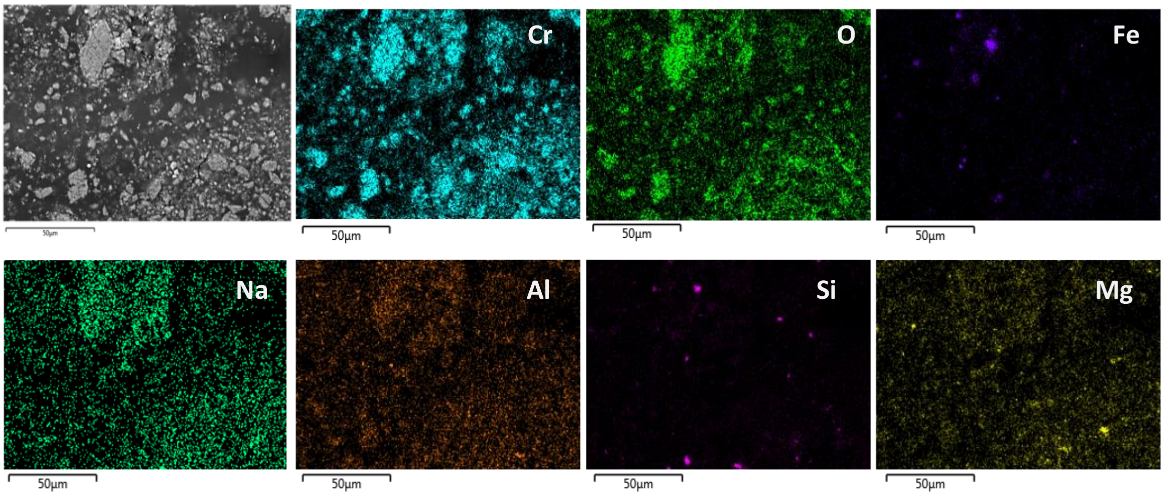

FIGURE 8-5. Elemental mapping of non-magnetic fraction obtained after two step magnetic separation. Chromite was reduced with Na_2CO_3 and charcoal (1050°C for 2.5 h).

TABLE 8-1. XRF analysis of magnetic and non-magnetic fractions after reduction of S.A. chromite ore with Na_2CO_3 and charcoal at 1050°C for 2.5 hours followed by grinding and magnetic separation.

wt.%	Cr_2O_3	Fe_2O_3	Na_2O	MgO	Al_2O_3	SiO_2	CaO
Magnetic fraction	21.10	71.20	1.60	1.99	1.85	0.45	0.59
Non-magnetic fraction	50.20	6.16	7.42	13.30	7.01	4.34	6.63

8.1.1.1. Magnetic separation of reduced Brazilian chromite samples

Magnetic separation of reduced samples of the Brazilian ores was performed following the same procedure. Reduced samples were obtained by reducing the Br.E4 and Br.E5 ores with Na_2CO_3 at 1050°C for 2.5 hours and a chromite:Na_2CO_3:C weight ratio of 1:1:0.2. The XRF analysis of the magnetic and non-magnetic samples can be seen in TABLE 8-2.

TABLE 8-2. XRF analysis of magnetic and non-magnetic fractions after reduction of Brazilian chromite ores with Na_2CO_3 and charcoal at 1050°C for 2.5 hours followed by grinding and magnetic separation.

Ore	wt.%	Cr_2O_3	Fe_2O_3	Na_2O	MgO	Al_2O_3	SiO_2	CaO
E4	**Magnetic fraction**	51.95	19.68	3.42	9.94	13.38	0.53	0.84
E4	**Non-magnetic fraction**	35.97	8.67	2.01	18.44	14.00	11.85	8.13
E5	**Magnetic fraction**	36.06	21.21	16.37	8.28	12.85	3.42	1.52
E5	**Non-magnetic fraction**	21.27	6.58	12.60	17.44	8.88	19.03	13.36

It is clear from TABLE 8-2 that the separation of metallic iron from the non-magnetic phases was poor. Both magnetic fractions are richer in iron than the corresponding non-magnetic fractions, however, the wt.% of Cr_2O_3 in the magnetic material is significantly high. This is due to the shape and size of the metallic Fe particles present in the reduced sample, which are small and have fine needle shape (FIGURE 8-6). Furthermore, the proportion of metallic Fe in the reduced sample is rather smaller than with S.A. chromite ore (the content of Fe_2O_3 in Brazilian ores is lower), and therefore the efficiency of magnetic separation falls dramatically. The phases formed during reduction from the rest of elements in chromite, such as $NaCrO_2$, $NaAlO_2$ and MgO, remain attached to the small metallic iron particles. This results in an important fraction of them being dragged into the magnetic fraction. By contrast, XRF results TABLE 8-2 show that SiO_2 is concentrated in the non-magnetic fraction, which suggests that the complex silicate phases formed during alkali reduction can be preferentially extracted into this fraction.

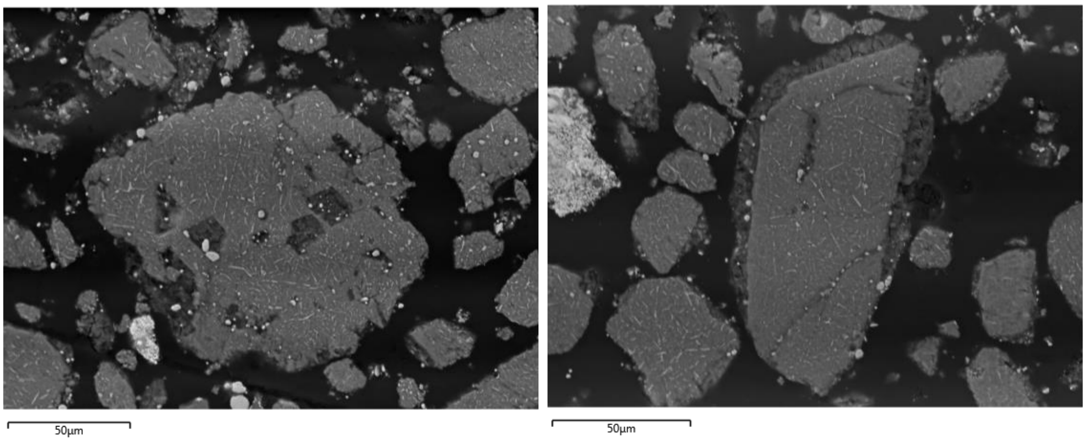

FIGURE 8-6. Backscattered SEM images of the magnetic fraction after reduction of Brazilian chromite ores with Na_2CO_3 and charcoal at 1050°C for 2.5 hours (wt. ratio chromite:Na_2CO_3:C = 1:1:0.2) followed by grinding and magnetic separation.

In order to consider this type of Brazilian ores as a raw material for the reductive alkali roasting process, the efficiency of the magnetic separation needs to be improved. Since the main limitation is the formation of metallic Fe, it is necessary to increase the fraction of iron oxides in the ores, so that the growth of metallic Fe during reduction is enhanced. The co-processing of COPR waste, containing high Fe_2O_3, and Brazilian ores by alkali reduction could be an interesting option since the Fe_2O_3 fraction in the charge would be increased with the simultaneous remediation of the waste.

8.1.2. EFFECT OF REDUCTION PROCESS PARAMETERS ON THE SEPARATION OF $NaCrO_2$ BY MAGNETIC SEPARATION IN THE TREATMENT OF S.A. CHROMITES

The influence of temperature, time, Na_2CO_3 and activated charcoal ratios during the reduction stage on the efficiency of the magnetic separation was studied. The wt.% Cr_2O_3 of chromium in the non-magnetic fraction is the key variable to study the efficiency of the separation. The XRF results of magnetic and non-magnetic fraction after reduction varying temperature, time and Na_2CO_3 and charcoal ratios are shown in FIGURE 8-7 A-D.

The stacked bars represent the composition of the samples as metal oxides that were analysed by XRF. The line shows the %extraction of chromium into the non-magnetic fraction taking into account the wt.% Cr_2O_3 in the non-magnetic fraction and initial chromite ore, and the weight of the non-magnetic fraction. The %extraction was calculated following equation (eq.14).

$$\%\ \text{Extraction} = \frac{\frac{\%\ Cr_2O_{3\ nonmag}}{100} \cdot Wt_{nonmag}}{\frac{\%\ Cr_2O_{3\ chromite}}{100} \cdot Wt_{chromite}} \cdot 100 \qquad \text{(eq.14)}$$

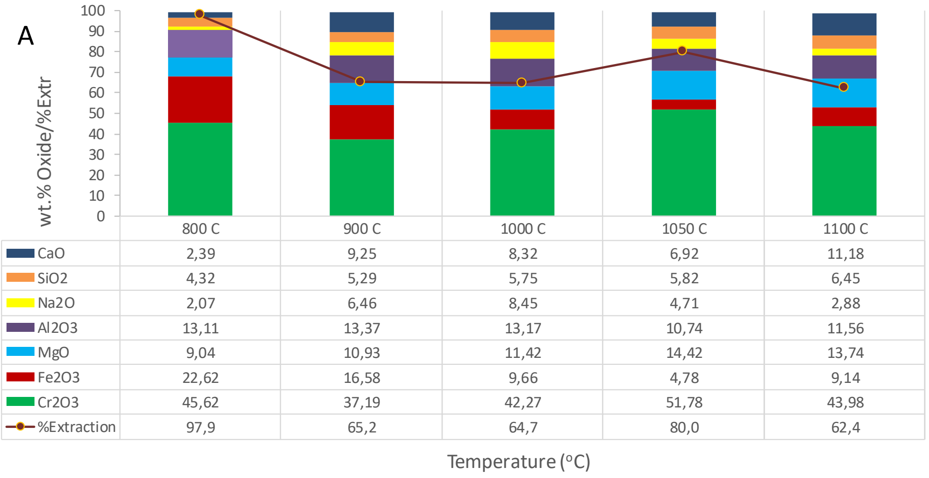

	800 C	900 C	1000 C	1050 C	1100 C
🟦 CaO	2,39	9,25	8,32	6,92	11,18
🟧 SiO2	4,32	5,29	5,75	5,82	6,45
🟨 Na2O	2,07	6,46	8,45	4,71	2,88
🟪 Al2O3	13,11	13,37	13,17	10,74	11,56
🟦 MgO	9,04	10,93	11,42	14,42	13,74
🟥 Fe2O3	22,62	16,58	9,66	4,78	9,14
🟩 Cr2O3	45,62	37,19	42,27	51,78	43,98
● %Extraction	97,9	65,2	64,7	80,0	62,4

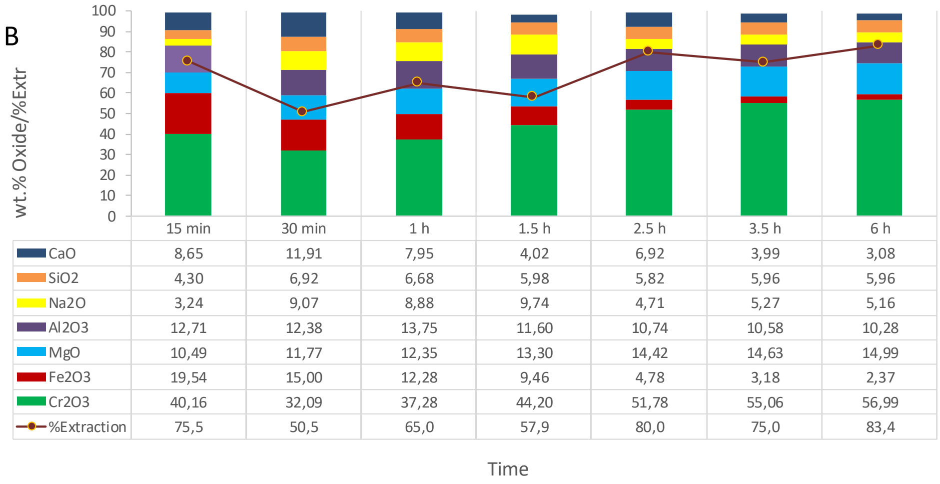

	15 min	30 min	1 h	1.5 h	2.5 h	3.5 h	6 h
🟦 CaO	8,65	11,91	7,95	4,02	6,92	3,99	3,08
🟧 SiO2	4,30	6,92	6,68	5,98	5,82	5,96	5,96
🟨 Na2O	3,24	9,07	8,88	9,74	4,71	5,27	5,16
🟪 Al2O3	12,71	12,38	13,75	11,60	10,74	10,58	10,28
🟦 MgO	10,49	11,77	12,35	13,30	14,42	14,63	14,99
🟥 Fe2O3	19,54	15,00	12,28	9,46	4,78	3,18	2,37
🟩 Cr2O3	40,16	32,09	37,28	44,20	51,78	55,06	56,99
● %Extraction	75,5	50,5	65,0	57,9	80,0	75,0	83,4

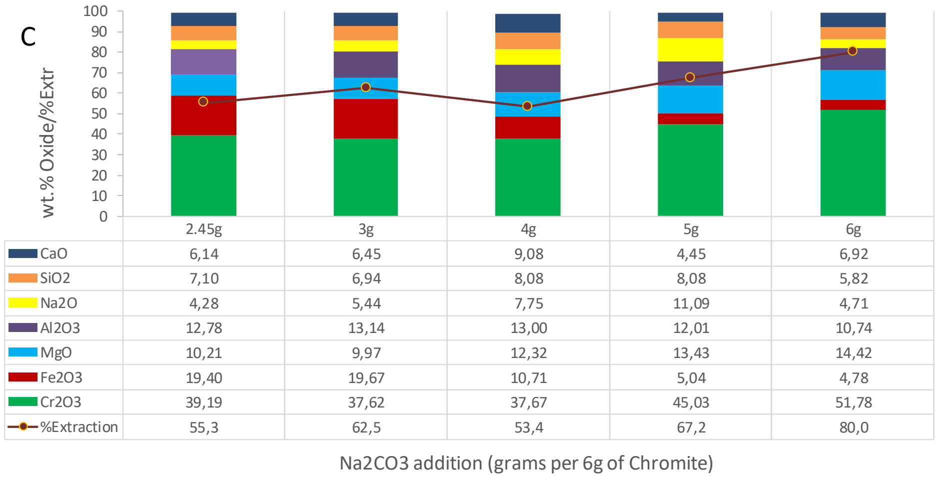

	2.45g	3g	4g	5g	6g
🟦 CaO	6,14	6,45	9,08	4,45	6,92
🟧 SiO2	7,10	6,94	8,08	8,08	5,82
🟨 Na2O	4,28	5,44	7,75	11,09	4,71
🟪 Al2O3	12,78	13,14	13,00	12,01	10,74
🟦 MgO	10,21	9,97	12,32	13,43	14,42
🟥 Fe2O3	19,40	19,67	10,71	5,04	4,78
🟩 Cr2O3	39,19	37,62	37,67	45,03	51,78
● %Extraction	55,3	62,5	53,4	67,2	80,0

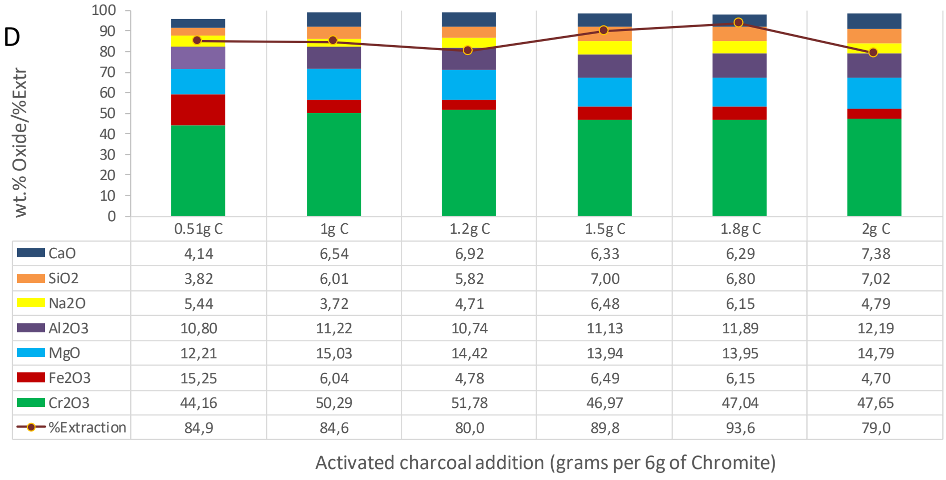

	0.51g C	1g C	1.2g C	1.5g C	1.8g C	2g C
CaO	4,14	6,54	6,92	6,33	6,29	7,38
SiO2	3,82	6,01	5,82	7,00	6,80	7,02
Na2O	5,44	3,72	4,71	6,48	6,15	4,79
Al2O3	10,80	11,22	10,74	11,13	11,89	12,19
MgO	12,21	15,03	14,42	13,94	13,95	14,79
Fe2O3	15,25	6,04	4,78	6,49	6,15	4,70
Cr2O3	44,16	50,29	51,78	46,97	47,04	47,65
%Extraction	84,9	84,6	80,0	89,8	93,6	79,0

FIGURE 8-7. Chemical composition of non-magnetic fraction samples from S.A. chromite reduced samples as a function of A) Reduction temperature (2.5 h, chromite:Na_2CO_3:C = 1:1:0.2); B) Reduction time (1050°C, chromite:Na_2CO_3:C = 1:1:0.2); C) Na_2CO_3 addition (1050°C, 2.5 hours, chromite:charcoal = 1:0.2);+ and D) Activated charcoal addition (1050°C, 2.5 hours and chromite:Na_2CO_3 = 1:1). Samples were analysed by XRF.

The main conclusions that can be obtained from the XRF results in FIGURE 8-7 are the following:

a) The higher extraction and wt.% Cr_2O_3 were obtained for reduction at 1050°C. At 800°C, both the %extraction and wt.% Cr_2O_3 in non-magnetic fraction are high. However, the reduced samples at this temperature did not show complete formation of metallic iron (see Chapter 7) and a magnetic fraction did not form. Therefore, no separation was achieved; all chromium is in the non-magnetic fraction, and the wt.% Cr_2O_3 is very close to that of S.A. chromite ore. The minimum wt.% Fe_2O_3 is also present in the sample reduced at 1050°C, which indicates a more efficient separation of iron-rich phases and chromium-rich phases after reduction at this temperature.

b) The %extraction of chromium into the non-magnetic fraction increases with increasing reduction time. The sample reduced for only 15 minutes falls out of this tendency due to the poor formation of magnetic fraction. The higher wt.% Cr_2O_3 is achieved after 6 hours reduction (56.99 wt.% Cr_2O_3), while the maximum figure for %extraction can be observed after 2.5 hours.

c) The optimum chromite:Na_2CO_3:charcoal weight ratio, according to XRF results, is 1:1:0.2. Higher addition of Na_2CO_3 achieves higher separation of $NaCrO_2$ into the non-magnetic fraction. On the other hand, separation improves with increasing charcoal addition until a weight ratio of chromite:charcoal = 1:0.2, and then decreases when the ratio is increased.

d) In order to maximise separation, a compromise between the wt.% Cr_2O_3 of the non-magnetic fraction and the %extraction is required. Based on the results presented, the optimum conditions selected for reduction of S.A. chromite ore are 1050°C, 2.5 hours and a chromite:Na_2CO_3:charcoal weight ratio equal to 1:1:0.2. With this set of parameters, a %extraction and wt.%Cr_2O_3 of 80% and 51,78 wt.% were achieved.

8.2. WATER LEACHING OF NON-MAGNETIC FRACTION

Following alkali reduction and magnetic separation, the non-magnetic fractions are water-leached at a temperature of 50°C for 1.5 hours (see section 3.2.4.2), as shown in FIGURE 8-8.

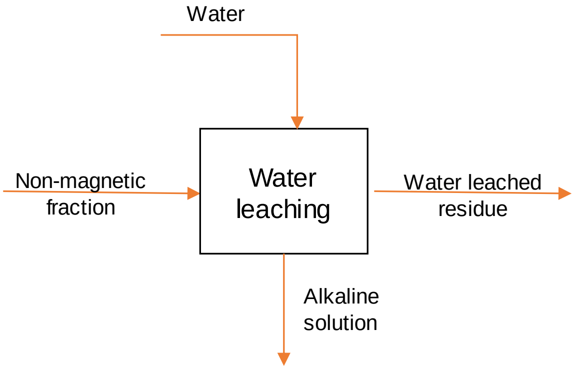

FIGURE 8-8. Sub-flowsheet of the water leaching stage.

The purpose of the water leaching stage is to selectively solubilise water-soluble impurities remaining in the non-magnetic fraction in order to:

a) recover as much sodium as possible from the non-magnetic fraction so that sodium carbonate can be recovered from the alkaline solution obtained.

b) obtain a water-soluble product richer in Cr_2O_3.

The Eh-pH diagram in FIGURE 8-9 shows the phase equilibria of the system Na-Cr-Al-H_2O at 323K (50°C), in terms of the potential and the pH of the aqueous media.

The typical pH values under the experimental conditions of water leaching are in the range of pH = 10. Since the leaching is carried out in air atmosphere, the potential of the solution is expected to be within the limit of O_2 = 1 atm and H_2 = 1 atm. Therefore, sodium and aluminium phases contained in the non-magnetic fractions are able to solubilise in aqueous media under the conditions of the water leaching process, while chromium as Cr_2O_3 remains in the water-leached solid product. According to the Eh-pH diagram computed, Cr_2O_3 coexists with $Al_2O_3 \cdot (H_2O)$ and Na^+ ions for a potential ranging between -0.9 and 1 volt approximately, and pH higher than 3.

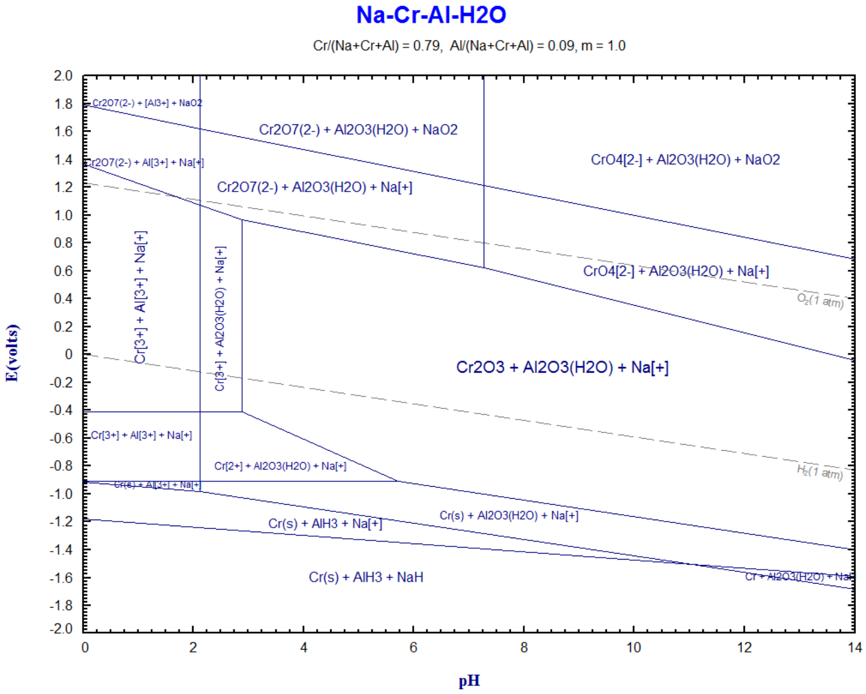

FIGURE 8-9. E_H-pH phase diagram of the Na-Cr-Al-H_2O system at 323K computed using FactSage 6.4.

If the water leaching achieves the extraction of most of the remaining sodium at this point, the consumption of acid during the subsequent acid leaching step may be decreased significantly. Water soluble compounds that were not removed during wet magnetic separation are also solubilized during water leaching, thereby increasing the purity of the resultant water-leached product. The leachate solution obtained is rich in alumina, silica and Na^+. The solution can be combined with the alkali solution obtained during magnetic separation for subsequent alumina and Na_2CO_3 recovery. There is a possibility of eliminating the water-leaching step from the process flowsheet if sodium solubilisation could be maximised during wet magnetic separation. Further tests with different set-ups for magnetic separation are required to study the water-leaching occurring at this stage.

8.2.1. CHARACTERIZATION OF WATER-LEACHED PRODUCTS

The chemical composition of the non-magnetic fraction and the water-leached residue, analysed by XRF, are compared in TABLE 8-3. The non-magnetic fraction was obtained by reduction of chromite with Na_2CO_3 and charcoal (chromite:Na_2CO_3:charcoal = 1:1:0.2) at 1050°C for 2.5 hours and succeeding magnetic separation. Water leaching of the non-magnetic fraction was carried out for 1.5 hours at 50°C, and a water-leached precipitate and an alkaline solution were obtained by filtration. The water from the alkaline solution was removed by heating obtaining a precipitate powder which could be analysed by semi-quantitative XRF analysis.

TABLE 8-3. Chemical composition of non-magnetic fraction, residue and solution after water leaching analysed by XRF.

wt.%	Cr_2O_3	Fe_2O_3	MgO	Al_2O_3	Na_2O	SiO_2	CaO
Non-mag fraction	50.1	5.16	13.3	7.01	7.42	4.34	0.29
Water-leached precipitate	55.3	5.3	13.2	6.04	1.83	3.64	0.17
Solution after water leaching (dried)	1.6	2.52	0.982	0.981	70.7	4.76	1.48

According to XRF results, most of the chromium remains in the water-leached precipitate, and only a small fraction solubilises during water leaching. The resulting water-leached product is 55.3 wt.% Cr_2O_3-rich, whereas the dried solution contains only 1.6 wt.% Cr_2O_3. The concentration of all impurities decreases after water leaching but the solubilisation of sodium is significantly higher. The 65.15 wt.% of the remaining sodium in the non-magnetic fraction is extracted at this stage. The results indicate that a 5% enrichment was attained by the water leaching step.

Since XRF analysis does not provide information about the oxidation state of the present elements, it is necessary to further analyse the solution to determine if chromium is present in either Cr^{3+} or Cr^{6+} state. In any case, this solution is incorporated back into the process at the alkali recovery stage, and therefore it is not a waste of the process that needs to be disposed of.

8.3. ACID LEACHING OF THE NON-MAGNETIC FRACTION

The material obtained from water leaching was further leached in inorganic/organic acid media with the aim of removing the remaining impurities obtaining a Cr_2O_3-rich material which is the final product of the process. The part of the process flowsheet corresponding to the acid leaching step is shown in FIGURE 8-10.

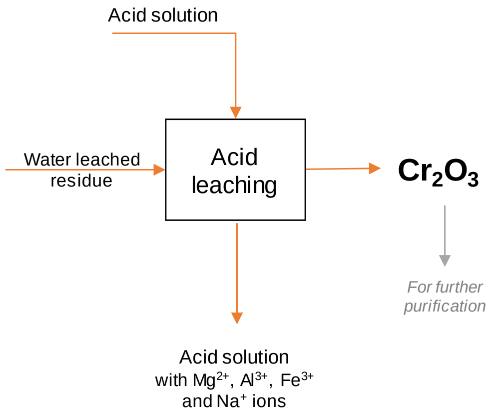

FIGURE 8-10. Sub-flowsheet of the acid leaching step.

The XRF analysis in TABLE 8-3 shows that the main impurities in the water-leached material are, in order of concentration, MgO, Al_2O_3, Fe_2O_3, SiO_2, CaO and Na_2O. The parameters of acid leaching were studied in order to remove the remaining sodium from the partially leached sodium chromite ($Na_{1-x}CrO_2$) and the sodium magnesium silicates present in the non-magnetic fraction. Remaining alumina in form of complex silicates also need to be removed at this stage. The parameters of acid leaching such as acid concentration, temperature, time and the acid employed were studied experimentally. A series of both inorganic and organic acids were tested, and the starting material used for the tests was standard water-leached material produced following standard conditions of the process.

8.3.1. LEACHING WITH DIFFERENT ACIDS

The nature of the acid used at the leaching stage is expected to influence the purity of the resulting material. The degree of solubilisation of the different impurities present in the water-leached material depending on the acid used has been studied by a set of leaching experiments. A selection of inorganic and organic acids were tested, namely citric, lactic, tartaric, acetic, sulfuric, oxalic, ascorbic, phosphoric, HCl and nitric. All experiments were carried out at a concentration of 0.5 M, at 50°C for 1.5 hours.

The dried precipitates were analysed by XRPD in order to determine any differences in terms of phase composition. As example, the XRPD patterns of the precipitates obtained after leaching with H_2SO_4 and oxalic acid are shown in FIGURE 8-11. The only phase identified in the patterns is Cr_2O_3. Broad peaks are also present in a range of 2θ of 5 to 20 which can be due to the presence of amorphous phases in the samples. The main difference between the samples is the relative intensity of the three main peaks of the Cr_2O_3 phase.

The acid-leached samples were analysed by XRF in order to determine their chemical composition. The results are shown in FIGURE 8-12.

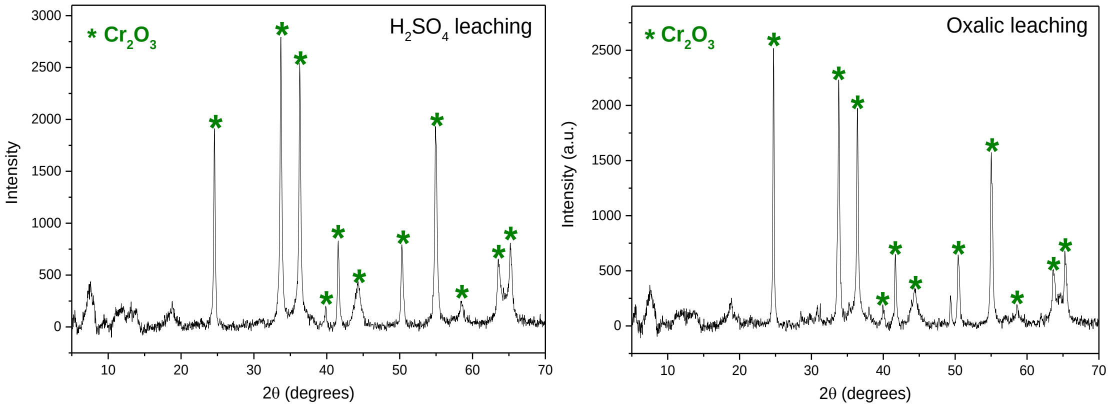

FIGURE 8-11. X-ray powder diffraction patterns residues after leaching with sulfuric and oxalic acid. Leaching experiments were carried out at 50°C for 2 hours.

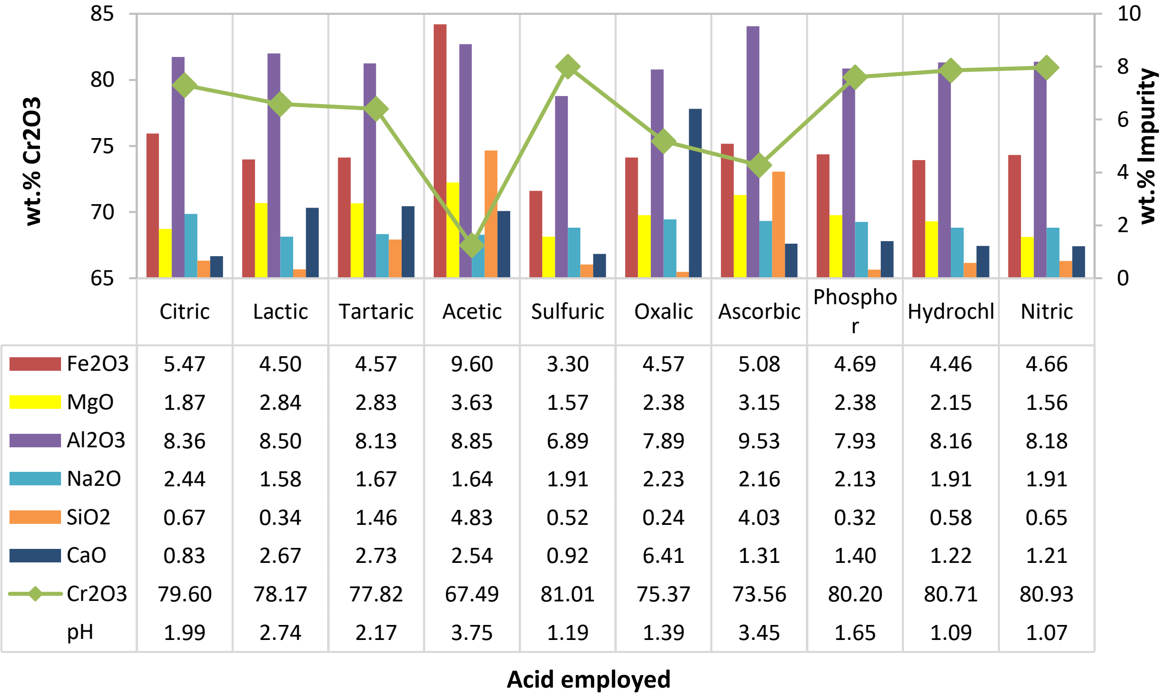

	Citric	Lactic	Tartaric	Acetic	Sulfuric	Oxalic	Ascorbic	Phosphor	Hydrochl	Nitric
Fe2O3	5.47	4.50	4.57	9.60	3.30	4.57	5.08	4.69	4.46	4.66
MgO	1.87	2.84	2.83	3.63	1.57	2.38	3.15	2.38	2.15	1.56
Al2O3	8.36	8.50	8.13	8.85	6.89	7.89	9.53	7.93	8.16	8.18
Na2O	2.44	1.58	1.67	1.64	1.91	2.23	2.16	2.13	1.91	1.91
SiO2	0.67	0.34	1.46	4.83	0.52	0.24	4.03	0.32	0.58	0.65
CaO	0.83	2.67	2.73	2.54	0.92	6.41	1.31	1.40	1.22	1.21
Cr2O3	79.60	78.17	77.82	67.49	81.01	75.37	73.56	80.20	80.71	80.93
pH	1.99	2.74	2.17	3.75	1.19	1.39	3.45	1.65	1.09	1.07

FIGURE 8-12. Chemical composition of acid-leached solid precipitates after leaching with different organic and inorganic acids of concentration 0.5 M. Samples were analysed by XRF.

The table shown in FIGURE 8-12 shows the values for wt.% of Cr_2O_3 and the different impurities, given by XRF analysis. The purity of the Cr_2O_3-rich products obtained range between 67.49 wt.% and 81.01 wt.% for acetic and sulfuric acids, respectively. The wt.% of Cr_2O_3 increases in the following order:

acetic < ascorbic < oxalic < tartaric < lactic < citric < phosphoric < hydrochloric < nitric < sulfuric

According to the trend shown, inorganic acids are able to achieve higher purities of Cr_2O_3 in the precipitates in general. The lower purity achieved with organic acids was 67.49 wt.% Cr_2O_3 with acetic acid, which was not able to solubilise Fe_2O_3 and SiO_2 in the same extent in comparison with other acids tested. SiO_2 and Al_2O_3 were also high in the sample leached with ascorbic acid, which produced a precipitate of 73.56 wt.% Cr_2O_3. In the case of oxalic acid, the content of CaO was significantly higher than the rest of acids, otherwise, the purity of the product could be comparable with that obtained with inorganic acids. The wt.% of Na_2O is very similar in all the samples and ranges between 1.58% to 2.44%.

The pH was measured during the leaching experiments with the different acids, and the values obtained are also shown in FIGURE 8-12. The pH of the solutions decreases in the following order:

acetic < ascorbic < lactic < tartaric < citric < phosphoric < oxalic < sulfuric < hydrochloric < nitric

This trend is very similar to the one followed by the wt.% of Cr_2O_3 in the leached products, which suggests that the pH of the solution plays an important role on the leaching chemistry. According to the results, the purity of the precipitates increases with decreasing pH. Oxalic acid, however, does not follow that tendency, as the purity achieved is lower than other acids with solutions of higher pH. The pH does not vary significantly for H_2SO_4, HCl and HNO_3 acids, which are in the range of 1.19 to 1.07, and all yielded leached products of similar purity. Sulfuric acid achieved the product with higher purity, which has a Cr_2O_3 content of 81.01 wt.%.

The leaching in acidic media for selective dissolution of metal ions has been previously studied by various authors for the treatment of many different mineral samples [126,127,128,129,130,131]. In particular, sulfuric acid has been extensively employed for the dissolution of metal ions and silicate minerals. In the case of the leaching of the non-magnetic fraction with H2SO4 0.5 M, the dissolution chemistry is expected to include reactions (r.73) to (r.77) below.

$$MgO\ (s) + 2\ H^+\ (aq) \rightarrow Mg^{2+}\ (aq) + 2\ H_2O\ (l) \qquad (r.73)$$

$$FeO\ (s) + 2\ H^+(aq) \rightarrow Mg^{2+}\ (aq) + 2\ H_2O\ (l) \qquad (r.74)$$

$$2\ NaCrO_2\ (s) +\ 2\ H^+\ (aq) \rightarrow\ 2\ Na^{2+}\ (aq) +\ Cr_2O_3\ (s) +\ H_2O\ (l) \qquad (r.75)$$

$$Na_4SiO_4\ (s)\ +\ 4\ H^+\ (aq) \rightarrow\ 4\ Na^+\ (aq) +\ H_4SiO_4(aq) \qquad (r.76)$$

$$NaAlSiO_4(s)\ +\ 4\ H^+(aq) \rightarrow\ Na^+(aq) +\ Al^{+3}(aq) + H_4SiO_4\ (aq) \qquad (r.77)$$

8.3.2. EFFECT OF ACID CONCENTRATION

The effect of acid concentration was studied by performing leaching experiments with four different concentrations of sulfuric acid, namely 0.05M, 0.1M, 0.25M and 0.5M. Experiments were performed at 50°C during 2 hours with a solid:liquid ratio of 1:100 g/mL. The solid precipitates were filtered, dried and analysed by XRF; and the results are presented in FIGURE 8-13.

The graph shows the percentage of the different impurities present in each sample represented by the bars. The weight percentage of Cr_2O_3 is represented by the green line and marker, which shows the trend followed. The exact figures are shown in the table underneath the graph. Results illustrate that the purity of Cr_2O_3-rich products increases with increasing acid molarity. The purity of the solid Cr_2O_3 precipitates obtained by XRF increases from 75.41 to 81.01 wt.% with increasing acid strength and acid concentrations ranging between 0.05 and 0.5 M.

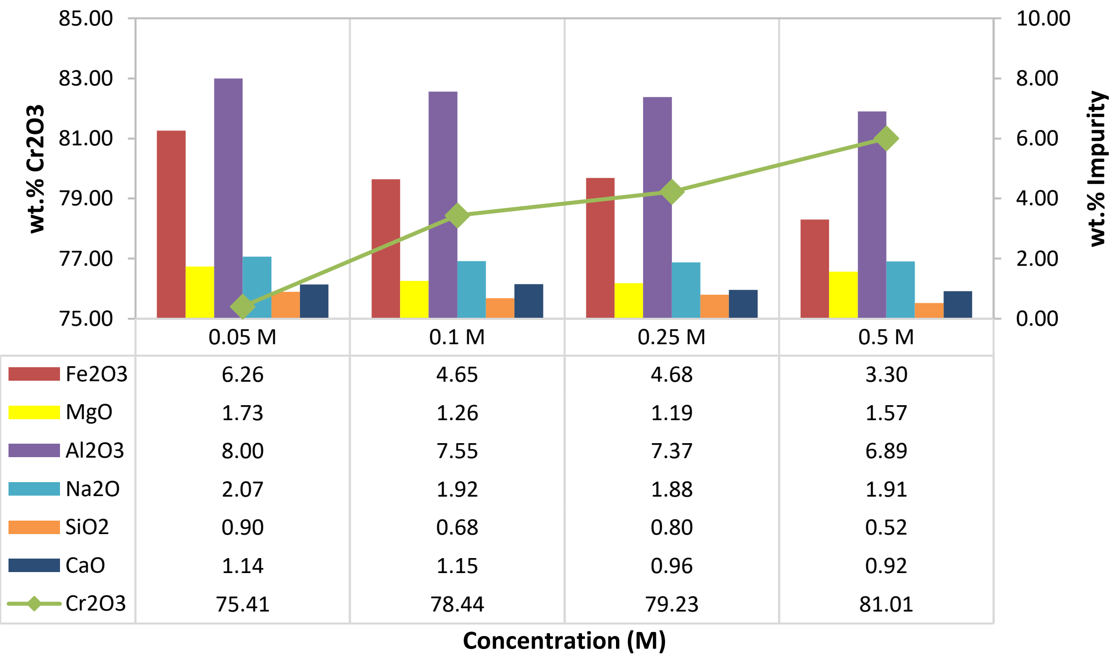

	0.05 M	0.1 M	0.25 M	0.5 M
🟥 Fe2O3	6.26	4.65	4.68	3.30
🟨 MgO	1.73	1.26	1.19	1.57
🟪 Al2O3	8.00	7.55	7.37	6.89
🟦 Na2O	2.07	1.92	1.88	1.91
🟧 SiO2	0.90	0.68	0.80	0.52
■ CaO	1.14	1.15	0.96	0.92
◆ Cr2O3	75.41	78.44	79.23	81.01

FIGURE 8-13. Chemical composition of acid-leached solid precipitates after leaching with sulfuric acid of concentrations 0.05M, 0.1M, 0.25M and 0.5M. Samples were analysed by XRF.

8.3.3. EFFECT OF SOLID-TO-LIQUID RATIO

The effect of the solid-to-liquid ratio on acid leaching of water-leached samples has been studied by testing different solid-to-liquid ratios (g/mL) ranging between 1:30 and 1:150 using a solution of H_2SO_4 in water of concentration 0.5M. Experiments were carried out at 50°C for 2 hours, and the residues obtained were dried and analysed by XRF. The chemical composition of the acid leached residues can be seen in FIGURE 8-14.

In this case, the effect of the solid-to-liquid ratio on the purity of the final product is not as pronounced as on the previous case. The wt.% of Cr_2O_3 increases in only 0.5% from the lower to the higher limits of solid-to-liquid ratio. The corresponding to a solid-to-liquid ratio of 1:50 does not follow totally this trend, and this can be due to experimental or analytical errors. The higher purity obtained in this set of experiments is 81.11 wt.% which corresponds to the sample leached with a ratio of 1:150. Since the range of purities obtained is not very wide, the optimisation of the solid-to-liquid ratio is required taking into account the increase of the cost of the leaching solution and the corresponding increase in purity achieved.

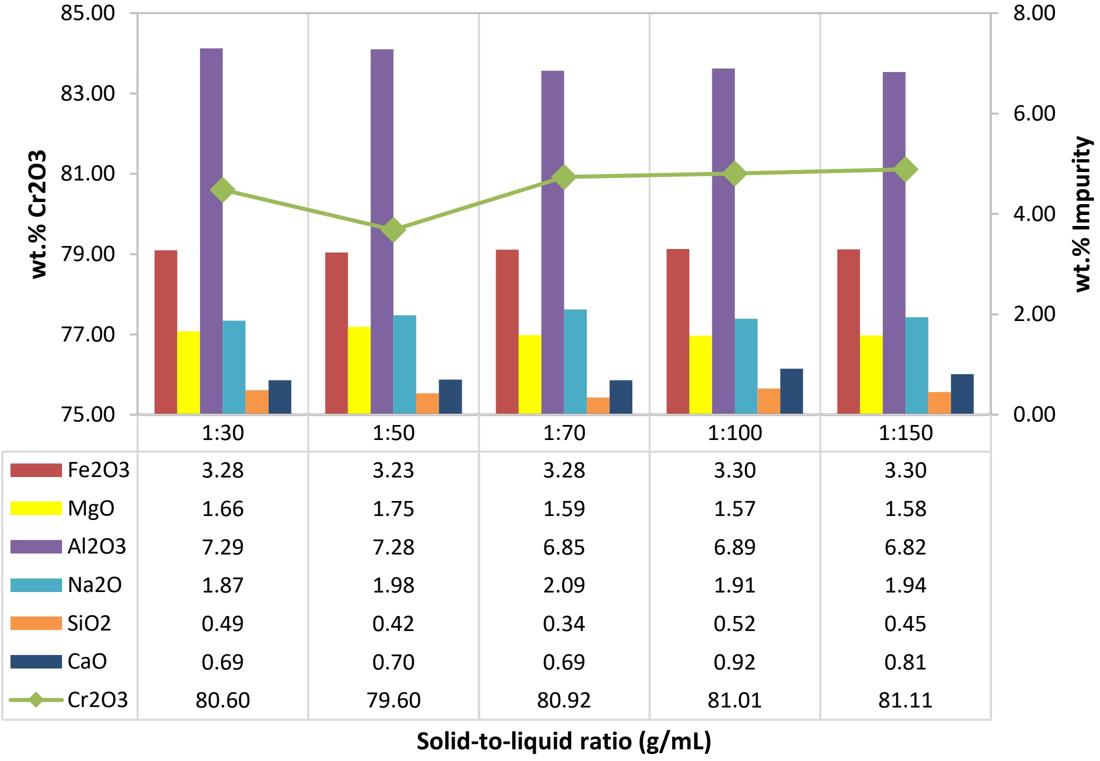

	1:30	1:50	1:70	1:100	1:150
Fe2O3	3.28	3.23	3.28	3.30	3.30
MgO	1.66	1.75	1.59	1.57	1.58
Al2O3	7.29	7.28	6.85	6.89	6.82
Na2O	1.87	1.98	2.09	1.91	1.94
SiO2	0.49	0.42	0.34	0.52	0.45
CaO	0.69	0.70	0.69	0.92	0.81
Cr2O3	80.60	79.60	80.92	81.01	81.11

FIGURE 8-14. Chemical composition of acid leached residues after sulfuric acid leaching with different solid:liquid ratios (g/mL) expressed in grams per millilitres. Samples were analysed by XRF.

8.3.4. EFFECT OF LEACHING TEMPERATURE AND TIME

The progress of leaching with time and the effect of temperature and time on the purity of Cr_2O_3-rich products were studied. Leaching experiments at three different temperatures, namely room-temperature (20°C), 50°C and 80°C, were performed to study the time and temperature effect. The experiments were carried out with 15 g of water-leached residue of composition 55.3 wt.% Cr_2O_3, 5.3 wt.% Fe_2O_3, 13.2 wt.% MgO, 6.04 wt.% Al_2O_3, 1.83 wt.% Na_2O, 3.64 wt.% SiO_2 and 0.17 wt.% CaO, which was leached with H_2SO_4 0.25M, a solid-to-liquid ratio of 1:100 and a total leaching volume of 1.5 L. In this case, liquid samples of 10 mL of volume were taken at continuous intervals and analysed by AAS in order to follow the solubilisation of the different impurities over time.

FIGURE 8-15 shows plots for the concentration of the different elements in solution against time. The elements analysed were Cr, Fe, Mg, Al, Na and Si; and the samples were taken at intervals of 2, 5, 8, 10, 15, 30, 45, 60, 75, 90, 105 and 120 minutes.

The plots showing the extraction of the different elements over time indicate that the impurities solubilise rapidly. The concentration in solution increases in the first instants of leaching and then flattens out. Therefore, the final concentration is reached within 5 to 10 minutes of leaching, which shows that the kinetics of acid leaching of the water-leached residues with H_2SO_4 are fast. The curves for Cr dissolution at different temperatures show that the final concentration of chromium in solution is approximately 40 mg/L when leaching at room temperature and 50°C. When the temperature is increased to 80°C, the concentration of Cr in solution is in the order of 40 mg/L after 2 minutes but keeps raising at a continuous pace until a final value of 106 mg/L after 2 hours of leaching. The various impurities present follow the same pattern, as they are extracted into solution within the first minutes of leaching. For Fe, Al and Mg, the final concentration in the solution is slightly higher at 80°C compared to room temperature and 50°C, but it seems that temperature does not have a big effect on their final concentration in solution. However, in the case of Na the effect of temperature is more significant, and the solubilisation increases with temperature from 115 mg/L at room temperature to 177 mg/L at 80°C. The dissolution of Si follows a similar tendency over time at room temperature and 80°C, but shows a decrease in solubility at 50°C, which can be due to precipitation of a silicate phase in the first minutes of leaching. As a conclusion, the results in FIGURE 8-15 indicate that the chemical equilibrium is achieved rapidly within 10 minutes of leaching a Cr_2O_3-rich water-leached material with H_2SO_4.

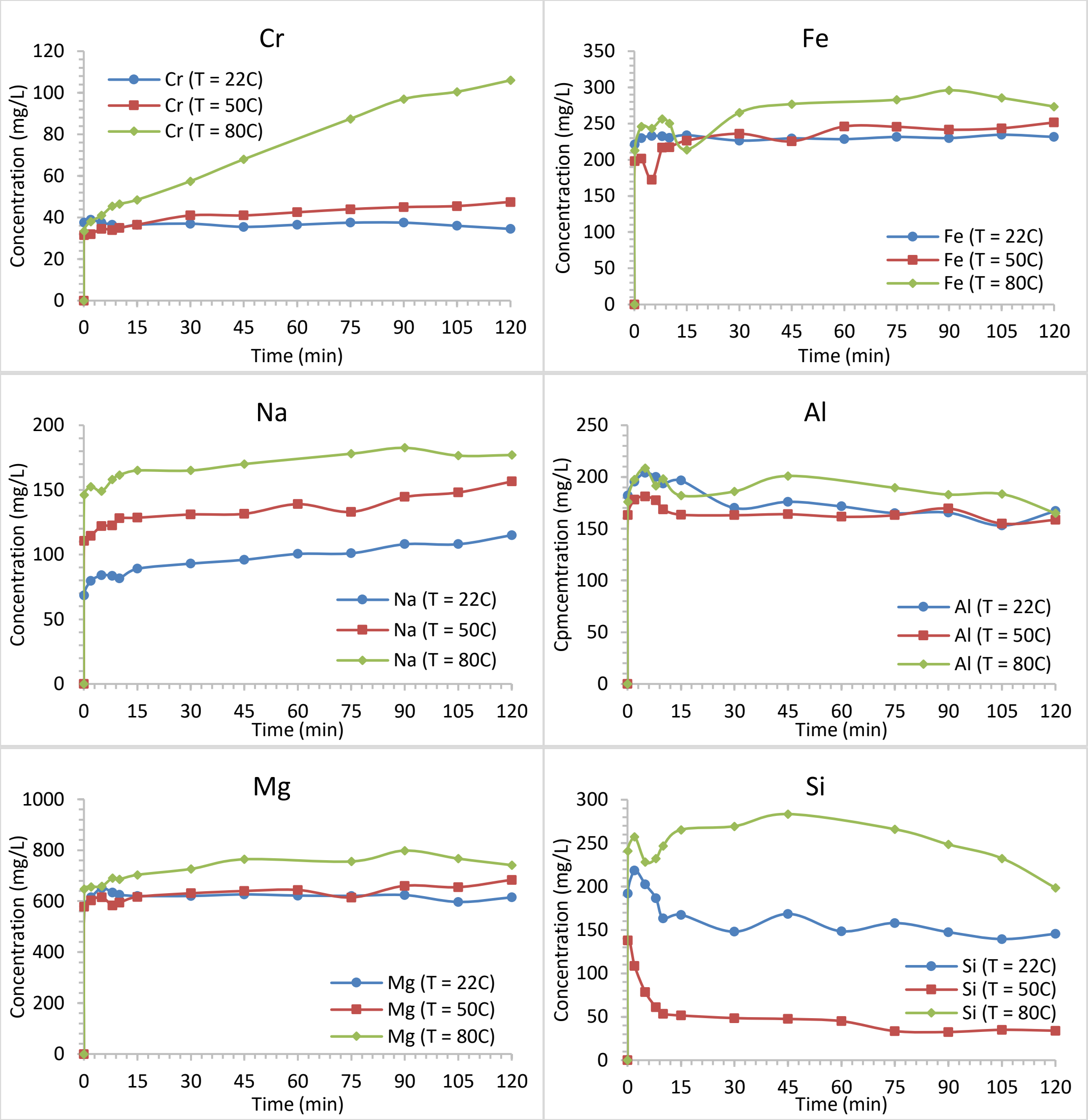

FIGURE 8-15. Concentration versus time curves of individual elements (Cr, Fe, Na, Al, Mg and Si) at different temperatures in acid leaching solutions.

Acid leaching experiments varying the leaching time were also performed at 50°C, yielding Cr_2O_3-products that were dried and analysed by XRF. The composition of the samples obtained with different leaching times is shown in FIGURE 8-16.

The results shown in FIGURE 8-16 confirm that the leaching kinetics are fast as already discussed in the previous set of experiments in FIGURE 8-15. The wt.% of Cr_2O_3 increases only 2 wt.% from a leaching time of 10 minutes to 6 hours. For a leaching time of 2 hours a solid precipitate with 81.01 wt.% Cr_2O_3 was obtained, and since there is not a significant increase in purity after leaching for 6 hours, 2 hours was the leaching time used for most of the leaching experiments carried out and discussed in this chapter.

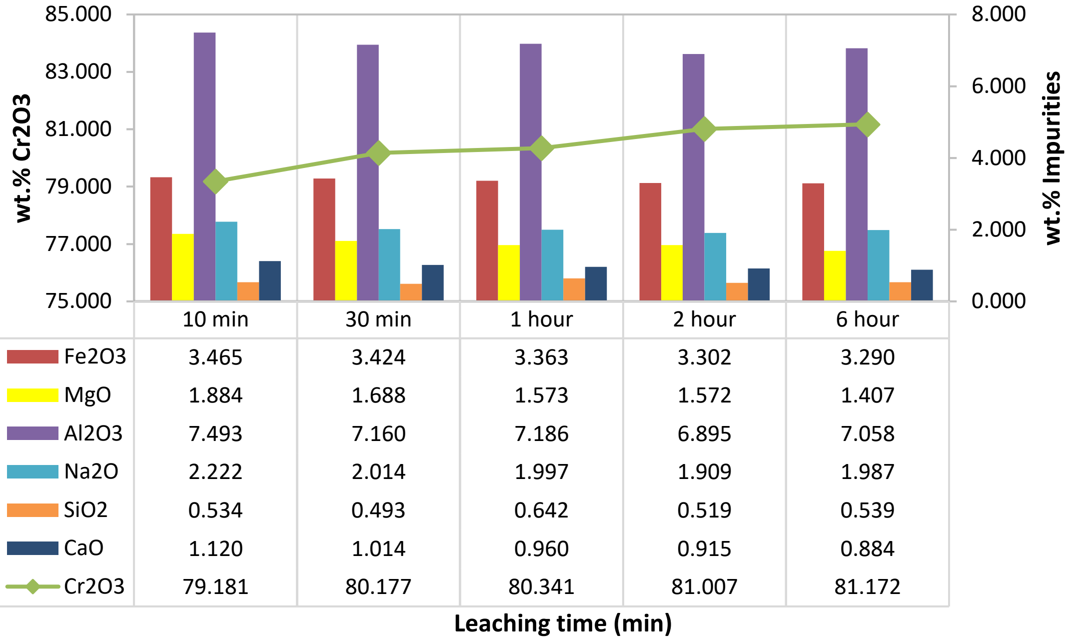

	10 min	30 min	1 hour	2 hour	6 hour
Fe2O3	3.465	3.424	3.363	3.302	3.290
MgO	1.884	1.688	1.573	1.572	1.407
Al2O3	7.493	7.160	7.186	6.895	7.058
Na2O	2.222	2.014	1.997	1.909	1.987
SiO2	0.534	0.493	0.642	0.519	0.539
CaO	1.120	1.014	0.960	0.915	0.884
Cr2O3	79.181	80.177	80.341	81.007	81.172

FIGURE 8-16. Chemical composition of acid-leached solid precipitates as a function of the leaching time. The acid used was H_2SO_4 0.5M and at a temperature of 50°C. The samples were analysed by XRF.

8.3.5. MULTIPLE STAGE ACID LEACHING

Since the equilibrium is achieved within the first minutes of leaching, increasing the leaching time does not provide an improvement on the purity of the acid-leached products obtained. Therefore, multiple-stage leaching has been tested with the purpose of obtaining higher purity of Cr_2O_3 products.

In a first set of experiments, leached products (previously leached in H_2SO_4 0.5M) were subjected to a second step of acid leaching with different acids of concentration 0.5M, at 50°C and for 2 hours. The acids chosen to carry out the second leaching step were citric acid, lactic acid, HCl and H_2SO_4, and the results are compared in FIGURE 8-17. The selection of these acids was done based on the results and discussion presented in 8.3.1.

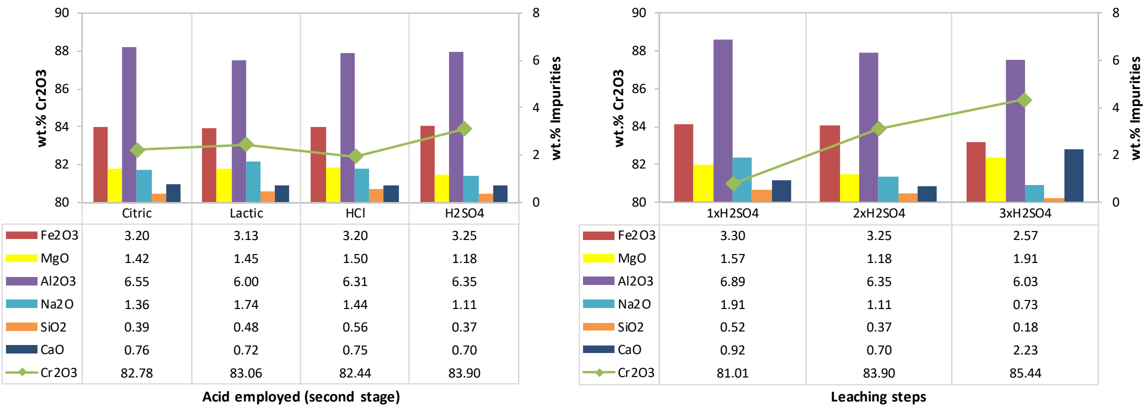

	Citric	Lactic	HCl	H2SO4
Fe2O3	3.20	3.13	3.20	3.25
MgO	1.42	1.45	1.50	1.18
Al2O3	6.55	6.00	6.31	6.35
Na2O	1.36	1.74	1.44	1.11
SiO2	0.39	0.48	0.56	0.37
CaO	0.76	0.72	0.75	0.70
Cr2O3	82.78	83.06	82.44	83.90

	1xH2SO4	2xH2SO4	3xH2SO4
Fe2O3	3.30	3.25	2.57
MgO	1.57	1.18	1.91
Al2O3	6.89	6.35	6.03
Na2O	1.91	1.11	0.73
SiO2	0.52	0.37	0.18
CaO	0.92	0.70	2.23
Cr2O3	81.01	83.90	85.44

FIGURE 8-17. Chemical composition of acid leached products after a second stage of acid leaching with different acids (left), and multiple-steps leaching with H_2SO_4 (right). Samples analysed by XRF.

It can be observed in FIGURE 8-17 that the second stage of acid leaching achieves higher purity of the Cr_2O_3-rich materials in all the cases. The slight enrichment of the products obtained is due to extraction of a small percentage of all the impurities present in the materials. It cannot be observed preferential extraction of any particular impurity after the second stage leaching with any of the acids tested. The product with the higher purity corresponds to the sample subjected to a second stage of leaching with H_2SO_4.

Since the best results were obtained with H_2SO_4, a third leaching step was carried out with H_2SO_4 and in the same conditions than the two previous steps (see FIGURE 8-17). The purity of the Cr_2O_3 increased from 81.01 wt.%, to 83.90 wt.% and 85.44 wt.% after two and three leaching steps, respectively. The number of leaching steps should be optimised based on the operating cost of leaching and the value of the product in the market as a function of its purity.

Chapter 9

PROCESS FLOWSHEET, MASS AND ENERGY BALANCE AND ENVIRONMENTAL CONSIDERATIONS

Chapter content

Chapter 9 shows a detailed description of the alkali reduction process illustrated in the process flowsheet. The composition and masses of the main process streams obtained experimentally were used to calculate the mass balance of the process; and the energy balance of individual steps and the overall process is included in this chapter. The environmental considerations of the process, including the water consumption, characterisation of liquid waste and greenhouse gas emissions are discussed in this chapter. Additionally, the novel process is compared with traditional technology in terms of energy consumption and waste generation.

Chapter conclusions

The flowsheet of the reductive alkali roasting process was developed and can be divided in 5 main sections: alkali reduction, magnetic separation, treatment of non-magnetic fraction, recovery of Na_2CO_3 *and heat exchange. According to the overall mass and energy balance, 85.6%* Cr_2O_3 *extraction was achieved in the final* Cr_2O_3*-rich product, which had a purity of 83.6 wt.%* Cr_2O_3*. The remaining is mainly in the magnetic fraction, which is enriched in metallic Fe. The alkali recovery stage is also able to recover 43.9% of the total* Na_2CO_3 *spent in the alkali reduction of the ore. The actual energy required for the alkali reduction stage is 7.49 MW, and the total energy consumption of the process adds up to a theoretical value of 77.59 MW. The heat released in the CO burning stage and condensation of steam from evaporation (67.75 MW) could be potentially recovered. Liquid waste from the acid leaching stage was free from* Cr^{6+}*, assuring the elimination of hazardous liquid waste production.*

9.1. PROCESS DESCRIPTION AND FLOWSHEET

A flowsheet of the entire alkali reduction process is shown in FIGURE 9-1. The diagram has been divided into five main sections as follows: 1- alkali reduction, 2- magnetic separation, 3- treatment of the non-magnetic fraction, 4- alkali recovery and 5- heat exchange section. A more detailed description of each section is given below.

9.1.1. ALKALI REDUCTION (SECTION 1)

Section 1 comprises the storage, milling and transport of the raw materials, i.e. chromite ore, sodium carbonate (Na_2CO_3) and charcoal, to the mixing section. The raw materials are stored in tanks TK-101, TK-102 and TK-103, milled in ball mills M-101, M-102 and M-103 until the appropriate particle size is reached, and transported in belt conveyors C-101, C-102 and C-103 to the blending area. The mixing is done in the blender B-101, where a homogeneous feed for the reduction stage is obtained. If the charge is preferred in the form of pellets, a pelletising step could be added to the process.

In the laboratory-scale experiments performed and presented in this document, the reduction was carried out in a batch tube furnace using argon to maintain an oxygen-free atmosphere in the reaction chamber. The mixture of reactants is fed into the furnace and heated up to a temperature within the range of 900-1050^{o}C, where the reduction of iron oxides to metallic iron and the formation of $NaCrO_2$ take place. However, for a larger production at industrial scale, the reduction could be carried out in a continuous kiln of conventional design similar to the kilns employed for the reduction of iron ores or for the alkali roasting of chromite [2,132]. In the case of industrial rotary kilns used for the reduction of iron ores to obtain sponge iron (Sarangi 2011), the reducing atmosphere is created by the CO gas formed by the gasification of carbon following the Boudouard reaction, and hence no argon flow is required.

The off-gas produced by the reduction of the ore is mainly CO -with a small proportion of CO_2- which may be burnt to produce a significant amount of the heat required by the kiln to maintain the required reaction temperature, as it will be shown in the energy balance analysis. The burning of the CO gas is carried out with air in the burner Q-501 shown in FIGURE 9-1.

The solid product of reduction -containing metallic Fe, $NaCrO_2$, MgO and $NaAlO_2$- is then cooled down to 50^{o}C in E-201 and sent to the magnetic separation stage (Section 2). The off-gas of the burner, after the CO gas burning, is mostly CO_2 which is cooled down to 50^{o}C in heat exchanger E-501 before being recycled to Section 4, where a CO_2 bubbling step is present.

9.1.2. MAGNETIC SEPARATION (SECTION 2)

Section 2 comprises the grinding and magnetic separation of the reduced sample. During reduction, the kiln load experiments slight sintering due to temperature and it is therefore required to grind the product of reduction (M-201). Liberation of metallic Fe particles is also favoured by the grinding of the material, which is crucial for the efficiency of magnetic separation. Experimental results indicate that particles of a maximum size of 40-50 µm should be obtained in the ball mill M-201 in order to maintain the efficiency of the magnetic separation.

The solid reduced product after cooling and grinding and the corresponding amount of water, both at 50°C, are fed into the magnetic separator (S-201) yielding a magnetic fraction, a non-magnetic fraction and an alkaline aqueous solution containing the soluble components present in the reduced sample. The non-magnetic fraction is separated from the alkali solution in the filter F-201 and sent to section 3 for further treatment; while the alkali solution is sent to Section 4 for alkali recovery. The magnetic fraction is separated and stored for further treatment.

9.1.3. TREATMENT OF THE NON-MAGNETIC FRACTION (SECTION 3)

In Section 3, the solid non-magnetic fraction is first water leached in a stirred reactor (R-301) at 50°C for 1.5 hours. The product is filtered in F-301 and the liquid filtrate, which is alkaline due to the significant solubilisation of sodium during water leaching, is sent to Section 4 for alkali recovery. The solid water leached precipitate is subsequently leached in an acidic solution in a stirred vessel reactor (R-302) at 50°C for 1.5 hours. The product is filtered in F-302 thereby obtaining a Cr_2O_3-rich material which is dried in D-301 and is the final product of the process.

9.1.4. ALKALI RECOVERY (SECTION 4)

Alkaline solutions from Sections 2 and 3, containing water soluble compounds extracted during magnetic separation and water leaching, i.e. excess sodium carbonate, sodium aluminate and soluble alkali silicates, are combined and treated in Section 4 with the aim of recovering part of the Na_2CO_3 used in the reduction of the ore. The alkali recovery process starts with the bubbling of CO_2 into the combined alkaline solution, and this is carried out in a two-phase reaction vessel (R-401) at 50°C and atmospheric pressure. The CO_2 gas required is obtained from the CO burner off-gas after cooling down to 50°C.

As a result of CO_2 bubbling in the alkaline solution, aluminium is selectively precipitated in the form of aluminium oxide ($Al(OH)_3$) and can be separated by filtering (F-401) and dried (D-401) yielding an Al_2O_3-rich material.

Sodium carbonate is recovered from the remaining alkaline solution after alumina separation by evaporation of the water in the boiler Q-401 shown in Section 4 in FIGURE 9-1. The Na_2CO_3 obtained is recycled back into the reduction stage (Section 1), and the heat content of the steam produced can be recovered in the heat exchange section (Section 5).

9.1.5. HEAT RECOVERY (SECTION 5)

A group of heat exchangers are used to maximise the heat utilisation in the different sections of the process, and this is included in Section 5. The burning of the CO gas from the kiln off-gas, the cooling of the CO_2 product from the burner in E-502, and the condensation and cooling in E-501 and E-503 of the steam produced in Section 4, are the three main sources of heat that were considered for recovery. The heat recovered may be used in the alkali reduction stage, the evaporation of water in the evaporator Q-401 and the heat of the water required for magnetic separation and leaching in E-501 and E-502. Theoretical values of heat recovered on each heat exchanger were calculated and discussed in the energy balance section.

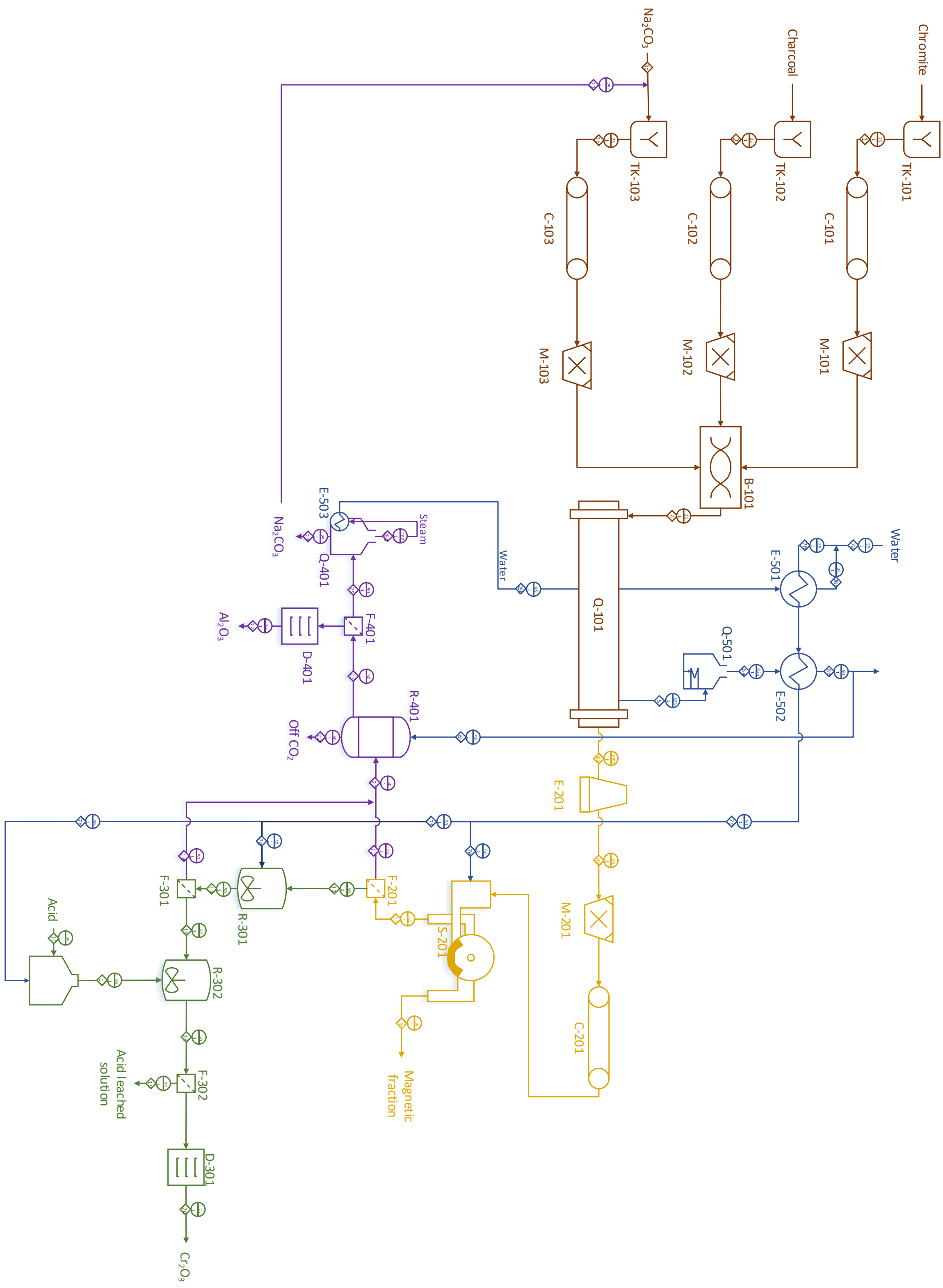

FIGURE 9-1. Flowsheet of the alkali reduction process divided into the following sections: 1- alkaline reduction (dark red), 2- magnetic separation (orange), 3- treatment of the non-magnetic fraction (green), 4-alkali recovery (purple) and 5- heat recovery (blue).

9.2. MASS AND ENERGY BALANCES BY STEP

A combination of experimental results and FactSage [46] and HSC [107] computations were used for the mass and energy balance calculation of the alkali reduction process. The experimental data was obtained from the treatment of 100 g of S.A. chromite ore, which was subjected to the entire process following the flowsheet shown in FIGURE 9-1 and with the experimental process parameters described below.

Experimental details. 100 g of S.A. chromite ore were roasted under reducing atmosphere with sodium carbonate (Na_2CO_3) and activated charcoal with a chromite:Na_2CO_3:charcoal weight ratio equal to 1:1:0.3. The sample was placed in an alumina crucible and the reduction was carried out in an electrically-heated tube furnace at 1050°C for 2.5 hours at atmospheric pressure with an argon flow rate of 2 L/min. Reduced samples were cooled and subjected to double grinding and wet magnetic separation using water at 50°C. The non-magnetic fraction was water leached with a solid:liquid ratio of 1:20 g/mL at 50°C and for 1.5 hours. Acid leaching was carried out using sulfuric acid 0.5 M, with a solid:liquid ratio of 1:70 g/mL at 50°C for 1.5 hours. Alkaline solutions from magnetic separation and water leaching were subjected to CO_2 bubbling in a 1 L vessel and with a CO_2 flow rate of 1 L/min. The $Al(OH)_3$ precipitate was filtered out and the remaining solution was evaporated until Na_2CO_3 precipitation.

The chemical compositions (analysed by XRF) of the main species of the process (excluding the reduced product and gas) were used to carry out the mass and energy balances and can be observed in TABLE 9-1 below. The reduced product and kiln off-gas equilibrium compositions were computed using the *Equilibrium Calculations* tool in FactSage software [46], and are presented in TABLE 9-2. The mass values shown in TABLE 9-1 and TABLE 9-2 were obtained by extrapolating the real mass values obtained from the mass balance experiment and taking into account a basis of calculation of 5000 kg/h of S.A. chromite ore treated.

The energy balance of the alkali reduction process was performed by estimating the energy requirement or energy generation of each of the steps of the process and calculating the overall energy need of the process. The mass balance of the input and output species and their corresponding temperatures were used as boundary conditions for the energy balance calculations of the alkali reduction stage and the burning of the kiln off-gas rich. Enthalpy calculations for the different stages were carried out using HSC software [107].

TABLE 9-1. Chemical composition in weight % of the main streams of the process obtained by XRF analysis.

Stream	Description	Mass (kg/h)	Cr_2O_3	Fe_2O_3	MgO	Al_2O_3	Na_2O	SiO_2	CaO
<1>	Chromite ore	5000	44.6	24.56	10.94	14.43	-	3.82	0.418
<9>	Magnetic fraction	1616.7	15.40	71.20 49.84	1.99	1.85	1.60	0.45	0.59
<10>	Non-magnetic fraction	3900	50.1	5.16	13.3	7.01	7.42	4.34	0.29
<11>	MS alkaline solution[*3]	3693.8	0.81	1.57	-	11.32	68.46	0.39	-
<15>	Water leached precipitate	3543.3	55.3	5.3	13.2	6.04	1.83	3.64	0.17
<14>	Water leachate	266.7	1.6	2.52	0.982	0.981	70.7	4.76	1.48
<24>	Alumina precipitate	421.7	0.619	0.41	-	80.8	4.42	7.93	3.48
<27>	Alkali recovered	2283.3	0.164	2.21	-	0.247	56.25 96.16	0.763	0.453
<19>	Acid leachate [*3]	861.0 6229.3[*4]	5.91	14.76	50.37	12.16	3.16	13.57	0.08
<20>	Cr_2O_3-rich product	2283	83.6	2.66	1.49	4.79	1.65	0.532	0.233

[*1] Expressed as metallic Fe.

[*2] Expressed as Na_2CO_3 and calculated by difference.

[*3] Composition calculated by difference.

[*4] Mass of dissolved solids including SO_3.

TABLE 9-2. Equilibrium composition, in mass (kg), of the reduced solid product, kiln off-gas and burner off-gas computed using FactSage [46].

Stream	Description	Total (kg)	$NaCrO_2$	Fe	MgO	$NaAlO_2$	Na_2CO_3
<8>	Reduced product	9210.5	3143.1	987.2	547.0	1159.7	1881.0

Stream	Description	Total (kg)	CO (g)	CO_2 (g)	N_2 (g)
<5>	Kiln off-gas	2289.5	2211.2	19.4	-
<6>	Burner off-gas	7713	-	3493.6	4159.6

The following general assumptions/observations were made for estimating the mass and energy balance of the process:

- No heat losses or efficiency of the equipment were accounted. All energy transformations and exchanges were considered ideal, and therefore the values obtained represent the best-case scenario.
- The burning of the kiln off-gas rich in CO was carried out with the stoichiometric air quantity, without taking into account any excess air required.

- The method to utilise the heat generated by the burning of the CO was not specified.
- The enthalpy of the reactions taking place during magnetic separation, water leaching, and acid leaching were not considered in the energy balance because of the difficulty to estimate the extent of these reactions. Moreover, the energy absorbed/released by these reactions was assumed not significant compared to the energy required to heat the water from 25 to 50°C.
- The cooling of the reduced product was not included in the heat exchange section, even though it is a potential source of heat.
- The mixing of the raw materials and the grinding of the reduced product before magnetic separation were not considered on the energy balance because of lack of data.

9.2.1. ALKALI REDUCTION IN A ROTARY KILN

Calculations were made based on the ore composition shown in TABLE 4-1 and the process flowsheet in FIGURE 9-1 and the basis of calculation set as 5000 kg/h of S.A. chromite ore. Mass and energy balance results of the reduction of chromite ore in a kiln are shown in TABLE 9-3.

The kiln load is a mixture of chromite ore, sodium carbonate and activated charcoal in the weight ratio chromite:Na_2CO_3:C = 1:1:0.2, which is fed into the kiln at a temperature of 25°C. The molar and mass flow of the input and output species are shown in TABLE 9-3.

The input quantities were 5000 kg of chromite, 5000 kg of Na_2CO_3 and 1500 kg of carbon; and the output gas and solid products in equilibrium were computed FactSage software (Bale, Pelton et al. 2013). The reaction temperature chosen was 1050°C, and the solid products are considered to leave the kiln at this temperature.

FactSage computations show that the off-gas contains above 96 %(v/v) CO, being the remaining mostly CO_2 and Na gas. In the present calculation Na gas was ignored and only CO and CO_2 were accounted, therefore the composition of the off-gas was 99.13% (v/v) CO and 0.87% (v/v) CO_2, as shown in FIGURE 9-2. Sarangi (2011) carried out a detailed mass an energy balance of the direct reduction of iron in a rotary kiln and, based on experimental process data, the author considered that the off-gas after CO burning leaves the kiln at a temperature of approximately 825°C (Sarangi 2011). In this case the generation of heat by burning of the CO is computed in a following section, but the data presented by Sarangi (2011) was used for the energy balance of the alkali reduction of chromite in the kiln, and the off-gas was considered to be at 825°C as seen in TABLE 9-3.

Table 9-3. Mass and energy balance of the alkali reduction stage in a rotary kiln. Basis of calculation 5000 kg/h of chromite ore.

INPUT SPECIES	T (°C)	kmol/h	kg/h	Enthalpy (MJ/kmol)	Latent H (MJ/h)	Total H (MJ/h)
Solid reactants	**25**	**226.24**	**11493.52**		**0.00**	**-98230.80**
Cr_2O_3	25	14.69	2233.01	-1134.70	0.00	-16670.78
FeO	25	13.65	981.01	-267.27	0.00	-3649.35
Fe_2O_3	25	2.00	320.01	-823.00	0.00	-1649.21
MgO	25	13.57	547.01	-601.60	0.00	-8164.85
Al_2O_3	25	7.08	721.50	-1675.69	0.00	-11857.52
SiO_2	25	3.18	191.00	-910.86	0.00	-2895.52
Na_2CO_3	25	47.18	4999.99	-1130.77	0.00	-53343.58
C	25	124.89	1500.00	0.00	0.00	0.00
Total		**226.24**	**11493.52**		**0.00**	**-98230.80**
OUTPUT SPECIES	**T (°C)**	**kmol/h**	**kg/h**	**Enthalpy (MJ/kmol)**	**Latent H (MJ/h)**	**Total H (MJ/h)**
Gas product	**825**	**79.38**	**2230.61**		**1988.78**	**-6911.10**
CO(g)	825	78.94	2211.21	-85.57	1971.67	-6754.71
CO_2(g)	825	0.44	19.40	-354.70	17.11	-156.39
Solid product	**1050**	**170.63**	**9203.05**		**10196.94**	**-67053.64**
$NaCrO_2$	1050	29.38	3143.14	-769.30	3149.61	-22601.46
Fe	1050	17.68	987.18	39.38	696.13	696.13
$NaAlO_2$	1050	14.15	1159.68	-1171.23	0.00	-16570.03
MgO	1050	13.57	547.01	-551.96	673.75	-7491.10
*$2Na_2O$*SiO_2	1050	3.18	585.05	-1878.31	725.83	-5970.97
Na_2CO_3	1050	17.75	1880.99	-932.31	3522.10	-16545.73
C	1050	74.93	900.00	19.08	1429.52	1429.52
Total		**250.02**	**11433.67**		**12185.72**	**-73964.74**

BALANCE	kmol/h	kg/h	Latent H (MJ/h)	Total H (MJ/h)
IN	226.237	11493.52	0	-98230.8
OUT	250.016	11433.67	12185.72	-73964.8
Balance	**23.779**	**-59.85**	**12185.72**	**24266.06**

The input-output energy balance indicates an energy requirement for the alkali reduction step of 24266.06 MJ/h (6.74 MW). The efficiency of the kiln considered is 90%, as calculated by Taylor (2018) [133], and therefore the actual energy requirement is 7.49 MW. Since the basis of calculation used was 5 tn/h of chromite ore, the energy requirement for the alkali reduction of S.A. chromite is therefore **1.5 MW/tn of chromite ore**.

9.2.2. BURNING OF THE CO GAS GENERATED

As explained in section 9.1.1, the reducing atmosphere is created by formation of CO gas in the reaction chamber by gasification of solid carbon. The kiln off-gas is therefore rich in CO, which may be oxidised to CO_2 to recover the heat content in the CO-rich gas, and the mass and energy balance for the CO burning is shown in Table 9-4.

TABLE 9-4. Mass and energy balance of the burning of the off-gas. Basis of calculation 5000 kg/h of chromite ore.

INPUT SPECIES	T (°C)	kmol/h	kg/h	Enthalpy (MJ/kmol)	Latent H (MJ/h)	Total H (MJ/h)
CO	825	78.94	2211.21	-85.57	1971.67	-6754.71
CO_2	825	0.44	19.40	-354.70	17.11	-156.39
Air	**25**	**187.96**	**5422.65**		**0.00**	**0.00**
O_2	25	39.47	1263.03	0.0000	0.00	0.00
N_2	25	148.49	4159.62	0.0000	0.00	0.00
Total		**267.34**	**7653.27**		**1988.7800**	**-6911.10**
OUTPUT SPECIES	**T (°C)**	**kmol/h**	**kg/h**	**Enthalpy (MJ/kmol)**	**Latent H (MJ/h)**	**Total H (MJ/h)**
CO_2	825	79.38	3493.64	-354.70	3080.16	-28157.54
N_2	825	148.49	4159.62	24.70	3667.29	3667.29
Total		**227.87**	**7653.27**		**6747.45**	**-24490.25**

ALANCE	kmol/h	kg/h	Latent H (MJ/h)	Total H (MJ/h)
IN	267.34	7653.27	1988.78	-6911.10
OUT	227.87	7653.27	6747.45	-24490.26
Balance	**-39.47**	**0.00**	**4758.67**	**-17579.16**

The air flow required for the burning of the CO gas was 5422.65 kg/h, equivalent to 4593.69 m^3/h of air at 25°C. In this case, no excess air was considered, and the air flow calculated is the stoichiometric value. The off-gas generated from the CO burning is a mixture of 34.8% v/v CO_2 and 65.2% v/v N_2, which comes off the burner at a temperature of 825°C. Theoretically, the energy balance of the CO gas burning **generates -4.88 MW** (17579.16 MJ/h, for 5000 kg/h chromite ore treated), which accounts for approximately 65% of the theoretical energy required for the alkali reduction stage.

The heat content of the burner off-gas can be used to increase the temperature of the water needed for the treatment of the non-mag fraction up to 50°C. The heat exchanging system which allows the optimisation of the process in terms of energy utilisation will be described in a following section.

9.2.3. MAGNETIC SEPARATION

The mass balance in the magnetic separation stage was carried out based on the theoretical composition of the reduced solid computed by FactSage software and the experimental XRF analysis of the magnetic and non-magnetic fractions. The mass and composition of dissolved solids was obtained by difference and the results are shown in TABLE 9-5. The table shows quantities of inputs and outputs, and also includes an elemental mass balance. The corresponding mass flow of magnetic and non-magnetic fractions are 1616.7 kg/h and 3900 kg/h, respectively. The Na_2O solubilised on this stage was 2528.78 kg/h.

TABLE 9-5. Mass balance of the magnetic separation stage.

INPUT SPECIES	**Reduced solid**					
	kmol/h	**kg/h**				
Total	**171.01**	**9223.95**				
$NaCrO_2$	29.38	3143.14				
Fe	17.68	987.18				
$NaAlO_2$(ia)	14.15	1159.68				
MgO	13.57	547.01				
$*2Na_2O*SiO_2$	3.18	585.05				
Na_2CO_3	17.75	1880.99				
C	74.93	900.00				
CaO	0.37	20.90				
OUTPUT SPECIES	**Magnetic fraction**		**Non-magnetic fraction**		**Alkaline solution**	
	kmol/h	**kg/h**	**kmol/h**	**kg/h**	**kmol/h**	**kg/h**
Total	**19.96**	**1616.67**	**77.55**	**3900.02**	**60.34**	**3693.83**
Cr_2O_3	1.64	248.97	12.86	1953.90	0.20	30.13
Fe_2O_3	7.21	1151.07	1.26	201.24	0.36	57.95
MgO	0.80	32.17	12.87	518.70	0.00	0.00
Al_2O_3	0.29	29.91	2.68	273.39	4.10	418.20
Na_2O	0.42	25.87	4.67	289.38	40.80	2528.78
SiO_2	0.12	7.28	2.82	169.26	0.24	14.47
CaO	0.17	9.54	0.20	11.35	0.00	0.00
C	9.31	111.87	40.20	482.80	14.64	644.30

Element balance (in kg/h)				
	IN	**OUT**	**BALANCE**	**% BALANCE**
Al	381.724	381.854	0.13	0.03
C	1113.16	770.514	-342.647	-30.78
Ca	14.937	14.928	-0.009	-0.06
Cr	1527.611	1527.823	0.211	0.01
Fe	987.179	986.378	-0.801	-0.08
Mg	329.865	332.195	2.331	0.71
Na	2109.008	2109.866	0.857	0.04
O	2671.188	2997.678	326.491	12.22
Si	89.281	89.28	-0.001	0.00

Since the composition of the alkaline solution was obtained by difference between the input (reduced sample) and the outputs (magnetic and non-magnetic fractions), the %balance is close to 0 for most of the elements. The difference in C and O may be due to the loss of ignition required for XRF sample preparation, which leads to the burning of part of carbon powder, and the limitations of this technique to accurately determine the amount of C and O in the samples.

For energy calculations, the values of processing capacity, wash water flow and power consumption of a commercial Wet High Intensity (WHI) pilot-scale magnetic separator (Technologies 2015) available in the market were taken into account.

The wash water flow and energy consumption specified for this equipment are 9000 L/h and 13 kW for a nominal capacity of 4 tn/h (Technologies 2015). Extrapolating these figures to a required capacity of 9203.05 kg/h of reduced material (as shown in TABLE 9-3), the water and energy consumption during the magnetic separation step can be estimated as 4.17 L and 5.98 W per kg of chromite ore treated, respectively. The power requirement was determined at maximum working intensity of the magnetic separator and including the rotor drive, coil and heat exchanger. Therefore, considering a basis of calculation of 5000 kg/h of chromite ore treated, the total amount of **water required** for magnetic separation is **20850 L/h** at 50°C, and the **energy consumption** is **29.9 kW**. The energy required for heating the water from room-temperature to 50°C is considered in the heat exchange section below.

9.2.4. WATER AND ACID LEACHING

A mass balance of the water and acid leaching steps was carried out based of XRF analysis of the non-magnetic fraction, water leached precipitate, dried aqueous leachate and acid leached precipitate. The acid leachate could not be dried and hence it was not analysed by XRF and its composition was obtained by difference. Table 9-6 and TABLE 9-7 show the input and output quantities of those three phases and their main components, along with the elemental balance of the leaching stage.

TABLE 9-6. Mass balance of the water leaching stage.

INPUT SPECIES	**Non-magnetic fraction**			
	kmol/h	**kg/h**		
Total	**77.55**	**3900.02**		
Cr_2O_3	12.86	1953.90		
Fe_2O_3	1.26	201.24		
MgO	12.87	518.70		
Al_2O_3	2.68	273.39		
Na_2O	4.67	289.38		
SiO_2	2.82	169.26		
CaO	0.20	11.35		
C	40.20	482.80		
OUTPUT SPECIES	**Water leached precipitate**		**Aqueous leachate**	
	kmol/h	**kg/h**	**kmol/h**	**kg/h**
Total	**71.27**	**3543.33**	**3.48**	**266.67**
Cr_2O_3	12.89	1959.46	0.03	4.27
Fe_2O_3	1.18	187.80	0.04	6.72
MgO	11.61	467.72	0.07	2.62
Al_2O_3	2.10	214.02	0.03	2.62
Na_2O	1.05	64.84	3.04	188.54
SiO_2	2.15	128.98	0.21	12.69
CaO	0.11	6.05	0.07	3.95
C	40.20	482.80		

Element balance (in kg/h)				
	IN	**OUT**	**BALANCE**	**% BALANCE**
Al	144.69	114.65	-30.04	-20.76
C	482.80	482.80	0.00	0.00
Ca	8.11	7.15	-0.97	-11.92
Cr	1336.86	1343.59	6.72	0.50
Fe	140.75	136.05	-4.70	-3.34
Mg	312.80	283.63	-29.16	-9.32
Na	214.68	187.97	-26.71	-12.44
O	1180.21	1111.00	-69.21	-5.86
Si	79.12	66.22	-12.90	-16.30

TABLE 9-7. Mass balance of the acid leaching stage.

INPUT SPECIES	**Water leached precipitate**			
	kmol/h	**kg/h**		
Total	71.27	3511.67		
Cr_2O_3	12.89	1959.46		
Fe_2O_3	1.18	187.80		
MgO	11.61	467.72		
Al_2O_3	2.10	214.02		
Na_2O	1.05	64.84		
SiO_2	2.15	128.98		
CaO	0.11	6.05		
C	40.20	482.80		
H_2SO_4(aq)	**67.35**	**6605.52**		
OUTPUT SPECIES	**Acid leached precipitate**		**Acid leachate**	
	kmol/h	**kg/h**	**kmol/h**	**kg/h**
Total	23.67	2283.00	71.20	6229.32
Cr_2O_3	12.56	1908.59	0.34	50.87
Fe_2O_3	0.38	60.73	0.80	127.07
MgO	0.84	34.02	10.76	433.70
Al_2O_3	1.07	109.36	1.03	104.66
Na_2O	0.61	37.67	0.44	27.17
SiO_2	0.20	12.15	1.94	116.83
CaO	0.10	5.32	0.01	0.73
SO_3	0.30	23.74	55.89	5368.28
C	7.61	91.43	0.00	0.00

Element balance (in kg)				
	IN	**OUT**	**BALANCE**	**% BALANCE**
Al	113.27	113.27	0.00	0.00
C	482.80	91.43	-391.37	-81.06
Ca	4.32	4.32	0.00	0.00
Cr	1340.67	1340.67	0.00	0.00
Fe	131.35	131.35	0.00	0.00
H	135.77	0.00	-135.77	-100.00
Mg	282.05	282.05	0.00	0.00
Na	48.10	48.10	0.00	0.00
O	5359.23	4639.58	-719.65	-13.43
S	2159.33	1801.20	-358.14	-16.59
Si	60.29	60.29	0.00	0.00

Since the inputs and outputs of the water leaching step were all calculated from experimental data, the resultant elemental balances have a greater deviation from 0. This can be attributed to experimental errors and XRF analysis. Carbon is an exception in this case because it was calculated by difference due to the difficulty of determining C in powder samples by XRF, as mentioned before, and therefore its balance is 0. This explains the mass loss shown in the water leaching stage in TABLE 9-7.

The water leaching of the non-magnetic fraction yields 3543.3 kg/h of water-leached residue with 55.3 wt.% Cr_2O_3. The amount of Na_2O extracted on this stage is 188.54 kg/h, and the total mass of solids extracted is 266.67 kg/h. These mass flow values correspond to solids in solution, excluding the water.

The mass balance shows that a total weight of 2283 kg/h of Cr_2O_3-rich product is obtained after acid leaching, of which 1908.59 kg/h are Cr_2O_3 (83.6 wt.% Cr_2O_3). The weight of the acid leachate shown in TABLE 9-7 excludes de water and only accounts for the dissolved solids (861 kg) and the SO_3 in solution (5368.28 kg) coming from the acid H_2SO_4.

As shown in FIGURE 9-1, both leaching steps are carried out in stirred leaching vessels. An estimation of the power consumed by the leaching, has been carried out by following guidelines about power requirements in stirred tanks found in literature [134,135]. The average power consumption for stirred vessels of 1.98 kW/m^3 has been estimated. The volume of solution treated during water leaching is approximately 78000 L/h and during acid leaching 248000 L/h, for a basis of calculation of 5000 kg/h of chromite ore treated. Based on these values and taking into a weight ratio of 1:1:0.2 account a leaching time of 1.5 h, the energy requirement of the stirred vessels during water and acid leaching steps is **234 kW** and **744 kW**, respectively.

9.2.5. CO_2 BUBBLING AND EVAPORATION

The input for the CO_2 bubbling and evaporation section is the combined alkaline solution from magnetic separation and water leaching, and the outputs are the alumina precipitate, the Na_2CO_3 recovered and the evaporated steam. The mass balance of these stage also present deviations. Besides the experimental errors and the analytical errors of XRF already mentioned, the fact that in previous stages some of the streams quantities and compositions were calculated by difference could lead to an important mismatch in the mass balance of this final stage. Examples of this are Ca, Mg, Si and Cr elemental balances, which also correspond to elements that are present in less percentage in the alkaline solution, and thus small variations on XRF results could cause important mismatches on the final elemental balance.

In the case of Na, TABLE 9-8 shows that only approximately the 50% of the theoretical quantity of Na was recovered in this stage, so the combined alkaline solution actually contains less sodium than the indicated in the input species.

TABLE 9-8. Mass balance of the CO_2 bubbling stage.

INPUT SPECIES	**Alkaline solution**					
	kmol/h	**kg/h**				
Total	**49.19**	**102120.93**				
Cr_2O_3	0.23	34.40				
Fe_2O_3	0.41	64.67				
MgO	0.07	2.62				
Al_2O_3	4.13	420.82				
Na_2O	43.84	2717.32				
SiO_2	0.45	27.16				
CaO	0.07	3.95				
$H_2O(l)$	5487.03	98850.00				
OUTPUT SPECIES	**Alumina precipitate**		**Na_2CO_3 recovered**		**Remaining water**	
	kmol/h	**kg/h**	**kmol/h**	**kg/h**	**kmol/h**	**kg/h**
Total	**4.49**	**421.67**	**42.30**	**2283.32**	**5487.03**	**98850.00**
Cr_2O_3	0.02	2.61	0.03	3.74	0.00	0.00
Fe_2O_3	0.01	1.73	0.32	50.46	0.00	0.00
MgO	0.00	0.00	0.00	0.00	0.00	0.00
Al_2O_3	3.34	340.71	0.06	5.64	0.00	0.00
Na_2O	0.30	18.64	20.72	1284.28	0.00	0.00
SiO_2	0.56	33.44	0.29	17.42	0.00	0.00
CaO	0.26	14.67	0.18	10.34	0.00	0.00
$H_2O(l)$	0.00	0.00	0.00	0.00	5487.03	98850.00
CO_2	0.00	0.00	20.71	911.44	0.00	0.00
Others	-	9.87				

Element balance (in kg/h)				
	IN	**OUT**	**BALANCE**	**% BALANCE**
Al	222.72	183.31	-39.41	-17.70
C	0.00	248.75	248.75	100.00
Ca	2.82	17.88	15.05	533.19
Cr	23.54	4.35	-19.19	-81.54
Fe	45.23	36.50	-8.73	-19.30
H	11060.76	11060.76	0.00	0.00
Mg	1.58	0.00	-1.58	-100.00
Na	2015.86	966.58	-1049.28	-52.05
O	88735.73	89003.23	267.50	0.30
Si	12.70	23.77	11.08	87.26

The mass balance results show that 421.7 kg of Al_2O_3-rich product (80+ wt.% Al_2O_3) can be recovered just by CO_2 bubbling on the alkaline solutions and subsequent filtering. The total amount of Na_2CO_3 recovered adds up to 2283.3 kg and has a purity of 96.2 wt.%.

The energy requirement of the CO_2 bubbling step has been estimated following the same guidelines than those applied to leaching. A two-phase reaction vessel with stirring is employed for the CO_2 bubbling, and a power requirement of 2.64 kW per m^3 of solution treated has been considered according to the values found in literature [134,135]. Consequently, the estimated power consumption of the CO_2 bubbling step, with a reaction time of 1.5 hours, is **1033 kW** for a total volume of alkaline solution of approximately 98850 L/h.

The higher energy consumption for the alkali recovery section is expected to be on the evaporation of the water for the precipitation and recovery of Na_2CO_3. TABLE 9-9 shows the energy input involved in the evaporation of 98850 litres of water per hour calculated using HSC software [107]; and indicates an energy requirement of 245023.07 (MJ/h) equal to **68.06 MW.** The water is assumed to enter the evaporator at 50°C, and the steam leaves the unit at 100 °C. The recovery of the steam heat content by condensation is crucial for the minimisation of the energy consumption and water consumption of the entire process. The condensation of the steam is considered in the energy analysis of the heat exchange system.

TABLE 9-9. Evaporation of water for Na_2CO_3 recovery

INPUT SPECIES	T (°C)	kmol/h	kg/h	Enthalpy (MJ/kmol)	Latent H (MJ/h)	Total H (MJ/h)
$H_2O(l)$	50	5487.03	98850.00	-283.95	10333.79	-1558023.22
OUTPUT	**T (°C)**	**kmol/h**	**kg/h**	**Enthalpy (MJ/kmol)**	**Latent H (MJ/h)**	**Total H (MJ/h)**
$H_2O(g)$	100	5487.03	98850.00	-239.29	13905.72	-1313000.15

BALANCE	kmol/h	kg/h	Latent H (MJ/h)	Total H (MJ/h)
IN	5487.03	98850.00	10333.79	-1558023.22
OUT	5487.03	98850.00	13905.72	-1313000.15
BALANCE	**0.00**	**0.00**	**3571.93**	**245023.07**

9.2.6. HEAT EXCHANGING SYSTEM

A simplified heat exchanging system has been included in the process flowsheet to give indications of how a heat exchange and recovery section can minimise the energy consumption of the process. Heat exchanges between the burner off-gas, the water required in the process and the steam produced during Na_2CO_3 recovery -corresponding to streams <6a>, <7a> and <26a> in FIGURE 9-1 has been designed to allow to recovery part of the energy spent in the process.

The burner off-gas, which is mainly composed of CO_2 and N_2, comes out the CO burner step at a temperature of 825°C. The heat content of the hot off-gas can be utilised to raise the temperature of the water required in the process. The heat recovered from the cooling of the off-gas adds up to **1.82 MW**, as shown in the energy balance in TABLE 9-10. All calculations were carried out based on 5 tonnes of chromite ore treated per hour.

TABLE 9-10. Energy balance of the cooling of the burner off-gas.

INPUT SPECIES	T (°C)	kmol/h	kg/h	Enthalpy (MJ/kmol)	Latent H (MJ/h)	Total H (MJ/h)
Burner off-gas	**825**	**227.87**	**7653.26**		**6747.44**	**-24490.15**
CO_2	825	79.38	3493.63	-354.70	3080.15	-28157.44
N_2	825	148.49	4159.63	24.70	3667.29	3667.29
OUTPUT SPECIES	**T (°C)**	**kmol/h**	**kg/h**	**Enthalpy (MJ/kmol)**	**Latent H (MJ/h)**	**Total H (MJ/h)**
Burner off-gas	**25**	**227.87**	**7653.26**		**183.02**	**-31054.57**
CO_2	25	79.38	3493.63	-392.56	74.87	-31162.72
N_2	25	148.49	4159.63	0.73	108.15	108.15

BALANCE	kmol/h	kg/h	Latent H (MJ/h)	Total H (MJ/h)
IN	227.87	7653.26	6747.45	-24490.15
OUT	227.87	7653.26	183.02	-31054.57
BALANCE	**0**	**0**	**-6564.43**	**-6564.43**

The energy required for the heating of the water flow used for magnetic separation, water leaching and acid leaching can be observed in TABLE 9-11. A total amount of **35558.59 MJ/h equal to 9.88 MW** are required to heat the liquid water from 25°C to 50°C degrees.

TABLE 9-11. Energy balance of the heating of the water flow required for magnetic separation, water leaching and acid leaching.

INPUT SPECIES	T (°C)	kmol/h	kg/h	Enthalpy (MJ/kmol)	Latent H (MJ/h)	Total H (MJ/h)
H_2O (liq)	25	18880.90	340143.1	-285.83	0.00	-5396720.43
OUTPUT	**T (°C)**	**kmol/h**	**kg/h**	**Enthalpy (MJ/kmol)**	**Latent H (MJ/h)**	**Total H (MJ/h)**
H_2O (liq)	50	18880.90	340143.1	-283.95	35558.59	-5361161.84

BALANCE	kmol/h	kg/h	Latent H (MJ/h)	Total H (MJ/h)
IN	18880.90	340143.10	0.00	-5396720.43
OUT	18880.90	340143.10	35558.59	-5361161.84
BALANCE	**0.00**	**0.00**	**35558.59**	**35558.59**

Another important source of heat in the process is the steam produced during evaporation of water in the alkali recovery section. A theoretical amount of **70.93 MW may be recovered** by condensation of the steam <26a> at 100°C to liquid water at 25°C [107]. In the diagram in FIGURE 9-2, it is proposed to use part of this available energy (8.06 MW) to preheat the water needed for magnetic separation and leaching, and the remaining (62.67 MW) could be employed to supply the required energy in the evaporation stage.

TABLE 9-12. Energy balance of the condensation of the steam produced in the alkali recovery section.

INPUT SPECIES	**T (°C)**	**kmol/h**	**kg/h**	**Enthalpy (MJ/kmol)**	**Latent H (MJ/h)**	**Total H (MJ/h)**
$H_2O(g)$	100	5487.03	98850.00	-239.29	13905.72	-1313000.15
OUTPUT	**T (°C)**	**kmol/h**	**kg/h**	**Enthalpy (MJ/kmol)**	**Latent H (MJ/h)**	**Total H (MJ/h)**
$H_2O(l)$	25	5487.03	98850.00	-285.83	0.00	-1568355.69
BALANCE	**kmol/h**	**kg/h**	**Latent H (MJ/h)**	**Total H (MJ/h)**		
IN	5487.03	98850.00	13905.72	-1313000.15		
OUT	5487.03	98850.00	0	-1568355.69		
BALANCE	**0.00**	**0.00**	**-3571.93**	**-255355.54**		

A total heat balance of the process is presented in section 9.2.7 where the setting of the heat exchangers and the overall heat recovered in the exchanging section is discussed.

9.2.7. OVERALL MASS AND ENERGY BALANCE

The overall mass and energy balance of the process is shown in FIGURE 9-2. The mass flow of all the main currents of the process has been indicated on the flowsheet, along with the main heat change occurring on each step. Positive and negative values of heat change represent energy requirement and energy released, respectively.

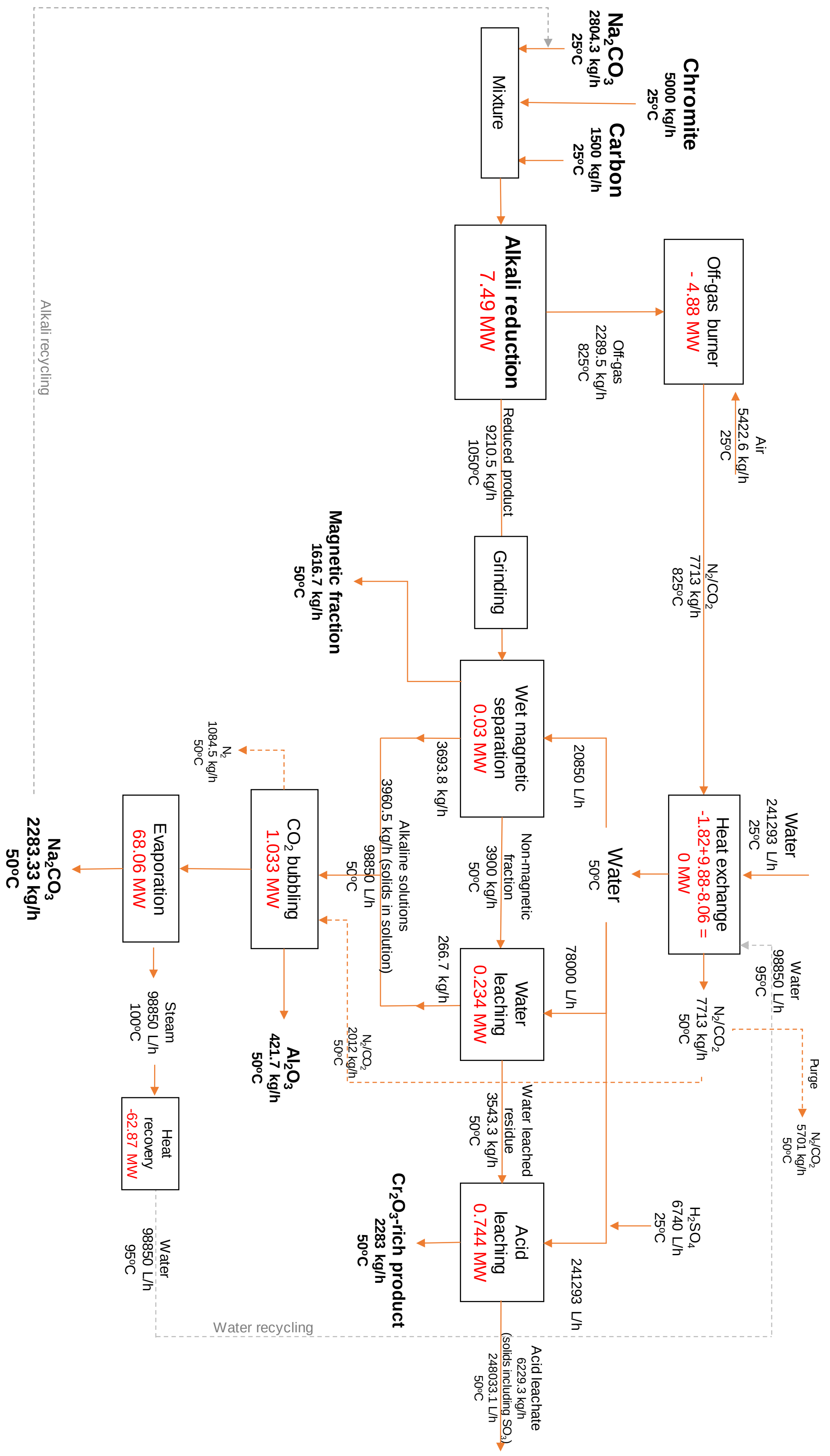

FIGURE 9-2. Overall mass and energy balance of the alkali reduction process.

According to the individual-step mass balances, the overall mass balance shown in FIGURE 9-2 and the chemical compositions in TABLE 9-1, the following observations may be obtained:

- The reduced product represents the 80.1 wt.% of the total charge, being the remaining 19.9 wt.% the kiln off-gas (>99.4 wt.% CO).
- The total kiln off-gas weight is 2289.5 kg, and after CO burning the total gas produced adds up to 7713 kg with a weight composition of 45.3 wt.% CO_2 and 53.9 wt.% N_2.
- After magnetic separation, the weight of the total reduced product is distributed between the magnetic fraction, the non-magnetic fraction and the alkaline solution with the following percentages 17.6 wt.%, 42.3 wt.% and 40.1wt.%, respectively.
- A total non-magnetic fraction weight of 3900 kg is obtained, with 50.1 wt.% Cr_2O_3. Further treatment of the non-magnetic fraction by water and acid leaching yields 2283 kg of Cr_2O_3 enriched product with 83.6 wt.% Cr_2O_3.
- One of the main objectives of water leaching is the extraction of Na_2O, and the mass balance shows that 188.5 kg of Na_2O are extracted from the non-magnetic fraction during water leaching, which represents a 65.1 wt.% Na_2O extraction.
- The Cr_2O_3-rich product represents the 45.7 wt.% of the initial chromite charge and, considering this material the target product of the process, the total Cr_2O_3 extraction yield achieved is 85.6 wt.%. Most of the remaining Cr_2O_3 is on the magnetic fraction, which can be used to make Fe-Cr alloy after melting on the magnetic fraction, and therefore should not be considered lost.
- The total Na_2CO_3-rich product recovered is 2283.3 kg with 96.2 wt.% Na_2CO_3 (2195.7 kg Na_2CO_3). The alkali recovery is thus approximately the 43.9 wt.% of the total amount of Na_2CO_3 required the alkali reduction step (5000 kg Na_2CO_3), and therefore and input of 2804.3 kg Na_2CO_3 is needed per every 5 tonnes of chromite treated.

Based on the individual-stage energy requirements and the overall energy balance detailed in sections 9.2.1 to 9.2.6, the following observations may be obtained:

- The theoretical energy required in the kiln is 6.74 MW. Considering that the kiln has 90% efficiency [133], the actual energy required is 7.49 MW.
- The most energy-intensive unit of the process is the evaporation of water for Na_2CO_3 recovery (68.06 MW), followed by the heat of water required for the process (9.88 MW) and the alkali reduction of chromite (7.49 MW).
- Theoretically, the energy balance of the CO gas burning generates 4.88 MW (17579.16 MJ/h, with 5000 kg/h chromite ore treated) which accounts for approximately 65% of the theoretical energy required for the alkali reduction stage.
- The heat exchanging system allows the optimisation of the process in terms of energetic efficiency by using the heat of the burner off-gas and steam of the evaporation stage to the water flow at 50°C required for the treatment of the non-magnetic fraction. A total of 62.87 MW can be recovered from the condensation of the steam from the evaporation stage, producing a current of hot water at 95°C which can be recycled back to the non-magnetic fraction treatment.

- The total energy consumption of the process adds up to a theoretical value of 77.59 MW, and a potential recovery of 9.88 MW can be recovery by simple heat exchange between currents and recycling of hot water. The heat released in the CO burning stage and condensation of steam from evaporation (67.75 MW) could be recovered by producing steam which could be used to supply energy to the different energy-consuming stages of the process.
- The heat consumed for mixing and grinding, and the heat recovered during the cooling of the reduced product, and heat produced during the burning of the remaining carbon in the acid leached residue have not been considered.

9.3. ENVIROMENTAL DESIGN CONSIDERATIONS

9.3.1. DETERMINATION OF Cr^{6+} IN WASTE PROCESSING SOLUTIONS

Solutions generated during the alkali reduction process, including alkaline solutions from magnetic separation and water leaching and acidified solutions from the leaching step, were analysed for the presence of Cr^{6+} ions, which potentially might have formed as a result of atmospheric oxidation. Any Cr^{6+} ions formed will solubilize readily and such ionic presence, therefore, will be manifested in the absorption spectra in the UV-visible region between 200 and 450 nm. The Cr^{3+}-ion absorption spectra were also compared between 300 and 700nm. In FIGURE 9-3, the absorption spectra for chromium 3+ and 6+ ionic states, measured as absorbance (A, cm^{-1}) are shown for different concentrations of these two ionic species. The shape and peak positions of absorption spectra represent the ligand field interaction which change with pH, depending on the oxidative potential of the analysed media [136]. These peak positions in FIGURE 9-3 are unique for the media analysed herein and, therefore, the calibration for concentrations were based on the intensity analysis of these peaks in the UV-visible absorption spectra using the Lambert-Beer's law equation. These calibrations are specifically designed for the Cr^{3+}-ions in the 10-1000 parts per million (ppm) and for Cr^{6+}-ions in the 0.46 ppm to 20.9 ppm concentrations. From these two ppm and sub-ppm range concentration ranges, the calibration curves for Cr^{3+} and Cr^{6+} ions were plotted and are shown in FIGURE 9-4 respectively.

Once the calibration ranges for characterisation of Cr^{3+} and Cr^{6+}-ions were established, the washed alkaline solution from magnetic separation (alkaline solution), water-washed leachate from sodium chromite precipitate and acid leachate were analysed using the UV-visible spectrophotometry in the range of 250-700 nm for characterising the absorbance via baseline subtraction technique, used for the calibration curves discussed above. It is known in the literature [136] that the presence of Cr^{6+}-ions in acidic media has more oxidative potential than at the same concentrations in basic media. For this reason, the analysis of both the acid and water-washed leachates were carried out at different stages - after two weeks and 6-months of leaching, for determining any likely change in the oxidation states of Cr-ions present. In FIGURE 9-5, the analysed peaks are compared, and from the comparison of peaks in FIGURE 9-3, in the immediately water-washed alkaline media, there appears to be little evidence for the presence of Cr^{6+} and Cr^{3+} ions.

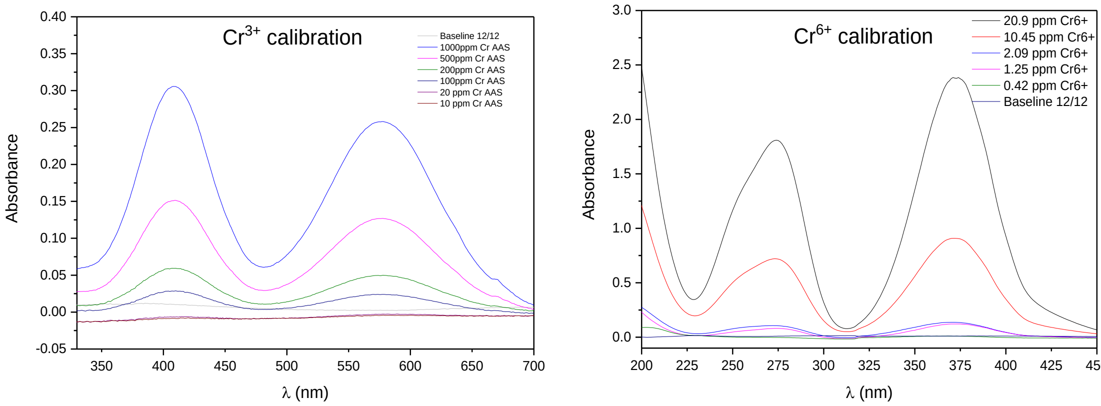

FIGURE 9-3. Absorbance versus λ (nm) UV-vis curves of aqueous calibration solutions of Cr^{3+} (concentrations of 1000 ppm, 500 ppm, 200 ppm, 100 ppm, 20 ppm and 10 ppm) and Cr^{6+} (concentrations of 20.9 ppm, 10.45 ppm, 2.09 ppm, 1.25 ppm and 0.42 ppm).

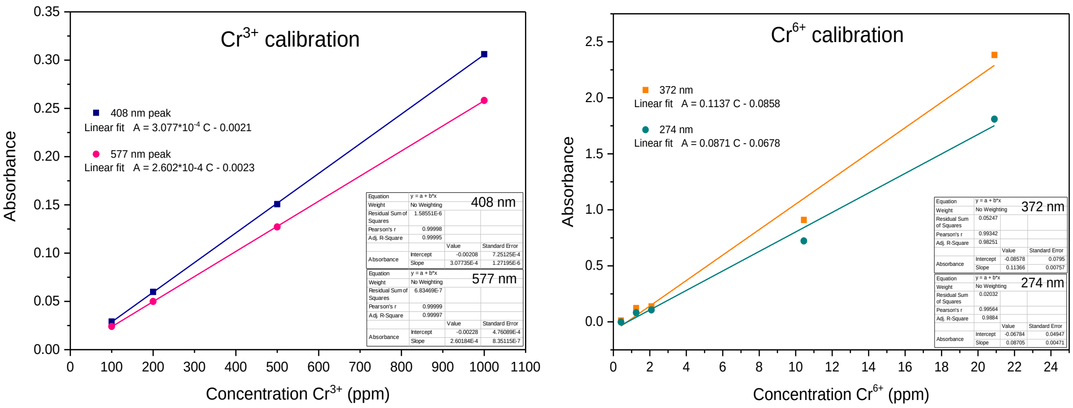

Equation	y = a + b*x		
Weight	No Weighting		
Residual Sum of Squares	1.58551E-6		
Pearson's r	0.99998		
Adj. R-Square	0.99995		
		Value	Standard Error
Absorbance	Intercept	-0.00208	7.25125E-4
	Slope	3.07735E-4	1.27195E-6

Equation	y = a + b*x		
Weight	No Weighting		
Residual Sum of Squares	6.83469E-7		
Pearson's r	0.99999		
Adj. R-Square	0.99997		
		Value	Standard Error
Absorbance	Intercept	-0.00228	4.76089E-4
	Slope	2.60184E-4	8.35115E-7

Equation	y = a + b*x		
Weight	No Weighting		
Residual Sum of Squares	0.05247		
Pearson's r	0.99342		
Adj. R-Square	0.98251		
		Value	Standard Error
Absorbance	Intercept	-0.08578	0.0795
	Slope	0.11366	0.00757

Equation	y = a + b*x		
Weight	No Weighting		
Residual Sum of Squares	0.02032		
Pearson's r	0.99564		
Adj. R-Square	0.9884		
		Value	Standard Error
Absorbance	Intercept	-0.06784	0.04947
	Slope	0.08705	0.00471

FIGURE 9-4. Absorbance versus concentration (ppm) calibration curves for Cr^{3+} and Cr^{6+} obtained by UV-vis spectroscopy.

In the case of the acid leachates, the main peak at 301nm is observed, which appears to be red shifted with respect to the 275nm peak for Cr^{6+}-ions in FIGURE 9-3, and in view of the crystal field dependence of the absorption peak for Cr^{6+}/Cr^{3+}-ions, there appears to be a strong possibility of Cr^{3+} and Cr^{6+} in the acidified media. In the absence of Cr^{6+} analysis with respect to 301nm peak, it was focussed on the absorption peaks at 580nm in FIGURE 9-5, with absorbance values in the range of 0.0079 and 0.0336 for the acid leachates after 6 months and after 2 weeks, respectively. Using the 577 nm peak in Figure 9-3 for Cr^{3+}-ions as a comparative reference, and the corresponding calibration equation: A (cm^{-1}) = $2.602 \cdot 10^{-4}$ C – 0.0023, it can be concluded that the residual concentrations of Cr^{3+} ions in acid leaching solutions after 6 months and two weeks are ~39 ppm and ~138 ppm, respectively. These two concentrations of Cr^{3+} are related with Cr^{6+}-ion peaks at 301nm for 2 weeks and 6 months old acid leachates, left in the lab environment. Using the analysed Cr^{3+}-ions from the calibration in Figure 9-3 and Figure 9-5, the residual concentrations of Cr^{6+}-ions in the acidified medium after 2 weeks and 6 months may be estimated by overall Cr-ion mass balance. The estimated Cr^{6+}-ion concentrations from the Cr-ion balance are 2 ppm and 101 ppm, respectively for 2 week and 6-month acid solutions.

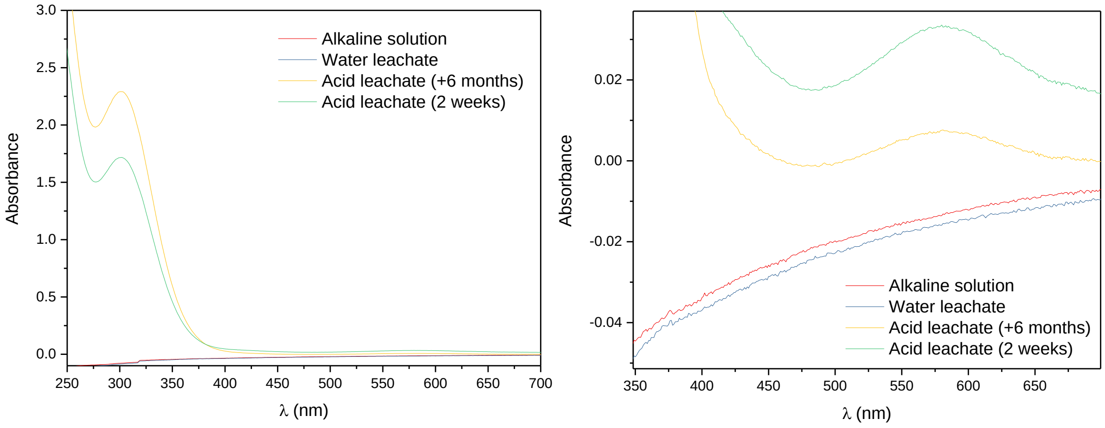

Figure 9-5. (a) Absorbance versus wavelength UV-vis curves of the alkaline solution from magnetic separation, water leachate and acid leachate analysed in the range of 250-700 nm and, (b) Zoomed in area of graph (a).

9.3.2. WATER CONSUMPTION AND CHARACTERISATION OF LIQUID WASTE

9.3.2.1. Water balance of the process

The quantification and characterisation of the process wastewater is the first step required for water recycling and/or disposing of the liquid waste.

The three main points of water consumption of the process are the magnetic separation, the water leaching and the acid leaching. Solutions from magnetic separation and water leaching are rich in dissolved sodium and are subjected to a combined treatment; whereas the acid leachate represents the main source of liquid waste of the process. The composition of the combined alkaline solution (solutions from magnetic separation and water leaching) and the acid leachate, in ppm, are shown in TABLE 9-13**.**

TABLE 9-13. Composition of the combined alkaline solution and the acid leachate in ppm.

Concentration (ppm)	Cr	Fe	Mg	Al	Na	Si	Ca
Combined alkaline solution	238.1	457.9	16.1	2253.8	20395.3	128.2	28.5
Acid leachate	140.3	358.6	1062.3	223.4	81.3	219.8	2.1

As shown in FIGURE 9-1 the total volume of the combined alkaline solutions is 98850 litres per 5000 kg of chromite ore treated. This solution is highly alkaline due to its Na^+ concentration, as shown in TABLE 9-13, and it is therefore suitable for recovery of Na_2CO_3. After CO_2 bubbling for Al_2O_3 precipitation, the remaining solution is subjected to evaporation. The steam produced is condensed in heat exchangers to recover part of the energy spent on the evaporation, and the water in liquid phase can be then recycled back into the process; thereby recovering all the water utilised on the magnetic separation and water leaching stages.

The total volume of **water consumed** by the alkali reduction process per 5000 kg/h of chromite ore treated is **241293 L/h**, which corresponds to the volume of water consumed by the acid leaching that is not recovered in this process.

In this case, the recovery of water from the acid leachate solution has not been considered and thus the acid leachate is a waste of the alkali reduction process. As identified by Hagare et al. [137], the most common pollutants present in the wastewater of the mining and mineral processing industry can be classified as: physical, chemical (organic and inorganic), biological and radiological pollutants [137]. In this process, the acid leachate, product of the leaching of the water leached residue with sulphuric acid (H_2SO_4), is a solution with pH<2 rich in Mg^{2+} ions, but it also contains variable amounts of Cr, Fe, Al, Si, Na and Ca (TABLE 9-13). The main pollutants of this waste stream have been identified by following the classification by Hagare et al. as shown in TABLE 9-14.

TABLE 9-14. Potential pollutants identified in the wastewater generated during acid leaching.

Physical pollutants	Temperature	50°C
	Colour	Transparent/pale green
	pH	<2
Chemical inorganic pollutants	Heavy metals	Cr (in trivalent form)
	Acids	H2SO4 in solution
	Dissolved salts (cations)	Mg^{+2}, Al^{3+},Fe^{2+},Na^{+},Ca^{2+}
	Dissolved salts (anions)	SO_4^{2-}

Heavy metals such as As, Cr, Cd, Cu, Au, Pb or Hg can be usually found in wastewater from the mining and mineral processing industry [137]. In the case of the alkali reduction process, the only heavy metal present in the wastewater is Cr. As shown in the results section, the chromium ions present in the acid leachate are in the form of Cr^{3+} and not as hexavalent chromium Cr^{6+}. This gives evidence of the absence of any Cr^{6+} in wastewaters generated, which represents the main advantage of the alkali reduction process compared to the process of alkali roasting of chromite ores in oxidising atmosphere.

Even though Cr^{6+} is not present in the solution, mass balance calculations and UV-vis analysis show that chromium is present in the solution in a concentration of approximately 140 ppm of Cr^{3+} (this was also verified by AAS analysis). This value is much higher than the values of total Cr allowed in wastewater from the country regulations limits or the industry guidelines, which is in the range of 0.1-2 ppm. This limit applies to wastewater that are discharge directly to surface drinking water without being treated [138]. It would be therefore necessary to treat the wastewater generated in order to lower down the concentration of Cr^{3+} under the legal limit depending on the country.

A simple solution to decrease the concentration of Cr^{3+} (and some of the other non-toxic metals) may be to increase the pH of the solution to promote precipitation of metals, which are more likely to be in solution at low pH. The adjustment of the solution to approximately neutral pH (usually a pH in the range of 6.5-8.5 is required) is in anyway necessary before the wastewater can be discharged [138,139]. The temperature would also need to be decreased to values below 35-40°C, depending on the country before discharging.

9.3.3. GREENHOUSE GAS BALANCE

According to the overall mass balance in FIGURE 9-2, the main source of gas emissions is the burner off-gas, which is a mixture of 34.8 %v/v CO_2 and 65.2 %v/v N_2. This corresponds to a total mass flow of CO_2 gas of 3493.6 kg/h produced. The CO_2 bubbling stage on the alkali recovery section requires CO_2, which is absorbed in the solution to form Na_2CO_3. This stage not only utilises part of the CO_2 produced decreasing its overall emissions, but also produces valuable Na_2CO_3. The 26.1% of the CO_2 produced (911.4 kg/h) is recycled back to be consumed in this CO_2 bubbling stage. The remaining mass flow is the overall **CO_2 generated** by the process, equal to **2582.5 kg/h** for 5000 kg/h of chromite ore treated.

In order to quantify the total GH emissions of the process, it is necessary to include the CO_2 emissions equivalent to the total energy consumed. The energy consumption of the process is equal to 77.6 MW (consumed) minus the potential energy recovery previously explained in this document. TABLE 9-15 shows the energy consumption considering different percentages of energy recovered, taking into account that the maximum potential recovery is 67.8 MW. The equivalent CO_2 emissions can be then calculated using the energy consumption [140,141] and the CO_2 produced calculated by mass balance. The results are shown in TABLE 9-15.

TABLE 9-15. Overall energy consumption (kWh) and total mass of CO_2 equivalent emissions (kg) per kg of Cr_2O_3-rich material produced.

	75% recovery	90% recovery	100% recovery
Energy consumption (kWh/kg product) (consumed-recovered)	11.7	7.3	4.3
kg CO_2 equivalent	9.8	6.5	4.2

The energy consumption of the process is an estimate based on laboratory scale results, which might obviously defer from industrial scale figures, which are expected to decrease after optimization of the process at a larger scale.

Chapter 10

REMEDIATION OF COPR WASTE AND Cr_2O_3 RECOVERY BY ALKALI REDUCTION

Chapter content

This chapter shows the characterisation of the COPR material produced and its treatment by the reductive alkali roasting process. The analysis of the reduced COPR samples is presented herein, as well as the results of their treatment by magnetic separation and leaching. The overall mass balance of the reduction of COPR was calculated and is presented with the process flowsheet. The chapter includes preliminary results obtained for the co-processing of COPR with chromite ores by alkali reduction.

Chapter conclusions

The analysis of COPR by different characterisation techniques provided information of the chemical composition of the material (27.37 wt.%Cr_2O_3*, 33.40 wt.%*Fe_2O_3*, 13.64 wt.%*Al_2O_3*, 14.03 wt.%MgO, 4.65 wt.%*SiO_2*, 0.78 wt.%CaO and 6.13 wt.%*Na_2O*) and the dominant phase observed was unreacted chromite spinel with areas enriched in iron oxide. The treatment of COPR reduced samples by magnetic separation and leaching yielded a* Cr_2O_3*-rich material with 80.23 wt.%* Cr_2O_3*, which demonstrates the possibility of eliminating* Cr^{6+} *from the waste obtaining a* Cr_2O_3*-rich material. Furthermore, the experimental conditions required for the processing of COPR are very similar to those of S.A. chromite ore, and therefore, its treatment would not require extra processing equipment.*

According to the results presented, the co-processing of chromite ores and COPR improve slightly the magnetic separation of the magnetic and non-magnetic fractions compared to the separation achieved when processing the chromite ores. However, XRPD and XRF results show that reduction was not complete and that the separation could be further improved by adjusting the parameters of both stages for each mixture.

10.1. CHARACTERISATION OF CHROMITE ORE PROCESSING RESIDUE

The chemical composition of the S.A. chromite and COPR materials was analysed by semi-quantitative XRF and is presented in TABLE 10-1. The XRPD pattern of the COPR material is compared with the original S.A. chromite ore in FIGURE 10-1. It is obvious from the comparison of the XRPD patterns that the main phase present in both samples is the chromite spinel phase ($((Fe,Mg)(Cr,Al,Fe)_2O_4)$). Rietveld refinement using GSAS software was carried out for both XRPD patterns for an accurate determination of the lattice parameter and atoms occupancies in the initial ore and the COPR samples, and the results can be seen in TABLE 10-2.

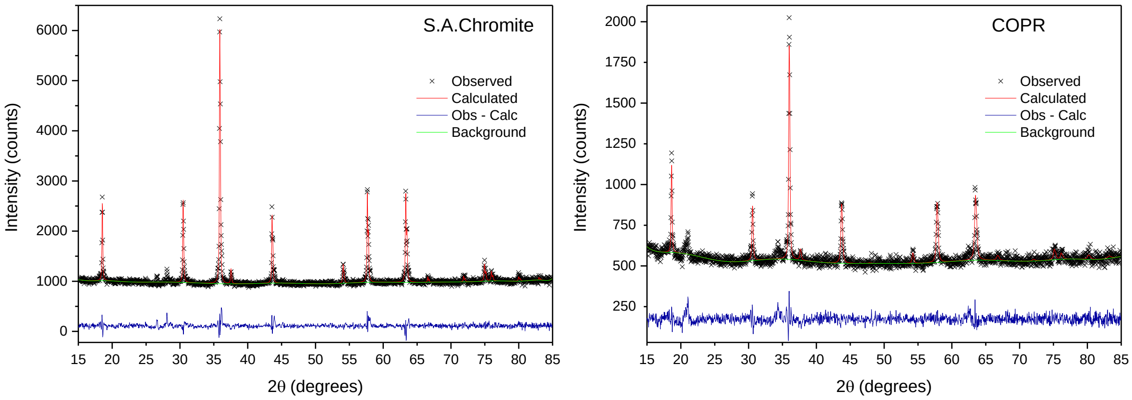

FIGURE 10-1. XRPD patterns of and Rietveld refinement of a) chromite ore and b) COPR. Recorded data is represented by crosses (x), while calculated data (red) and background (green) are shown as a solid lines. The difference plots (blue) are displayed below the recorded patterns. Cu- Kα radiation of λ = 1.5418 Å was used.

TABLE 10-1. Chemical composition of the chromite ore and COPR analysed by X-ray fluorescence.

(%wt.)	Cr_2O_3	Fe_2O_3	Al_2O_3	MgO	SiO_2	CaO	Na_2O
Chromite ore	44.66	24.56	14.43	10.94	3.82	0.42	-
COPR	27.37	33.40	13.64	14.03	4.65	0.78	6.13

TABLE 10-2. Lattice parameter and ions occupancies of S.A. chromite and COPR materials calculated by Rietveld refinement of XRPD data.

Sample	Lattice/Space Group	Lat.parameter (Å)	Octahedral sites		Tetrahedral sites	
			F_{Cr}	F_{Al}	F_{Fe}	F_{Mg}
Chromite	F-centered cubic / Fd-3m	8.306	0.684	0.316	0.510	0.490
COPR	F-centered cubic / Fd-3m	8.298	0.746	0.254	0.439	0.561

According to Rietveld results, the lattice parameter of the spinel phase decreased from 8.306 Å for the initial ore to 8.298 Å for the COPR. This represents approximately a diminution of 0.1% of the lattice parameter of the unit cell, and can be due to the change in the relative composition of the chromite spinel after roasting. The occupancies (or fractions) of each atom in an octahedral/tetrahedral site were refined assuming that the sum of fractions in each site needs to be equal to 1, this means $f_{Cr} + f_{Al} = 1$ (for octahedral sites), and $f_{Fe} + f_{Mg} =1$ (for tetrahedral sites). The fraction of Fe decreases with respect to the fraction of Mg. This is expected due to the formation of Fe_2O_3 observed in oxidative alkali roasted samples. Even though magnesium is also extracted from the chromite spinel during roasting forming MgO, it tends to form $MgCr_2O_4$ which remains in the form of spinel. The formation of $MgCr_2O_4$ has been reported in previous publications [29,34] and it is considered the one of the main limiting factors for the formation of Na_2CrO_4 during alkali roasting with Na_2CO_3. Regarding octahedral sites, the results indicate that the fraction of Cr increases with respect to that of Al. This could be explained by the higher stability of $MgCr_2O_4$ under oxidative alkali roasting conditions compared to other spinel members [24]. However, according to XRF results the wt.% of Cr_2O_3 decreased more significantly than that of Al_2O_3, as seen in TABLE 10-1.

The microstructure of the S.A. chromite ore and COPR materials were examined by secondary electron microscopy and are compared in FIGURE 10-2. FIGURE 10-2a shows a backscattered SEM image of the chromite ore, and FIGURE 10-2b and FIGURE 10-2c of the COPR. The S.A. ore contains chromite as the main phase besides small quantities of silicates phases which account for a total wt.% SiO_2 of 3.82%. The partially-reacted chromite particles in COPR are not homogeneous in composition as they exhibit different extents of reaction. For instance, the appearance of COPR particles shown in FIGURE 10-2b is very similar to particles of the chromite ore. The porosity on the surface of these particles is slightly higher than that of the chromite ore, but the particles still conserve their shape and no phase segregation is observed, which means that the extent of reaction on this specific particle was low. This is confirmed by the EDX chemical quantification analysis presented in TABLE 10-3.

Points 1 and 2 (chromite ore particles) may be compared with point 3 (COPR), where the wt.% Cr is similar to that in chromite ore particles as it would be expected. However, in a different COPR particle shown in FIGURE 10-2c, the phase segregation is obvious just by observation, which indicates that, in this particle, reaction of the chromite phase and the alkali did take place, and part of the chromium was extracted as Na_2CrO_4. As a result, there are different areas on this particle (areas 4-6 have been chosen as examples in this case) with different elemental composition. Area 4 corresponds to the unreacted part where the %wt. of Cr is comparable to the one seen in unreacted chromite, while areas 5 and 6 are Fe-rich areas depleted in Cr found at the rim and at reaction bands within the particle.

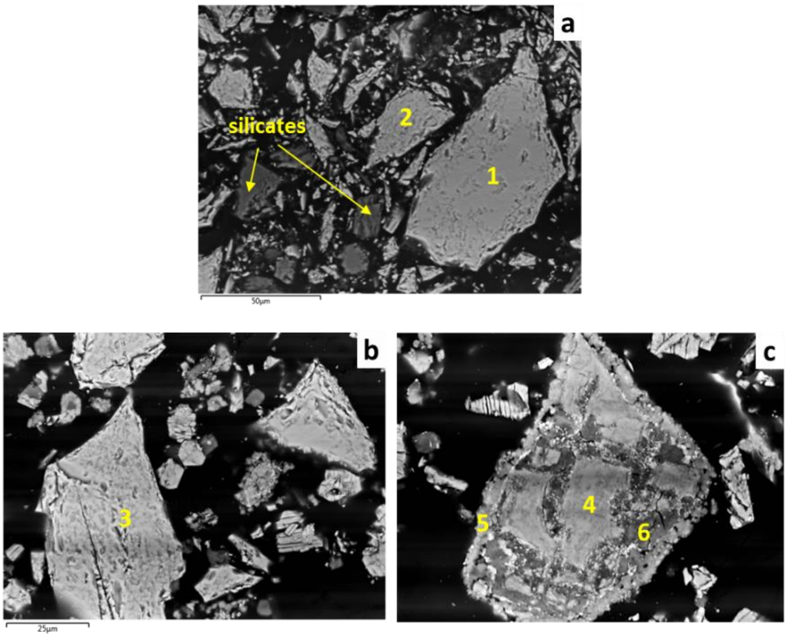

FIGURE 10-2. Backscattered scanning electron microscopy images of COPR (OV = 20 kV).

TABLE 10-3. Elemental composition of points 1-7 in FIGURE 10-2 a-c analysed by EDX.

Sample	Point	%wt. Cr	%wt. Fe	%wt. Mg	%wt. Al	%wt. Na	%wt. Si	%wt. Ca	%wt. O
Chromite ore	1	32.9	23.5	5.8	8.9	0	0	0	27.9
	2	37.6	21.6	5.7	7.9	0	0	0	26.5
COPR	3	30.9	23.8	7.0	9.9	5.4	3.7	0.6	18.4
	4	38.9	10.7	10.2	9.8	1.1	0.3	0.2	27.5
	5	3.0	51.1	1.9	6.9	7.4	6.3	3.0	19.8
	6	7.2	29.1	6.2	9.6	8.8	7.3	1.0	29.8

The elemental mapping shown in FIGURE 10-3 clearly exposes the phase segregation at this particle and the elemental distribution in agreement with what it was described above.

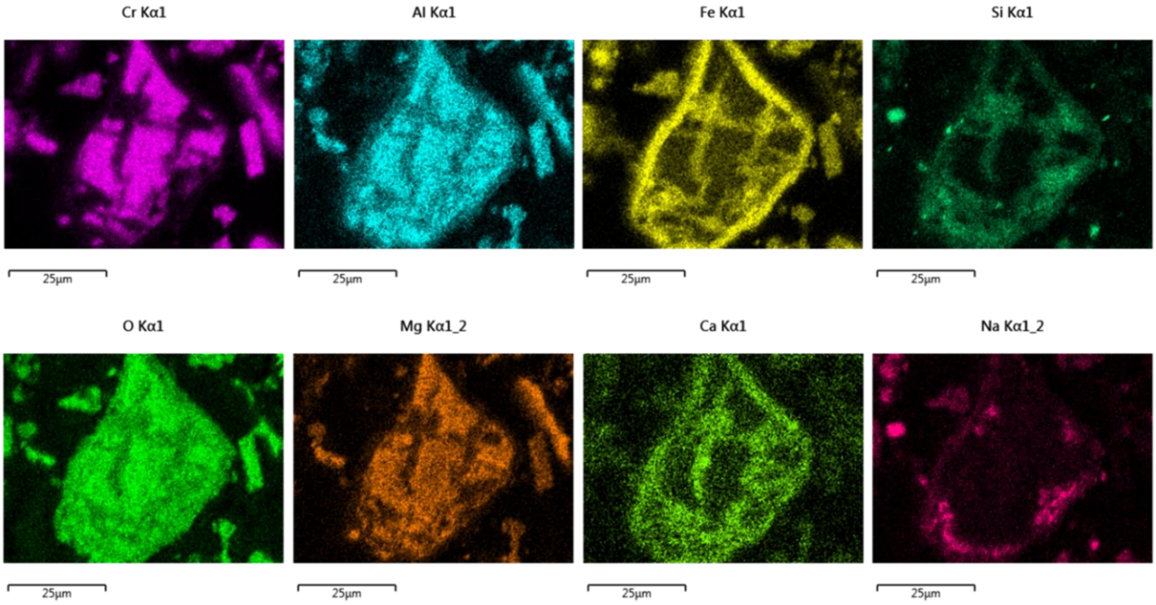

FIGURE 10-3. Elemental EDX mapping of image c in Figure 10-2, including maps (from top-left to bottom-right) of Cr, Al, Fe, Si, O, Mg, Ca and Na.

10.2. TREATMENT OF CHROMITE ORE PROCESSING RESIDUE BY THE REDUCTIVE ALKALI ROASTING PROCESS

10.2.1. CHARACTERISATION OF COPR REDUCED SAMPLES

The COPR material was subjected to alkali reduction in reductive atmosphere and in the presence of Na_2CO_3. Different temperatures, times and alkali ratios were tested, and the results obtained are comparable to the alkali reduction of chromite ores; and as a result, s temperature of 1050°C and a reaction time of 2 to 3 hours were considered appropriate for the alkali reduction of COPR.

Since the COPR contains less Cr_2O_3 than chromite ores, the alkali ratio was adjusted for this material. Reduction of COPR with Na_2CO_3 and carbon using weight ratios of COPR:Na_2CO_3 of 6:1, 6:2, 6:3, 6:4, 6:5 and 6:6 were tested, and the reduced samples obtained were analysed by XRPD and are presented in FIGURE 10-4.

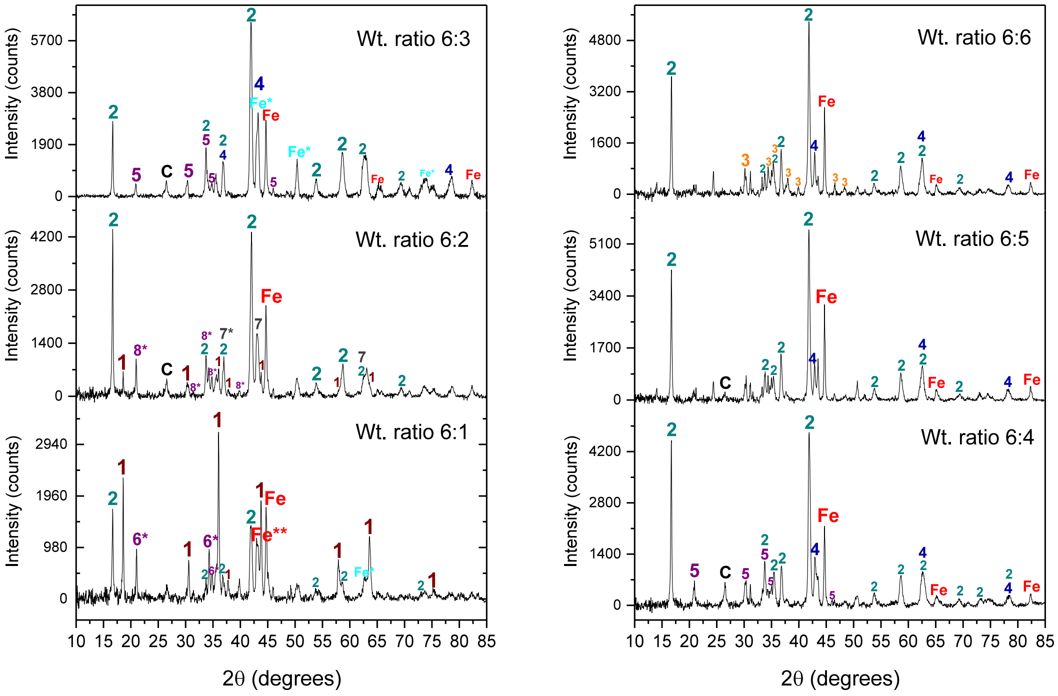

FIGURE 10-4. X-ray diffraction patterns of COPR samples reduced at 1050°C for 2.5 hours with Na_2CO_3 and carbon in a COPR:Na_2CO_3:C weight ratio of 6:1:1.2, 6:2:1.2, 6:3:1.2, 6:4:1.2, 6:4:1.2, 6:5:1.2 and 6:6:1.2. [1=$Mg_{0.58}Cr_{1.52}Fe_{0.42}Al_{0.48}O_4$, 2=$NaCrO_2$, 3=$Na_2CO_3$, 4=MgO, 8=$Na_{0.9}Mg_{0.45}Si_{0.55}O_2$, Fe=metallic Fe, Fe*=γ-Fe].

Since the chromium content in COPR is lower than that in chromite ore, the alkali ratio required is expected to be lower than 1:1. The XRPD patterns confirm this, showing than for and alkali ratio of 1:1 (6:6 in the figure) there is unreacted Na_2CO_3 which remains in the reduced sample. By contrast, for low alkali ratios like 6:1 or 6:2, unreacted chromite spinel from the COPR is still present. For a ratio of 6:3, part of the metallic Fe formed is γ-Fe, which is not desired. Therefore, the optimum alkali ratio can be set at 6:4, or 1:0.67.

FIGURE 10-5 shows the backscattered SEM images of COPR reduced samples at 1050°C, with a COPR:Na_2CO_3:C weight ratio of 1:0.67:0.2 for 30 minutes (a) and 2.5 hours (b). The reduction in this case takes place following the same mechanism than that for the reduction of chromite. Image (a) in FIGURE 10-5 shows the formation of the metallic Fe needles, which then grow and aggregate to form metallic sphere as the ones shown in image (b).

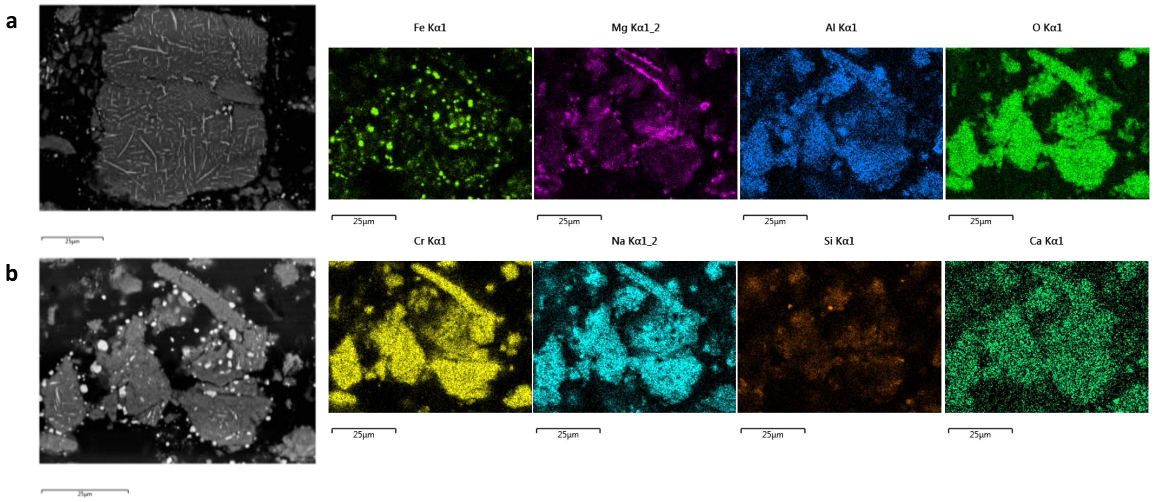

FIGURE 10-5. Backscattered SEM images of COPR samples reduced with Na_2CO_3 and activated charcoal (weight ratio COPR:Na_2CO_3:C = 1:0.67:0.2) at 1050°C for a) 30 minutes and b) 2.5 hours; and EDX elemental mappings of image b).

10.2.2. EXTRACTION OF Cr_2O_3-RICH PRODUCT FROM COPR REDUCED SAMPLES

A sample of COPR was reduced for 2.5 hours at 1050°C with a COPR:Na_2CO_3:C weight ratio of 1:0.67:0.2 and subjected to the complete alkali reduction process including magnetic separation, water leaching, acid leaching, CO_2 bubbling and Na_2CO_3 recovery. The XRPD patterns of the main streams of the process are shown in FIGURE 10-6. Its chemical composition was also analysed by XRF, and the results obtained can be seen in TABLE 10-4.

The starting COPR material contains 27.37wt.% Cr_2O_3, and after reduction, this is separated in a magnetic fraction with 13.02wt.% Cr_2O_3 and a non-magnetic fraction with 36.92wt.% Cr_2O_3. Separation of metallic Fe and the non-magnetic fraction was successfully achieved, as seen in the XRPD patterns in FIGURE 10-6, where it can be seen that the main phase in the magnetic fraction is Fe. The magnetic fraction is lower in Cr_2O_3 than the one obtained after reduction of chromite ore because of the lower content of chromium of the residue compared to the ore (see TABLE 10-4). The non-magnetic fraction is also poorer in Cr_2O_3, and after being subjected to two stages of leaching with water and sulfuric acid 0.5 M, the material produced is rich in Cr_2O_3. The acid-leached residue obtained is 80.23wt.% Cr_2O_3.

It was also possible in this case to recover an Al_2O_3-rich material with 75+ wt.% Al_2O_3 and 95+ wt.% Na_2CO_3 with 3.23wt.% Cr_2O_3. The amount of Na_2CO_3 recovered was the 59.6% of the initial amount used on the reduction stage.

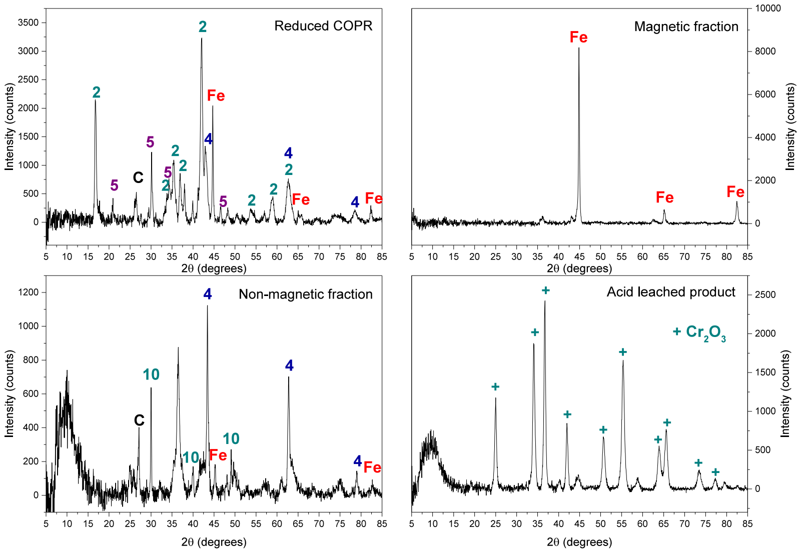

FIGURE 10-6. XRPD patterns of a COPR reduced sample (reduction at 1050°C, for 2.5 hours, with a COPR:Na_2CO_3:C weight ratio of 1:0.67:0.2), the magnetic and non-magnetic fractions and the product after acid leaching with H_2SO_4 0.5 M. [2 = na_2CO_3, 4 = MgO, 5 = $na_{1.95}al_{1.95}Si_{0.05}O_4$, Fe = metallic iron, 10 = $CaCO_3$, C = carbon].

TABLE 10-4. Chemical composition of the main streams of the alkali reduction process after treating a sample of COPR material with Na_2CO_3 and activated charcoal (weight ratio COPR:Na_2CO_3:C = 1:0.67:0.2) at 1050°C for 2.5 hours.

wt%	Cr_2O_3	Fe_2O_3	MgO	Al_2O_3	Na_2O	SiO_2	CaO	SO_3
COPR	27.37	33.40	14.03	13.64	6.13	4.65	0.78	-
Mag	13.02	74.10	5.19	5.28	1.96	0.45	0	-
Non-mag	36.92	10.54	17.74	12.63	7.95	9.23	4.99	-
Water leached	39.07	9.76	17.97	12.79	4.58	9.96	5.88	-
Acid leached	80.23	3.59	2.57	4.95	3.16	1.33	1.93	2.25
Al_2O_3 recovered	2.57	-	-	75.92	11.66	8.30	1.56	-
Na_2CO_3 recovered	3.23	1.04	-	0.80	94.93	-	-	-

10.2.3. CO-PROCESSING OF COPR WITH CHROMITE ORES BY ALKALI REDUCTION

In the sight of the results on the alkali reduction of COPR, the co-processing of COPR and chromite ores has been tested with two main objectives:

a) The landfilling of highly toxic COPR could be decreased, or even eliminated, by the co-processing of this material with chromite ores by the reductive alkali roasting process. This would not only solve the problem of COPR treatment, handling and landfilling, but would also enable to recover a value product concentrated in Cr_2O_3 from this material waste.

b) Increasing the content of iron oxides in the charge to the kiln with the aim of increasing the size of the metallic Fe particles achieved and therefore maximise the efficiency of magnetic separation achieved when processing chromite ore itself.

Preliminary tests including reduction and magnetic separation were performed with three mixtures of S.A chromite, Brazilian chromite E4 and Brazilian chromite E5 and COPR. The reduction of these samples was carried out at 1050°C for 2.5 hours and a mix:Na_2CO_3:charcoal weight ratio of 1:0.8:0.2; where the mix represents a mixture of 50%-50% of the corresponding chromite ore and COPR. The reduced samples were then subjected to magnetic separation, obtaining magnetic and a non-magnetic sample. FIGURE 10-7 shows the XRPD patterns of the reduced samples and magnetic fractions obtained.

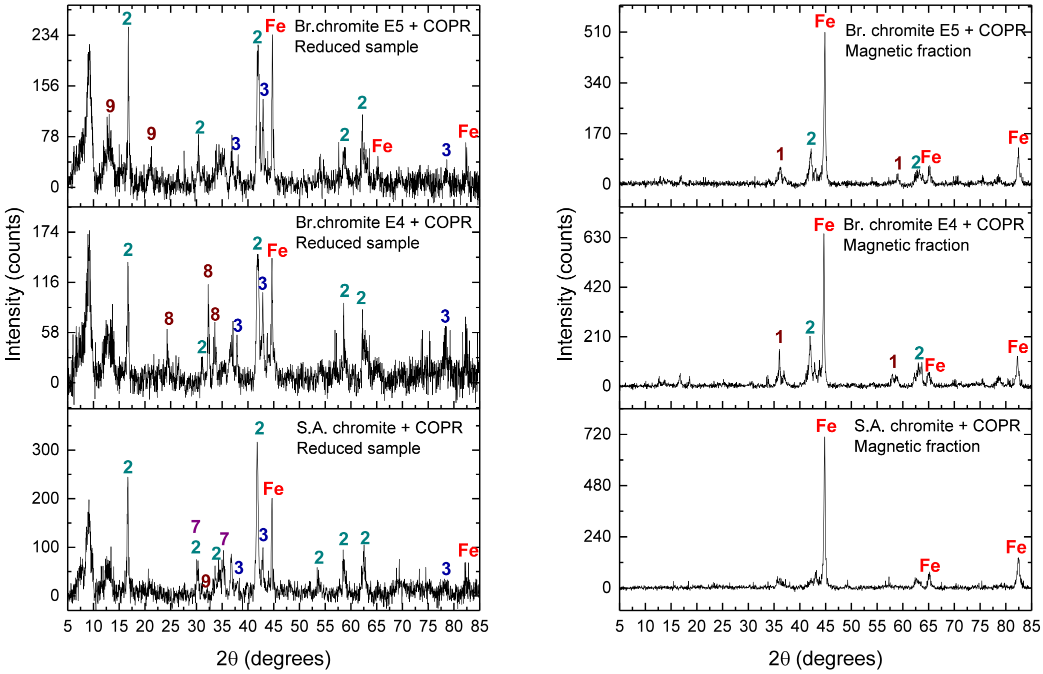

FIGURE 10-7. XRPD patterns of reduced and magnetic fraction samples after reduction of chromite + COPR mixtures. [1 = $FeCr_2O_4$, 2 = $NaCrO_2$, 3 = MgO, 7 = $Mg_{0.64}Fe_{2.36}O_4$, 8 = $Na_2SiO_3*H_2O$, 9 = $Na_{3.93}Al_{3.93}Si_8O_{24}$].

The main phases identified in the XRPD patterns in FIGURE 10-7 were $NaCrO_2$, Fe and MgO in reduced samples, and Fe in magnetic fractions. Other phases such as unreacted spinel, and alkali silicates were also present in the reduced samples. The patterns of magnetic samples show that the best separation was achieved with the S.A. chromite + COPR mixture, in agreement form reduction and magnetic separation results of the processing of each ore.

The chemical composition of magnetic and non-magnetic fractions is shown in TABLE 10-5 below, and can be compared with magnetic and non-magnetic fractions after reduction of the three different chromite ores shown in TABLE 8-1 and TABLE 8-2.

TABLE 10-5. Chemical composition of magnetic and non-magnetic fractions obtained after magnetic separation of S.A chromite + COPR, Br. Chromite E4 + COPR and Br. Chromite E5 + COPR reduced mixtures.

Weight (%)	Cr_2O_3	Fe_2O_3	MgO	Al_2O_3	Na_2O	SiO_2	CaO
S.A.+COPR mag	19.60	69.04	3.57	2.96	2.53	1.28	1.02
S.A.+COPR non-mag	52.47	4.09	14.57	9.21	6.27	7.91	6.48
Br.E4+COPR mag	36.75	28.25	10.25	13.07	10.29	0.48	0.64
Br.E4+COPR non-mag	28.00	12.36	17.19	13.81	8.82	11.49	6.83
Br.E5+COPR mag	32.75	34.26	8.39	10.98	11.26	0.33	0.97
Br.E5+COPR non-mag	31.77	5.82	20.77	12.60	5.31	14.29	8.23

The magnetic separation of reduced samples of S.A. chromite and COPR mixtures show a slight improve on the concentration of Cr_2O_3 of the non-magnetic fraction, while the wt.% of Cr_2O_3 in the magnetic fraction decreased 2%. The addition of COPR to the S.A. chromite ore increased the overall MgO wt.%, and therefore both magnetic and non-magnetic fractions are richer in MgO.

For Brazilian chromites and COPR mixtures, the magnetic and non-magnetic fractions are richer in iron and chromium, respectively. This means that in both cases the magnetic fraction obtained contains higher quantities of metallic Fe, and the non-magnetic fractions are richer in Cr_2O_3. However, the Fe_2O_3 wt.% of the non-mag from reduction of Br. Chromite E4 and COPR is higher than that from the reduction the ore itself, due to the higher quantity of Fe_2O_3 present in the charge initially.

Chapter 11

CONCLUSIONS AND FUTURE WORK

The last chapter of this document includes a summary of the main conclusions of the research project. A section with the proposed future work is also presented.

11.1. CONCLUSIONS

This section includes the main conclusions of the research project presented in the different chapters of this document, which have been summarised as follows:

- The alkali roasting of chromite ores in oxidising atmosphere with different alkali salts is a well-stablished process for the production of chromium chemicals, including Cr_2O_3, and it has been extensively investigated. The generation of processing waste containing Cr^{6+} in a range of concentrations and the need of low silica feedstock (<1wt.% SiO_2) required for the process, are still important limitations of the process. On the other side, the production of ferro-chrome for stainless steel by smelting of chromite ore with coke is a high energy-demanding process which requires high temperatures (above 1600°C). In this context, the reductive alkali roasting process aims to extract a Cr_2O_3-rich product from chromite ores at lower temperature (900-1050°C) and avoiding any generation of Cr^{6+}-containing waste. South African and Brazilian chromite ores have been used as raw materials for the experiments performed.

- The S.A. chromite is a chemical grade ore of composition 44.66 wt.% Cr_2O_3, 24.56 wt.% Fe_2O_3, 10.94 wt.% MgO, 14.43 wt.% Al_2O_3, 3.82 wt.% SiO_2 and 0.52 wt.% TiO_2. The main phases present in the ore is chromite spinel with the stoichiometric formula $(Fe_{0.56}Mg_{0.44})(Cr_{0.61}Al_{0.29}Fe_{0.08})_2O_4$ (as calculated from EPMA results) and Na-Al-Ca-silicate. In the S.A. chromite, the chemical composition of the chromite phase is homogeneous from particle to particle. However, in the case of the Brazilian ores, the SEM analysis indicated that the silicate gangue can be found embedded in the chromite particles. The content of silica in the Brazilian ores is significantly higher, with 8.48 wt.% and 13.20 wt.% SiO_2 in chromite E4 and chromite E5 respectively. The chromite spinel is also the main phase present, but a higher variety of silicates and other gangue minerals can be found, including $(Mg,Fe,Al)_6(Si,Al)_4O_{10}(OH)_8$, SiO_2, $NaCa_2Mg_5AlSi_7O_{22}(OH)_2$, $K_{0.7}Na_{0.4}Ca_{1.1}Al_{3.3}Si_{8.7}O_{24}(H_2O)_3$, $NaCa_2Mg_5AlSi_7O_{22}(OH)_2$, $Ca(Mg_{0.67}Fe_{0.33+2})(CO_3)_2$ and $(Mg_7Al_4(OH)_{22})_{0.09091}$.

- The ΔG of formation of the metallic oxides present in chromite were calculated (300°C to 1300°C) and the following sequence was obtained from highest to lowest stability: $MgO > Al_2O_3 > Cr_2O_3 > FeO > Fe_3O_4 > Fe_2O_3$. The Ellingham diagram computed indicates that the temperatures required to reduce FeO and Cr_2O_3 with carbon are 725°C and 1250°C, respectively.

The decomposition tendency of magnesiochromite in reducing atmosphere is lower than that of ferrochromite; and ΔG calculations confirmed that $MgCr_2O_4$ is harder to decompose also under oxidising conditions. The predominance area diagram for the Fe-Cr-Na-O-C system showed that metallic Fe and $NaCrO_2$ co-exist at 1050°C for a certain range of partial pressures of CO/CO_2, and under these conditions the instability of Cr^{6+} is maintained. Thermal analysis indicated that the decomposition of chromite in $NaCrO_2$ and Fe starts from 800°C, and the phases can be observed in XRPD patterns at 1000°C and 1050°C. When roasting in air atmosphere in the absence of alkali and carbon, exsolution of Fe_2O_3 can be observed at temperatures of 900°C and above.

- In the study performed on the oxidative alkali roasting of S.A. chromite ore with NaOH/KOH, approximately 95% Na_2CrO_4/K_2CrO_2 yield was achieved when chromite was roasted with NaOH and KOH at 1000°C for 2 hours and water leached. The study showed that at low temperature (400°C) the recovery of chromate in solution was higher for chromite roasted with KOH than with NaOH. However, at high temperatures (700°C and 1000°C) the recoveries were similar for both hydroxides. Equilibrium data showed the need of a Cr_2O_3:MOH ratio higher than the stoichiometric in order to fully decompose the chromite spinel phase and confirmed that formation of alkali ferrites, aluminates and silicates is possible and may influence the properties of the molten salt.

- The reaction mechanism of the oxidative alkali roasting of S.A. chromite with different alkali ratios of NaOH/KOH was discussed based on experimental results and thermodynamic data. The main phases found in water leached residues were partially-reacted chromite, Fe_2O_3, MgO and complex silicates. Sodium chromate was not present in water leached residues as shown by XRPD and SEM results, which suggests high efficiency of the leaching step. It was shown that the addition of excess alkali increases the extraction of the alkali chromate, but it also generates a higher volume of molten phase, leading to lower reaction rates as it represents an obstacle to the pore diffusion of oxygen.

- The effect of process parameters on the reductive alkaline roasting of S.A. chromite ore including temperature, time, alkali ratio and carbon ratio was studied, and the best results were obtained for a chromite:Na_2CO_3:C weight ratio of 1:1:0.2, a temperature of 1050°C and a reduction time of 2.5 hours.

- The use of other sodium salts (NaOH, $NaHCO_3$, $NaHSO_4$) provided similar results to those achieved with Na_2CO_3. However, reduction with K_2CO_3 was not found successful since the metallic Fe did not form.

- The alkali reduction of Brazilian ores was achieved yielding $NaCrO_2$ and metallic Fe, however, the metallisation observed was lower than in the case of S.A. chromite. Moreover, the alkali present reacted with silica forming complex silicate phases at high temperature which in some cases formed a sim of silicate product surrounding the partially-reacted chromite spinel core.

- The kinetic study of the alkali reduction of S.A. chromite and Brazilian chromite E4 suggests that the kinetics of the reaction can be described by the mixed model. The Ea of the reduction of the S.A. and Brazilian E4 ores are 217 kJ/mol and 205 kJ/mol for regime 1, and 211 kJ/mol and 177 kJ/mol for regime 2, respectively. The mechanism of the reduction of chromite in the presence of alkali and a solid reducing agent has been divided into steps and discussed based on experimental results.

- The treatment of reduced samples by magnetic separation yielded magnetic and non-magnetic fractions. The chemical composition of this materials is strongly dependant on the parameters of alkali reduction stage. The extraction of Cr_2O_3 into the non-magnetic fraction increased with increasing temperature and time of reduction. A total Cr_2O_3 extraction of 80% and a non-magnetic fraction of 51.78 wt.%Cr_2O_3 were achieved after magnetic separation of samples reduced at 1050°C for 2.5 hours and chromite:Na_2CO_3:C=1:1:0.2. The water leaching of the non-magnetic fraction achieved the extraction of 65.15 wt.% of the remaining Na_2O in the non-magnetic fraction and the results indicate that a 5% enrichment of the non-magnetic fraction was attained by the water leaching step.

- Different organic and inorganic acids were tested, and the acid leached products obtained have a wt.%Cr_2O_3 that increases in the following sequence: acetic < ascorbic < oxalic < tartaric < lactic < citric < phosphoric < hydrochloric < nitric < sulfuric. The best leaching results were achieved with H_2SO_4 with a concentration of 0.5M, a solid:liquid ratio equal to 1:100 g/mL, temperature of 80°C and 2 hours leaching. Multiple-stage H_2SO_4 leaching increased the wt.% Cr_2O_3 from 81.01 wt.%, to 83.90 wt.% and 85.44 wt.% after two and three leaching steps, respectively.

- The flowsheet of the reductive alkali roasting of chromite divides the process in 5 main sections, namely alkali reduction, magnetic separation, treatment of non-magnetic samples, recovery of Na_2CO_3 and heat exchange.

- According to the overall mass and energy balance performed, 85.6% Cr_2O_3 extraction was achieved in the final Cr_2O_3-rich product, which had a purity of 83.6 wt.% Cr_2O_3. The remaining is mainly in the magnetic fraction, which is enriched in metallic Fe. The alkali recovery stage is also able to recover 43.9% of the total Na_2CO_3 spent in the alkali reduction of the ore. The actual energy required for the alkali reduction stage is 7.49 MW, and the total energy consumption of the process adds up to a theoretical value of 77.59 MW. The heat released in the CO burning stage and condensation of steam from evaporation (67.75 MW) could be potentially recovered.

- The only waste stream produced by the alkali reduction process is the acidic solution from the acid leaching stage. This liquid waste was characterised by UV-vis technique, and no evidence of Cr^{6+} could be observe in the results. This confirms that the concentration of hexavalent chromium in the solution is lower than 0.42 ppm, which is the limit of analysis resolution achieved.

- The treatment of COPR reduced samples by magnetic separation and leaching yielded a Cr_2O_3-rich material with 80.23wt.% Cr_2O_3, which demonstrates the possibility of eliminating Cr^{6+} from the waste and obtaining a Cr_2O_3-rich material. Furthermore, the experimental conditions required for the processing of COPR are very similar to those of S.A. chromite ore, and therefore, its treatment would not require extra processing equipment.

- According to the results presented, the co-processing of chromite ores and COPR improve slightly the magnetic separation of the magnetic and non-magnetic fractions compared to the separation achieved when processing the chromite ores. However, XRPD and XRF results show that reduction was not complete and that the separation could be further improved by adjusting the parameters of both stages for each mixture.

11.2. FUTURE WORK

On the grounds of the experimental work carried out and the results presented and discussed in this manuscript, the main recommendations for further research are:

- ✓ **Reductive alkaline roasting of chromite ores in a rotary kiln.** The potential industrial processing of chromite ore by the reductive alkali roasting process should be carried out in an industrial rotary kiln similar to that used in the oxidative alkali roasting process. The process parameters, kinetics and technical details of the reduction in the kiln would require further investigation and optimisation.

- ✓ **Growth of metallic Fe during reduction.** The growth of metallic Fe particles during the reduction stage is key in order to maximise the magnetic separation of the different fractions. The effect of $NaHSO_4$ or a final high temperature stage on the growth of iron particles was observed in preliminary experiments and needs to be further studied, confirmed and understood.

- ✓ **Magnetic fraction treatment and/or applications.** The magnetic separation does not achieve 100% separation of Cr_2O_3 into the non-magnetic fraction and thus the magnetic fraction can still contain approximately 20 wt.% Cr_2O_3. Different options for the beneficiation of the magnetic fraction produced could be:

    - ▪ Study the treatment of the magnetic fraction by smelting in reducing atmosphere. Preliminary results obtained showed that metallic Fe could be separated by smelting, thereby obtaining a slag phase containing Cr_2O_3 as $NaCrO_2$. The slag could be further treated by incorporating it back to the alkali reduction process.
    - ▪ The magnetic fraction is a material rich in metallic Fe (around 70%) and containing variable amount of chromium as $NaCrO_2$, and therefore could be used as feedstock for the production of ferrochrome metallurgical products.
    - ▪ If the magnetic fraction would be recycled back into the reduction process, the magnetic separation could be improved by increasing the fraction of iron in the initial charge. Furthermore, the Cr_2O_3 in the magnetic fraction would be incorporated back into the process, increasing the overall recovery.

- ✓ **Further purification of the Cr_2O_3-rich product.** The purification of the material obtained after acid leaching could be required depending on the application of the Cr_2O_3 obtained by the alkali reduction process. Two of the possible methods are proposed:
  - Roasting of the Cr_2O_3-rich residue with $NaHSO_4$ followed by water leaching.
  - Application of ammonium salts for Cr_2O_3 purification.

- ✓ **Alkali reduction of chromite using potassium salts.** The reduction experiments carried out with potassium carbonate did not yield positive results in terms of Fe metallisation and $KCrO_2$ formation. However, extensive breakage of the particles was observed, and it is therefore recommended to investigate further on the physico-chemistry of the reduction of chromite with potassium salts.

- ✓ **Maximize alkali recovery and minimize water and acid consumption**. Further study on the alkaline solutions treatment for alkali recovery is required. It is necessary to look at water balance in more detail by studying solid/liquid ratio in leaching experiments in order to decrease overall water consumption. Further leaching experiments will be carried out for optimization of the acid leaching step.

APPENDICES

APPENDIX 1. RIETVELD REFINEMENT DATA

Rietveld refinement was carried out on the XRPD patterns obtained from the analysis of chromite samples heated under different chemical potentials (see Chapter 5). A summary of the results obtained from the main parameters refined is presented in TABLE 0-1 to TABLE 0-3.

TABLE 0-1. Rietveld analysis of S.A. chromite ore heated isothermally in air atmosphere at different temperatures.

Phase	Temperature (°C)	Lattice parameter (Å)	Fractions				Oxygen coordinate	Thermals * 100 U_{iso}		Rp(%)
			Cr	Al	Fe	Mg		Cr/Al	Fe/Mg	
Chromite	As-received	8.306	0.718	0.258	0.510	0.485	0.266	3.45	2.86	2.74
Chromite	100	8.291	0.703	0.298	0.530	0.486	0.262	1.85	2.32	2.24
Chromite	200	8.302	0.643	0.356	0.503	0.482	0.262	2.61	3.7	1.80
Chromite	300	8.305	0.717	0.283	0.515	0.498	0.264	1.03	1.78	3.25
Chromite	400	8.290	0.720	0.280	0.515	0.486	0.262	1.42	2	2.25
Chromite	500	8.278	0.687	0.314	0.498	0.500	0.262	1.61	2.99	2.25
Chromite	600	8.273	0.639	0.361	0.499	0.498	0.259	1.78	3.97	2.21
Chromite	700	8.269	0.695	0.305	0.493	0.498	0.265	1.52	1	2.28
Chromite	800	8.269	0.712	0.288	0.412	0.490	0.256	1.08	2.9	1.80
Chromite	900	8.256	0.745	0.255	0.393	0.491	0.257	0.82	3.47	1.50
Chromite	1000	8.249	0.799	0.201	0.382	0.483	0.261	0.98	2.11	1.93
Chromite	1050	8.259	0.798	0.202	0.327	0.494	0.259	1.68	3.73	1.77
Chromite phase: general formula $(Fe,Mg)(Cr,Al)_2O_4$, and space group Fd-3m										

Phase	Temperature (C°)	Lattice parameters (Å)		Fe Coord.(z)	O Coord.(x)	Thermals*100 U_{iso}		Rp(%)
		a = b	c			Fe	O	
Fe_2O_3	900	4.993	13.565	0.352	0.677	3.77	2.61	1.50
Fe_2O_3	1000	4.984	13.539	0.351	0.684	3.64	0.73	1.93
Fe_2O_3	1050	4.986	13.548	0.351	0.681	2.37	0.02	1.77
Hematite phase: general formula Fe_2O_3, and space group R-3c								

TABLE 0-2. Rietveld analysis of S.A. chromite ore heated isothermally in Ar at different temperatures.

Phase	Temperature (^{o}C)	Lattice parameter (Å)	Fractions				Oxygen coordinate	Thermals * 100 U$_{iso}$		Rp(%)
			Cr	Al	Fe	Mg		Cr/Al	Fe/Mg	
Chromite	As-received	8.306	0.718	0.258	0.510	0.485	0.266	3.45	2.86	2.74
Chromite	100	8.295	0.748	0.252	0.510	0.492	0.263	1.84	1.98	2.07
Chromite	200	8.309	0.712	0.288	0.523	0.505	0.261	2.09	2.65	2.89
Chromite	300	8.297	0.712	0.288	0.514	0.507	0.262	2.09	2.03	1.81
Chromite	400	8.287	0.705	0.295	0.514	0.495	0.260	2.2	2.5	1.83
Chromite	500	8.291	0.715	0.285	0.517	0.502	0.263	2.07	1.86	2.57
Chromite	600	8.290	0.727	0.273	0.519	0.490	0.262	1.88	1.76	2.01
Chromite	700	8.276	0.723	0.277	0.509	0.488	0.259	2.3	2.68	1.87
Chromite	800	8.261	0.751	0.249	0.490	0.492	0.261	0.98	1.06	1.76
Chromite	900	8.275	0.786	0.214	0.489	0.448	0.257	1.81	3.46	2.23
Chromite	1000	8.279	0.789	0.211	0.474	0.457	0.261	2.36	3.11	1.59
Chromite	1050	8.280	0.786	0.214	0.474	0457	0.259	2.19	3.25	2.06
Chromite phase: general formula (Fe,Mg)(Cr,Al)$_2$O$_4$, and space group Fd-3m										

TABLE 0-3. Rietveld analysis of S.A. chromite ore and activated charcoal mixed in a weight ratio of chromite:C = 1:0.2, and heated isothermally in argon at different temperatures.

Phase	Temperature (^{o}C)	Lattice parameter (Å)	Fractions				Oxygen coordinate	Thermals * 100 U$_{iso}$		Rp(%)
			Cr	Al	Fe	Mg		Cr/Al	Fe/Mg	
Chromite	As-received	8.306	0.683	0.317	0.509	0.484	0.683	2.91	2.50	2.70
Chromite	100	8.297	0.721	0.279	0.514	0.498	0.721	2.64	3.51	2.36
Chromite	200	8.298	0.698	0.303	0.513	0.495	0.698	2.68	3.04	2.47
Chromite	300	8.302	0.719	0.281	0.510	0.489	0.719	1.69	2.76	1.63
Chromite	400	8.294	0.748	0.253	0.514	0.514	0.748	1.47	2.60	3.18
Chromite	500	8.288	0.722	0.278	0.516	0.514	0.722	0.95	1.01	1.94
Chromite	600	8.296	0.771	0.229	0.513	0.500	0.771	1.83	2.63	2.47
Chromite	700	8.288	0.690	0.310	0.520	0.513	0.690	2.19	2.77	2.06
Chromite	800	8.288	0.692	0.308	0.515	0.508	0.692	2.60	2.05	1.25
Chromite	900	8.293	0.680	0.320	0.517	0.508	0.680	2.14	2.52	2.06
Chromite	1000	8.289	0.702	0.298	0.517	0.521	0.702	3.09	2.13	1.54
Chromite	1050	8.289	0.638	0.362	0.535	0.467	0.263	1.95	2.96	2.05
Chromite phase: general formula (Fe,Mg)(Cr,Al)$_2$O$_4$, and space group Fd-3m										

Phase	Temperature (^{o}C)	Lattice parameters (Å)		Rp(%)
		a = b	c	
Carbon	200	2.431	10.044	2.47
Carbon	500	2.486	10.035	1.94
Carbon	600	2.48	10.046	2.47
Carbon	700	2.481	10.048	2.06
Carbon	800	2.464	10.046	1.25
Carbon	900	2.478	10.029	2.06
Carbon	1050	2.463	10.027	2.05
Carbon phase: formula C, space group R-3m				

APPENDIX 2. COMPARISON OF REAL VS CALCULATED CONCENTRATION OF STANDARD MIXTURES FOR XRF SEMI-QUANTITATIVE ANALYSIS.

Oxide mixtures of known concentration were used as standards for XRF analysis. TABLE 0-4 shows a comparison of the standards chemical composition and the XRF results obtained by analysis of the standards using a quick-scan and the program developed.

TABLE 0-4. Known chemical composition of standards and XRF analysis of the standards obtained by the semi-quantitative program and quick-scan (QS).

wt.%	Cr_2O_3			Fe_2O_3			MgO			Al_2O_3		
	Value	Program	QS	Value	Program	QS	Value	Program	QS	Value	Program	QS
LS1	99	90.35	94.24	0.5	2.56	1.01	0.3	0.00	0.54	0.2	0.05	0.49
LS2	80	79.07	81.20	20	20.55	16.13	0	0.00	0.29	0	0.19	0.57
LS3	60	70.91	67.45	40	39.54	28.25	0	0.00	0.20	0	0.05	0.36
LS4	40	44.74	45.18	60	59.54	49.63	0	0.00	0.23	0	0.13	0.46
LS5	20	20.25	20.21	80	81.27	74.32	0	0.00	0.30	0	0.04	0.45
LS6	10	11.69	10.40	90	92.13	83.30	0	0.00	0.39	0	0.15	0.61
LS7	46.4	57.07	54.36	19.4	27.41	20.35	10.8	13.11	8.64	0	17.20	11.87
LS8	30	28.25	30.69	20	20.16	18.85	20	20.88	17.29	20	19.62	17.46
LS9	30	27.49	30.45	20	19.75	19.56	20	20.00	16.84	10	9.60	9.30
LS10	30	26.62	30.05	20	19.06	19.25	20	19.12	16.61	5	4.97	5.06
LS11	30	27.80	32.04	20	20.04	20.47	25	24.87	21.61	25	23.76	22.27
LS12	30	27.37	30.45	20	19.76	19.06	10	9.72	8.48	20	19.51	17.78
LS13	30	26.22	29.89	20	18.79	19.22	5	4.75	4.80	20	18.21	17.64
LS14	75	66.69	72.76	4	5.08	3.53	8	8.41	6.81	8	8.51	7.47
LS15	50	44.61	49.95	25	24.45	22.72	10	10.28	8.56	5	5.42	5.00
L16	20	18.09	20.03	30	29.26	30.83	20	17.59	16.07	5	4.27	4.71
LS17	5	7.22	5.50	45	44.80	43.18	20	20.73	17.14	20	20.47	17.71
LS18	2	5.25	3.15	48	46.94	46.79	10	9.78	8.72	20	19.15	17.90
LS19	1	3.75	1.37	70	70.43	65.82	5	5.09	4.72	10	10.40	9.36

TABLE 0-4. Continued.

wt.%	Na_2O			SiO_2			CaO		
	Value	Program	QS	Value	Program	QS	Value	Program	QS
LS1	0	0.00	1.96	0	0.42	1.18	0	0.17	0.22
LS2	0	0.00	0.78	0	0.00	0.58	0	0.10	0.14
LS3	0	0.00	2.86	0	0.00	0.36	0	0.12	0.17
LS4	0	0.28	3.37	0	0.00	0.50	0	0.17	0.20
LS5	0	0.00	3.58	0	0.00	0.55	0	0.12	0.18
LS6	0	0.12	3.68	0	0.00	0.84	0	0.15	0.22
LS7	0	0.00	1.95	0.61	0.64	1.19	0.16	0.15	0.19
LS8	4	4.64	7.99	4	4.18	4.77	2	2.12	2.44
LS9	10	10.68	12.83	7	6.82	7.26	3	2.82	3.32
LS10	15	15.62	18.09	7	6.72	7.40	3	2.63	3.05
LS11	0	0.00	1.44	0	0.33	1.30	0	0.34	0.47
LS12	10	10.40	12.98	7	7.13	7.52	3	2.71	3.27
LS13	15	14.04	16.64	7	6.63	7.50	3	3.12	3.83
LS14	2	2.30	4.95	2	2.45	2.83	1	1.07	1.13
LS15	5	3.99	7.14	3	3.00	3.45	2	2.47	2.76
L16	15	10.33	13.33	7	9.77	10.73	3	3.40	4.15
LS17	4	5.84	8.69	4	4.38	4.80	2	2.24	2.60
LS18	10	9.80	12.58	7	6.52	7.28	3	2.71	3.21
LS19	5	5.77	8.24	7	7.48	7.49	2	2.17	2.45

APPENDIX 3. CHARACTERISATION OF CHROMITE ORE AND TREATED SAMPLES USING ZEISS MINERALOGIC MINING.

ORE CHARACTERISATION

The Mineralogic Mining system was used to characterise the Brazilian chromite with high silica content. The purpose of this analysis was to identify the main phases present in the ore, their average chemical composition and the distribution of elements between the different minerals. The main results obtained from the characterisation of the ore by Mineralogic Mining are presented in FIGURE 0-1 and TABLE 0-5, TABLE 0-6a and TABLE 0-6b.

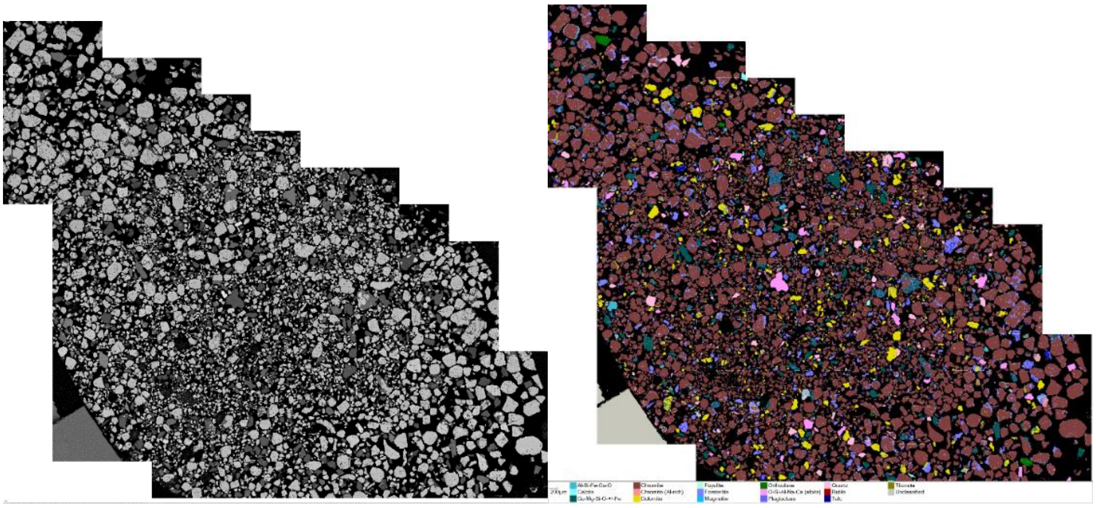

FIGURE 0-1. SEM backscattered montage image (left) and Mineralogic Mining montage image of the Brazilian chromite ore sample.

TABLE 0-5. List of target minerals identified in the Brazilian chromite sample including values of weight%, area%, average composition and grain size.

Target Mineral	Weight %	Area %	Average Composition	Grain Size (µm)	Grain Size Std Dev
Chromite	**65.718**	69.170	Cr 52.36; Fe 18.84; Al 12.42; Mg 8.52; O 7.86;	92.64	89.68
Dolomite	**12.605**	4.655	O 51.07; Ca 33.16; Mg 15.1; Fe 0.37; Si 0.3;	49.35	61.38

Forsterite	**7.879**	8.293	Si 34.5; O 30.94; Mg 29.01; Cr 3.63; Fe 1.91;	24.60	30.99
Ca-Mg-Si-O+/-Fe	**4.881**	5.138	O 36.92; Si 31.88; Mg 13.95; Ca 12.81; Fe 3.47; Cr 0.96;	42.73	60.92
Quartz	**4.334**	1.721	Si 55.33; O 44.55; Fe 0.12; K 0;	28.66	49.19
O-Si-Al-Na-Ca (albite)	**1.546**	1.628	O 40.51; Si 36.93; Al 13.48; Na 6.38; Ca 2.71;	75.13	83.24
Talc	**0.689**	0.725	O 47.87; Si 28.34; Mg 23.78;	16.33	15.59
Magnetite	**0.361**	0.380	Fe 78.99; O 20.99; Ti 0.03;	13.98	13.96
Rutile	**0.137**	0.032	Ti 58.94; O 41.06;	21.86	24.19
Fayalite	**0.007**	0.007	Fe 53.8; O 33.04; Si 13.08; Cr 0.08;	10.46	2.11

TABLE 0-6a. Assay and distribution values for the different elements in the different minerals identified in the Brazilian chromite sample.

Target Mineral	Weight %	Assay (O)%	Distrib. (O)%	Assay (Na)%	Distrib. (Na)%	Assay (Mg)%	Distrib. (Mg)%	Assay (Al)%	Distrib. (Al)%	Assay (Si)%	Distrib. (Si)%
Ca-Mg-Si-O-+/-Fe	4.881	1.798	9.363	---	0.040	0.679	6.417	0.009	0.106	1.553	19.295
Chromite	65.718	5.121	26.668	0.008	7.332	5.551	52.425	8.094	94.442	0.372	4.621
Dolomite	12.605	6.398	33.317	---	0.156	1.892	17.871	---	---	0.037	0.462
Fayalite	0.007	0.002	0.012	---	---	---	0.001	---	0.002	0.001	0.011
Forsterlite	7.879	2.368	12.331	---	0.182	2.221	20.972	0.014	0.165	2.641	32.818
Magnetite	0.361	0.064	0.332	---	0.095	0.004	0.040	0.002	0.018	0.017	0.212
O-Si-Al-Na-Ca (albite)	1.546	0.625	3.256	0.098	90.068	---	---	0.208	2.427	0.570	7.083

Quartz	4.334	1.904	9.913	0.002	1.477	0.031	0.290	---	---	2.364	29.382
Rutile	0.137	0.055	0.287	---	---	---	---	---	0.001		0.001
Talc	0.689	0.326	1.698	---	---	0.162	1.530	---	---	0.193	2.400
Sample		**19.202**	---	**0.109**	---	**10.588**	---	**8.570**	---	**8.046**	---

TABLE 0-6b. Assay and distribution values for the different elements in the different minerals identified in the Brazilian chromite sample (continued.)

Target Mineral	**Assay (K)%**	**Distrib. (K)%**	**Assay (Ca)%**	**Distrib. (Ca)%**	**Assay (Ti)%**	**Distrib. (Ti)%**	**Assay (Cr)%**	**Distrib. (Cr)%**	**Assay (Fe)%**	**Distrib. (Fe)%**
Ca-Mg-Si-O-+/-Fe	0.001	0.215	0.624	12.049	0.001	1.261	0.047	0.135	0.169	1.299
Chromite	0.032	12.714	0.029	0.563	0.007	7.459	34.118	98.041	12.276	94.394
Dolomite	---	0.007	4.154	80.229	0.001	0.826	0.055	0.157	0.047	0.361
Fayalite	---	---	---	---	---	---	---	---	0.004	0.028
Forsterlite	0.102	41.001	0.103	1.998	0.001	1.539	0.278	0.799	0.146	1.125
Magnetite	---	0.015	0.001	0.013	---	0.081	0.033	0.095	0.240	1.842
O-Si-Al-Na-Ca (albite)	0.002	0.847	0.042	0.806	---	0.055	---	---	0.001	0.005
Quartz	---	0.066	0.011	0.209	---	0.169	0.014	0.041	0.005	0.040
Rutile	---	---	---	0.002	0.079	84.571	0.002	0.004	0.001	0.004
Talc	0.004	1.639	---	0.003	---	0.132	---	---	0.003	0.025
Sample	**0.250**	---	**5.178**	---	**0.093**	---	**34.799**	---	**13.005**	---

The results show that the Brazilian ore has an elemental composition of 34.80% Cr, 19.20% O, 13.01% Fe, 10.56% Mg, 8.57% Al, 8.05% Si and 5.18% Ca, with smaller quantities of Na (0.11%) and K (0.25%). The main phases present are chromite, with an average Cr content of 52%, dolomite, containing 80% of the total Ca in the ore, and different silicate phases such as forsterite, quartz and two other silicate phases, a Ca-Mg-Fe-silicate and a Na-Ca-Al-silicate.

The ore was previously analysed by X-ray powder diffraction (XRPD) and the resulting analysed pattern is compared in Figure 0-2 with XRPD patterns of pure chromite spinel, dolomite, forsterite and quartz, which were the main minerals identified in the Brazilian ore sample by using Mineralogic Mining. Most of the main peaks of the analysed pattern can be matched with chromite, dolomite, forsterite and quartz peaks, which indicates good agreement between the Mineralogic Mining and XRD results.

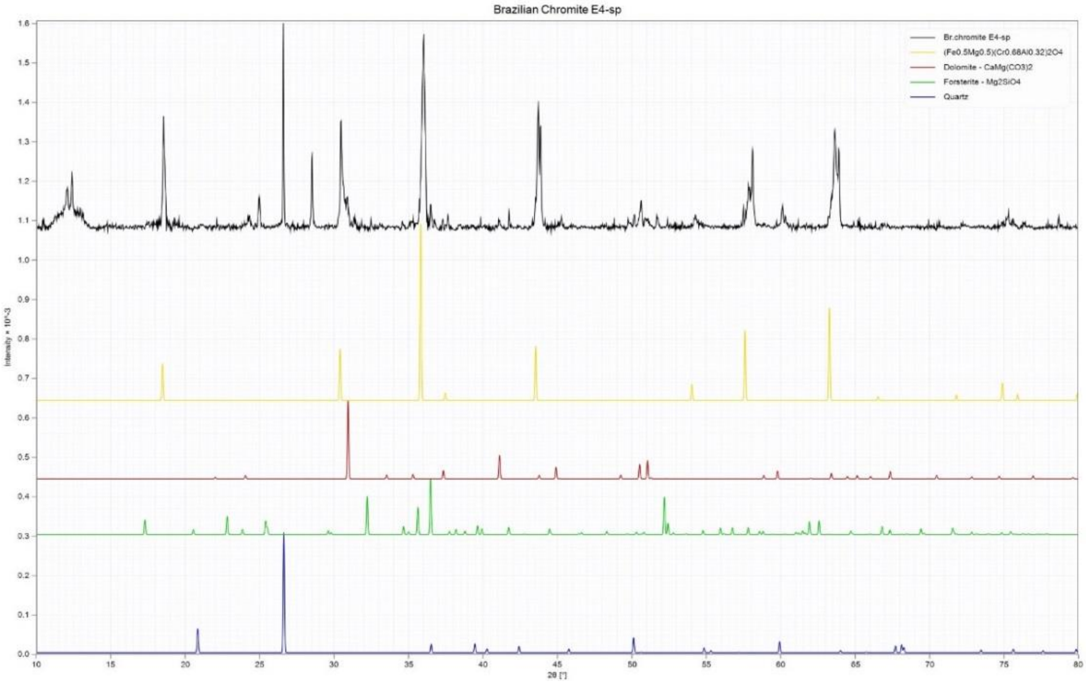

FIGURE 0-2. X-ray powder diffraction pattern of the Brazilian ore (black) compared to patterns of pure chromite spinel (yellow), dolomite (red), forsterite (green) and quartz (blue).

The mineralogy of the ore is the initial point to be understood before it is subjected to any beneficiation or extraction process, and therefore all the data generated by Mineralogic Mining was key for a more efficient design of the ore treatment by alkali reduction.

CHARACTERISATION OF TREATED SAMPLES

A sample of S.A. chromite ore reduced in the presence of Na_2CO_3 and activated charcoal at 1050°C for 30 minutes was analysed by Mineralogic Mining with the aim of determining and quantifying the main phases present. In this case, the main phases of interest were the expected products of reduction, namely $NaCrO_2$ and metallic iron. It was also useful to observe the formation of other products such as MgO, calcium carbonate and silicate phases. The main results obtained are presented in FIGURE 0-3, TABLE 0-7 and TABLE 0-8.

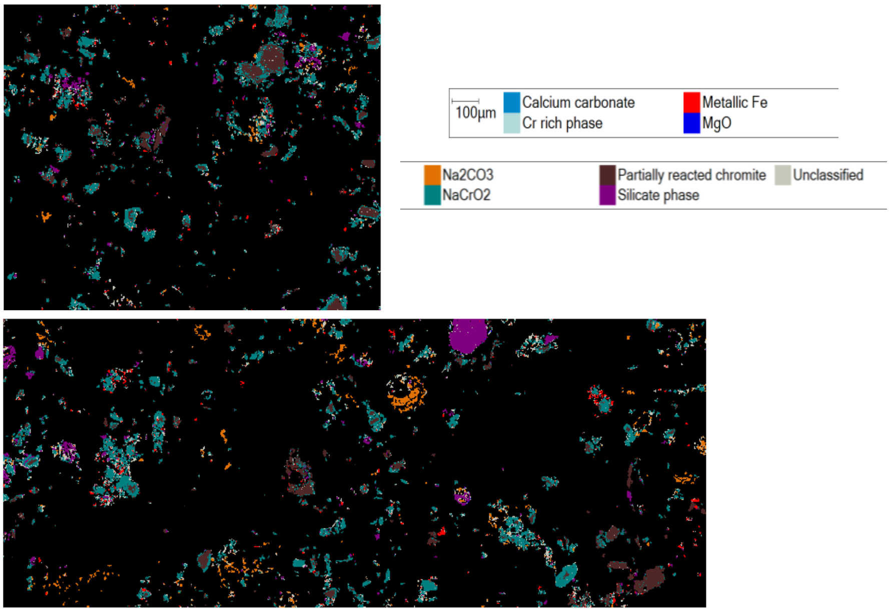

FIGURE 0-3. Mineralogic Mining images of random fields of a treated S.A. chromite sample reduced with Na_2CO_3 and activated charcoal at 1050°C for 30 minutes.

TABLE 0-7. List of target minerals identified in a reduced S.A. chromite sample including values of weight%, area%, average composition and grain size.

Target Mineral	Weight %	Area %	Average Composition	Grain Size (µm)
$NaCrO_2$	45.777	40.314	Cr 38.78; Fe 19.77; O 14.99; Na 12.96; Al 8.08; Mg 3.65; Si 1.17; Ca 0.59;	5.05
Partially reacted chromite	29.945	26.372	Cr 43; Fe 27.07; O 15.11; Al 8.77; Mg 5.71; Si 0.34;	3.95
Silicate phase	10.411	9.168	Si 32.98; O 24.1; Na 12.41; Fe 9.46; Cr 6.95; Mg 6.75; Al 5.32; Ca 2.04;	3.48

Na_2CO_3	8.420	7.416	Na 100;	4.03
Metallic Fe	4.665	4.108	Fe 84.37; Cr 15.63;	2.37
Cr rich phase	0.682	0.601	Cr 100;	1.64
MgO	0.088	0.078	Mg 61.71; O 28.75; Cr 9.54;	2.29
Calcium carbonate	0.011	0.010	Ca 53.12; O 46.88;	1.45
Unclassified	---	11.933	Fe 30.7; Na 20.27; O 19.63; Cr 17.57; Al 3.85; Si 2.76; Ca 2.33; Mg 1.72; P 0.44; Cl 0.41; Zr 0.13; Ni 0.1; Zn 0.03; Cu 0.02; Ti 0.01; K 0.01;	2.60

TABLE 0-8. Assay and distribution values for the elements of interest in the different minerals identified in the reduced S.A chromite sample.

Target Mineral	**Distribution (O)%**	**Distribution (Na)%**	**Distribution (Mg)%**	**Distribution (Al)%**	**Distribution (Si)%**	**Distribution (Cr)%**	**Distribution (Fe)%**
$NaCrO_2$	41.39	50.27	40.38	53.04	12.77	53.65	40.35
Partially reacted chromite	27.15	---	41.07	37.47	2.38	38.72	35.94
Silicate phase	15.14	10.95	17.00	7.94	81.64	2.19	4.39
Na_2CO_3	15.17	37.25	0.09	0.73	1.73	1.87	3.00
Metallic Fe	0.86	1.50	0.33	0.53	1.25	1.98	15.77
Cr rich phase	0.13	0.00	0.04	0.27	0.08	1.56	0.51
MgO	0.13	0.01	1.10	---	0.12	0.02	0.03

The sample was treated for a short period of time, just 30 minutes, and therefore unreacted/partially reacted chromite particles and unreacted Na_2CO_3 are still present. The diffusion of sodium towards the centre of the chromite particles can be observed in Figure 0-3. Formation of $NaCrO_2$ (product of reaction of Na_2O and Cr_2O_3 contained in the chromite spinel) can be observed at the edges of partially reacted chromite particles, whereas the centre is mainly unreacted chromite (brown phase), suggesting that the reaction progresses following the Shrinking core model. Formation of small metallic iron particles can be also seen after 30 minutes.

The analysis, both qualitative and quantitative, of the different products of reaction provides useful information for the study of the reaction mechanism. This novel approach could allow us to develop a suitable single-particle and multiple-particle reaction models for the reduction of chromite ore in the presence of alkali, by phase analysing and phase quantification of samples treated by alkali reduction at different temperatures, times and with different alkali addition.

ACKNOWLEDGEMENTS

The author wants to acknowledge the support and guidance from Mr. Shaun Graham and Miss Laura Ward who kindly gave access to the use of the Mineralogic Mining/SEM system, provided the required training and guided through the entire analysis, which was carried out in the ZEISS facilities located in Cambridge (ZEISS Natural Resources Lab, 509 Coldhams Lane, Cambridge, CB1 3JS).

REFERENCES

1 Escudero-Castejon, L, Sanchez-Segado, S, Parirenyatwa, S, Hara, Y and Jha, A (2017) 'A Cr6+-Free Extraction of Chromium Oxide from Chromite Ores Using Carbothermic Reduction in the Presence of Alkali', in *Applications of Process Engineering Principles in Materials Processing, Energy and Environmental Technologies*, Springer, pp. 179–188.

2 Maliotis, G (1996) *Chromium uses and markets*, Industrial Minerals Information Ltd., London.

3 Cunat, Pierre-Jean (2004) 'Alloying elements in stainless steel and other chromium-containing alloys'. *International Chromium Development Association, Paris*.

4 Brown, T J, Bide, T, Idoine, N E, Shaw, R A, et al. (2015) *World mineral production 2009-2013*, British Geological Survey.

5 Ober, Joyce A (2017) *Mineral commodity summaries 2017*, US Geological Survey.

6 Statista (n.d.) 'Global stainless steel production from 2005 to 2017'. [online] Available from: https://www.statista.com/statistics/223028/world-stainless-steel-production/ (Accessed 7 February 2018)

7 Tarasov, A V (1998) 'The main trends in investigations and development of the processes in the heavy nonferrous metals metallurgy'. *Proceedings of the IV International Conference on Clean Technologies for the Mining Industry*, I(State Research Institute of Non-Ferrous Metals, Moscow, Rusia. Environment & Innovation in mining and mineral technology).

8 Freese, Kevin, Miller, Robert, J Cutright, Teresa and Senko, John (2014) 'Review of chromite ore processing residue (COPR): past practices, environmental impact and potential remediation methods'. *Current Environmental Engineering*, 1(2), pp. 82–90.

9 Barnhart, Joel (1997) 'Occurrences, uses, and properties of chromium'. *Regulatory toxicology and pharmacology*, 26(1), pp. S3–S7.

10 Papp, John F (1994) *Chromium life cycle study*, US Department of the Interior, Bureau of Mines.

11 Kekkonen, Marko, Xiao, Yanping and Holappa, Lauri (1995) 'Kinetic study on solid state reduction of chromite pellets'. *Proc. Int. Ferroalloy Cong., Trondhein, Norway*, pp. 351–360.

12 Dawson, N F and Edwards, R I (1986) 'Factors affecting the reduction of chromite', in *Proceedings of INFACON IV 4th International Ferro Alloys Congress*, pp. 105–113.

13 Ding, Y L and Warner, N A (1997) 'Kinetics and mechanism of reduction of carbon-chromite composite pellets'. *Ironmaking & steelmaking*, 24(3), pp. 224–229.

14 Antony, M P, Tathavadkar, V D, Calvert, C C and Jha, A (2001) 'The soda-ash roasting of chromite ore processing residue for the reclamation of chromium'. *Metallurgical and materials Transactions B*, 32(6), pp. 987–995.

15 Geveci, A, Topkaya, Y and Ayhan, E (2002) ‘Sulfuric acid leaching of Turkish chromite concentrate’. *Minerals Engineering*, 15(11), pp. 885–888.

16 Tinjum, James M, Benson, Craig H and Edil, Tuncer B (2008) ‘Mobilization of Cr (VI) from chromite ore processing residue through acid treatment’. *Science of the Total Environment*, 391(1), pp. 13–25.

17 Sun, Zhi, Zheng, Shi-li, Xu, Hong-bin and Zhang, Yi (2007) ‘Oxidation decomposition of chromite ore in molten potassium hydroxide’. *International Journal of Mineral Processing*, 83(1), pp. 60–67.

18 Hundley, Gary L, Nilsen, D N and Siemens, Richard E (1985) *Extraction of chromium from domestic chromites by alkali fusion*, US Department of the Interior, Bureau of Mines.

19 Jha, Animesh (2011) ‘The alkali roasting of complex oxide minerals for high purity chemicals-beyond the Le Chatelier era into the 21st century’. *JOM*, 63(1), pp. 39–42.

20 Foley, E and MacKinnon, Kathryn P (1970) ‘Alkaline roasting of ilmenite’. *Journal of Solid State Chemistry*, 1(3), pp. 566–575.

21 Tathavadkar, Vilas, Antony, M P and Jha, A (2002) ‘Improved extraction of aluminium oxide from bauxite and redmud’, in *LIGHT METALS-WARRENDALE-PROCEEDINGS-*, TMS, pp. 199–204.

22 Tathavadkar, V and Jha, A (2004) ‘The effect of molten sodium titanate and carbonate salt mixture on the alkali roasting of ilmenite and rutile minerals’, in *VIIInternational Conference on Molten Slags Fluxes and Salts, The South African Institute of Mining and Metallurgy,[2004],(255-261)*.

23 Nafeaa, I A, Zekry, A F, Farag, A B, Khalifa, M G, et al. (2013) ‘Kinetic Study of Formation of Sodium Titanets by Roasting of Soda Ash and Ilmenite Ore Concentrate’. *Indian Chemical Engineer*, 55(4), pp. 283–293.

24 Parirenyatwa, Stephen, Escudero-Castejon, Lidia, Sanchez-Segado, Sergio, Hara, Yotamu and Jha, Animesh (2015) ‘Comparative study of alkali roasting and leaching of chromite ores and titaniferous minerals’. *Hydrometallurgy*.

25 Sanchez-Segado, Sergio, Lahiri, Abhishek and Jha, Animesh (2015) ‘Alkali roasting of bomar ilmenite: rare earths recovery and physico-chemical changes’. *Open Chemistry*, 13(1).

26 Sanchez-Segado, S, Makanyire, T, Escudero-Castejon, L, Hara, Y and Jha, A (2015) ‘Reclamation of reactive metal oxides from complex minerals using alkali roasting and leaching–an improved approach to process engineering’. *Green Chemistry*, 17(4), pp. 2059–2080.

27 Moon, Deok Hyun, Wazne, Mahmoud, Dermatas, Dimitris, Christodoulatos, Christos, et al. (2007) ‘Long-term treatment issues with chromite ore processing residue (COPR): Cr6+ reduction and heave’. *Journal of hazardous materials*, 143(3), pp. 629–635.

28 Tathavadkar, Vilas D, Jha, A and Antony, M P (2003) ‘The effect of salt-phase composition on the rate of soda-ash roasting of chromite ores’. *Metallurgical and Materials transactions B*, 34(5), pp. 555–563.

29 Antony, M P, Jha, A and Tathavadkar, V (2006) ‘Alkali roasting of Indian chromite ores: thermodynamic and kinetic considerations’. *Mineral Processing and Extractive Metallurgy*, 115(2), pp. 71–79.

30 Nickens, Kristen P, Patierno, Steven R and Ceryak, Susan (2010) ‘Chromium genotoxicity: a double-edged sword’. *Chemico-biological interactions*, 188(2), pp. 276–288.

31 Antony, M P, Tathavadkar, V, Clavert, C C, Wilkinson, M and Jha, A (2000) ‘Recovery of chromium from industrial wastes’, in Singhal Raj K. and Mehrotra Anil K. (eds.), *Environmental Issues and Waste Management in Energy and Mineral Production* , Balkema, Rotterdam, pp. 751–755.

32 Tathavadkar, V D, Jha, A and Antony, M P (2001) ‘The soda-ash roasting of chromite minerals: Kinetics considerations’. *Metallurgical and Materials Transactions B*, 32(4), pp. 593–602.

33 Tathavadkar, Vilas D (2001) ‘The process physical chemistry of extraction of sodium chromate from chromite ores’. [online] Available from: http://leeds.summon.serialssolutions.com/2.0.0/link/0/eLvHCXMwY2AwNtIz0EUrE0wszS2TUoB5yTAZ1EBPSza1sEw1T0kGVk7JaWbgrTHBPiYhTiZBYaZBiLOjQd35HGApXox2ej6w3rEwNrOsCwbtLgc2yEFr-erqooANTLBqpBrCTZCBxwVpZluIgSk1T4QhCBgJCgWQpfgKBdAQUUiG3bGmkJ-mACwbiyB7C0C84vyUzNJco

34 Sanchez-Segado, Sergio and Jha, Animesh (2013) ‘Physical Chemistry of Roasting and Leaching Reactions for Chromium Chemical Manufacturing and Its Impact on Environment - A Review’, in *Materials Processing Fundamentals*, John Wiley & Sons, Inc., pp. 225–236. [online] Available from: http://dx.doi.org/10.1002/9781118662199.ch25

35 Li, P, Chen, Y, Zheng, S, Wang, W and Zhang, Y (2016) ‘Phase transformation and structure evolution of chromite in the late stages of soda ash roasting process’. *Mineral Processing and Extractive Metallurgy*, 125(2), pp. 64–70.

36 Zhang, Yi, Xu, H, Zheng, S and Qi, T (2008) ‘A Clean Production Process of Chromic Oxide’, in *The 2008 Annual Meeting*.

37 Guertin, Jacques, Jacobs, James A and Avakian, Cynthia P (2004) *Chromium(VI) Handbook*, Hoboken, CRC Press. [online] Available from: http://leeds.summon.serialssolutions.com/2.0.0/link/0/eLvHCXMwXZ2xDsIwDEQjdhYk-ItUCXbasIKoGJhKxB5fkrET_y8cxIDY_AHWPZ_k0xlDx8HZP03oQRUoS5XfLVdMwOgrYRQn8FJ7bvhx53Tm5RmWH4Gfd2ZT171J8zVdbvbbD2ArR7ZcpDco6YUfEYKSqSlqwBPY6wQBQf1MI8onkVCaGnfdv4DgxYEj-YPZ5v5Gvr4-c

38 ICDA (2015) ‘International Chromium Development Association’. [online] Available from: http://www.icdacr.com/index.php?lang=en

39 Papp, John F (2002) ‘US Geological Survey Minerals yearbook: Volume I’. *Metals and Minerals: Chromium*.

40 U.S.A. Iron Steel Division and Administration, Business Defense Services (1962) *Materials survey : chromium*, [online] Available from:

http://leeds.summon.serialssolutions.com/2.0.0/link/0/eLvHCXMwjV3PS8MwFH6IAxE8ONSqU-jJW0ubH23j0eEQXEHmlLHLSNIEB67i1gn-9762umnpwUMPD9KPwAvve1_IlwBQ4gdeoyZIS02YWCRnlWB5TJQOlFVhrLG9pZksdwoeh2x8w0bPfLT1rjduG2gIdWxNYlRYlfZB0Ma5vdKy8IsqBofQMaV_oAs7Jj-CXiqLOsfua

41 Smith, Lewis A (1932) *Chromium : general information*, [online] Available from: http://leeds.summon.serialssolutions.com/2.0.0/link/0/eLvHCXMwjV1LS8NAEB7EgggeLGp8k5O3hOw78WixCLYgbZHSS9lHogUNSNv_72xSWw05eMhhIPuxZJb5Zjb7zQIwGidRIyYQowpuhXEJ8rFmzimnMytFxjmTrPozMx7wyQMfvYrRTrve6DbQKNSRDGlKKv00xZjbOLfnJQu_qKJ_DJ3c6we6sJeXJ3Drm89-Ltaf4X34V

42 Cross, H J, Beach, J, Levy, L S, Sadhra, S, et al. (1999) *Manufacture, processing and use of stainless steel: a review of the health effects*, Eurofer.

43 National Research Council (1995) *High-Purity Chromium Metal: Supply Issues for Gas-Turbine Superalloys*, Washington, DC, The National Academies Press. [online] Available from: http://www.nap.edu/catalog/9248/high-purity-chromium-metal-supply-issues-for-gas-turbine-superalloys

44 Darrie, Grant (2001) 'Commercial extraction technology and process waste disposal in the manufacture of chromium chemicals from ore'. *Environmental Geochemistry and Health*, 23(3), pp. 187–193.

45 Pourbaix, Marcel (1974) 'Atlas of electrochemical equilibria in aqueous solutions'.

46 Bale, C, Pelton, A and Thompson, W (2013) 'FactSage 6.4, 1976-2013. CRCT-ThermFact Inc. & GTT-Technologies'.

47 Patton, Temple C (1973) 'Pigment handbook.(Vols 1-3)'.

48 Covington, Anthony D (1997) 'Modern tanning chemistry'. *Chem. Soc. Rev.*, 26(2), pp. 111–126.

49 Sposito, Garrison (2008) *The chemistry of soils*, Oxford university press.

50 Barthelmy, D (2014) 'Mineralogy Database: Chromium'. , 2015. [online] Available from: http://webmineral.com/data/Chromium.shtml.

51 Rollinson, C L (1973) 'Chromium: the element'. *Comprehensive Inorganic Chemistry. Oxford: Pergamon Press Ltd*, pp. 624–700.

52 Burns, Roger George (1993) *Mineralogical applications of crystal field theory*, Cambridge University Press.

53 Shannon, R D t and Prewitt, C Tfc (1969) 'Effective ionic radii in oxides and fluorides'. *Acta Crystallographica Section B: Structural Crystallography and Crystal Chemistry*, 25(5), pp. 925–946.

54 Klein, C and Philpotts, A (2012) *Earth Materials: Introduction to Mineralogy and Petrology*, Cambridge University Press. [online] Available from: https://books.google.co.uk/books?id=8rUZBAAAQBAJ

55 Burns, Virginia Mee and Burns, Roger G (1975) 'Mineralogy of chromium'. *Geochimica et Cosmochimica Acta*, 39(6), pp. 903–910.

56 Pauling, Linus (1929) ‘The principles determining the structure of complex ionic crystals’. *Journal of the american chemical society*, 51(4), pp. 1010–1026.

57 Tathavadkar, V D, Antony, M P and Jha, A (2004) ‘An investigation of the mineralogical properties of chemical grade chromite minerals’. *Scandinavian journal of metallurgy*, 33(2), pp. 65–75.

58 Palmer, D (2009) ‘CrystalMaker Software’.

59 Dunitz, J D t and Orgel, L E (1957) ‘Electronic properties of transition-metal oxides-II: Cation distribution amongst octahedral and tetrahedral sites’. *Journal of Physics and Chemistry of Solids*, 3(3), pp. 318–323.

60 Karbowniczek, M, Gładysz, J and Ślęzak, W (2012) ‘Current situation on the production market of FeMn and FeCr’. *Journal of Achievements in Materials and Manufacturing Engineering*, 55(2), pp. 870–875.

61 Soykan, O, Eric, R H and King, R P (1991) ‘The reduction mechanism of a natural chromite at 1416 C’. *Metallurgical Transactions B*, 22(1), pp. 53–63.

62 Niayesh, M J and Dippenaar, R J (1992) ‘The solid-state reduction of chromite’. *INFACON 6.*, 1, pp. 57–63.

63 Chakraborty, Dolly, Ranganathan, S and Sinha, S N (2005) ‘Investigations on the carbothermic reduction of chromite ores’. *Metallurgical and Materials Transactions B*, 36(4), pp. 437–444.

64 Rankin, Willaim John (1979) ‘The composition and structure of chromite during reduction with carbon’. *Arch. Eisenhuttenwes.*, 50(9), pp. 373–378.

65 Algie, Stephen Hopetoun and Finn, Charles William Paul (1984) *Reaction mechanisms in the reduction of Winterveld chrome spinel with graphite and carbon*, Council for Mineral Technology, Randburg (South Africa).

66 Perry, K P D, Finn, C W P and King, R P (1988) ‘An ionic diffusion mechanism of chromite reduction’. *Metallurgical transactions B*, 19(4), pp. 677–684.

67 Soykan, O, Eric, R H and King, R P (1991) ‘Kinetics of the reduction of Bushveld complex chromite ore at 1416 C’. *Metallurgical Transactions B*, 22(6), pp. 801–810.

68 Weber, P and Eric, R H (1993) ‘The reduction mechanism of chromite in the presence of a silica flux’. *Metallurgical Transactions B*, 24(6), pp. 987–995.

69 Xiao, Y, Schuffeneger, C, Reuter, M, Holappa, L and Seppälä, T (2004) ‘Solid state reduction of chromite with CO’, in *Proceedings International Ferroalloy Congress*, pp. 1–4.

70 Wang, Y, Wang, L, Yu, J and Chou, K C (2014) ‘Kinetics of carbothermic reduction of synthetic chromite’. *Journal of Mining and Metallurgy, Section B: Metallurgy*, 50(1), pp. 15–21.

71 Rankin, W J (1979) ‘Reduction of chromite by graphite and carbon monoxide’. *Trans. Inst. Min. Metall. C*, 88.

72 Sundarmurti, N S and Seshadri, V (1985) ‘Kinetics of chromite ore reduction with carbon’. *Transactions of the Indian Institute of Metals*, 38(5), pp. 423–425.

73 Murti, N S Sundar and Seshadri, V (1982) ‘Kinetics of reduction of synthetic chromite with carbon’. *Transactions of the Iron and Steel Institute of Japan*, 22(12), pp. 925–933.

74 Barcza, N (1971) ‘The Mechanism and Kinetics of Reduction of Transvaal Chromite Ores.(Retroactive Coverage)’, in *Electric Furnace Proceedings.*, pp. 88–93.

75 Duong, Hoang Van and Johnston, Rankin F (2000) ‘Kinetics of solid state silica fluxed reduction of chromite with coal’. *Ironmaking & steelmaking*, 27(3), pp. 202–206.

76 Weber, Peter and Eric, R Hurman (2006) ‘The reduction of chromite in the presence of silica flux’. *Minerals engineering*, 19(3), pp. 318–324.

77 Wang, Y, Wang, L and Chou, K C (2015) ‘Effects of CaO, MgO, Al2O3 and SiO2 on the carbothermic reduction of synthetic FeCr2O4’. *Journal of Mining and Metallurgy, Section B: Metallurgy*, 51(1), pp. 17–24.

78 Ding, Y L and Warner, N A (1997) ‘Catalytic reduction of carbon-chromite composite pellets by lime’. *Thermochimica Acta*, 292(1), pp. 85–94.

79 El-Tawil, S Z, Morsi, I M, Shalabi, M E H and Mohamed, O (1991) ‘Soda Ash Roasting of Chromite Concentrate Pellets’. *Neue Hutte(Germany)*, 36(4), pp. 140–145.

80 Xu, Hong-Bin, Zhang, Yi, Li, Zuo-Hu, Zheng, Shi-Li, et al. (2004) ‘Development of a new cleaner production process for producing chromic oxide from chromite ore’. *Journal of Cleaner Production*, 14(2), pp. 211–219.

81 Zheng, Shi-li, Zhang, Yi, Li, Zouhu, Qi, Tao, et al. (2006) ‘Green metallurgical processing of chromite’. *Hydrometallurgy*, 82(3), pp. 157–163.

82 Arslan, Cüneyt and Orhan, Gökhan (1997) ‘Investigation of chrome (VI) oxide production from chromite concentrate by alkali fusion’. *International journal of mineral processing*, 50(1), pp. 87–96.

83 Tel’pish, V V and Vil’nyanskii, Ya E (1969) ‘Kinetics of sodium chromate formation during roasting of chromite charges’. *J. Appl. Chem, USSR*, 42, pp. 1118–1120.

84 Kowalski, Zygmunt and Gollinger-Tarajko, Marta (2003) ‘Environmental evaluation of different variants of the chromium compound production model using chromic waste’. *Waste Management*, 23(8), pp. 771–783.

85 L͡iakishev, Nikolaĭ Pavlovich and Gasik, Mikhail Ivanovich (1998) *Metallurgy of chromium*, Allerton Pr.

86 Sun, Zhi, Zheng, S L and Zhang, Yi (2007) ‘Thermodynamics Study on the Decomposition of Chromite with KOH’. *Acta Metallurgica Sinica (English Letters)*, 20(3), pp. 187–192.

87 Qi, Tian-gui, Liu, Nan, Li, Xiao-bin, Peng, Zhi-hong, et al. (2011) ‘Thermodynamics of chromite ore oxidative roasting process’. *Journal of Central South University of Technology*, 18, pp. 83–88.

88 Moharty, B P and Smith, K (1993) ‘Alkali metal catalysis of carbothermic reduction of ilmenite’. *Transactions--Institution of Mining and Metallurgy, Section C: Mineral Processing & Extractive Metallurgy*, 102.

89 El-Tawil, S Z, Morsi, I M, Yehia, A and Francis, A A (1996) 'Alkali reductive roasting of ilmenite ore'. *Canadian metallurgical quarterly*, 35(1), pp. 31–37.

90 Guo, Yufeng, Huang, Dan, Qiu, Guangzhou and Jiang, Tao (2010) 'Study on Preparation of Titanium-Rich Material Form Ilmenite by Reduction-Magnetic Separation Process'.

91 Rao, Y K (1983) 'Catalysis in extractive metallurgy'. *JOM*, 35(7), pp. 46–50.

92 Yang, Da-Wei, Sun, Ti-Chang, Yang, Hui-Fen, Xu, Cheng-Yan, et al. (2010) 'Dephosphorization mechanism in a roasting process for direct reduction of high-phosphorus oolitic hematite in west Hubei Province, China'. *Journal of University of Science and Technology Beijing*, 32(8), pp. 968–974.

93 Xu, C Y, Sun, T C, Qi, C Y, Li, Y L, et al. (2011) 'Effects of reductants on direct reduction and synchronous dephosphorization of high-phosphorous oolitic hematite'. *Chin. J. Nonferrous Met*, 21, p. 680.

94 Cullity, B D and Stock, S R (2001) 'Elements of X-ray Diffraction'.

95 Hammond, Christopher (2009) *The basics of crystallography and diffraction*, Oxford University Press Oxford.

96 The Australian Radiation Protection and Nuclear Safety Agency (ARPANSA) (2013) 'No Title'. , 2013. [online] Available from: http://www.arpansa.gov.au/AboutUs/index.cfm

97 Tyler Boyd and Barron, Andrew R (2013) *An Introduction to Single-Crystal X-Ray Crystallography*, OpenStax CNX. [online] Available from: http://cnx.org/contents/a1d2bdad-bed2-4b40-aaa2-43e15b3010e4@2.

98 Young, R A (1993) *Introduction to Rieltveld method* Oxford University Press, O. (ed.),

99 Toby, Brian H (2006) 'R factors in Rietveld analysis: How good is good enough?' *Powder diffraction*, 21(1), pp. 67–70.

100 Larson, A C and Von Dreele, R B (1998) 'GSAS General Structure Analysis System, LANSCE, MS-H805'. *Los Alamos: Los Alamos National Laboratory*.

101 Anon (2017) 'Crystallography Open Database'. [online] Available from: http://www.crystallography.net/cod/

102 Jeol Ltd (n.d.) 'Scanning Electron Microscope A to Z'. [online] Available from: http://www.jeoluk.com/

103 Nixon, W C (1971) 'The general principles of scanning electron microscopy'. *Philosophical Transactions of the Royal Society of London. Series B, Biological Sciences*, 261(837), pp. 45–50.

104 Peter, B (2003) 'Theory of XRF, Getting acquainted with the principles'. *The Netherlands: PANalytical BV, Almelo*.

105 Levinson, Ralph (2001) *More modern chemical techniques*, Royal Society of Chemistry.

106 Welz, Bernhard and Sperling, Michael (2008) *Atomic absorption spectrometry*, John

Wiley & Sons.

107 Roine, A and Outokumpu, H S C (2002) ‘Chemistry for Windows: Chemical Reaction and Equilibrium Software with Extensive Thermodynamical Database, Version 5.1, User’s Guide’. *Outokumpu Research Oy, Finland*.

108 Droop, G T R (1987) ‘A general equation for estimating Fe3+ concentrations in ferromagnesian silicates and oxides from microprobe analyses, using stoichiometric criteria’. *Mineralogical magazine*, 51(361), pp. 431–435.

109 Habashi, Fathi (1970) *Principles of extractive metallurgy*, CRC Press.

110 Xiao, Y, Reuter, M and Holappa, L (2001) ‘Reduction of Chromite Pellet with CO’, in *Proceedings of The ninth International Ferroalloys Congress and the Manganese 2001 Health Issues Symposium*, pp. 147–156.

111 Tathavadkar, Vilas D, Antony, M P and Jha, Animesh (2005) ‘The physical chemistry of thermal decomposition of South African chromite minerals’. *Metallurgical and Materials Transactions B*, 36(1), pp. 75–84.

112 Motzfeldt, Ketil (1955) ‘The thermal decomposition. of sodium carbonate by the effusion method’. *The Journal of Physical Chemistry*, 59(2), pp. 139–147.

113 Haasen, Peter (1991) *Phase transformations in materials*, Wiley-VCH.

114 Perry, Dale L (2016) *Handbook of inorganic compounds*, CRC press.

115 Reshetnikov, N A and Vilutis, N I (1958) ‘Fusibility Diagrams of some Binary Systems of Alkali Metal Hydroxides and Salts’. *Zhur. Neorg. Khim*, 3, p. 177.

116 Janz, George J, Allen, Carolyn B, Downey, Joseph R and Tomkins, R P T (1978) *Physical properties data compilations relevant to energy storage. I. Molten salts: eutectic data*, Manchester Coll. of Science and Technology (UK). Dept. of Chemistry.

117 Handbook, Metals and Metallography, Structures (1973) ‘Phase Diagrams, Vol. 8, ASM Handbook Committee, Metals Park, Ohio: Am’. *Soc. Met*.

118 Escudero-Castejon, Lidia, Sanchez-Segado, Sergio, Parirenyatwa, Stephen and Jha, Animesh (2016) ‘Formation of Chromium-Containing Molten Salt Phase during Roasting of Chromite Ore with Sodium and Potassium Hydroxides’. *Journal for Manufacturing Science and Production*, 16(4), pp. 215–225.

119 Ginstling, A M and Brounshtein, B I (1950) ‘Concerning the diffusion kinetics of reactions in spherical particles’. *J. Appl. Chem. USSR*, 23(12), pp. 1327–1338.

120 Spencer, Wilfred Devonshire and Topley, Bryan (1929) ‘CCCLIV.—Chemical kinetics of the system Ag 2 CO 3⇌ Ag 2 O+ CO 2’. *Journal of the Chemical Society (Resumed)*, pp. 2633–2650.

121 Lin, Q, Zhang, M, Xu, R.J. and Song, B (1995) ‘No Title’. *Journal of Chinese Rare Earth Soc.*, 18(9), pp. 209–211.

122 Xiao, Yanping, Reuter, M A and Holappa, Lauri (2001) ‘Kinetic modelling of chromite pellet reduction with CO gas under rising temperatures from 700 to 1520 C’, in *Proceedings of the Ninth International Ferroalloys Congress and the Manganese 2001 Health Issues Symposium: INFACON*.

123 von Bogdandy, Ludwig and Engell, H-J (2013) *The reduction of iron ores: scientific basis and technology*, Springer Science & Business Media.

124 Xiao, Yanping and Holappa, Lauri (1998) 'Kinetic modelling on solid state reduction of chromite pellet with CO', in *8 th International Ferroalloys Congress*, pp. 135–140.

125 Thompson, S and Lawson, F (1984) 'Chromite for the production of chromium chemicals'. *Proc. Australas. b~ st. Min. Metall*, 289, pp. 113–116.

126 Son, Hae-Jun and Lee, Woo-Keun (n.d.) 'Leaching Characteristics of Magnesium from Mine Residues by H2SO4 and HNO3'.

127 Luo, Zheng, Yang, Jing, Ma, Hongwen, Liu, Meitang and Ma, Xi (2015) 'Recovery of magnesium and potassium from biotite by sulfuric acid leaching and alkali precipitation with ammonia'. *Hydrometallurgy*, 157, pp. 188–193. [online] Available from: http://www.sciencedirect.com/science/article/pii/S0304386X15300724

128 Apostolidis, C I and Distin, P A (1978) 'The kinetics of the sulphuric acid leaching of nickel and magnesium from reduction roasted serpentine'. *Hydrometallurgy*, 3(2), pp. 181–196. [online] Available from: http://www.sciencedirect.com/science/article/pii/0304386X78900191

129 Taxiarchou, M, Panias, D, Douni, I, Paspaliaris, I and Kontopoulos, A (1997) 'Removal of iron from silica sand by leaching with oxalic acid'. *Hydrometallurgy*, 46(1), pp. 215–227. [online] Available from: http://www.sciencedirect.com/science/article/pii/S0304386X97000157

130 Yoo, Kyoungkeun, Kim, Byung-Su, Kim, Min-Seuk, Lee, Jae-chun and Jeong, Jinki (2009) 'Dissolution of magnesium from serpentine mineral in sulfuric acid solution'. *Materials transactions*, 50(5), pp. 1225–1230.

131 Panias, D, Taxiarchou, M, Paspaliaris, I and Kontopoulos, A (1996) 'Mechanisms of dissolution of iron oxides in aqueous oxalic acid solutions'. *Hydrometallurgy*, 42(2), pp. 257–265. [online] Available from: http://www.sciencedirect.com/science/article/pii/0304386X9500104O

132 Sarangi, Arabinda (2011) *Sponge Iron Production in rotary kiln*, PHI Learning Pvt. Ltd.

133 Taylor, James (2018) 'Carbothermic Alkali Reduction of Indonesian Chromite'.

134 Hall, Stephen (2017) *Rules of thumb for chemical engineers*, Butterworth-Heinemann.

135 Sonic Corporation (2017) 'Thyphoon Propeller Mixers'. [online] Available from: https://www.sonicmixing.com/propeller-mixer/ (Accessed 20 January 2018)

136 Cotton, Albert F, Wilkinson, Geoffrey, Bochmann, Manfred and Murillo, Carlos A (1999) *Advanced inorganic chemistry*, Wiley.

137 Hagare, Dharma, Sivakumar, Muttucumaru and Singh, Raghu N (2009) 'Wastewater characteristics, management and reuse in mining & mineral processing industries'. *Wastewater Recycle, Reuse, and Reclamation. Volume 1*, pp. 337–371.

138 Anon (2015) 'Textile Industry Wastewater Discharge Quality Standards'. [online] Available from:

http://www.roadmaptozero.com/fileadmin/pdf/WastewaterQualityGuidelineLitReview.pdf

139 United States Environmental Protection Agency (2018) ‘Industrial Wastewater’. [online] Available from: https://www.epa.gov/npdes/industrial-wastewater#mining

140 Carbonfund.org (n.d.) ‘Calculate your footprint’. [online] Available from: https://carbonfund.org/how-we-calculate/

141 United States Environmental Protection Agency (2018) ‘Greenhounse gas emmisions calculator’. [online] Available from: https://www.epa.gov/energy/greenhouse-gas-equivalencies-calculator